# Modélisation 3D du transfert radiatif avec polarisation pour l'étude des surfaces terrestres par télédétection

Yingjie Wang

## To cite this version:

Yingjie Wang. Modélisation 3D du transfert radiatif avec polarisation pour l'étude des surfaces terrestres par télédétection. Sciences de la Terre. Université Paul Sabatier - Toulouse III, 2022. Français. NNT : 2022TOU30173 . tel-03975776

HAL Id: tel-03975776
https://theses.hal.science/tel-03975776v1

Submitted on 6 Feb 2023

# THÈSE

En vue de l'obtention du

## DOCTORAT DE L'UNIVERSITÉ DE TOULOUSE

**Délivré par l'Université Toulouse 3 - Paul Sabatier**

**Présentée et soutenue par**

**Yingjie WANG**

Le 30 septembre 2022

# Modélisation 3D du transfert radiatif avec polarisation pour l'étude des surfaces terrestres par télédétection

Ecole doctorale : **SDU2E - Sciences de l'Univers, de l'Environnement et de l'Espace**

Spécialité : **Surfaces et interfaces continentales, Hydrologie**

Unité de recherche :
**CESBIO - Centre d'Etudes Spatiales de la BIOsphère**

Thèse dirigée par
**Jean philippe GASTELLU ETCHEGORRY et Adrien DESCHAMPS**

Jury
**M. Stéphane JACQUEMOUD,** Rapporteur (Président)
**Mme Gabriela SCHAEPMAN-STRUB,** Rapporteure
**M. Abdelaziz KALLEL,** Examinateur
**M. Zbynek MALENOVSKY,** Examinateur
**M. Tiangang YIN,** Examinateur
**M. Jean-Pierre JESSEL,** Examinateur
**M. Jean-Philippe GASTELLU ETCHEGORRY,** Directeur de thèse
**M. Adrien DESCHAMPS,** Co-directeur de thèse
**M. Ferran Gascon,** Invité
**M. Philippe Maisongrande,** Invité

# DART: AN EFFICIENT 3D MONTE CARLO VECTOR RADIATIVE TRANSFER MODEL FOR REMOTE SENSING APPLICATIONS

by

Yingjie Wang (王英杰)

A thesis submitted for the degree of

*Doctor of Philosophy*

September 2022

# Acknowledgements

First and foremost, I would express my sincere gratitude to my supervisor Jean-Philippe Gastellu-Etchegorry, who led me into the palace hall of the 3D radiative transfer theory and provided continuous guidance, inspirations and supports throughout my PhD study. Without his dedicated and passionate investment in constantly improving DART model over the past 30 years, this dissertation would not have been possible. His conscientious attitude and hard work for pursuing truth and excellence in research deeply infected me and will benefit me through my life. I must thank my co-supervisor Adrien Deschamps as well, who reviewed my progress constantly and gave valuable advice and supports whenever I encountered a bottleneck.

Words cannot express my gratitude to computer scientists in DART team, Nicolas Lauret, Jordan Guilleux and Eric Chavanon. Discussions with Nicolas were always a great pleasure, his insights and differing point of view were a great help in developing new ideas. Many thanks to Jordan who provided me important scripts and templates for managing GUI and SQL database. Finally, thanks should also go to Eric, who was always there for troubleshooting technical issues with compilers, software, operation system, *etc*.

I could not have undertaken this journey without the help of oversea members of DART team, Abdelaziz Kallel, Zbynek Malenovsky and Tiangang Yin. I really enjoy the discussion with Abdelaziz, he provided plenty of insightful explanations and rigorous theoretical derivations that greatly improves my physical understanding of the radiative transfer problem. I greatly benefited from Zbynek’s expertise in the plant science as well as his perceptive comments on presenting my research outcome. Tiangang helped me in getting started the PhD work, collaborating with him was always fruitful because he is very serious and efficient.

I am also grateful to my previous supervisors before the PhD study, Wenzhe Fa, Jean-Baptiste Feret and Claudia Lavalley. Wenzhe supervised my first research project and gave me the first scientific training during my undergraduate study. He also gave me constructive suggestions and encouragement whenever I was in doubt. I am also thankful to Jean-Baptiste and Claudia, who initially recommended me to work in DART team, they led my first collaborative coding project and helped me a lot in studying vegetation using remote sensing data.

I enjoy working with all past and current students and visiting scientists in DART team, including Biao Cao, Ronan Paugam, Florian de Boissieu, Omar Regaieg, Xuebo Yang, Jianbo Qi, Paul Boitard, Zhijun Zhen, Zhu Tao, Quang-Thang Nguyen, Najmeddine Ben Romdhane, *etc*. I owe a great debt to Xuebo who reviewed every stage of the adapted bidirectional path tracing algorithm presented in Chapter 3, she also freely shared her knowledge on LiDAR technologies. Omar is a very good officemate, who was always available for discussion. Many thanks to Biao and Jianbo who gave me many useful suggestions about the research career.

I would like also to extend my thanks to Guanjian Yan, Donghui Xie, Xihan Mu, Yi Li, Kun Zhou, Hailan Jiang from State Key Laboratory of Remote Sensing Science for their hospitality and help during my international mobility funded by Toulouse Graduate School of Earth and Space Science. We had fruitful collaboration work and meaningful discussions, and I also benefited from their experiences in planning and carrying out the field measurement.

This thesis is funded by University of Toulouse and Région Occitanie of France. I also thank Toulouse Metropole, in particular M. Pagès, head of the Digital Land Modelling Service, for providing the urban geometric database of the district of Toulouse used in this work.

In addition, I also want to mention the COVID-19 pandemic without which this dissertation would have been finished one year earlier. It disrupted my work schedule and forced me to distance myself with others and to live in endless loneliness for over a year. This unexpected and special experience strengthened my mental strength and made me recognize the preciousness of the family kinship and friendship from the bottom of my heart.

Finally, but the most importantly, I would like to thank my family for their constant love, confidence, and support and to thank my friends for their company and help.

# List of publications

## Articles

1. **Wang, Y.**, Lauret, N. and Gastellu-Etchegorry, J.-P., 2020. DART radiative transfer modelling for sloping landscapes. *Remote Sensing of Environment*, *247*, p.111902. (DOI: 10.1016/j.rse.2020.111902)

2. **Wang, Y.** and Gastellu-Etchegorry, J.-P., 2020. DART: Improvement of thermal infrared radiative transfer modelling for simulating top of atmosphere radiance. *Remote Sensing of Environment*, *251*, p.112082. (DOI: 10.1016/j.rse.2020.112082)

3. **Wang, Y.** and Gastellu-Etchegorry, J.-P., 2021. Accurate and fast simulation of remote sensing images at top of atmosphere with DART-Lux. *Remote Sensing of Environment*, *256*, p.112311. (DOI: 10.1016/j.rse.2021.112311)

4. Yang, X., Wang, C., Xi, X., **Wang, Y.**, Zhang, Y. and Zhou, G., 2021. Footprint size design of large-footprint full-waveform LiDAR for forest and topography applications: A theoretical study. *IEEE Transactions on Geoscience and Remote Sensing*, *59*(11), pp.9745-9757. (DOI: 10.1109/TGRS.2021.3054324)

5. **Wang, Y.**, Kallel, A., Yang, X., Regaieg, O., Lauret, N., Guilleux, J., Chavanon, E. and Gastellu-Etchegorry, J.-P., 2022. DART-Lux: An unbiased and rapid Monte Carlo radiative transfer method for simulating remote sensing images. *Remote Sensing of Environment*, *274*, p.112973. (DOI: 10.1016/j.rse.2022.112973)

6. Yang, X., **Wang, Y.**, Yin, T., Wang, C., Lauret, N., Regaieg, O., Xi, X. and Gastellu-Etchegorry, J.-P., 2022. Comprehensive LiDAR simulation with efficient physically-based DART-Lux model (I): Theory, novelty, and consistency validation. *Remote Sensing of Environment*, *272*, p.112952. (DOI: 10.1016/j.rse.2022.112952)

7. Regaieg, O., Lauret, N., **Wang, Y.**, et al., 2022. DART Monte-Carlo based modelling of chlorophyll solar-induced fluorescence images of 3D canopies. [ready to submit].

8. **Wang Y.**, Gastellu-Etchegorry J.-P. et al., 2022, 3D Monte Carlo radiative transfer modelling in the Earth-Atmosphere system for simulating adjacency effects. *Remote Sensing of Environment* [ready to submit].

9. Yang, X., Wang, C., Yin, T., **Wang, Y.**, Lauret, N., Xi, X., Li, D. and Gastellu-Etchegorry, J.-P., 2022, Comprehensive LiDAR simulation with efficient physically based DART-Lux model (II): Validation with GEDI and ICESat-2 measurements. *Remote Sensing of Environment* [ready to submit].

## Conferences

1. **Wang., Y.**, Gastellu-Etchegorry, J.-P., Lauret, N., Chavanon, E., Guilleux, J., Al-Bitar, A., Yin, T., Qi, J., Malenovský, Z., Kallel, A., Delavois, A. and Regaieg, O., 2019, April. DART: a tool for studying earth surfaces from space. *2nd edition of Agri AnalyticDays*, Benguerir, Morocco. (Oral)

2. **Wang, Y.** and Gastellu-Etchegorry, J.-P., 2019, July. Improvement and validation of DART atmosphere thermal infrared radiative transfer modelling. *7ème colloque scientifique du groupe Hyperspectral de la Société Française de Photogrammétrie et de Télédétection*, Toulouse, France. (Oral)

3. **Wang, Y.**, Grimaldi, J., Landier, L., Chavanon, E. and Gastellu-Etchegorry, J.-P., 2020, August. Introduction of clouds in DART model. *24th ISPRS Congress-Technical Commission III* (Vol. 43, No. B3, pp. 843-848), Nice, France.

4. Gastellu-Etchegorry, J.-P., **Wang, Y.**, Regaieg, O., Yin, T., Malenovsky, Z., Zhen, Z., Yang, X., Tao, Z., Landier, L., Al Bitar, A. and Lauret, N., 2020, September. Why to model remote sensing measurements in 3D? recent advances in dart: atmosphere, topography, large landscape, chlorophyll fluorescence and satellite image inversion. *5th International Conference on Advanced Technologies for Signal and Image Processing (ATSIP)* (pp. 1-6), Sousse, Tunisia. (Oral)

5. Gastellu-Etchegorry, J.-P., **Wang, Y.**, Regaieg, O., Yin, T., Malenovsky, Z., Zhen, Z., Yang, X., Tao, Z., Landier, L., Al-Bitar, A. and Lauret, N., 2020, September. Recent improvements in the dart model for atmosphere, topography, large landscape, chlorophyll fluorescence, satellite image inversion. *IGARSS 2020-2020 IEEE International Geoscience and Remote Sensing Symposium* (pp. 3455-3458), Hawaii, the United States of America. (Oral)

6. Regaieg, O., **Wang, Y.**, Malenovský, Z., Yin, T., Kallel, A., Delavois, A., Qi, J., Chavanon, E., Lauret, N., Guilleux, J. and Cook, B., 2020, September. Simulation of solar-induced chlorophyll fluorescence from 3d canopies with the dart model. *IGARSS 2020-2020 IEEE International Geoscience and Remote Sensing Symposium* (pp. 4846-4849), Hawaii, the United States of America. (Oral)

7. **Wang, Y.**, Kallel, A., Yang, X., Regaieg, O., Yin, T., Lauret, N., Guilleux, J., Chavanon, E., Malenovský, Z. and Gastellu-Etchegorry, J.-P., 2021, December. DART-Lux: An unbiased and rapid Monte Carlo radiative transfer method for simulating remote sensing images. *American Geophysical Union, Fall Meeting*, New Orleans, the United States of America. (Oral)

8. Malenovský, Z., Janoutová, R., Homolová, L., Regaieg, O., **Wang, Y.**, Lauret, N., Guilleux, J., Chavanon, E. and Gastellu-Etchegorry, J.-P., 2022, May. Impacts of forest structures on canopy SIF modelled for FLEX Cal/Val purposes with Discrete Anisotropic Radiative Transfer. *ESA living planet symposium*, Bonn, Germany. (Oral)

9. Gastellu-Etchegorry, J.-P., Lauret, N., Leon-Tavares, J., Lamquin, N., Bruniquel, V., Roujean, J.-L., Hagolle, O., Zhen, Z., **Wang, Y.**, Regaieg, O., Guilleux, J., Chavanon, E. and Goryl, P., 2022, July. Correction of directional effects in sentinel-2 and -3 images with sentinel-3 time series and dart 3d radiative transfer model. *IGARSS 2022-2022 IEEE International Geoscience and Remote Sensing Symposium*. Kuala Lumpur, Malaysia. (Oral)

10. Malenovský, Z., Regaieg, O., Janoutová, R., **Wang, Y.**, Yin, T., Kallel, A., Lauret, N., Guilleux, J., Chavanon, E. and Gastellu-Etchegorry, J.-P., 2022, September. Advances in the 3D discrete anisotropic radiative transfer model for optical remote sensing of forests. *ForestSAT*, Berlin, Germany. (Oral)

# Abstract

Accurate understanding of the land surface functioning, such as the energy budget, carbon and water cycles, and ecosystem dynamics, is essential to better interpret, predict, and mitigate the impact of the expected global changes. It thus requires observing our planet at different spatial and temporal scales that only the remote sensing (RS) can achieve because of its ability to provide systematic and synoptic radiometric observations. These observations can be transformed to surface parameters (temperature, vegetation biomass, *etc*.) used as input in process models (*e.g.*, SCOPE and ORCHIDEE) or be assimilated in the latter. Understanding the radiation interactions in the land surface and atmosphere is essential in two aspects: interpret RS signals as information about the observed land surfaces and model the processes of functioning of land surfaces where the radiation participates. This explains the development of radiative transfer models (RTMs) that simulate the radiative budget and RS observations. The initial 3D RTMs in the 1980s simulated basic radiation mechanisms in very schematic representations of land surfaces (*e.g.*, turbid medium, geometric primitive). Since then, their accuracy and performance have been greatly improved to address the increasing need of accurate information about land surfaces as well as the advances of RS instruments. So far, two types of improvements are still needed:

1. More accurate and efficient radiative transfer (RT) modelling (polarization, specular reflection, atmospheric scattering, and emission, *etc*.)
2. Representation of land surfaces at different realism degrees and spatial scales.

DART (http://dart.omp.eu) is one of the most accurate and comprehensive 3D RTMs. It simulates the radiative budget and RS observations of urban and natural landscapes, with topography and atmosphere, from the ultraviolet to the thermal infrared domains. Its initial version, DART-FT, in 1992, used the discrete ordinates method to iteratively track the radiation along finite number of discrete directions in voxelized representations of the landscapes. It has been validated with other RTMs, and also RS and field measurements. However, it cannot

simulate RS observations with the presently needed precision because of its voxelized representation of landscapes, and absence of some physical mechanisms (*e.g*., polarization).

During this thesis, in collaboration with the DART team, I developed in DART a new Monte Carlo vector RT mode called DART-Lux that takes full advantage of the latest advances in RT modelling, especially in computer graphics. The central idea is to transfer the radiation transfer problem as a multi-dimensional integral problem and solve it with the Monte Carlo method that is considerably efficient and accurate in computing multi-dimensional integral such as the complex mechanisms (*e.g*., polarization) in realistic representations of 3D landscapes. For that, I implemented the bidirectional path tracing algorithm that generates a group of "source-sensor" paths by connecting two sub-paths, one is generated starting from the light source and another one is generated starting from the sensor. Then, the contribution of these paths to the integral is estimated by the multiple importance sampling. This method allows to accurately and efficiently simulate polarimetric RS observations of kilometre-scale realistic landscapes coupled with plane-parallel atmosphere, with consideration of the anisotropic scattering, the thermal emission, and the solar induced fluorescence. Compared to DART-FT, DART-Lux improves the computer efficiency (*i.e.*, computer time and memory) usually by a factor of more than 100 for large-scale and complex landscapes. It provides new perspectives for studying the land surface functioning and also for preparing Earth observation satellite missions such as the missions TRISHNA (CNES and ISRO), LSTM and next generation Sentinel-2 (ESA), and CHANGE (NASA).

# Résumé

La connaissance du fonctionnement des surfaces terrestres, comme le bilan énergétique, les cycles du carbone et de l’eau et la dynamique des écosystèmes, est essentielle pour mieux interpréter, prévoir et atténuer l’impact des changements globaux. Elle nécessite d’observer notre Planète à différentes échelles de temps et d’espace que seule la télédétection permet de par sa capacité d'observations radiométriques systématiques et synoptiques. Ces dernières sont transformées en paramètres de surface (température, biomasse végétale, *etc.*) utilisés en entrée des modèles de processus (*e.g.*, SCOPE et ORCHIDEE) ou bien assimilées dans ces derniers. Comprendre l'interaction du rayonnement dans les surfaces terrestres et l’atmosphère est essentiel à deux niveaux : interpréter le signal de télédétection en tant qu’information sur les surfaces terrestres observées, et modéliser les processus du fonctionnement des surfaces terrestres où le rayonnement intervient. Ceci explique le développement de modèles de transfert radiatif (MTR) qui simulent le bilan radiatif et les mesures de télédétection. Les premiers MTRs 3D datent des années 1980. Ils simulaient uniquement des mécanismes radiatifs assez simples dans des représentations très schématiques des surfaces terrestres (*e.g.*, milieu turbide, primitive géométrique). Depuis, leur précision et leurs performances ont été énormément améliorées pour répondre au besoin croissant d’informations précises sur les surfaces terrestres et aux progrès en instrumentation de télédétection. A ce jour, deux types d’améliorations sont particulièrement nécessaires :

1. Modélisation plus précise et efficace du transfert radiatif (TR) avec réflexion spéculaire de surface, diffusion polarisée et émission atmosphériques, *etc.*
2. Représentation des surfaces terrestres à différents degrés de réalisme et échelles spatiales.

DART (http://dart.omp.eu) est l’un des MTRs 3D les plus précis et les plus complets. Il simule le bilan radiatif et les observations de télédétection des paysages urbains et naturels, avec relief et atmosphère, de l’ultraviolet à l’infrarouge thermique. Sa version initiale de 1992, appelée DART-FT, utilise la méthode des ordonnées discrètes pour le suivi des rayons selon un nombre

fini de directions dans une représentation voxélisée du paysage. DART-FT a été validé avec d'autres modèles et des mesures terrain et de télédétection. Cependant, il ne peut simuler les mesures de télédétection avec la précision désormais attendue, du fait de son mode de représentation des paysages, de l'absence de certains mécanismes radiatifs et de l'algorithme de suivi des rayons.

Durant cette thèse, en collaboration avec l'équipe DART, j'ai conçu et implanté dans DART le nouveau mode de TR vectoriel DART-Lux qui permet de bénéficier des dernières avancées en infographie. Ainsi, j'ai exprimé le problème du TR en une intégrale multidimensionnelle, résolue avec une méthode Monte Carlo bi-directionnelle très efficace. Cette méthode calcule tout trajet "Source de lumière – Capteur" en combinant un sous-trajet issu des sources de lumière et un sous trajet issu du capteur. La contribution de ces trajets à l'intégrale est estimée par l'échantillonnage préférentiel multiple. Il en résulte une simulation précise et efficace des mesures de télédétection polarimétrique de paysages réalistes à l'échelle kilométrique avec une atmosphère "plan-parallèle", et tous les mécanismes physiques majeurs (diffusion anisotrope, émission thermique, fluorescence chlorophyllienne induite par le soleil, *etc.*). DART-Lux améliore l'efficacité informatique (*i.e.*, temps de calcul, volume mémoire) de DART-FT d'un facteur souvent supérieur à 100 pour de grands paysages 3D complexes. Il ouvre de nouvelles perspectives pour modéliser le fonctionnement des surfaces terrestres, et pour préparer des missions satellitaires d'observation de la Terre comme les missions TRISHNA (CNES et ISRO), LSTM et Sentinel-2 nouvelle génération (ESA), et CHANGE (NASA).

# Contents

# List of figures

# List of tables

# General introduction

Since the industrial revolution, the comfort, health, education, and wealth of human populations have been greatly improved. At the same time, the increasing human activities (*e.g.*, urbanizing, deforestration, burning fossil fuels, *etc*.) significantly impact our planet system and cause most current environmental issues. For example, the rapid and large-scale accumulation of $CO_2$ in the atmosphere is intensifying the global warming and accelerating the climate change, which causes increasingly frequent and more extreme meteorological events such as droughts, floods, and fires. The sharp decline in forest cover accelerates the soil erosion and biodiversity loss, reduces the carbon sink, and disrupts the water cycle. Our society is increasingly aware of environmental issues and their serious consequences for human well-being whereas the impact of global change on land surfaces and the feedback of land surfaces on global change are still not adequately understood and quantified. Therefore, the scientific community is mobilized to study land surface functioning at a variety of spatial and temporal scales, including physical, chemical, and biological processes, urban and ecosystem dynamics, *etc*. These studies are crucial to understand, predict, and mitigate the impact of the expected global changes. They are also important in many other thematic research domains, such as agriculture, forest, urban, climate, snow, *etc*.

Remote sensing, especially with Earth observation satellites, is proving to be a unique and increasingly efficient technology for gathering synoptic information about our planet. The continuous improvement of temporal and spatial resolutions further enhances its ability to monitor the status of, and the changes in, the natural and urban landscapes. In the last decades, there were significant advances in transforming remote sensing data into parameters and surface processes (*e.g.*, temperature, emissivity, albedo, vegetation coverage, evapotranspiration, *etc*.) that provide insight into land surface functioning. In general, the observed radiation is not directly related to the land surface parameter of interest, as it is often the result of complex radiation mechanisms at the observed land surface and is strongly influenced by the atmosphere.

For example, the remote sensing observation of a crop does not directly reveal its instantaneous photosynthetic behaviour and growth stage. Indeed, the observation varies with observing direction that is a function of the anisotropy of radiation emitted and reflected by plant canopies which depends on their optical and structural properties and thus on their physiological status and growth stage. In addition, a remote sensing sensor can only measure one or a few radiometric quantities (*e.g.*, intensity and polarization) in limited spectral ranges and angular directions. It illustrates that remote sensing data depend on both experimental (*e.g.*, land surface three-dimensional (3D) architecture, optical properties, atmospheric conditions, *etc*.) and instrumental (*e.g.*, spectral band, observing direction, field of view, *etc*.) configurations. Therefore, obtaining accurate land surface parameters from remote sensing observations requires a good physical understanding of all the radiation mechanisms involved. This understanding is also important in the preparation of Earth observation satellite missions, especially to predict the accuracy of the information that they plan to provide.

The radiation plays two important roles in the study of land surface functioning. 1) It contributes to major processes in the functioning of land surfaces. For example, the radiation absorbed by vegetation contributes to its photosynthesis and evapotranspiration mechanisms. 2) It carries essential information about the surfaces that emit and scatter it. For example, the spectral and directional variation of radiation originating, and therefore measured, from plants depends on the characteristics (*e.g.*, growth stage) that are often represented by surface parameters (*e.g.*, total biomass and its spatial distribution) adapted to land surface functioning models. Ideally, the application of inversion techniques to remote sensing data gives this information. These two roles of radiation underline the increasing need for physical models, called radiative transfer models (RTMs), that simulate remote sensing observations and the radiation budget (*e.g.*, absorption, thermal emission) of natural and urban landscapes. This simulation should, if possible, be carried out using the same RTM and the same representation of the landscape to ensure good consistency between the simulated remote sensing measurements and radiative budget. MTRs use more or less realistic descriptions of direct (*e.g.*, sun, thermal emitter) and indirect (*e.g.*, atmosphere) light sources, sensors (*e.g.*, camera, pushbroom) and land surfaces if possible, at different scales of analysis (*e.g.*, a crop field and a landscape). Their usefulness depends a lot on their precision and is generally twofold. (1) Establish, study, and quantify the relationships between remote sensing observations and surface parameters (*e.g.*, albedo, thermal exitance and chlorophyll content of the canopy), taking into account the conditions for acquiring these measurements (*e.g.*, solar and observation). (2) Obtain the radiative budget of land surfaces, for example to simulate surface gas and energy fluxes with urban models such as SOLENE (https://aau.archi.fr/crenau/solene) and global land surface models such as ORCHIDEE (https://orchidee.ipsl.fr).

Pioneering 3D RTMs that describe the radiative transfer at land surface were developed in the 1980s. In these models, the studied landscape was usually discretized as cell arrays and the vegetation inside was abstracted as turbid medium (*i.e.*, homogeneous medium consists of infinite number of statistically distributed infinitely small elements). Also, they used relatively simple radiation transfer approaches such as the finite element method. Since then, scientists in radiative transfer field greatly improved the accuracy and performance of RTMs. It is typically the case of DART (https://dart.omp.eu), developed in CESBIO since 1992, that is one of the most general-purpose 3D RTMs. It simulates remote sensing observations (*e.g.*, spectro-radiometer, LiDAR) and the radiative budget of urban and natural land surfaces with topography and atmosphere, including sun induced chlorophyll fluorescence (SIF), from the ultraviolet to the thermal infrared domains. Its initial radiative transfer modelling, called DART-FT, depended on the discrete ordinates method. In this method, the radiation propagates iteratively along a finite number of discrete directions. In addition, the propagation medium is represented by a matrix of voxels which may contain turbid matters that represent vegetation and surface elements (*i.e.*, facets) that represent vegetation (*i.e.*, wood and leaf elements), topography, the building (*i.e.*, houses, roads, *etc*.), …

The RAMI initiative, dedicated to benchmark RTMs under well controlled experiment conditions, illustrates the continuous improvement of RTMs through its five phases from 1999 to 2022 (Pinty et al., 2004, 2001; Widlowski et al., 2015, 2013, 2007). Its third phase (RAMI-III, 2005-2007) was a milestone in terms of quality and number of participating (*i.e.*, 18) RTMs. Up to 52 structurally homogeneous canopy scenarios (turbid vegetation) and 8 structurally heterogeneous canopy scenarios (floating geometric primitives) were tested. It demonstrated, for the first time, a general convergence of the simulated directional reflectance and radiative budget for all canopy scenarios. The submissions of six selected benchmark models (*i.e.*, DART, drat, FLIGHT, Rayspread, raytran, Sprint3) were in unprecedented agreement (relative difference below 1%). The fourth phase of RAMI (RAMI-IV, 2009-2015) significantly improved the representation of land surfaces, with detailed description of plant stems, branches, and leaves. However, many participating models, including the benchmark models selected in RAMI-III, were not adapted to such a degree of complexity, because of their initial design limitations and/or the enormous computation cost. Approximations in the representation of plants and in the modelling of radiative transfer resulted in dispersion between the participating RTMs. This result emphasizes that the improvement of RTMs should be coupled with the improvement of the 3D representation of land surfaces at different spatial scales and complexity degrees. The fifth phase of RAMI (RAMI-V, 2021-present) continues to focus on realistic representations of land surfaces. It takes this further by simulating atmospheric-corrected satellite observations of eight study sites. The new RAMI initiative (RAMI4ATM, 2022-present) is dedicated to the simulation of radiative processes at the land surface, in the atmosphere and the coupling between the two. The continuous efforts of RAMI show the importance of 3D RTMs to support the calibration and validation of satellite observations of land surfaces.

The increasing requirements of precise information about land surfaces requires to improve the modelling of the radiative budget of land surfaces and their remote sensing observations, in connection with the continuous technological advances in remote sensing instruments. In particular, two types of improvements are needed:

- More accurate and efficient modelling of radiative transfer, with the consideration of the nature of the polarized radiation, the radiative coupling of surface-atmosphere, the better description of the anisotropic scattering and emission of land surface elements (*e.g.*, specular scattering, aerosol forward scattering).
- More realistic representations of natural and urban land surfaces and less costly in terms of computer memory.

Due to its initial design limitations, *i.e.*, the discrete ordinates method, it is difficult, if not impossible, that DART-FT to be adapted to address the above-mentioned accuracy and efficiency. For example, hundreds of discrete directions must be set to accurately describe the peak angular distribution of the specular reflection which greatly slows down the computation. On the other hand, since the design of DART-FT, much progress is realised to represent complex 3D artificial landscape and to simulate complex radiation mechanisms such as specular scattering. In addition to this, it is more and more feasible to reconstruct land surfaces at different resolutions in computer using LiDAR signals, photogrammetry, and graphics software (*e.g.*, *xfrog*, *arbaro*).

To meet the increasing requirements of RTMs for simulating remote sensing observations of land surfaces, I developed, in collaboration with DART team, a new Monte Carlo vector radiative transfer mode in DART. This new mode, called DART-Lux, takes full advantage of the latest advances in the modelling of land surfaces and radiative transfer, especially in the computer graphics domain. The central idea of DART-Lux is to transform the complex 3D radiative transfer problem as a multi-dimensional integral problem over the whole path space. The path space includes all possible light paths between the light sources and the sensor, after propagation in the land surfaces and atmosphere. The integral is then solved by the Monte Carlo bidirectional path tracing that generates a group of paths based on sub-paths starting from both the light sources and the sensor. This thesis presents the theory, implementation, and validation of DART-Lux.

Chapter 1 gives an overview of the basic principles and theory of radiometry and radiative transfer. It reviews the properties of the electromagnetic radiation, the related fundamental quantities and definitions that are used in the following chapters. The radiation-matter interactions and their mathematical formulations are also described.

Chapter 2 presents the 3D radiative transfer models and stress their challenges and limitations. The DART model is then presented as well as the motivated developments for better studying the land surface functioning.

Chapter 3 details the preliminary theory and implementation of DART-Lux. The mathematical formulation of the 3D radiative transfer problem as a Lebesgue integral is introduced as well as its Monte Carlo solution. The bidirectional path tracing algorithm and the stochastic process to efficiently generate a group of light paths and evaluate their contributions to the integral are then presented. Finally, the accuracy of DART-Lux and its performance are discussed.

Chapter 4 describes the modelling of atmospheric radiative transfer. The mathematical formulation of the 3D radiative transfer is generalized for both surfaces and volumes. A new Earth-Atmosphere system designed for modelling atmospheric effects based on the bidirectional path tracing algorithm is then presented. Its accuracy is assessed with the atmospheric radiative transfer model MODTRAN. In addition, an experiment that studies the adjacency effect due to the atmospheric scattering is also presented.

Chapter 5 centres on the modelling of polarization. The representation of the polarized radiation and the associated interactions are described. The mathematical formulation of the vector radiative transfer problem in a Lebesgue integral is given, as in Chapter 3 and Chapter 4. The bidirectional path tracing algorithm is then adapted, and its accuracy is evaluated. Then, the impact of polarization on the remote sensing observations is analysed.

# Introduction générale

Depuis la révolution industrielle, le confort, la santé, l'éducation et la richesse des populations humaines se sont considérablement améliorés. Dans le même temps, les activités humaines croissantes (*e.g.*, l'urbanisation, le déboisement, la combustion de combustibles fossiles, *etc.*) ont un impact fort sur notre système planétaire et causent la plupart des problèmes environnementaux actuels. Par exemple, l'accumulation rapide et à grande échelle de $CO_2$ dans l'atmosphère accroît le réchauffement climatique et accélère le changement climatique, ce qui provoque des événements météorologiques de plus en plus fréquents et extrêmes comme les sécheresses, les inondations et les incendies. La forte diminution du couvert forestier accélère l'érosion des sols et la perte de biodiversité, réduit les puits de carbone et perturbe le cycle de l'eau. Notre société est de plus en plus consciente des enjeux environnementaux et de leurs graves conséquences sur le bien-être humain alors que l'impact du changement global sur les surfaces terrestres et la rétroaction des surfaces terrestres sur le changement global ne sont pas encore suffisamment compris et quantifiés. Par conséquent, la communauté scientifique est mobilisée pour étudier le fonctionnement de la surface terrestre à différentes échelles spatiales et temporelles, y compris les processus physiques, chimiques et biologiques, la dynamique urbaine et écosystémique, *etc.* Ces études sont cruciales pour comprendre, prévoir et atténuer l'impact des changements globaux attendus. Elles sont également importantes pour beaucoup d'autres domaines de recherche *(e.g.*, agriculture, forêts, villes, neige).

La télédétection, notamment avec les satellites d'observation de la Terre, s'avère être une technologie unique et de plus en plus efficace pour recueillir des informations synoptiques sur notre planète. L'amélioration constante des résolutions temporelles et spatiales renforce encore sa capacité à suivre l'état et l'évolution des paysages naturels et urbains. Au cours des dernières décennies, des progrès considérables ont été réalisés dans la transformation des données de télédétection en paramètres et processus de surface (*e.g.*, température, émissivité, albédo, taux de couvert végétal, évapotranspiration, *etc.*) qui aident à mieux comprendre le fonctionnement des surfaces terrestres. En général, le rayonnement observé n’est pas directement lié aux paramètres de surface d’intérêt, en particulier parce qu’il résulte de mécanismes radiatifs complexes et dépend de l’atmosphère. Par exemple, l’observation par télédétection d’une culture ne révèle pas directement son comportement photosynthétique instantané et son stade de croissance. En effet, cette observation varie avec la direction d’observation en fonction de l’anisotropie des rayonnements émis et réfléchis par les couverts végétaux qui dépend des propriétés optiques et structurales du couvert et par suite de leur état physiologique et stade de croissance. De plus, un capteur de télédétection ne peut mesurer qu’une ou quelques grandeurs radiométriques (*e.g.*, intensité et polarisation) dans des bandes spectrales et des directions angulaires limitées. Ceci illustre que les données de télédétection dépendent des configurations expérimentales (*e.g.*, architecture tridimensionnelle (3D) de la surface terrestre, propriétés optiques, conditions atmosphériques, *etc.*) et instrumentales (*e.g.*, bande spectrale, direction d’observation, champ de vision, *etc.*). Par conséquent, l’obtention de paramètres de surface terrestre précis à partir d’observations de télédétection nécessite une bonne compréhension physique de tous les mécanismes de rayonnement inclus. Cette compréhension est également importante dans la préparation des missions des satellites d’observation de la Terre, notamment pour prévoir la précision des informations qui seront acquises.

Le rayonnement a 2 rôles majeurs dans le cadre de l’étude du fonctionnement des surfaces terrestres. 1) Il contribue aux processus majeurs du fonctionnement des surfaces terrestres. Ainsi, le rayonnement absorbé par la végétation contribue aux mécanismes de photosynthèse et d’évapotranspiration. 2) Il renseigne sur les surfaces qui l’émettent et le diffusent. Ainsi, la variation spectrale et directionnelle du rayonnement issu, et donc mesuré, des plantes dépend de caractéristiques (*e.g.*, stade de croissance) qui sont souvent représentées par des paramètres de surface (*e.g.*, biomasse totale et sa distribution spatiale) adaptées aux modèles de fonctionnement. Idéalement, l’application de techniques d’inversion aux images de télédétection fournit ces paramètres. Ces deux rôles du rayonnement soulignent le besoin croissant de modèles physiques, appelés modèles de transfert radiatif (MTR), qui simulent les mesures de télédétection et le bilan radiatif (*e.g.*, absorption, émission thermique) des paysages naturels et urbains. Cette simulation doit si possible être réalisée par le même MTR et la même représentation du paysage pour assurer une bonne cohérence entre les simulations des mesures de télédétection et du bilan radiatif. Les MTRs utilisent des descriptions plus ou moins réalistes des sources de lumière directes (*e.g.*, soleil, émetteur thermique) et indirectes (*e.g.*, atmosphère), des capteurs (*e.g.*, caméra, pushbroom) et des surfaces terrestres si possible à différentes échelles d'analyse (*e.g.*, champ de culture et paysage). Leur utilité dépend beaucoup de leur précision et est en général double. (1) Établir, étudier et quantifier les relations entre mesures de télédétection et paramètres de surface (*e.g.*, albédo, exitance thermique et teneur en chlorophylle des couverts), compte tenu des conditions d'acquisition de ces mesures (*e.g.* directions solaire et d'observation). (2) Obtenir le bilan radiatif des surfaces terrestres, par exemple pour simuler les flux de gaz et d'énergie des surfaces avec des modèles urbains comme SOLENE (https://aau.archi.fr/crenau/solene) et des modèles globaux des surfaces terrestres comme ORCHIDEE (https://orchidee.ipsl.fr).

Les premiers MTRs 3D adaptés aux surfaces terrestres ont été développés dans les années 1980. Dans ces modèles, le paysage étudié était généralement discrétisé sous forme de matrice de cellules et la végétation était représentée en tant que milieu turbide (*i.e.*, milieu homogène constitué par une infinité d'éléments infiniment petits, statistiquement distribués). En outre, ils utilisés souvent des approches de transfert de rayonnement relativement simples comme la méthode des éléments finis. Depuis lors, les scientifiques dans le domaine de transfert radiatif ont considérablement amélioré la précision et les performances des MTRs. C'est le cas du modèle DART (https://dart.omp.eu), développé au CESBIO depuis 1992, qui est un des MTRs 3D les plus précis et les plus complets. Il simule les observations de télédétection (*e.g.*, spectro-radiomètre, LiDAR) et le bilan radiatif des paysages urbains et naturels avec relief et atmosphère, y compris la fluorescence chlorophyllienne induite par le soleil (SIF), de l'ultraviolet à l'infrarouge thermique. Sa modélisation initiale du transfert radiatif, appelée DART-FT, dépendait de la méthode des ordonnées discrètes. Dans cette méthode, le rayonnement se propage selon de manière itérative selon un nombre fini de directions. De plus, le milieu de propagation est représenté par une matrice de voxels qui peuvent contenir de la matière turbide qui représentent la végétation et des éléments de surface (*i.e.*, facettes) qui représentent la végétation (*i.e.*, éléments ligneux et foliaires), la topographie, le bâti (*i.e.*, maisons, routes, *etc.*), …

Les cinq phases de l'initiative RAMI de comparaison des MTRs dans des conditions expérimentales bien contrôlées, illustre les améliorations constantes de ces modèles de 1999 à

2022 (Pinty et al., 2004, 2001; Widlowski et al., 2015, 2013, 2007). La troisième phase RAMI-III, de 2005 à 2007, a marqué une étape importante en termes de qualité et nombre (*i.e.*, 18) de MTRs participants. 52 scénarios de canopée structurellement homogène (milieu turbide) et 8 scénarios de canopée structurellement hétérogène ont pour la première fois permis de montrer la convergence des réflectances directionnelle et du budget radiatif simulés de nombreux MTRs. Ainsi, les simulations des six modèles 3D de référence (*i.e.*, DART, drat, FLIGHT, Rayspread, raytran, Sprint3) concordaient avec une différence relative inférieure à 1 %. La quatrième phase RAMI-IV, de 2009 à 2015, a considérablement amélioré la représentation des surfaces terrestres, avec une description détaillée des tiges, branches et feuilles des plantes. Cependant, de nombreux modèles participants, y compris les modèles de référence de RAMI-III, n'étaient pas adaptés au degré de complexité proposé, en raison de limitations dues à leur conception initiale et / ou à un énorme coût de calcul. Par suite, les nécessaires approximations réalisées pour représenter les plantes et la modélisation du transfert radiatif ont résulté en une dispersion des simulations réalisées par les MTRs participants. Ce résultat souligne que l'amélioration des modèles de transfert radiatif doit être couplée à l'amélioration de la représentation 3D des surfaces terrestres à différents échelles spatiales. La cinquième phase RAMI-V, de 2021 à 2022, met aussi l'accent sur la représentation réaliste des surfaces terrestres, avec en plus la simulation des observations satellitaires corrigées des effets atmosphériques pour huit sites d'étude. La nouvelle initiative RAMI4ATM, à partir de 2022, est dédiée à la simulation des processus radiatifs à la surface terrestre, dans l'atmosphère et le couplage entre les deux. L'effort continu de l'expérience RAMI illustre l'importance des MTRs 3D pour l'étalonnage et la validation des observations satellitaires des surfaces terrestres.

Le besoin d'information de plus en plus précis sur les surfaces terrestres nécessite d'améliorer la modélisation du bilan radiatif des surfaces terrestres et de leurs observations de télédétection, en lien avec les incessantes avancées technologiques des instruments de télédétection. En particulier, deux types d'améliorations sont nécessaires :

- Modélisation plus précise et efficace du transfert radiatif, avec prise en compte de la nature du rayonnement polarisé, du couplage radiatif “Terre -Atmosphère”, de l'anisotropie des diffusions et émissions thermiques des éléments de surface terrestre (*e.g.*, diffusion spéculaire et diffusion avant des aérosols).

- Représentations plus réalistes des paysages naturels et urbains, et peu couteuses en termes de mémoire informatique.

Du fait des limites de sa conception initiale basée sur la méthode des ordonnées discrètes, il est difficile, si ce n'est impossible, que DART-FT puisse être adapté pour répondre aux exigences de précision et d'efficacité indiquées ci-dessus. Ainsi, des centaines de directions discrètes sont nécessaires pour décrire précisément la distribution angulaire de la réflexion spéculaire, ce qui ralentit considérablement les calculs. Par contre, depuis la conception de DART-FT, de nombreux progrès ont été réalisés pour simuler à la fois des paysages 3D très réalistes et les mécanismes radiatifs complexes comme la réflexion spéculaire. De plus, il est de plus en plus facile de reconstruire des surfaces terrestres numériques à différentes résolutions avec des mesures LiDAR, la photogrammétrie et des logiciels graphiques (*e.g.*, *xfrog, arbaro*).

Pour répondre aux besoins croissants en termes simulation des mesures de télédétection des surfaces terrestres, j'ai développé, en collaboration avec l'équipe DART, un nouveau mode Monte Carlo de transfert radiatif vectoriel au sein de DART. Ce nouveau mode, appelé DART-Lux, bénéficie des dernières avancées en modélisation des paysages et du transfert radiatif, en particulier dans le domaine de l'infographie. L'idée centrale de DART-Lux est de transformer le problème complexe du transfert radiatif 3D en un problème intégral multidimensionnel sur tout l'espace des trajets de rayon. L'espace de ces trajets comprend tous les trajets possibles entre les sources de lumière et le capteur, après propagation dans les surfaces terrestres et l'atmosphère. L'intégrale est résolue avec la méthode de Monte Carlo de suivi de rayon bidirectionnelle qui génère des trajets "Source-Lumière" à partir de sous trajets issus des sources de lumière et issus du capteur. Cette thèse présente la théorie, l'implémentation et la validation de DART-Lux.

Le chapitre 1 donne un aperçu des principes de base et la théorie de la radiométrie et du transfert radiatif. Il résume les propriétés du rayonnement électromagnétique, les quantités fondamentales et les définitions associées utiles pour les chapitres suivants. Les interactions rayonnement-matière et leurs formulations mathématiques sont aussi décrites.

Le chapitre 2 présente les modèles numériques de transfert radiatif 3D et souligne leurs défis et limites. Le modèle DART est ensuite présenté ainsi que les axes de développement pour mieux étudier le fonctionnement des surfaces terrestres.

Le chapitre 3 détaille la théorie préliminaire et la mise en œuvre de DART-Lux. La formulation mathématique du problème de transfert radiatif 3D est introduite en tant qu'intégrale de Lebesgue ainsi que sa solution Monte Carlo. L'algorithme de suivi de rayon bidirectionnel, le processus stochastique de génération efficace de trajets de rayon, et l'évaluation des contributions des trajets à l'intégrale sont ensuite présentés. Finalement, la précision de DART-Lux et sa performance sont discutées.

Le chapitre 4 décrit la modélisation du transfert radiatif atmosphérique. La formulation mathématique du transfert radiatif 3D pour les surfaces et les volumes est généralisée. Le nouveau système Terre-Atmosphère conçu pour modéliser les effets atmosphériques à partir du suivi de rayon bidirectionnel est présenté. Sa précision est évaluée avec le modèle de transfert radiatif atmosphérique MODTRAN. De plus, une expérience qui quantifie les effets d'environnement du fait de la diffusion atmosphérique est aussi présentée.

Le chapitre 5 est centré sur la modélisation de la polarisation. La représentation du rayonnement polarisé et les interactions associées sont décrites. Une formulation mathématique du problème du transfert radiatif vectoriel dans une intégrale de Lebesgue est donnée, comme dans les chapitres 3 et 4. L'algorithme de suivi de rayon bidirectionnel est ensuite adapté, et sa précision est évaluée. Finalement, l'impact de la polarisation sur les observations de télédétection est analysé.

# Chapter 1

# Radiometry and radiative transfer

This chapter describes the quantities and equations that are used for radiative transfer calculations. We start by describing the nature and the representation of electromagnetic radiation. We then define the radiometric quantities, including the energy flux, irradiance, and radiance, that are needed in radiation measurements and in radiative transfer calculations. We also describe how the radiation is scattered, emitted, and absorbed by a surface or a medium and how these interactions can be mathematically formulated.

Relevant references include (Chandrasekhar, 1960; Mishchenko et al., 2006; Petty, 2006; Pharr et al., 2016). Chandrasekhar (1960) is the most classic reference to radiative transfer. Mishchenko et al. (2006) derive the mathematical formulation of radiative transfer using the theory of statistical electromagnetics instead of the rule of the radiant energy conservation. Petty (2006) gives a good introduction to the basic quantities and principles of the radiative transfer in the atmosphere. Pharr et al. (2016) focuses on the theory and implementation of the physically based rendering. It is a good reference for studying the radiative transfer in land surfaces.

# 1.1 Electromagnetic radiation

## 1.1.1 Radiation representation

The electromagnetic radiation or the electromagnetic wave is a form of energy propagated through space or medium by the periodic vibration of electric and magnetic fields. The propagation direction is always perpendicular to the vibration direction (transverse wave). The radiation in radiative transfer calculations is often represented by the monochromatic plane wave, which is more or less true if the radiation is far from the source or the scatterer. The electric field vector $\boldsymbol{E}$ of a monochromatic plane wave propagating in direction $\hat{\boldsymbol{z}}_P = \hat{\boldsymbol{x}}_P \times \hat{\boldsymbol{y}}_P$ can be represented as the sum of two orthogonal complex vectors $E_{x_P}\hat{\boldsymbol{x}}_{\boldsymbol{P}}$ and $E_{y_P}\hat{\boldsymbol{y}}_P$ (Eq. (1.1)) vibrated in the plane transverse to $\hat{\boldsymbol{z}}_P$. In our definition, $E_{x_P}$ is perpendicular to the meridional plane and $E_{y_P}$ is in the meridional plane (Figure 1.1). Usually, $E_{x_P}$ and $E_{y_P}$ are defined as the horizontal and the vertical oscillation component, respectively.

$$\boldsymbol{E} = E_{x_P}\hat{\boldsymbol{x}}_P + E_{y_P}\hat{\boldsymbol{y}}_P \tag{1.1}$$

with $E_{x_P} = A_{x_P} \cdot e^{-i(kz_P - \omega t - \delta_{x_P})}$ and $E_{y_P} = A_{y_P} \cdot e^{-i(kz_P - \omega t - \delta_{y_P})}$

where $A_{x_P}$ and $A_{y_P}$ are the *amplitude*. $k = 2\pi/\lambda$ is the *wavenumber*, $z_P$ is the propagation distance from the source, $t$ is the oscillation time with *period* $T$, $\omega = 2\pi/T$ is the *angular frequency*, $\delta_{x_P}$ and $\delta_{y_P}$ are the initial phases when $z_P = 0$ and $t = 0$.

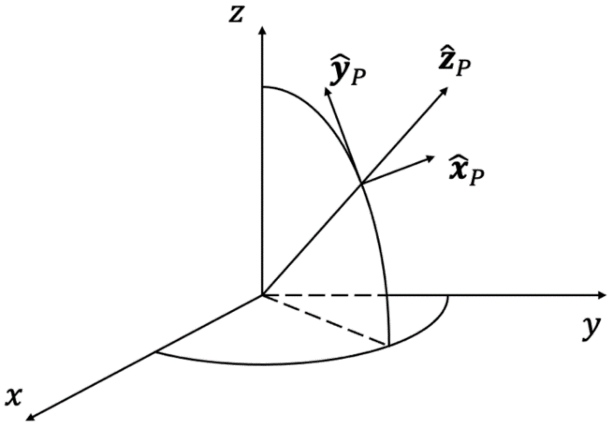

Figure 1.1. The reference coordinate $(\hat{\boldsymbol{x}}_P, \hat{\boldsymbol{y}}_P, \hat{\boldsymbol{z}}_P)$ of a plane wave used to define the Stokes vector. $\hat{\boldsymbol{z}}_P$ is the unit vector of the direction of propagation. $\hat{\boldsymbol{x}}_P$ and $\hat{\boldsymbol{y}}_P$ are orthogonal unit vectors in the plane perpendicular to $\hat{\boldsymbol{z}}_P$, with $\hat{\boldsymbol{x}}_P = \frac{\hat{\boldsymbol{z}} \times \hat{\boldsymbol{z}}_P}{\|\hat{\boldsymbol{z}} \times \hat{\boldsymbol{z}}_P\|}$ perpendicular to the meridional plane ($\hat{\boldsymbol{z}}$, $\hat{\boldsymbol{z}}_P$), and $\hat{\boldsymbol{y}}_P = \hat{\boldsymbol{z}}_P \times \hat{\boldsymbol{x}}_P$ in the meridional plane. Then: $\hat{\boldsymbol{z}}_P = \hat{\boldsymbol{x}}_P \times \hat{\boldsymbol{y}}_P$.

The electromagnetic radiation can also be characterized by quantum properties. Conversely to the continuous wave representation, it sometimes behaves like a series of discrete packets of energy, called *photons*. The energy content $Q_{\text{photon}}$ of each individual photon is solely determined by the *frequency* $\nu$ or *wavelength* $\lambda$ of the radiation via the relationship:

$$Q_{\text{photon}} = h\nu$$

with $h$=$6.62607015 \times 10^{-34}$ J·s the *Planck constant* and $\nu$=$\omega/2\pi$ the frequency that has unit of cycles per second or Hertz (Hz). $\lambda$=$c/\nu$ with $c$ the speed of light in the propagation medium.

Although the electromagnetic radiation has wave and quantum properties, an important point is to know when it should be viewed as wave or as photons. Usually, the wave property matters when considering medium and surface scattering, and the quanta property matters when considering the emission and absorption by individual atoms or molecules. Sometimes, the property point of view does not matter, such as when comping the radiant energy.

### 1.1.2 Polarization and Stokes vector

The transverse wave property is well adapted to inform about the polarization state of the radiation. The geometrical orientation of the oscillation can be any direction perpendicular to the propagation direction. The polarization state is often represented by a column of four real quantities $\boldsymbol{S} = [I, \quad Q, \quad U, \quad V]^{\mathrm{T}}$ (unit: W/m$^2$) known as the *Stokes vector*. $I$ is the radiation intensity. $Q$ is the horizontal/perpendicular (+) or vertical/parallel (–) polarization. $U$ is the 45° (+) and 135° (–) diagonal polarization, with the angle counted anticlockwise starting from $\hat{\boldsymbol{x}}_P$. $V$ is the clockwise (+) and anticlockwise (–) circular polarization (Lee and Pottier, 2017). The Stokes vector of the monochromatic plane wave is computed in Eq. (1.2), with $\varepsilon$ the *permittivity* and $\mu$ the *permeability*, $\delta = \delta_{y_P} - \delta_{x_P}$ is the initial phase difference.

$$\boldsymbol{S} = \begin{bmatrix} I \\ Q \\ U \\ V \end{bmatrix} = \frac{1}{2}\sqrt{\frac{\varepsilon}{\mu}} \begin{bmatrix} E_{x_P}E_{x_P}^* + E_{y_P}E_{y_P}^* \\ E_{x_P}E_{x_P}^* - E_{y_P}E_{y_P}^* \\ E_{x_P}E_{y_P}^* + E_{y_P}E_{x_P}^* \\ i\left(E_{x_P}E_{y_P}^* - E_{y_P}E_{x_P}^*\right) \end{bmatrix} = \frac{1}{2}\sqrt{\frac{\varepsilon}{\mu}} \begin{bmatrix} A_{x_P}^2 + A_{y_P}^2 \\ A_{x_P}^2 - A_{y_P}^2 \\ 2A_{x_P}A_{y_P}\cos(\delta) \\ 2A_{x_P}A_{y_P}\sin(\delta) \end{bmatrix} \tag{1.2}$$

For a monochromatic plane wave: $I = \sqrt{Q^2 + U^2 + V^2}$. However, the amplitude and phase of an actual electric field vector $\boldsymbol{E}$ can fluctuate in time. Indeed, an actual wave can be viewed as a superposition of many monochromatic plane waves with angular frequency randomly distributed in $[\omega - \Delta\omega, \omega + \Delta\omega]$, $\Delta\omega/\omega \ll 1$. It is the so-called quasi-monochromatic plane wave. Its instantaneous Stokes vector cannot be traced by most optical sensors (Mishchenko et al., 2006). Then, the definition of the Stokes vector is extended by averaging the instantaneous component over a time interval $\Delta t$ long compared to the typical period of fluctuation of $\boldsymbol{E}$. (Mishchenko et al., 2006) show that Eq. (1.3) holds for the quasi-monochromatic plane wave. The equality holds only if the ratio $A_{x_P}/A_{y_P}$ and the phase difference $\delta$ are independent of time. Then, $E_{x_P}$ and $E_{y_P}$ are totally correlated (*i.e.*, full polarization).

$$I \geq \sqrt{Q^2 + U^2 + V^2} \tag{1.3}$$

If the amplitudes $A_{x_P}$, $A_{y_P}$ and the initial phases $\delta_{x_P}$, $\delta_{y_P}$ are totally uncorrelated and their averages over a time interval $\Delta t$ verify $\langle A_{x_P}\rangle_{\Delta t}$=$\langle A_{y_P}\rangle_{\Delta t}$ (operator $\langle f(t)\rangle_{\Delta t}$=$\frac{1}{\Delta t}\int_t^{t+\Delta t} f(t')dt'$). Then, the wave is unpolarized ($Q = U = V = 0$). Usually, waves are partially polarized with a state of polarization between the full and un-polarized state with a degree of linear polarization defined as $P_L$=$\sqrt{Q^2 + U^2}/I$, a degree of circular polarization defined as $P_C$=$V/I$, and a degree of polarization $P$:

$$P = \frac{\sqrt{Q^2 + U^2 + V^2}}{I} \tag{1.4}$$

The Stokes vectors $\boldsymbol{S}_\mathrm{A}$ and $\boldsymbol{S}_\mathrm{B}$ of two independent quasi-monochromatic plane waves can be summed up and represented by the combined Stokes vector $\boldsymbol{S}_\mathrm{AB} = \boldsymbol{S}_\mathrm{A} + \boldsymbol{S}_\mathrm{B}$ (Goldstein, 2017).

### 1.1.3 Electromagnetic spectrum

Frequency $\nu$ is the most fundamental characteristic of a harmonic electromagnetic field. It is constant until the radiation is absorbed or converted to another form of energy. In radiative transfer calculations, it is more convenient to use the wavelength $\lambda$ rather than the frequency $\nu$, because the frequencies of interest to Earth observation tend to be numerically large and unwieldy. The two parameters are related by Eq. ((1.5)) in which $c = c_0/n$ is the speed of light in a medium with refractive index $n$, and $c_0 = 299792458$ m/s is the speed of light in vacuum. The corresponding wavelength in vacuum is $\lambda_0 = c_0/\nu = n\lambda$.

$$\lambda = \frac{c}{\nu} \tag{1.5}$$

The electromagnetic spectrum spans a wide range of frequencies, from zero to very high frequencies associated to energetic photons released by nuclear reactions. For practical reasons, scientists and engineers subdivided the spectrum into a few discrete spectral domains, and it exists different definitions of discrete spectral domains in literature. Table 1.1 shows the spectral domains commonly used for vegetation studies.

Table 1.1. Standard definitions of spectral regions of the electromagnetic spectrum for vegetation studies.

| **Region** | **Spectral range** |
|---|---|
| Visible | 0.4 < $\lambda$ < 0.75 $\mu$m |
| Near infrared | 0.75 < $\lambda$ < 1.4 $\mu$m |
| Short wave infrared | 1.4 < $\lambda$ < 3 $\mu$m |
| Mid-wave infrared | 3 < $\lambda$ < 8 $\mu$m |
| Long wave infrared | 8 < $\lambda$ < 15 $\mu$m |
| Far infrared | 15 < $\lambda$ < 1000 $\mu$m |
| Microwave | $\lambda$ > 1000 $\mu$m |

## 1.2 Radiometric quantities

Any radiation transports energy. Considering the wave nature of radiation, the *Poynting vector* gives the instantaneous direction and magnitude of the transported energy. For the harmonic wave, we are interested in the average energy over one complete cycle. This is the *intensity* [W/m$^2$] of the radiation incident onto a unit area perpendicular to the propagation direction. It is proportional to the square of the scalar amplitude $A_E$ of the electric filed at the location:

$$I = \frac{1}{2}\sqrt{\frac{\varepsilon}{\mu}} = \langle A_E^2 \rangle_{\Delta t} \quad \text{with } A_E^2 = A_{x_P}^2 + A_{y_P}^2 \text{ (\textit{cf.} Eq. (1.2))}$$

Considering the quantified nature of radiation, the intensity of a monochromatic plane wave is:

$$I = \phi \cdot Q_{\text{photon}} = \phi \cdot h\nu$$

with $\phi$ the *photon flux* defined as the number of photons per unit area per unit of time.

Several quantities can characterize the energy of the radiation, in relation to the various ways of measuring it, including measurements per unit area, solid angle [sr], time, *etc*. These quantities are described below:

**Radiant energy $\boldsymbol{Q_{\mathrm{e}}}$ [J].** It is the energy that is emitted, reflected, transmitted, or received in the form of electromagnetic radiation during a period of time.

**Radiant flux $\boldsymbol{\Phi(\lambda)}$ [W/$\boldsymbol{\mu}$m].** It is the radiant energy per unit time per unit wavelength interval. Actually, it should be called *spectral radiant flux*. It can be for a unique direction, a cone or a hemisphere, depending on the measurement geometry. It is sometimes called radiant power.

$$\Phi(\lambda) = \frac{d^2 Q_e}{d\lambda dt}$$

**Radiant intensity $\boldsymbol{I(\lambda, \Omega)}$ [W/sr/$\boldsymbol{\mu}$m].** It is the radiant flux that is emitted, reflected, transmitted, or received along direction Ω per unit solid angle per unit wavelength interval.

$$I(\lambda, \Omega) = \frac{d\Phi(\lambda)}{d\Omega}$$

**Irradiance $\boldsymbol{E(\lambda)}$ [W/m$^2$/$\boldsymbol{\mu}$m].** It is the radiant flux incident onto a surface *A* per unit area per unit wavelength interval.

$$E(\lambda) = \frac{d\Phi(\lambda)}{dA}$$

**Exitance (or emittance) $\boldsymbol{M(\lambda)}$ [W/m$^2$/$\boldsymbol{\mu}$m].** It is the radiant flux that exits (*e.g.*, thermal emission, scattering) a surface *A* per unit area per unit wavelength interval.

$$M(\lambda) = \frac{d\Phi(\lambda)}{dA}$$

**Radiance $\boldsymbol{L(\lambda, \Omega)}$ [W/m$^2$/sr/$\boldsymbol{\mu}$m].** It is the radiant flux that exits or is incident onto a surface *A* per unit solid angle per unit projected area of *A* per unit wavelength interval. It is a directional quantity. With $\Omega$ the radiation direction and $\theta$ the angle between the surface normal and the radiation direction, radiance is written:

$$L(\lambda,\Omega)=\frac{d^2\Phi(\lambda)}{d\Omega dA\cos\theta}$$

The irradiance $E(\lambda)$ and exitance $M(\lambda)$ are angular integrals of the radiance. With $2\pi^+$ and $2\pi^-$ the $2\pi$ space of the surface upper and lower hemisphere, respectively, we have:

$$E(\lambda)=\int_{2\pi^-}L(\lambda,\Omega)\cdot\cos\theta d\Omega \quad \text{and} \quad M(\lambda)=\int_{2\pi^+}L(\lambda,\Omega)\cdot\cos\theta d\Omega$$

## 1.3 Radiation interactions in a medium

A radiation $dL(\Omega)$ that crosses any media along a direct $\Omega$ is attenuated by absorption (*i.e.*, $dL_a(\Omega)$) and scattering (*i.e.*, $dL_s^{\text{out}}(\Omega)$) and is increased by thermal emission along $\Omega$ (*i.e.*, $dL_e(\Omega)$) and scattering along $\Omega$ (*i.e.*, $dL_s^{\text{in}}(\Omega)$) of radiation from other incident directions over the $4\pi$ space of directions. Eq. (1.6) expresses the radiation budget for a direction $\Omega$. Absorption converts the energy of the incident radiation into internal energy of the absorbing volume or surface, which gives rise to radiant energy through thermal emission. Scattering does not convert the incident radiant energy into another form of energy. It simply redirects part of the incident radiation. The terms of Eq. (1.6) are detailed below. The radiative properties of molecules and particles used to describe these processes are defined in 1.Appendix A.

$$dL(\Omega)=dL_a(\Omega)+dL_s^{\text{out}}(\Omega)+dL_e(\Omega)+dL_s^{\text{in}}(\Omega) \tag{1.6}$$

### 1.3.1 Scattering

The attenuation due to the scattering of the radiation $L(\lambda,\Omega)$ to other line of sight through an infinitesimal volume (infinitesimal segment $ds$ in the line of sight) for any direction $\Omega$ is proportional to the *scattering coefficient* $\alpha_s(\lambda,\Omega)$ (Eq. (1.7)).

$$\frac{dL_s^{\text{out}}(\lambda,\Omega)}{ds}=-\alpha_s(\lambda,\Omega)\cdot L(\lambda,\Omega) \tag{1.7}$$

Besides, the scattering of the radiation $L(\lambda,\Omega')$ from all directions $\Omega'$ in the $4\pi$ angular space into the line of sight $\Omega$ contributes to the radiation along the direction $\Omega$:

$$\frac{dL_s^{\mathrm{in}}(\lambda,\Omega)}{ds} = \frac{1}{4\pi}\int_{4\pi} L(\lambda,\Omega')\cdot\alpha_s(\lambda,\Omega')\cdot P(\lambda,\Omega'\to\Omega)\,d\Omega' \tag{1.8}$$

with $P(\lambda,\Omega'\to\Omega)$ the *scattering phase function* ($\frac{1}{4\pi}\int_{4\pi} P(\lambda,\Omega'\to\Omega)\,d\Omega'=1$). It gives the angular distribution of the scattered radiation energy due to the incident radiation from $\Omega'$.

In the atmosphere, as most molecules and particles are either spherical or randomly oriented, the extinction coefficient (unit: 1/m, *cf.* Annex A.1) is invariant by rotation (*i.e.*, $\alpha_s(\lambda,\Omega)\equiv\alpha_s(\lambda)$), Eq. (1.7) and (1.8) can be simplified:

$$\frac{dL_s^{\mathrm{out}}(\lambda,\Omega)}{ds} = -\alpha_s(\lambda)\cdot L(\lambda,\Omega)$$
$$\frac{dL_s^{\mathrm{in}}(\lambda,\Omega)}{ds} = \frac{\alpha_s(\lambda)}{4\pi}\cdot\int_{4\pi} L(\lambda,\Omega')\cdot P(\lambda,\Omega'\to\Omega)\,d\Omega'$$

Scattering phase functions commonly used in radiative transfer calculation are presented below.

**Isotropic scattering.** It characterizes the simpler angular distribution of scattering with a constant scattering phase function (Eq. (1.9)). Although scattering is rarely isotropic in nature, it is frequently employed in theoretical studies as a preliminary approximation.

$$P(\lambda,\Omega'\to\Omega) = 1 \tag{1.9}$$

**Rayleigh scattering.** It is the major atmospheric scattering mechanism for elements (*e.g.*, gases) whose *size parameter* $\chi$ (*cf.* Annex A.1) is much smaller than the radiation wavelength (0.002 $<\chi<$ 0.2). The scattered radiation has an intensity that is inversely proportional to the fourth power of the wavelength, with forward and backward scattering that are symmetric. Its phase function is:

$$P_{Rayleigh}(\lambda,\Omega'\to\Omega) = \frac{3}{4}(1+\cos^2\gamma) \tag{1.10}$$

with $\gamma$ the phase angle between the incident direction $\Omega'$ and scattered direction $\Omega$: $\cos\gamma=\Omega'\cdot\Omega$.

Actually, the anisotropy of scattering elements influences $P_{Rayleigh}$. This influence is usually represented by a depolarization factor $\delta$ that modifies $P_{Rayleigh}$ in Eq. (1.11). $\delta$ is a spectral quantity (Bates, 1984; Bucholtz, 1995) that decreases from 0.04545 at 0.2 $\mu$m down to 0.02955 at 0.4 $\mu$m, 0.02730 at 0.8 $\mu$m, and is nearly constant for longer wavelengths. Its relative influence on $P_{Rayleigh}$ of dry air is smaller than 0.1% for wavelengths larger than 0.4 $\mu$m. It is commonly assumed to be equal to 0.0279 as advised by (Young, 1980).

$$P_{Rayleigh}(\lambda, \Omega' \to \Omega) = \frac{3}{2} \cdot \frac{1-\delta}{2+\delta} \cdot \left(\frac{1+\delta}{1-\delta} + \cos^2\gamma\right) \tag{1.11}$$

**Mie scattering.** It is the major scattering mechanism if the size parameter is comparable or larger than the radiation wavelength ($0.2 < \chi < 2000$). The *Maxwell's equations* give its scattering coefficient and phase function for homogeneous spheres with any size parameter $\chi$ and any relative refractive index $m$ (ratio of the particle refractive index to that of the surrounding medium) (Frisvad et al., 2007; Hulst and van de Hulst, 1981). The Mie scattering phase function is:

$$P_{Mie}(\lambda, \Omega' \to \Omega) = \frac{\lambda^2}{2\pi\sigma_s(\lambda)}(|S_1|^2 + |S_2|^2)$$

with $\sigma_S(\lambda) = \frac{\lambda^2}{2\pi}\sum_{n=1}^{\infty}(2n+1) \cdot (|a_n|^2 + |b_n|^2)$

$S_1 = \sum_{n=1}^{\infty}\frac{2n+1}{n(n+1)} \cdot (a_n\pi_n + b_n\tau_n)$

$S_2 = \sum_{n=1}^{\infty}\frac{2n+1}{n(n+1)} \cdot (a_n\tau_n + b_n\pi_n)$

with coefficients $a_n$ and $b_n$ depend on the size parameter $\chi$ and relative refractive index $m$. The coefficients $\pi_n$ and $\tau_n$ depend on the phase angle $\gamma$.

The Henyey-Greenstein phase function (Eq. (1.12)) is frequently used to represent $P_{Mie}$ because it has a convenient mathematical form and is physically meaningful. In most cases $P_{HG}$ is a good approximation of $P_{Mie}$, but in specific cases such as short wave with a small solar zenith, the difference with $P_{Mie}$ can reach 20% (Boucher, 1998).

$$P_{HG}(\lambda, \Omega' \to \Omega) = \frac{1-\mathrm{g}^2}{(1+\mathrm{g}^2 - 2\mathrm{g} \cdot \cos\gamma)^{1.5}} \tag{1.12}$$

with $\mathrm{g} = \frac{1}{4\pi}\int_{4\pi} P(\lambda, \Omega' \to \Omega) \cdot \cos\gamma d\Omega$ the *asymmetry parameter*. Eq. (1.12) can well mimic the scattering forward peak (*i.e.*, $\gamma$=0). In order to also correctly simulate the backward peak (*i.e.*, $\gamma = \pi$), the double Henyey-Greenstein phase function (Eq. (1.13)) is frequently used (Kattawar, 1975).

$$P_{DHG}(\lambda, \Omega' \to \Omega) = \frac{a \cdot (1 - \mathrm{g}_1{}^2)}{(1 + \mathrm{g}_1{}^2 - 2\mathrm{g}_1 \cdot \cos\gamma)^{1.5}} + \frac{(1 - a) \cdot (1 - \mathrm{g}_2{}^2)}{(1 + \mathrm{g}_2{}^2 - 2\mathrm{g}_2 \cdot \cos\gamma)^{1.5}} \tag{1.13}$$

with $\mathrm{g}_1 > 0$, $\mathrm{g}_2 < 0$ and $0 < a < 1$.

## 1.3.2 Absorption and emission

The absorption attenuation of the radiation $L(\lambda, \Omega)$ through an infinitesimal volume is proportional to the *absorption coefficient* $\alpha_a(\lambda, \Omega)$ (Eq. (1.14)).

$$\frac{dL_a(\lambda, \Omega)}{ds} = -\alpha_a(\lambda, \Omega) \cdot L(\lambda, \Omega) \tag{1.14}$$

Figure 1.2 shows the absorption vertical transmittance over [0.3 $\mu$m, 50 $\mu$m] (without cloud or aerosol) for each major absorbing gas (*e.g.*, $H_2O$, $CO_2$, $O_3$, $CH_4$, $N_2O$). For a given wavelength $\lambda$, the total atmospheric absorption vertical transmittance is the product of the absorption vertical transmittance of all individual gases.

$\alpha_a(\lambda, \Omega)ds$ can be thought as the *directional absorptance* of a volume of depth $ds$ because it is the fraction of the incident energy that is absorbed. *Kirchhoff's law* tells that the directional absorptance is equal to the directional emissivity under *thermodynamics equilibrium condition*. Therefore, the thermal emission of the volume of depth $ds$ is:

$$dL_e(\lambda, \Omega) = \alpha_a(\lambda, \Omega) \cdot L_{\mathrm{B}}(\lambda, T) \cdot ds = \alpha_a(\lambda, \Omega) \cdot \frac{2hc^2}{\lambda^5} \cdot \frac{1}{\exp\left(\frac{hc}{\lambda k_{\mathrm{B}} T}\right) - 1} \cdot ds \tag{1.15}$$

where $L_{\mathrm{B}}(\lambda, T)$ is the thermal emission of a blackbody defined in Annex A.1.

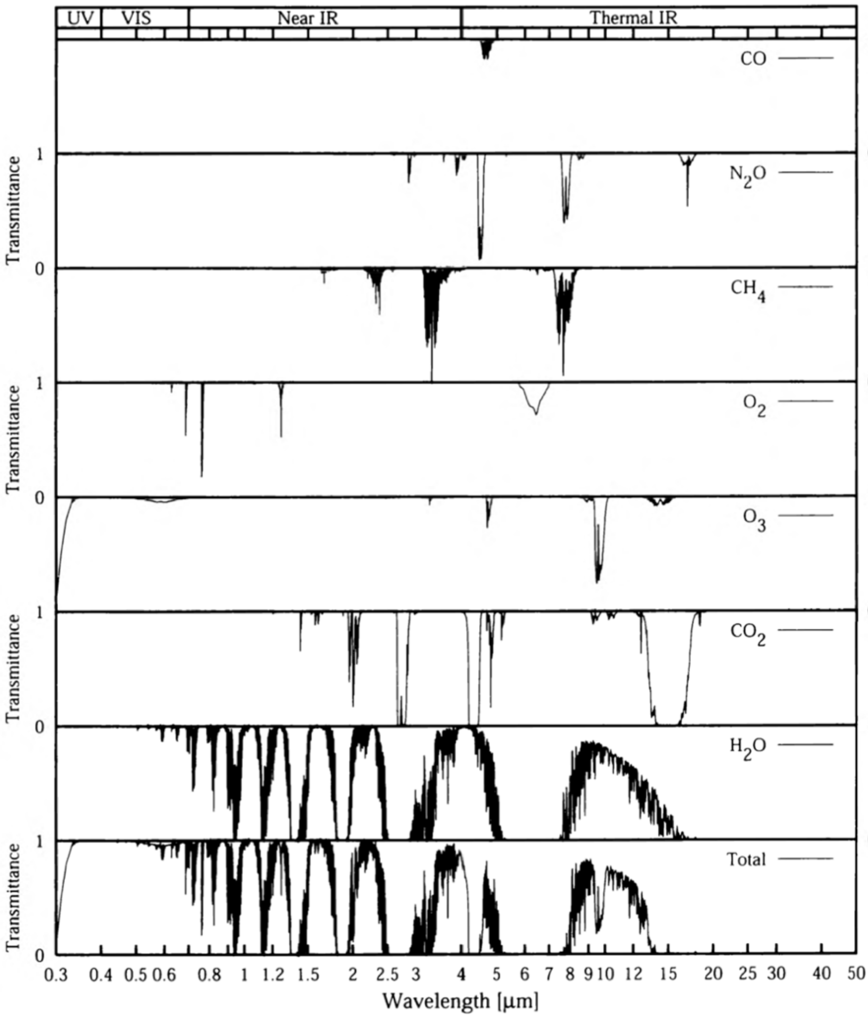

Figure 1.2. Absorption vertical transmittance of a cloud- and aerosol-free midlatitude summer atmosphere, adapted from (Petty, 2006). The seven upper panels are for the seven major gases, and the bottom panel is for the total atmospheric molecules

### 1.3.3 Radiative transfer equation and its formal solution

The combination of the equations (1.6), (1.7), (1.8), (1.14), and (1.15), gives the *radiative transfer equation* (Chandrasekhar, 1960) that describes the radiative transfer in a medium.

$$\frac{dL(\lambda,\Omega)}{ds} = -\alpha_e(\lambda,\Omega)\cdot L(\lambda,\Omega) + \int_{4\pi} \frac{\alpha_s(\lambda,\Omega')}{4\pi}\cdot L(\lambda,\Omega')\cdot P(\lambda,\Omega'\to\Omega)\,d\Omega' + \frac{dL_e(\lambda,\Omega)}{ds} \tag{1.16}$$

For a medium whose elements are spheres, this equation is reduced to:

$$\frac{dL(\lambda,\Omega)}{ds} = -\alpha_e(\lambda)\cdot L(\lambda,\Omega) + \frac{\alpha_s(\lambda)}{4\pi}\cdot \int_{4\pi} L(\lambda,\Omega')\cdot P(\lambda,\Omega'\to\Omega)\,d\Omega' + \frac{dL_e(\lambda,\Omega)}{ds} \tag{1.17}$$

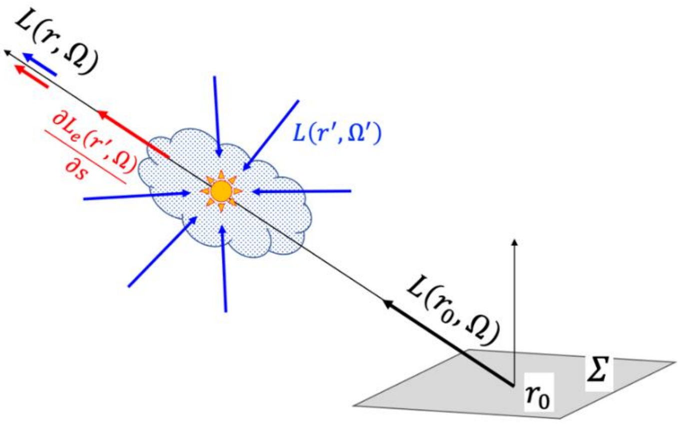

Figure 1.3. Exit radiance $L(r_0,\Omega)$ leaving a surface $\Sigma$ from $r_0$ and transmitted to $r$, with scattering and thermal emission along the path $\overrightarrow{r_0 r}$.

The method of variation of parameters applied to the integro-differential equation (Eq. (1.16)) gives the so-called formal solution of the radiative transfer equation (*cf.* (Chandrasekhar, 1960)).

$$L(r,\Omega) = L(r_0,\Omega)\cdot\mathcal{T}(r\leftrightarrow r_0) + \int_0^s \frac{dL_s(r',\Omega)}{ds}\cdot\mathcal{T}(r\leftrightarrow r')ds' \tag{1.18}$$

with $s = \|r - r_0\|$ the distance between $r$ and $r_0$ (Figure 1.3), $r' = r - s'\Omega$ the location at the distance $s'$ from $r$ along the direction $\Omega$, and the source function:

$$\frac{dL_s(r,\Omega)}{ds} = \int_{4\pi} \frac{\alpha_s(r,\Omega')}{4\pi}\cdot L(r,\Omega')\cdot P(r,\Omega'\to\Omega)d\Omega' + \frac{dL_e(r,\Omega)}{ds} \tag{1.19}$$

Eq. (1.18) shows that radiance $L(r,\Omega)$ at $r$ in a medium is the sum of (1) the transmitted radiance $L(r_0\,,\Omega)$ from $r_0$, with $\mathcal{T}(r\leftrightarrow r_0)$=exp$\left(-\int_0^s \alpha_e(r')ds'\right)$ the *transmittance function*, and (2) the cumulated scattering and thermal emission from $r_0$ to $r$ (Figure 1.3).

## 1.4 Radiation interactions at a surface

When a radiation encounters a surface, part of its energy is scattered in the surface upper hemisphere, transmitted in the surface lower hemisphere, and absorbed by the surface. The absorption increases the surface internal energy, which increases the thermal emission of that surface. Therefore, the surface radiance $L(\Omega)$ is the sum of three radiance terms due to thermal emission $L_e(\Omega)$, scattering $L_r(\Omega)$ and transmittance $L_t(\Omega)$. Surface radiative properties (i.e., reflectance, absorptance, emissivity, transmittance) and definitions are given in 1.Appendix B.

$$L(\Omega) = L_e(\Omega) + L_r(\Omega) + L_t(\Omega) \tag{1.20}$$

### 1.4.1 Reflection

A radiation $L_i(\lambda,\Omega')$ incident in a direction $\Omega'$ onto a surface of normal $\vec{n}$ can generate reflected radiation $L_r(\lambda,\Omega)$ in directions $\Omega$ in the surface upper hemisphere $2\pi^+$ centred on $\vec{n}$. A surface that scatters light isotopically is said to be Lambertian. Natural surfaces are usually not Lambertian. A surface that scatters an incident mono-directional light in a unique direction with a zenith angle equal to the zenith angle of the incident radiation is said to be specular. It is the case of a perfectly smooth water surface. Then, the direction of the scattered radiation is commonly called "specular direction". The scattering behaviour natural surfaces is usually between "Lambertian" and "specular", often with a peak in the specular direction and a peak in the hot-spot direction (*i.e.*, configuration with equal sun and viewing directions).

$$L_r(\lambda,\Omega) = \int_{2\pi^+} L_i(\lambda,\Omega') \cdot f_r(\lambda,\Omega' \to \Omega) \cdot \cos\theta' \, d\Omega' \tag{1.21}$$

with $\theta'$ the angle between $\Omega'$ and $\vec{n}$. $f_r(\lambda,\Omega' \to \Omega)$ is the *bidirectional reflectance distribution function* (BRDF). It is equal to the *bidirectional reflectance factor* (BRF) divided by π. $\Omega$, $\Omega'$ and $\vec{n}$ can be defined in different reference systems; *e.g.*, use of $f_r(\lambda,-\Omega' \to \Omega)$ if $\Omega'$ and $\Omega$ point away from the surface.

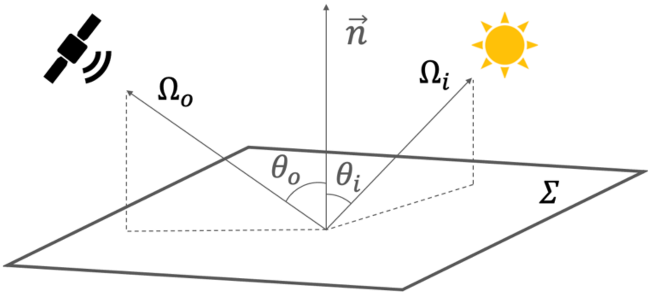

Figure 1.4. Light transport at a surface $\Sigma$. Exit radiance along direction $\Omega$ is due to the reflection of incident radiance along direction $-\Omega'$. Incident angle $\theta'$ is the angle between $\Omega'$ and $\vec{n}$, and exit angle $\theta$ is the angle between $\Omega$ and $\vec{n}$.

BRFs can be derived from many sources, such as laboratory and field measurements, numeric simulations, analytical models, and geometric optics. They are characterized by two important properties: *reciprocity* and *radiant energy conservation*. The reciprocity indicates that a BRF is invariant by changing its incident and exit radiation direction arguments.

$$f_r(\lambda, \Omega' \to \Omega) = f_r(\lambda, \Omega \to \Omega')$$

The radiant energy conservation implies that the reflected radiant flux cannot be greater than the incident radiant flux. Therefore:

$$\int_{2\pi^+} f_r(\lambda, \Omega' \to \Omega) \cdot \cos\theta \, d\Omega \leq 1$$

Five common reflectance models are presented below.

**Lambertian model.** It represents the isotropic reflection and transmission of an ideal matte surface (Eq. (1.22)). A Lambertian surface has equal directional-hemispherical reflectance, bi-hemispherical and bi-directional reflectance: $\mathcal{R}_{\mathrm{DH}}(\lambda, \Omega) = \mathcal{R}_{\mathrm{HH}}(\lambda) = \rho(\lambda) \quad \forall\Omega$. Then:

$$f_r(\lambda, \Omega' \to \Omega) = \frac{\rho(\lambda)}{\pi} \tag{1.22}$$

**RPV (Rahman-Pinty-Verstraete) model.** This parametric model was designed to represent the land surface anisotropy patterns (Rahman et al., 1993). It depends on four parameters: the amplitude $\rho_0$, parameter $k$ in the modified Minnaert function $M_{\mathrm{a}}(k)$ to give the overall BRF angular shape, the asymmetric parameter $g$ of the Henyey-Greenstein function $F_{\mathrm{HG}}(g)$, and the parameter $\rho_c$ of the hotspot function $H_{\mathrm{s}}(\rho_c)$.

$$f_r(\lambda, \Omega' \to \Omega) = \frac{\rho_0}{\pi} \cdot M_{\mathrm{a}}(k) \cdot F_{\mathrm{HG}}(g) \cdot H_s(\rho_c) \tag{1.23}$$

with $M_{\mathrm{a}}(k) = \frac{(\cos\theta' \cos\theta)^{k-1}}{(\cos\theta' + \cos\theta)^{1-k}}$

$F_{\mathrm{HG}}(g) = \frac{1-g^2}{(1+g^2+2g\cos\gamma)^{1.5}}$, $\gamma$ is the phase angle

$H_s(\rho_c) = 1 + \frac{1-\rho_c}{1+\sqrt{\tan^2\theta' + \tan^2\theta - 2\tan\theta' \tan\theta \cos(\varphi - \varphi')}}$

**Hapke model.** It describes the reflection distribution of a plane-parallel and semi-infinite medium made of irregular, randomly distributed particles (single scattering albedo $\omega(\lambda)$, scattering phase function $P(\lambda, \Omega' \to \Omega)$) of large size relative to the radiation wavelength (Hapke, 1986, 1981). It is an approximate solution of the radiative transfer equation (*cf.* section 1.5) with exact computation of single scattering and approximate computation of multiple scattering. It uses three parameters: the single scattering $\omega$ of particles, and the parameters $b_0$ and $h$ that respectively describe the height and the width of the hotspot function $B(b, h, \cos\theta)$.

$$f_r(\lambda, \Omega' \to \Omega) = \frac{\omega}{4\pi(\cos\theta' + \cos\theta)} \cdot \{[1 + B(b, h, \Omega', \Omega)] \cdot P(\lambda, \Omega' \to \Omega) \\ + H(\omega, \cos\theta') \cdot H(\omega, \cos\theta) - 1\} \tag{1.24}$$

with $B(b, h, \cos\theta) = \frac{b}{1+\tan(\gamma/2)/h}$ and $H(\omega, \cos\theta) = \frac{1+2\cos\theta}{1+2\cos\theta\sqrt{1-\omega}}$

**Specular model.** Specular reflection and transmission occur at the interface between two different media (Figure 1.5). In this figure, the axis Ox is in the incidence plane. It is the axis Ox in Figure 1.1 after a rotation of $\pi/2$ around the axis of the radiation propagation. The *Fresnel's law* gives the ratio of the reflected radiation's electric field to that of the incident radiation. It leads to the specular bidirectional reflectance:

$$\mathcal{R}_s(\lambda, \Omega' \to \Omega) = \frac{\mathcal{R}_{x_p} + \mathcal{R}_{y_p}}{2} \tag{1.25}$$

with the reflectance for parallel ($x_p$) and perpendicular ($y_p$) polarized radiation:

$$\mathcal{R}_{x_p} = \left(\frac{\frac{n}{n'}\cos\theta' - \cos\theta}{\frac{n}{n'}\cos\theta' + \cos\theta}\right)^2 \text{ and } \mathcal{R}_{y_p} = \left(\frac{\cos\theta' - \frac{n}{n'}\cos\theta}{\cos\theta' + \frac{n}{n'}\cos\theta}\right)^2 \tag{1.26}$$

$n'(\lambda_0)$ and $n(\lambda_0)$ are respectively the refractive indices of the medium where the incident and transmitted radiation propagate, with $\lambda_0 = n\lambda$ the wavelength in vacuum. $\theta'$ is the local incident zenith angle, and $\theta$ is the local transmitted zenith angle. They are related by the *Snell's law*:

$$n' \sin\theta' = n \sin\theta$$

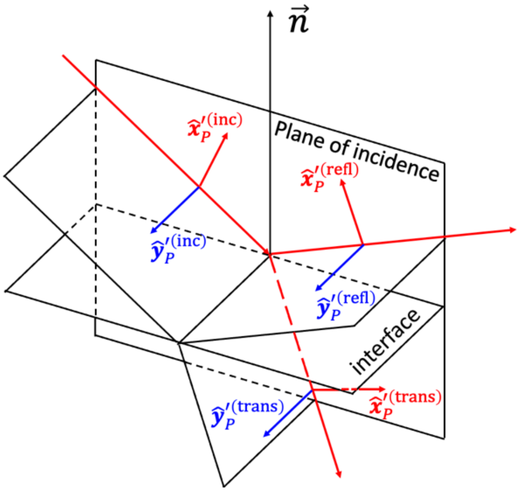

Figure 1.5. Coordinate system at the local surface adapted from (Collett, 1971; Hecht, 1987). The parallel ($\hat{x}'_P$, red colour) and perpendicular ($\hat{y}'_P$, blue colour) components of the incident, reflected and transmitted radiation in the local coordinates are marked.

As the incident and reflected radiation are monodirectional (*i.e.*, infinitesimal solid angle) and symmetric about the normal to the interface, the delta function $\delta(\Omega'\text{-}\Omega'^{*})$ can define the specular BRDF, with $\Omega'^{*}$ symmetric to the reflected direction $\Omega$ with respect to the normal of the interface.

$$f_r(\lambda, \Omega' \rightarrow \Omega) = \mathcal{R}_s(\lambda, \Omega' \rightarrow \Omega) \cdot \frac{\delta(\Omega' - \Omega'^{*})}{\cos\theta'} \tag{1.27}$$

**Microfacet model.** This geometric-optics-based model gives the reflection and transmission of a rough surface idealized as a collection of microfacets characterized by areas much smaller than the considered surface, and statistical distributions of their normals and positions. Two conditions are generally verified in the local coordinates of a differential rough surface $dA$:

(1) The area of the vertical projection of the microfacets is $dA$ (*i.e.*, no overlap in projection). Therefore, with $\Omega_\mathrm{f}$ the normal of facets and $D_\mathrm{m}(\Omega_\mathrm{f})$ the *microfacet distribution function*:

$$\int_{2\pi^+} D_\mathrm{m}(\Omega_\mathrm{f}) \cdot \cos\theta_\mathrm{f}\, d\Omega_\mathrm{f} = 1$$

(2) The visible area in direction $\Omega$ is $dA\cos\theta$. Microfacets can be invisible or shaded by other microfacets depending on the viewing-illumination directions. With $G_\mathrm{m}(\Omega, \Omega_\mathrm{f})$ the *masking-shadowing function*; *i.e.*, area fraction of microfacets with normal $\Omega_\mathrm{f}$ visible in direction $\Omega$:

$$\int_{2\pi^+} G_{\mathrm{m}}(\Omega,\Omega_{\mathrm{f}}) \cdot D_{\mathrm{m}}(\Omega_{\mathrm{f}}) \cdot \max(0,\Omega \cdot \Omega_{\mathrm{f}})\, d\Omega_{\mathrm{f}} = \cos\theta$$

With the microfacet assumption, the BRF of a rough surface depends on $D_{\mathrm{m}}(\Omega_{\mathrm{f}})$ and $G_{\mathrm{m}}(\Omega,\Omega_{\mathrm{f}})$. Frequently, microfacets are assumed to exhibit perfect specular reflection and transmission, as with the *Beckmann distribution* (Beckmann and Spizzichino, 1987)

$$D_{\mathrm{m}}(\Omega_{\mathrm{f}}) = \frac{\exp\left(-\frac{\tan^2\theta_{\mathrm{f}}}{2\sigma^2}\right)}{2\pi\sigma^2 \cdot \cos^4\theta_{\mathrm{f}}} \tag{1.28}$$

with $\sigma$ the RMS of the microfacet slopes. The fraction of microfacet differential area both visible for the incident and exit directions $G_{\mathrm{m}}(\Omega',\Omega)$ is frequently given by the modified *Smith's masking-shadowing function* independent of the microfacet normal and neglect of the height correlation between neighbouring microfacets (Heitz et al., 2013; Smith, 1967):

$$G_{\mathrm{m}}(\Omega',\Omega) = \frac{1}{1+\Lambda(\Omega')+\Lambda(\Omega)} \tag{1.29}$$

with $\Lambda(\Omega) = \frac{1}{2}\left(\mathrm{erf}\left(\frac{1}{\sqrt{2}\sigma\tan\theta}\right) - 1 + \frac{\exp\left(-\frac{1}{2\sigma^2\tan^2\theta}\right)}{\sqrt{2\pi}\sigma\tan\theta}\right)$ and $\mathrm{erf}(x)$ the error function.

The BRDF defined by (Torrance and Sparrow, 1967; Walter et al., 2007) is frequently used:

$$f_r(\lambda,\Omega' \to \Omega) = \frac{\mathcal{R}_s(\lambda,\Omega' \to \Omega) \cdot D_{\mathrm{m}}(\Omega_{\mathrm{f}}) \cdot G_{\mathrm{m}}(\Omega',\Omega)}{4\cos\theta'\cos\theta} \tag{1.30}$$

### 1.4.2 Transmission

A surface illuminated by an incident radiation $L_i(\lambda,\Omega')$ transmits the radiation $L_t(\lambda,\Omega)$ to direction $\Omega$ in the surface lower hemisphere $2\pi^-$.

$$L_t(\lambda,\Omega) = \int_{2\pi^-} L_i(\lambda,\Omega') \cdot f_t(\lambda,\Omega' \to \Omega) \cdot \cos\theta'\, d\Omega' \tag{1.31}$$

with $f_t(\lambda,\Omega' \to \Omega)$ the *bidirectional transmittance distribution function* (BTDF). If the wavelength changes from $\lambda'=\lambda_0/n'$ in the medium that contains the incident radiation, to $\lambda=\lambda_0/n$ in the medium that contains the transmitted radiation, Eq. (1.31) should be written:

$$L_t(\lambda,\Omega) = \int_{2\pi^-} L_i(\lambda',\Omega') \cdot f_t(\lambda' \to \lambda,\Omega' \to \Omega) \cdot \cos\theta'\, d\Omega'$$

The radiant energy conservation requires that $\int_{2\pi^-} f_t(\lambda, \Omega' \to \Omega) \cdot \cos\theta \, d\Omega \leq 1$.
The reciprocity property of BTDF is not always valid because the refraction changes the solid angle $d\Omega'$ and wavelength $\lambda'$ of the incident radiation: $\cos\theta' \, d\Omega' / \cos\theta \, d\Omega = (n/n')^2$ and $\lambda'/\lambda = n/n'$. (Veach, 1997) proves a symmetric relationship for any physically valid BTDF:

$$n'^3 \cdot f_t(\lambda' \to \lambda, \Omega' \to \Omega) = n^3 \cdot f_t(\lambda \to \lambda', \Omega \to \Omega') \tag{1.32}$$

Below, we present three commonly used BTDFs in radiative transfer calculations.

**Lambertian transmission.** Its directional-hemispherical transmittance and bi-hemispherical transmittance are equal: $\mathcal{T}_{\mathrm{DH}}(\lambda, \Omega) = \mathcal{T}_{\mathrm{HH}}(\lambda) = \tau(\lambda), \forall\, \Omega$. The corresponding BTDF is:

$$f_t(\lambda, \Omega' \to \Omega) = \frac{\tau(\lambda)}{\pi} \tag{1.33}$$

**Specular transmission.** The Fresnel's law gives the ratio of the transmitted radiation's electric field to that of the incident radiation. The resulting bidirectional transmittance is:

$$\mathcal{T}_{\mathrm{s}}(\lambda, \Omega' \to \Omega) = \frac{\mathcal{T}_{x_p} + \mathcal{T}_{y_p}}{2} \tag{1.34}$$

with the transmittance for parallel and perpendicular polarized radiation

$$\mathcal{T}_{x_p} = \left(\frac{2\cos\theta'}{\frac{n}{n'}\cos\theta' + \cos\theta}\right)^2 \quad \text{and} \quad \mathcal{T}_{y_p} = \left(\frac{2\cos\theta'}{\cos\theta' + \frac{n}{n'}\cos\theta}\right)^2 \tag{1.35}$$

The BTDF expression in Eq. (1.36) considers the change of solid angle and wavelength of the radiation, with $\Omega'^*$ the incident angle that induces transmittance along $\Omega$ by the Snell's law.

$$f_t(\lambda, \Omega' \to \Omega) = \mathcal{T}_s(\lambda, \Omega' \to \Omega) \cdot \frac{\left(\frac{n}{n'}\right)^3 \cdot \delta(\Omega' - \Omega'^*)}{\cos\theta'} \tag{1.36}$$

**Microfacet model.** The transmission of a rough surface idealized as a collection of specular microfacets considers the change of solid angle and wavelength of the incident radiation due to the refraction. (Walter et al., 2007) propose the following BTDF definition:

$$f_t(\lambda, \Omega' \to \Omega) = \frac{|\Omega' \cdot \Omega_{\mathrm{f}}| \cdot |\Omega \cdot \Omega_{\mathrm{f}}|}{\cos\theta' \cdot \cos\theta} \cdot \frac{\left(\frac{n}{n'}\right)^3 \cdot \mathcal{T}_s(\lambda, \Omega' \to \Omega) \cdot D_{\mathrm{m}}(\Omega_{\mathrm{f}}) \cdot G_{\mathrm{m}}(\Omega', \Omega)}{\left(|\Omega' \cdot \Omega_{\mathrm{f}}| - \frac{n}{n'}|\Omega \cdot \Omega_{\mathrm{f}}|\right)^2} \tag{1.37}$$

### 1.4.3 Absorption and emission

The *absorptance* $\mathcal{A}(\lambda)$ characterizes the absorption of a surface. For an arbitrary surface, it is related to BRDF and BTDF:

$$\mathcal{A}_{\mathrm{D}}(\lambda,\Omega') = 1 - \left[\iint_{2\pi^+} f_r(\lambda,\Omega' \to \Omega) \cdot \cos\theta \, d\Omega + \int_{2\pi^-} f_t(\lambda,\Omega' \to \Omega) \cdot \cos\theta \, d\Omega\right]$$

For a Lambertian surface, *i.e.*, $\mathcal{A}_{\mathrm{D}}(\lambda,\Omega')$=$\mathcal{A}_{\mathrm{H}}(\lambda)$=$a(\lambda)$ ∀ $\Omega',\lambda$, we have: $a(\lambda)$=1-$\rho(\lambda)$-$\tau(\lambda)$.

The internal energy of a surface gives rise to the emission of radiation. The *emissivity* $\varepsilon(\lambda)$ characterizes the capacity of emission. Under the thermodynamic equilibrium condition, the absorptance is equal to the emissivity. The thermal emitted radiance is:

$$L_e(\lambda,\Omega) = \varepsilon_{\mathrm{D}}(\lambda,\Omega) \cdot L_{\mathrm{B}}(\lambda,T) = \varepsilon_{\mathrm{D}}(\lambda,\Omega)\left[\frac{2hc^2}{\lambda^5} \cdot \frac{1}{\exp\left(\frac{hc}{\lambda k_{\mathrm{B}} T}\right) - 1}\right] \tag{1.38}$$

### 1.4.4 Light transport equation

The *light transport equation*, also called *Rendering equation* (Kajiya, 1986; Pharr et al., 2016), describes the surface radiative interaction. It is derived from equations (1.20), (1.21), (1.31) and (1.38):

$$L_o(\lambda,\Omega) = L_e(\lambda,\Omega) + \int_{4\pi} L_i(\lambda,\Omega') \cdot f_s(\lambda,\Omega' \to \Omega) \cdot \cos\theta' \, d\Omega' \tag{1.39}$$

with $f_s(\lambda,\Omega' \to \Omega)$ the *bidirectional scattering distribution function* (BSDF). It is BRDF (*i.e.*, $BRF/\pi$) for reflection and BTDF for transmission.

## 1.5 Introduction to polarized radiative transfer

The radiative transfer is mathematically defined by the radiative transfer equation (Eq. (1.16)) for media and by the light transport equation (Eq. (1.39)) for surfaces. Both are scalar equations based on the heuristic principles of radiometry, *i.e.*, the principle of radiant energy conservation and the notions of ray and ray pencil (*cf.* section 1.3 and 1.4). This approach is intuitive, easy to understand and accurate enough for many radiative transfer applications in particular if the size of objects is much larger than the radiation wavelengths. However, not taking polarization into account is a source of inaccuracy that is less and less acceptable as the need for accuracy increases for many scientific and societal applications. For example, accuracy requirements is ≈ 0.0025 for surface albedo (https://gcos.wmo.int/en/essential-climate-variables/albedo/ecv-requirements) and ≈ 1-2 K for land surface temperature (Sobrino et al., 2016). The consideration of polarization implies to introduce equations directly related to principles of electromagnetism, *i.e.*, Maxwell's equations. Below, we present the vector radiative transfer equation deduced from the statistical electromagnetics and the vector light transport equation deduced from the geometric optics. Their scalar approximations are consistent with the equations in previous sections. Here, the notation $\lambda$ is thus omitted because all the equations are for a monochromatic radiation.

### 1.5.1 Vector radiative transfer equation

(Mishchenko, 2002) demonstrated a microphysical derivation of the vector radiative transfer equation from statistical electromagnetics in case of a medium composed of sparsely positioned, arbitrarily shaped and arbitrarily oriented particles (Eq. (1.40)).

$$\frac{d\boldsymbol{L}(r,\Omega)}{ds} = -\mathbf{K}_e(r,\Omega)\boldsymbol{L}(r,\Omega) + \int_{4\pi} \mathbf{P}(r,\Omega' \to \Omega)\cdot \boldsymbol{L}(r,\Omega')d\Omega' + \frac{d\boldsymbol{L}_e(r,\Omega)}{ds} \qquad (1.40)$$

with $\boldsymbol{L}=L\boldsymbol{S}^*$ the radiance vector defined as the product of scalar radiance $L$ and the reduced Stokes vector $\boldsymbol{S}^*=[1,\ Q/I,\ U/I,\ V/I\ ]^{\mathrm{T}}$. $s$ is the propagation distance along the line of sight and $r$ is the position in the absolute reference. $\mathbf{K}_e$ is the ensemble average of 4×4 *extinction matrix*. $\mathbf{P}$ is the 4×4 *phase matrix* that describes the distribution of the scattered radiance vectors. $\boldsymbol{L}_e$ is the polarized thermal emitted radiance vector averaged over particle state.

This approach links the radiative transfer theory and Maxwell's equations. By replacing the vectors and matrices by their first element, we get the usual form of radiative transfer equation (Eq. (1.16)). (Mishchenko et al., 2006) proved that the scalar approximation is quite accurate if the first order scattering approximation is valid and that the error increases if the contribution of multiple scattering increases. For example, for an homogeneous Rayleigh scattering atmosphere layer (single scattering albedo 0.8, vertical transmittance 0.6) over a black surface, the maximum error of scalar equation can reach ±8%. Also, he proved that the scalar equation gives results accurate enough if particles have a size far larger than the radiation wavelength. For example, for a layer of polydisperse, randomly oriented oblate spheroids (single scattering albedo 1.0, vertical transmittance 0.6, reflective index 1.33, size parameter 0.01) over a black surface, the maximum error of scalar approximation can reach ±10%. The maximum error is reduced to less than ±1.0% if the size parameter is larger than five (Mishchenko et al., 2006).

### 1.5.2 Vector light transport equation

Most land surface elements (*e.g.*, crops, trees, buildings, *etc*.) have dimensions much larger than wavelengths (*i.e.*, size parameter $\gg 1$) in spectral regions from ultraviolet to thermal infrared (Table 1.1). Then, we are in the scattering regime of geometric optics (Petty, 2006). It means that the geometric optics and radiant energy conservation are very good approximations to the electromagnetic theory. Also, the exit radiance vector $\boldsymbol{L}_o(r,\Omega)$ in direction $\Omega$ is the sum of the emitted radiance vector $\boldsymbol{L}_e(r,\Omega)$ in direction $\Omega$ and scattered radiance vector to direction $\Omega$ due to all incident radiance $\boldsymbol{L}_i(r,\Omega')$ from the $4\pi$ space (Eq.(1.41)). $\boldsymbol{L}_e(r,\Omega)$ can be polarized depending on the surface optical properties. For example, it is isotropic and unpolarized for Lambertian surfaces and linearly polarized for specular surfaces (Mishchenko et al., 1999; Tsang et al., 1985).

$$\boldsymbol{L}_o(r,\Omega) = \boldsymbol{L}_e(r,\Omega) + \int_{4\pi} \mathbf{P}(r,\Omega' \to \Omega) \cdot \boldsymbol{L}_i(r,\Omega')\, d\Omega' \qquad (1.41)$$

By replacing the vectors and matrices by their first element, we get the light transport equation (Eq. (1.39)) proposed by (Kajiya, 1986).

# Chapter 2

# Numerical models for radiative transfer

The chapter presents computational approaches to radiative transfer calculations. We review the importance of knowledge about radiative transfer. We then discuss how radiative transfer can be simulated on a computer and review the numerical methods commonly used to solve the radiative transfer problem. Finally, we present the DART model. The improvement of the DART model is the main objective of this thesis.

Good references are (Disney et al., 2000; Gastellu-Etchegorry et al., 1996; Myneni et al., 1989; Pinty et al., 2004, 2001; Wang and Gastellu-Etchegorry, 2021; Widlowski et al., 2015, 2013, 2007). Myneni et al. (1989) review the theory of radiation transport in vegetation canopies. Pinty et al. (2004, 2001) and Widlowski et al. (2015, 2007) document the advances of numerical models that simulate radiative transfer at or near land surfaces. Gastellu-Etchegorry et al. (1996) is the first paper about DART that details its underlying theory.

## 2.1 Why radiative transfer modelling is important

A major interest of the study of radiative transfer is to improve the understanding of the radiation related processes in our environment (*e.g.*, cities, forests, countryside, atmosphere). For example, knowledge of the solar radiation absorbed by a vegetation canopy provides information on its photosynthesis activity. The propagation of radiation in a medium can be described mathematically by the equations of radiative transfer, which allows to study quantitatively the radiation behaviour. Because these equations cannot be solved exactly except under very simplifying assumptions, numerical modelling of radiative transfer is an essential tool to obtain reasonably accurate solution of the radiative transfer in a complex environment.

Electromagnetic radiation carries not only energy but also a wealth of information about the environment in which it originates and/or propagates. However, in general, this information (*e.g.*, moisture, biomass, thermodynamic temperature) cannot be measured directly by a radiometric instrument. This highlights a major objective of radiative transfer modelling: to help retrieve information about our environment through the inversion of radiometric measurements, provided that forward modelling can link the desired information and the radiometric measurements.

Radiative transfer modelling also allows to conduct virtual experiments. It is particularly useful for the preparation of Earth observation satellite missions for which measurements cannot be deduced in advance. The virtual experiment provides preliminary results according to the defined experimental and instrumental configurations which allows to test the mission and improve the calibration and validation activities. The virtual experiment can also generate data sets if existing measurements are not sufficient. For example, it can effectively simulate huge volumes of input data to train deep learning algorithms. It can also help filling gaps in time series measurements of our environment.

If accurate, efficient, and robust methods for radiative transfer modelling can be found, they will inevitably be widely used in many fields such as earth and atmosphere science, thus contributing greatly to the study of increasingly pressing environmental problems.

## 2.2 Radiative transfer models

### 2.2.1 An overview

The radiative transfer model (RTM) is the computer realization of radiative transfer. It provides a platform to manage a virtual environment (also called scene), including the geometry and radiative properties (*e.g.*, scattering, absorption, thermal emission) of its elements, with light sources and sensors, which can be instruments or the environment itself, for example for simulating the radiative budget (*i.e.*, 3D radiation intercepted, scattered, absorbed and emitted). This platform runs a computer algorithm that tracks the radiation in this virtual environment to simulate the required quantities, such as instrument observations and radiation balance.

The design of RTMs depends on the scientific context. Here, for the study of land surface functioning, RTMs aim at simulating radiative transfer at or near land surfaces. Depending on their numerical solution of the radiative transfer equations, these RTMs are often divided into three categories: (i) radiosity methods, (ii) Monte Carlo methods and (iii) discrete ordinates methods.

Radiosity methods, such as DIANA (Goel et al., 1991) and RGM (Qin and Gerstl, 2000), solve the equations of radiative transfer through the inversion of a square matrix that includes the geometric view factors of each surface relative to all other surfaces in the environment. The advantage of the radiosity method is that once the inverse square matrix is computed, the bidirectional reflectance factor (BRF), directional brightness temperature (DBT), images and radiation balance of the environment can be very easily derived. However, the major limitation is that its computation time and computer memory dramatically increase with the complexity of the radiative transfer problem. Also, these methods are limited to simulate certain physical phenomena such as polarization and atmospheric scattering. Monte Carlo methods, such as FLIGHT (North, 1996), Raytran (Govaerts, 1996) and librat (Lewis, 1999), estimate the solution of the equations of radiative transfer by repeatedly sampling the light paths in the environment. This stochastic process converges to the exact solution after sufficient trials and repetitions. The Monte Carlo method is usually considered as the most accurate, flexible, but also the most computer expensive solution of the radiative transfer problem (Goel, 1988; Myneni et al., 1989). Discrete ordinates methods solve the radiative transfer problem for a finite number of radiation propagation directions. Many models use them such as the models of (Kimes and Kirchner, 1982; Myneni et al., 1990), DART (Gastellu-Etchegorry et al., 1996), and DIRSIG (Kraska, 1996). Like the Monte Carlo method, the discrete ordinates method is flexible to simulate a variety of light sources, sensors, radiometric quantities and radiative processes of a complex environment. It is known as a good compromise between accuracy and efficiency. A more detailed table that lists the functionalities of some of the best 3D RTMs are in Annex F.

### 2.2.2 Development and challenge

The RTMs designed in the 1980s and 1990s are usually suited to very abstract representations of land surfaces. For example, plants are represented by turbid medium or simple geometric primitives. They simulate basic radiative processes and limited radiometric measurements (e.g., BRF, images). Since then, many efforts have been made to improve their accuracy and capability. For example, RAPID (Huang et al., 2013), developed on the basis of RGM, significantly improved the computation efficiency of RGM by representing complex vegetation canopies by porous objects (i.e., clusters of triangle/rectangle flat leaves) instead of facets while retaining reasonable accuracy. Rayspread, a speeded up successor of Raytran, implemented the photon spreading method that sends a group of virtual photons to all possible sensors after each interaction (Widlowski et al., 2006). It also provided the absorption, transmission, and albedo products for studying photosynthesis and other physiological processes. DART and DIRSIG were designed upon the discrete ordinates method that they greatly adapted for general-purpose remote sensing applications and land surface studies (Brown and Schott, 2010; Gastellu-Etchegorry et al., 2017, 2015).

The RAdiation transfer Model Intercomparison (RAMI) initiative is a very good indicator of the progress of RTMs. It benchmarks the latest generation RTMs under well controlled experimental conditions close to in-situ measurements. About 60-65% existing RTMs participated to this program. Launched in 2005, the RAMI-III made significant progress compared to RAMI-II (2002-2004) and RAMI-I (1999-2000) in terms of model agreement, model capacity, and model participation. Six benchmark models (*i.e.*, DART, drat, FLIGHT, Rayspread, Raytran, Sprint3) among eighteen participants have good agreement (difference below 1% in relative) for abstract vegetation canopies in which vegetation was represented by layers of homogeneous turbid or geometric primitives (*e.g.*, cuboid, sphere, cylinder, ellipsoid, cone) (Widlowski et al., 2007). It has concluded that RTMs in the 2000s were able to reproduce benchmark results for small-scale abstract representations of land surfaces.

RAMI-IV (2009-2015) significantly improved the representation of the vegetation canopy by representing plants with detailed facet-based descriptions of stems, branches and leaves (Widlowski et al., 2015). Totally six well reconstructed agricultural fields and forests, namely actual canopies, were defined. Plant models were extracted from LiDAR observations or constructed by professional software (*e.g.*, *xfrog*, *arbaro*) using plant allometric measurements. Due to the increase of the complexity of the simulated land surfaces, the participant RTMs, including the benchmark models in RAMI-III, were much less consistent. Indeed, for most of them, the exact and accurate simulations of the RAMI-IV exercises required very high-performance computers. In addition, some of them could only represent plants by geometric primitives. Thus, many RTMs were run with approximations in plant representation and radiative transfer modelling, leading to inaccuracies and differences between participants' models. For example, DART used a relatively small number of discrete directions, and represented pine shoots by turbid foliage medium. As a result, RAMI-IV failed to provide benchmark results as RAMI-III. The successor RAMI-V (2021-present) added two more actual canopies and required participative RTMs to reproduce atmospheric-corrected satellite images of eight experiment fields in addition to in-situ measurements such as BRF and radiation fluxes. The latest initiative, RAMI4ATM (2022-present), proposes to simulate satellite observations under a variety of atmospheric conditions. Although the analysis of submissions in RAMI-V and RAMI4ATM is not yet published, it shows the ambition to use RTMs in the calibration and validation activities of Earth observation satellite missions.

RAMI and many remote sensing applications highlight four challenges for RTMs:

1. Realism of land surface representations. It greatly impacts the accuracy of the simulation of the radiative budget and remote sensing observations of the land surfaces. For example, row orientations in crop fields and tree plantations lead to very large directional effects in satellite images. The required realism of the representation of land surfaces depends on the expected accuracy on the simulated radiative budget and remote sensing observations. It also depends on the scale of analysis. For example, the spatial variation

of the row orientation changes its influence on the radiative budget and remote sensing observations at different spatial scales.

2. Realism of radiation representation. Radiation is usually characterized by its wavelength, intensity, direction, and polarization. However, up to now, most RTMs do not consider polarization both in the atmosphere and land surfaces. Its simulation should increase the accuracy of radiative transfer modelling (*cf*. section 1.5.1).
3. Surface-atmosphere radiative coupling. This coupling influences the spectral irradiance of the Earth's surface, in particular in presence of high reflectance surfaces and at small wavelengths where the atmosphere tends to be highly scattering. However, most RTMs neglect this radiative coupling or treat it in an approximated way (*e.g.*, the spatially heterogeneous upwelling radiation from land surfaces is considered as homogeneous).
4. Optical properties of scene elements. Most RTMs assume that scenes are made of Lambertian surfaces (*i.e.*, isotropic reflectance). It is a very large simplification in many cases. In particular, the specular behaviour of surfaces (*e.g.*, foliar elements in vegetation canopies and windows in buildings) should be considered. Depending on the viewing direction and the scene considered, it should greatly improve the simulation of observations in all spectral ranges, including the thermal infrared range.

Also, the 3D RTMs are more and more used in generating datasets for the inversion of land surface parameters. For example, Miraglio (2021) simulated DART images to train machine learning models to derive the leaf equivalent water thickness (EWT) and leaf mass per area (LMA) from synthetic spectral images of forests (Miraglio, 2021). Makhloufi (2021) and Abdelmoula (2021) did massive DART simulations (order of 400,000) to create look-up tables in order to train machine learning models to derive biophysical properties (LAI, leaf chlorophyll content, leaf water content, leaf mesophyll structure) of olive trees from Sentinel-2 satellite images (Abdelmoula et al., 2021; Makhloufi et al., 2021). In the frame of DIAPOS project financed by French Space Agency (CNES), CESBIO simulated more than 1 million high-resolution DART images to train a machine learning model in order to assess the potential of high-resolution satellites to detect a specific type of tree (*i.e.*, Babassu: palm tree) in a forest. To make these applications operational, 3D RTMs must be improved in terms of accuracy and also computer time and memory.

## 2.3 The classic DART model

### 2.3.1 A general introduction

DART (Discrete Anisotropic Radiative Transfer) is a large code (≈ 500,000 lines of C++) developped at CESBIO since 1992 (Gastellu-Etchegorry et al., 2015, 1996). It is one of the most accurate and comphrehensive 3D RTMs in the remote sensing community. Based on the discrete ordinate method, it can simulate the radiative budget and remote sensing observations (*e.g.*, in-situ, ariborne and satellite measurements.) of urban and natural land surfaces, with topography and atmopshere, from ultraviolet to thermal infrared domain. It can simulate also the solar induced fluorescence of vegetation canopies and the terrestrial, airborne, and space-based LiDAR signal (point cloud, waveform, photon counting). DART shows good agreement (differences below 1% in relative) with the other five benchmark models (*i.e.*, drat, FLIGHT, Rayspread, Raytran, Sprint3) in RAMI-III (Widlowski et al., 2007). It was also successfully evaluated by satellite, airborne and ground-based measurements. For example, Landier et al. (2018) found shortwave albedo ≈ 2.5% between DART and time series flux tower measurements for the whole year of 2016 (Landier et al., 2018) in the frame of URBANFLUX projet. In the thermal infrared, RMSE was less than 2 K between DART and measured (in-situ, airborne hyperspectral ASH, spaceborne ASTER) brightness temperature of three homogeneous land surfaces (bare soil, green grass, sand) at 5 thermal bands (8.1 - 8.5, 8.5 - 8.9, 8.9 - 9.3, 10.3 - 11.0, 11.0 - 11.7 $\mu$m) (Sobrino et al., 2011). These authors found the same accuracy between directional brightness temperature (viewing zenith between -60° and 60°) simulated by DART and measured by a goniometric system. Similarly (Guillevic et al., 2003), an RMSE = 1.25 K was found between DART and in-situ infrared thermometer (spectral band: 8 - 14 $\mu$m) brightness temperature of a cotton row crop, for five viewing zenith angles (0°, 20°, 40°, 60°, 80°).

DART was initially designed for simulating directional reflectance and images of turbid vegetation canopies in the visible and near infrared domains (Gastellu-Etchegorry et al., 1996). Later, it included a specifically designed atmospheric radiative transfer modelling module (Gascon et al., 2001) and was extended to the thermal infrared domain with the provision of 3D radiation balance of canopies (Guillevic et al., 2003). Afterwards, it supported an additional representation of the vegetation and urban elements by polygons with various surface scattering properties (*e.g.*, Lambertian, Hapke and RPV models) (Gastellu-Etchegorry, 2008). It was also improved to simulate LiDAR, passive sensors (*e.g.*, pushbroom scanner, frame camera, hemispheric camera) (Gastellu-Etchegorry et al., 2015; Yin et al., 2016), and the solar induced fluorescence (SIF) and polarization (Gastellu-Etchegorry et al., 2017). Subsequently, it integrated a powerful ray-object intersection kernel Embree (Wald et al., 2014) that considerably accelerated its modelling (Qi et al., 2019b).

### 2.3.2 Numerical modelling

DART tracks the radiation from the source, through the environment to the sensor with an adapted iterative discrete ordinates method. The light sources can be the sun, the sky, the laser, and any thermal emitter in the land surfaces and in the atmosphere. The sensor can be a pushbroom scanner, a frame camera, a hemispheric camera, an orthographic camera, a LiDAR receiver at an arbitrary position with an arbitrary orientation. It is also the scene itself for simulating the scene 3D radiation balance.

The environment (classic DART scene) consists of the stratified atmosphere and the 3D heterogeneous land surface (Figure 2.1). The land surface is made up of surfaces (*e.g.*, facets, triangles) and volumes (*e.g.*, turbid vegetation, air, soot). It is placed in a 3D voxel matrix to ease the transfer of radiation and to ease the computation of radiation fluxes on any interface. The elements in the environment (*e.g.*, 3D object, triangle cloud, digital elevation model (DEM), and digital surface model) can either be directly imported or be constructed by DART object generating modules. The surface scattering is characterized by BSDF, such as the Lambertian, RPV, Hapke and specular model. The media (*e.g.*, turbid vegetation, air, soot) are defined by their physical and optical properties. For example, the fluid (*e.g.*, gases, aerosols, soot) is defined by its concentration, cross-section, single scattering albedo, and scattering phase function. The atmosphere is made up of three levels: (1) bottom atmosphere inside the land surface voxel matrix, (2) mid-atmosphere made up of voxels, and (3) high atmosphere made up of layers. The atmosphere SQL database stores vertical profiles of atmospheric constituents (temperature, pressure, concentration, *etc*.) of six standard atmospheres (*e.g.*, USSTD76, MIDLATSUM) (Anderson et al., 1986) and five standard aerosol models (*e.g.*, rural, urban) (Shettle and Fenn, 1979). It also stores the associated spectral optical properties (*e.g.*, vertical transmittance, single scattering albedo, scattering phase function, *etc*.) of these atmosphere models that are derived from MODTRAN (Berk et al., 1987) simulations and LOWTRAN

(Kneizys et al., 1983) source code. The vertical profiles and the optical properties of gases and aerosols derived from the reanalysis datasets (*e.g.*, ECMWF reanalysis: https://www.ecmwf.int) or the measurements (*e.g.*, Aeronet: https://aeronet.gsfc.nasa.gov) can also be imported.

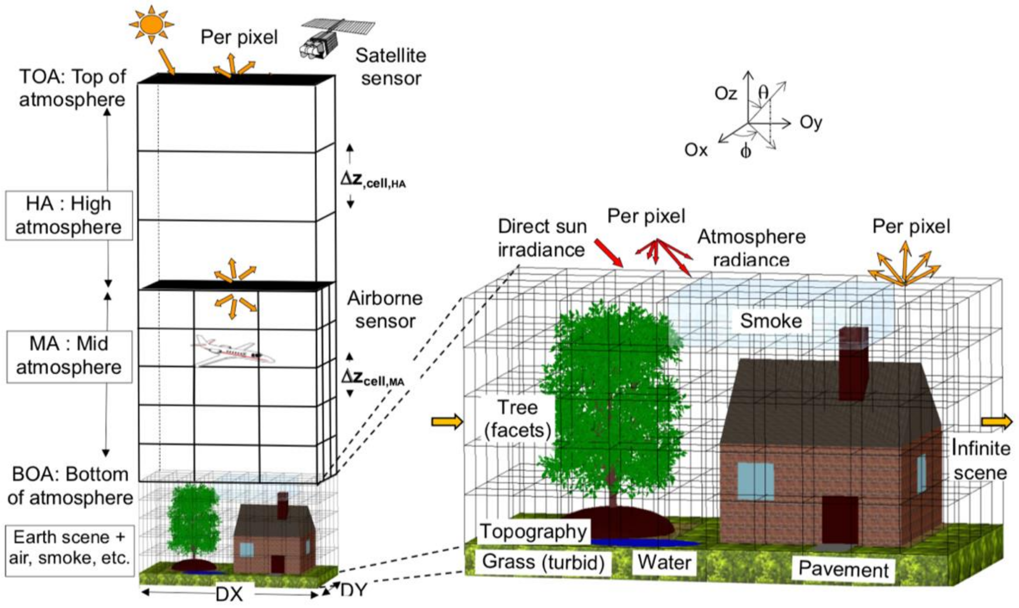

Figure 2.1. The classic DART scene, adapted from Gastellu-Etchegorry et al. (2015). Land surface elements are made up of triangles, and/or fluid and turbid vegetation. The land surface itself is in a voxel matrix in order to ease the transfer of radiation. The atmosphere has three levels: upper level made of layers, middle level made of voxels of any size, and lower level in the landscape.

The radiation intercepted by the surface/volume in the iteration $k$ is scattered to $N$ discrete directions $\{\Omega_n\}_{n=1,2,\dots,N}$ in the iteration $k+1$. The radiant flux of the exit radiation along any direction is computed by solving the equations of radiative transfer at the local surface/volume. The iterative procedure ends if the radiation is totally absorbed, escapes from the environment, is captured by the sensor or reaches the predefined maximum iteration number. The radiation scattered into the field of view (FOV) of the sensor contributes to the corresponding sensor measurements (Gastellu-Etchegorry et al., 1996; Yin et al., 2013). The transfer of radiation in the atmosphere and at the land surface is modelled sequentially. The land surface is set up in one of three ways: isolated scene (Figure 2.2.a) for isolated land surface; repetitive scene (Figure 2.2.b) for infinitely repeated land surface; and infinite slope (Figure 2.2.c) for infinitely repeated sloping land surface (Wang et al., 2020). The atmosphere is assumed to be an infinitely parallel plane with implicit consideration of its curvature. Figure 2.3 illustrates the five major steps of modelling in the environment in order to simulate images with atmospheric effects (Grau and Gastellu-Etchegorry, 2013; Wang et al., 2020): (1) Source illumination followed by the atmospheric scattering and emission; (2) Land surface emission and radiative transfer; (3) Surface-atmosphere radiative coupling; (4) Land radiative transfer of the atmosphere backscattered radiation; (5) Transfer of the bottom of atmosphere (BOA) upward radiation to the sensor and top of atmosphere (TOA).

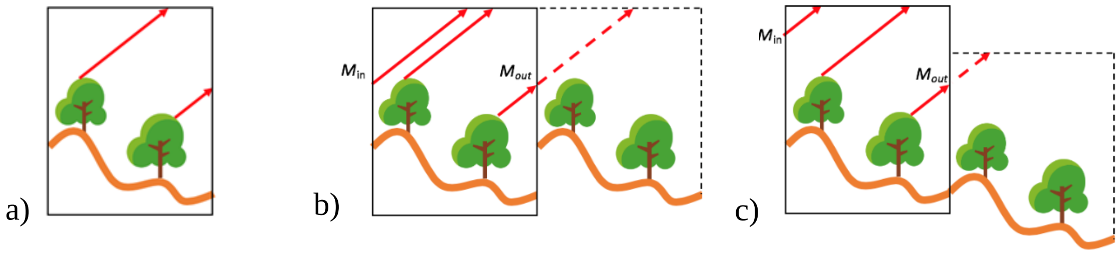

Figure 2.2. The three ways to arrange the DART 3D land surface. a) Isolated scene. b) Repetitive scene. c) Infinite slope. The simulated land surface is framed by a black box. The dotted box frames one of the fictive neighbourhoods of the simulated scene.

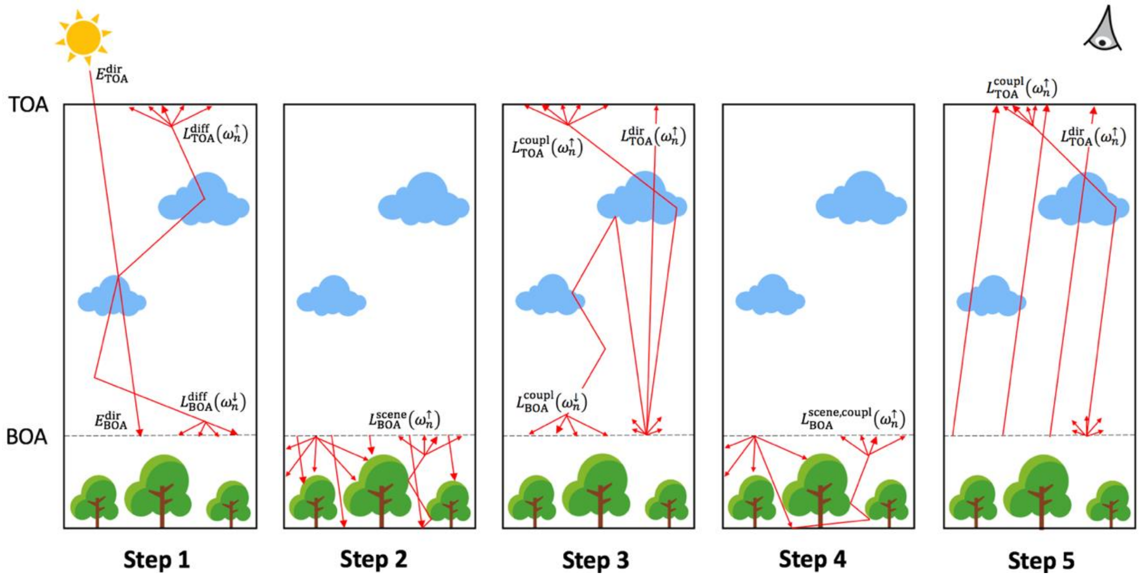

Figure 2.3. Major steps of the radiative transfer in classic DART. Step 1: Sun illumination and atmospheric scattering and emission. Step 2: Land surface radiative transfer, including scattering, absorption, and emission. Step 3: Atmosphere - Land surface radiative coupling. Step 4: Land surface transfer of the atmosphere backscattered radiation. Step 5: Transfer of the BOA upward radiation to the sensor and TOA.

### 2.3.3 Framework architecture

DART has a complete framework for 3D radiative transfer modelling (Gastellu-Etchegorry et al., 2015), with specific input data, processing modules and output data (Figure 2.4).

**Input data.** Input data set up all the parameters to run a DART simulation. A graphical user interface (GUI) allows one to import/manage 3D objects and DEM, to define and assign optical and temperature properties, to configure the atmosphere (geometry, vertical profile and optical properties of gases, aerosols and/or clouds) and to select the products. All the input parameters are encoded in extensible markup language (XML) for easy data access.

**Processing modules.** Four major modules process the input data. (1) Direction: it subdivides the $4\pi$ space into $N$ user-defined discrete directions for the transfer of radiation. (2) Phase: it computes bandpass optical properties, temperature properties, and scattering phase functions of turbid and fluid (gas, aerosol, cloud, soots, *etc*.) media. (3) Mock-up: it creates the 3D mock-up of the land surface and the atmosphere, assigns the temperature and optical properties per scene element, and computes the atmosphere vertical profiles (pressure, temperature, density). (4) Dart: it simulates the transfer of radiation at the land surface and in the atmosphere and generates the requested measurements.

**Output data.** Two types of products are simulated. (1) Remote sensing observation: satellite/airborne/in-situ radiometric images, BRF/DBT, LiDAR signal, solar induced fluorescence, *etc*. (2) Radiative budget: 1D/2D/3D distribution of intercepted, absorbed, scattered, and emitted (*i.e.*, thermal emission, solar induced fluorescence) radiation. All products (*i.e.*, images and 1D/2D/3D radiative budget) can be stored per type of scene element (*e.g.*, leaf, trunk) and in a look-up-table. In addition, DART also generates geometric products such as the digital surface model, the area per type of scene element, the leaf area index, *etc*.

In addition to the above mentioned bacis modules, DART contains many useful modules for quick and easy simulations and subsequent analysis of the simualted results. For example, the PROSPECT and FLUSPECT modules simulate leaf optical properties as a function of leaf structural and biochemical properties (Féret et al., 2017; Jacquemoud and Baret, 1990; Vilfan et al., 2016). The MARMIT module (Bablet et al., 2018; Dupiau et al., 2022) module simulates the soil reflectance as a function of water content. The object module can construct 3D urban and natural object (*e.g.*, geometric primitive of trees, DEMs, buildings). The application programming interface (API) can create complex 3D environment (DART scene) without manipulating the interface. The sequence module can manage and launch a series of simulations with any set of variable input parameters. The broadband module can generate broadband radiative budget and sensor measurements with specific sensor response functions. Several display tools can visualize the input data and the simulated results, and so on.

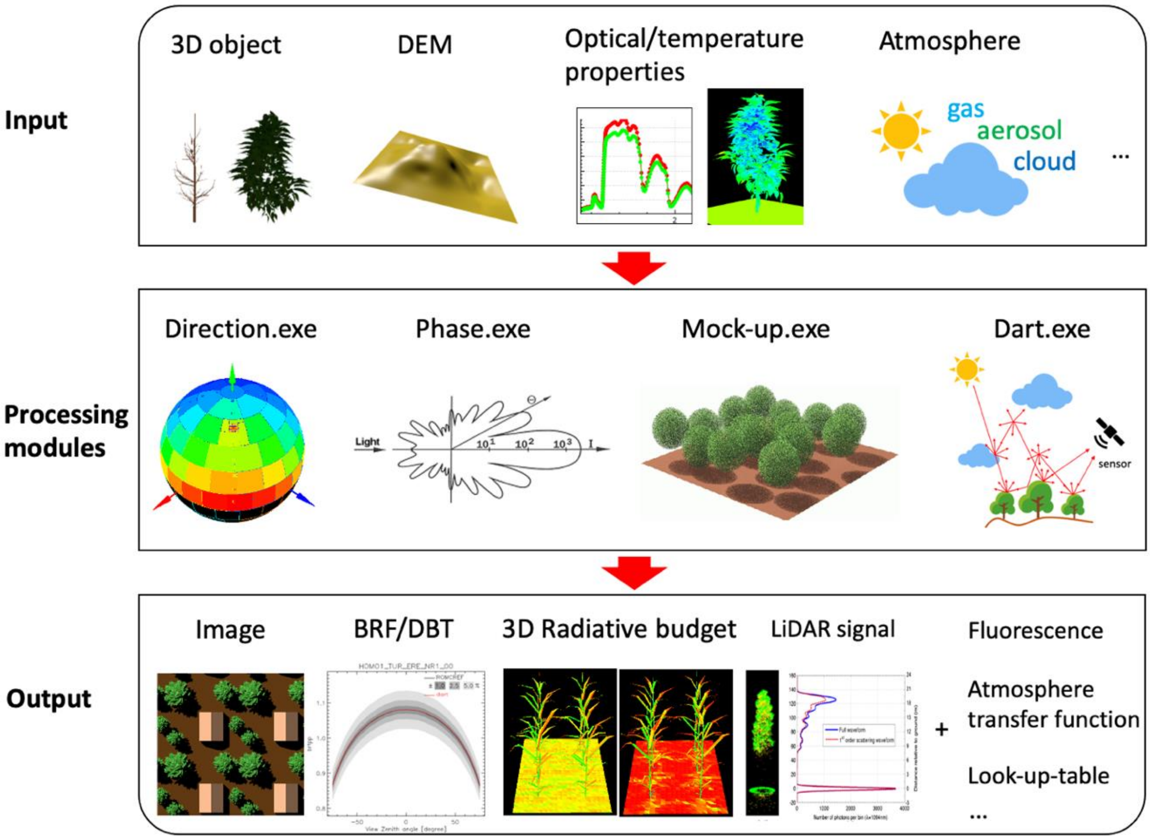

Figure 2.4. DART framework. Its four modules (Direction, Phase, Mock-up, Dart) simulate remote sensing observations and the radiative budget for any instrumental/experimental configurations.

## 2.3.4 Motivations and objectives

The flux tracking method of standard DART, called DART-FT hereinafter, uses a breadth-first strategy to simulate radiation transfer: the radiation intercepted in each iteration $k$ is stored in computer memory (*e.g.*, location, direction, spectral flux, *etc*. per radiation), to be absorbed and scattered to $N$ discrete directions, one by one, at iteration $k+1$. Because this approach leads to an unmanageable number of rays to track, several accelerating techniques were implemented to limit the numbers of rays and scattering points. Three examples are given here. (1) In each turbid voxel, possibly with facets: scattering is simulated from only two optimally located points per incident direction in this voxel. In addition, for each sub-voxel, the scattering points associated to the same or very close incident directions are grouped as a single scattering point, which greatly decreases the number of scattering points. (2) In each voxel with facets: points of a same facet that intercept radiation with same or very close incident directions and that are spatially very close are grouped as a unique interception point, which greatly decreases the number of scattering points. (3) In any voxel: rays that exit a cell in a same direction through very close points on the same cell face are grouped, which greatly decreases the number of rays.

However, even with all its accelerating techniques, DART-FT becomes less and less adapted for simulating larger and larger scenes at high spatial resolution, as is increasingly needed in research works. Indeed, the computational time and memory of DART-FT increase dramatically with the complexity of the radiative transfer problem (*e.g.*, more detailed description of the scene) and scattering events (*e.g.*, larger scattering albedo of atmospheric constituents or surfaces). Two examples are given here. (1) DART-FT treats any ray regardless of its contribution to the expected result. For example, when simulating a sensor image, all possible rays are tracked, even those that have a negligible impact on the sensor signal. The computational problem is even worse when simulating accurate specular reflectance, the hot spot phenomena and the polarization. (2) DART-FT does not optimize the modelling strategy (*e.g.*, geometry instancing) if scene elements (*e.g.*, trees) are identical to a scaling xyz and rotation xyz.

Actually, most limitations of DART-FT for efficient and accurate simulations with realistic 3D scenes are due to its initial design: the discrete ordinate method that discretizes the space of coordinates and directions. On the other hand, the Monte Carlo method, known as a good solver of high dimensional problem, shows great potential to overcome these limitations (*cf.* section 2.2). In addition, scientists in computer graphics made great progress in the design of variance reduction methods, the acceleration of raytracing and the optimization of representation of realistic artificial landscape. This is why we have chosen to develop in DART an accurate, efficient, and robust Monte Carlo method for vector radiative transfer modelling at the Earth’s surface and in the atmosphere, that takes full advantage of the latest advances in computer graphics.

# Chapter 3

# DART-Lux: theory and implementation

The main goal of this chapter is to develop a new 3D Monte Carlo radiative transfer mode in DART namely DART-Lux to accurately and efficiently simulate the remote sensing observations of an environment represented by a collection of surfaces (Chapter 4 further generalizes its formalism and implementation for fluids and turbid media in the volumes). We first demonstrate how to transform the 3D radiative transfer problem to a multi-dimensional integral problem of the form

$$L^{(j)} = \int_{\mathcal{D}} f^{(j)}(\bar{r})\, d\mu(\bar{r})$$

Then, we present how to estimate this integral with a robust Monte Carlo integration method, *i.e.*, the *multiple importance sampling*. Usually, both the straightforward sampling of a series of random variables (more precisely, the vertices of a random light path in the environment) and the straightforward evaluation of their contribution to the integral estimate are computationally expensive. We thereby implement the *bidirectional path tracing algorithm* to efficiently sample a group of paths that connect the light source and the sensor and to incrementally evaluate the estimate without any redundant computation. Finally, the performance of this new DART-Lux is assessed and discussed.

# 3.1 Theoretical background

## 3.1.1 The three-point form of the light transport equation

Eq. (1.39) indicates the radiation leaving a surface is the sum of scattered and emitted radiation. It can be alternatively expressed in a *three-point form* or *area form* (Figure 3.1) where an integral over all surfaces $A$ replaces the integral over the angular space using the dependence of the solid angle of the incident radiation on the surface area $d\Omega_i(r') = \frac{dA(r'').\cos\theta_o^{r''}}{\|r''-r'\|^2}$:

$$L(r' \to r) = L_e(r' \to r) + \int_A L(r'' \to r') \cdot f_s(r'' \to r' \to r) \cdot G(r' \leftrightarrow r'') dA(r'') \qquad (3.1)$$

with vertex $r \in A(r) \subseteq$ surface $A$ whose BSDF is $f_s(r''{\to}r'{\to}r)$ and $L_e(r' \to r)$ the surface thermal radiance from $r'$ to $r$. For compactness, the wavelength notation is omitted since all wavelength-dependent quantities are monochromatic and defined for the same medium. The *geometric term* $G(r' \leftrightarrow r'')$ defines the geometric relationship between vertices $r'$ and $r''$:

$$G(r' \leftrightarrow r'') = V(r' {\leftrightarrow} r'') \cdot \frac{\cos\theta_i^{r'} \cdot \cos\theta_o^{r''}}{\|r'' - r'\|^2}$$

with $V(r' \leftrightarrow r'')$ the *visibility function* ($V(r' \leftrightarrow r'') = 1$ if there is nothing between $r'$ and $r''$, and 0 otherwise), $\theta_i^{r'}$ the incident angle at $r'$ and $\theta_o^{r''}$ the exit angle at $r''$.

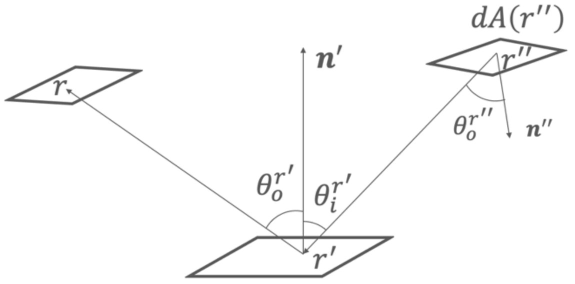

Figure 3.1. Geometry of the three-point form: a ray from $r''$ on $dA(r'')$ is intercepted at $r'$, then scattered to $r$, with exit angle $\theta_o^{r''}$ at $r''$, incident angle $\theta_i^{r'}$ at $r'$, and exit angle $\theta_o^{r'}$ at $r'$.

In the absence of medium, an incident radiation on a surface is the exit radiation from a previous surface. Therefore, we can incrementally expand Eq. (3.1) to an infinite sum of multi-dimensional integration with $r_0$ a vertex on the sensor lens, $r_1$ a previous vertex, and so on. Each term is the result of emitted radiance $L_e(r_n \to r_{n-1})$ from the light source after $n-1$ scattering events:

$$\begin{aligned} L(r_1 \to r_0) = {} & L_e(r_1 \to r_0) + \int_A L_e(r_2 \to r_1) \cdot f_s(r_2 \to r_1 \to r_0) \cdot G(r_1 \leftrightarrow r_2) dA(r_2) \\ & + \int_A \int_A L_e(r_3 \to r_2) \cdot f_s(r_3 \to r_2 \to r_1) \cdot G(r_2 \leftrightarrow r_3) \cdot f_s(r_2 \to r_1 \to r_0) \cdot G(r_1 \leftrightarrow r_2) dA(r_3) dA(r_2) \\ & + \int_A \int_A \int_A L_e(r_4 \to r_3) \cdot f_s(r_4 \to r_3 \to r_2) \cdot G(r_3 \leftrightarrow r_4) \cdot f_s(r_3 \to r_2 \to r_1) \cdot G(r_2 \leftrightarrow r_3) \cdot f_s(r_2 \to r_1 \\ & \qquad \to r_0) \cdot G(r_1 \leftrightarrow r_2) dA(r_4) dA(r_3) dA(r_2) + \cdots \end{aligned}$$

It can be rewritten in the form:

$$L(r_1 \to r_0) = \sum_{n=1}^{\infty} L(\bar{r}_n) \tag{3.2}$$

with $L(\bar{r}_n)$ the radiance from $r_1$ to $r_0$ integrated over all paths of length $n$, *i.e.*, paths of $n+1$ vertices and $n$ edges, vertex $r_n$ on the light source, vertex $r_0$ on the sensor lens and $\bar{r}_n = r_0 r_1 \ldots r_n$ with $r_{k=0,1,\ldots,n} \in A$, and $\bar{r}_n \in$ path space $\mathcal{D}_n$ ($n \in \mathbb{N}^*$). $\mathcal{D}_n$ is the set of paths of length $n$.

Figure 3.2 shows a path of length 4. If $n = 1$, we have $L(\bar{r}_1) = L_e(r_1 \to r_0)$. If $n > 1$, we have:

$$\begin{aligned} L(\bar{r}_n) = {} & \int_A f_s(r_2 \to r_1 \to r_0) \cdot G(r_1 \leftrightarrow r_2) \int_A \cdots \int_A f_s(r_{n-1} \to r_{n-2} \to r_{n-3}) \cdot G(r_{n-2} \leftrightarrow r_{n-1}) \\ & \cdot \int_A L_e(r_n \to r_{n-1}) \cdot f_s(r_n \to r_{n-1} \to r_{n-2}) \cdot G(r_{n-1} \leftrightarrow r_n) dA(r_n) dA(r_{n-1}) \cdots dA(r_2) \end{aligned}$$

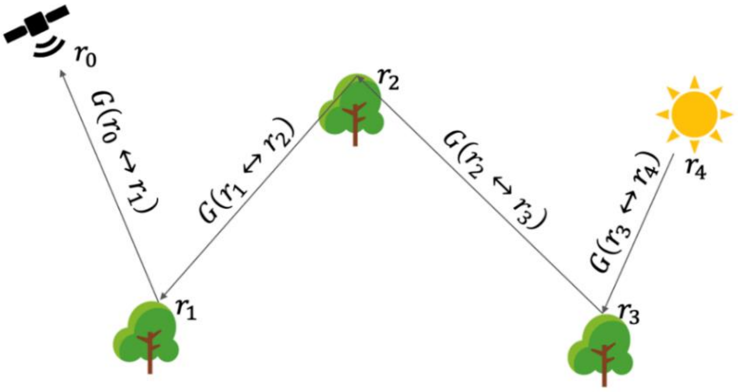

Figure 3.2. Path of length 4 from light source at $r_4$, successively scattered at $r_3$, $r_2$, $r_1$, and incident on the sensor at $r_0$.

### 3.1.2 Sensor and radiance measurement

The *sensor response* $S^{(j)}$ (*cf.* Annex A.3) at the level of sensor pixel $j$ is due to a radiation in direction $\Omega_0$ that reaches the sensor lens at vertex $r_0$. Figure 3.3 shows the acquisition configuration of a pinhole camera. $S^{(j)}$ corresponds to the measured radiance $L^{(j)}$. The so-called *flux responsivity* ${W_e}^{(j)}(r_0,\Omega_0)$ (*cf.* Annex A.3), usually defined as the *importance function*, links the total incident radiant flux to the measured radiance:

$$L^{(j)} = \int_{A_0}\int_{\Delta\Omega_0} {W_e}^{(j)}(r_0,\Omega_0)\cdot L(r_1 \to r_0)\cdot \cos\theta_i^{r_0}\, d\Omega_0 dA(r_0) \tag{3.3}$$

with ${W_e}^{(j)}(r_0,\Omega_0) = 0$ if the incident ray is outside the support of pixel $j$. $\theta_i^{r_0}$ is the angle between the incident direction and the principal optical axis. $\Delta\Omega_0$ is the solid angle that encloses all directions of the incident radiation. $A_0 \equiv A(r_0)$ is the lens area.

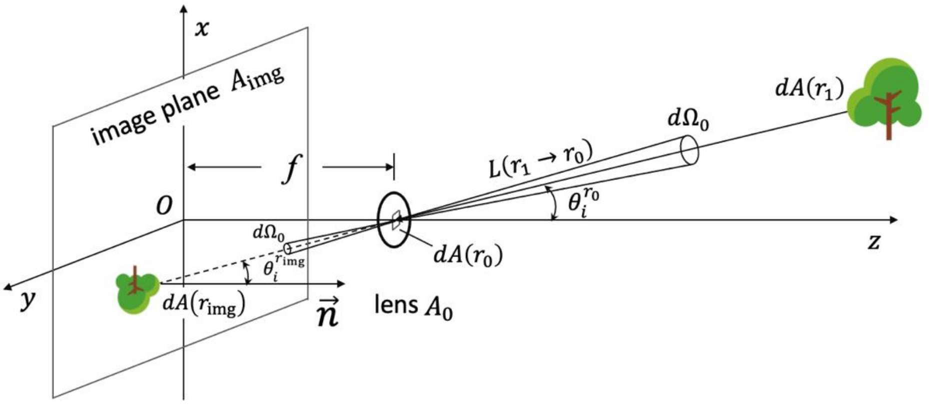

Figure 3.3. Pinhole camera. The lens (area $A_0$) is at a distance $f$ in front of the image plane of normal $\vec{n}$. Radiation from a differential surface $dA(r_1)$ in the scene along direction $r_1 \to r_0$ is focused by the lens onto the differential surface $dA(r_{\text{img}})$ in the image plane.

The analytical expression of $W_e$ depends on sensor properties (lens surface, FOV, focal length $f$, optics aperture, *etc*.). The radiance $L(r_{\text{img}})$ on the image plane (Figure 3.3) is a continuous function of the location $r_{\text{img}}$. The averaged radiance over the pixel $A_{\text{img}}^{(j)}$ is the pixel radiance:

$$L^{(j)}=\frac{1}{A_{\mathrm{img}}^{(j)}}\int_{A_{\mathrm{img}}^{(j)}}L(r_{\mathrm{img}})dA(r_{\mathrm{img}}) \tag{3.4}$$

Below, we give the theoretical expression of $W_e$ for two sensors: pinhole camera ($A_0$→0) and orthographic camera ($\Delta\Omega_0 \rightarrow 0$). Their optical system does not change the radiation direction.

Pinhole camera. Only the radiance that crosses the lens at the position $r_{\mathrm{d}}$ is recorded:

$$L^{(j)}=\frac{1}{A_{\mathrm{img}}^{(j)}}\int_{A_{\mathrm{img}}^{(j)}}L(r_{\mathrm{img}})dA(r_{\mathrm{img}})=\frac{1}{A_{\mathrm{img}}^{(j)}}\cdot\int_{\Delta\Omega_0^{(j)}}L(r_1\rightarrow r_0)\cdot\mathcal{J}_T d\Omega_0$$

with the Jacobian determinant $\mathcal{J}_T=\frac{\partial A(r_{\mathrm{img}})}{\partial\Omega_0}=\frac{f^2}{(\cos\theta_i^{r_0})^3}$ [m$^2$/sr], and $\Delta\Omega_0^{(j)}$ the solid angle that contains the directions to $A_{\mathrm{img}}^{(j)}$.

By comparing $L^{(j)}$ with its expression in Eq. (3.3) we get the importance function:

$$W_e^{(j)}(r_0,\Omega_0)=\begin{cases}\dfrac{f^2\cdot\delta(r_0-r_{\mathrm{d}})}{A_{\mathrm{img}}^{(j)}\cdot\left(\cos\theta_i^{r_0}\right)^4}, & \Omega_0\in\Delta\Omega_0^{(j)}\\ 0, & \Omega_0\notin\Delta\Omega_0^{(j)}\end{cases} \tag{3.5}$$

with $\delta(r_0\text{-}r_{\mathrm{d}})$ the Dirac function: $\delta(0)=\lim\limits_{A_0\rightarrow 0}\frac{1}{A_0}$; therefore, the unit of $\mathcal{J}_T\cdot\delta(r_0\text{-}r_{\mathrm{d}})$ is sr$^{-1}$.

Orthographic camera (orientation $-\Omega_{\mathrm{d}}$). The sensor lens is supposed to have the same size and shape as the image plane. Only the radiance in direction $\Omega_{\mathrm{d}}$ is recorded:

$$L^{(j)}=\frac{1}{A_{\mathrm{img}}^{(j)}}\int_{A_{\mathrm{img}}^{(j)}}L(r_{\mathrm{img}})dA(r_{\mathrm{img}})=\frac{1}{A_0^{(j)}}\int_{A_0^{(j)}}L(r_{\mathrm{img}})dA(r_{\mathrm{img}})$$

with surface $A_0^{(j)}$ the projection of the pixel support $A_{\mathrm{img}}^{(j)}$ to the sensor lens along $-\Omega_{\mathrm{d}}$.

The comparison of $L^{(j)}$ to its expression in Eq. (3.3) gives the importance function:

$$W_e^{(j)}(r_0,\Omega_0)=\begin{cases}\dfrac{\delta(\Omega_0-\Omega_{\mathrm{d}})}{A_{\mathrm{img}}^{(j)}}, & r_0\in A_0^{(j)}\\ 0, & r_0\notin A_0^{(j)}\end{cases} \tag{3.6}$$

with $\delta(\Omega_0-\Omega_{\mathrm{d}})$ the Dirac function: $\delta(0)=\lim\limits_{\Delta\Omega_0\rightarrow 0}\frac{1}{\Delta\Omega_0}$ [sr$^{-1}$].

### 3.1.3 The integral formulation

The expansion of Eq. (3.3) by substituting the incident radiance (Eq. (3.2)) gives:

$$\begin{aligned} L^{(j)} &= \int_{A_0}\int_{\Delta\Omega_0} W_e{}^{(j)}(r_0,\Omega_0)\cdot L(r_1\to r_0)\cdot\cos\theta_i^{r_0}\,d\Omega_0 dA(r_0) \\ &= \sum_{n=1}^{\infty}\int_A\int_A\cdots\int_A W_e{}^{(j)}(r_0,\Omega_0)\cdot L(\bar{r}_n)\cdot G(r_0\leftrightarrow r_1)dA(r_n)\cdots dA(r_1)dA(r_0) \end{aligned} \tag{3.7}$$

Eq. (3.7) can be expressed in the more compact form:

$$L^{(j)} = \int_{\mathcal{D}} f^{(j)}(\bar{r})\,d\mu(\bar{r}) \tag{3.8}$$

with $f^{(j)}(\bar{r})$ the measurement contribution function at pixel $j$ and $\mu$ the area-product measure, $\mu(\mathcal{D}_n) = \int_{\mathcal{D}_n} d\mu(\bar{r}_n) = \int_{\mathcal{D}_n} dA(r_n)dA(r_{n-1})\ldots dA(r_0)$. $\bar{r}$ is a path connecting the light source and the sensor, it is an element of the path space $\mathcal{D} = \bigcup_{n=1}^{\infty}\mathcal{D}_n$.

For a path of length $n$, the function $f^{(j)}(\bar{r}_n)$ is defined by:

$$f^{(j)}(\bar{r}_n)=L_e(r_n\to r_{n\text{-}1})\cdot G(r_0\leftrightarrow r_1)\cdot W_e{}^{(j)}(r_0\to r_1)\cdot\prod_{k=2}^{n} f_s(r_k\to r_{k\text{-}1}\to r_{k\text{-}2})\cdot G(r_{k\text{-}1}\leftrightarrow r_k) \tag{3.9}$$

We call $C_{\mathcal{D}_n}$ the contribution $\int_{\mathcal{D}_n} f^{(j)}(\bar{r}_n)d\mu(\bar{r}_n)$ due to the $(n-1)^{\text{th}}$ scattering order. Then, $C_{\mathcal{D}_1}$ is the contribution of direct illumination, $C_{\mathcal{D}_2}$ is the contribution of first order scattering, and so on. The radiance measurement is simply the sum of $C_{\mathcal{D}_n}$ terms:

$$L^{(j)} = \int_{\mathcal{D}} f^{(j)}(\bar{r})\,d\mu(\bar{r}) = \sum_{n=1}^{\infty} C_{\mathcal{D}_n} \tag{3.10}$$

## 3.2 Bidirectional path tracing

The Monte Carlo integration (*cf.* Annex C) can assess the multi-dimensional integral form of $L^{(j)}$ in Eq. (3.8). For example, a random path $\bar{R}\in\mathcal{D}$ sampled according to a choosing probability density function $p(\bar{r})$, can give an unbiased estimate of $L^{(j)}$:

$$F^{(j)} = \frac{f^{(j)}(\bar{R})}{p(\bar{R})} \tag{3.11}$$

with the unbiased expected value $\mathbb{E}(F^{(j)}) = \int_{\mathcal{D}} \frac{f^{(j)}(\bar{r})}{p(\bar{r})} p(\bar{r})\, d\mu(\bar{r}) = \int_{\mathcal{D}} f^{(j)}(\bar{r})\, d\mu(\bar{r}) = L^{(j)}$

The efficiency function (Eq. (C.14)) indicates that Eq. (3.11) can be efficiently evaluated if (1) the path samples are rapidly generated (to minimize computer time) and (2) the sample distribution $p(\bar{r})$ is close to the distribution of $f^{(j)}(\bar{r})$ in the path space (to minimize variance). Both requirements depend on the illumination conditions, the sensor characteristics, the surface optical properties and the heterogeneity of the environment. This section presents a robust algorithm namely bidirectional path tracing that has quite good performance for a wide variety of scenarios. This algorithm can efficiently sample a group of light paths and determine the paths with a large integrand $f^{(j)}(\bar{r})$ using an ingenious weighting method (Lafortune and Willems, 1996; Veach and Guibas, 1995a, 1995b).

### 3.2.1 The adjoint transport

It is intuitive to sample a path by a *random walk* (a stochastic *Markov chain*) from the light source and to connect it to the sensor since it is what happens in nature. This *light transport* or *forward ray tracing* has long been used in many 3D radiative transfer models (*e.g.*, FLiES, FLIGHT and Raytran). Usually, the 3D radiative transfer modelling considers a path connecting the light source and the sensor, *i.e.*, *end-to-end* modelling. Although counterintuitive, it is also possible to sample a path by a random walk from the sensor and to connect it to the light source. This sampling way, called *adjoint transport*, *importance transport* or *backward path tracing*, has proved to be more efficient than the light transport for simulating images. It is increasingly used in 3D radiative transfer models (*e.g.*, DIRSIG and LESS).

From the mathematical point of view, the light transport is equivalent to the adjoint transport. Using the *Fubini's theorem*, (Christensen et al., 1993) prove that the radiance $L_e$ and *importance* $W_e$ are interchangeable in Eq. (3.7): $W_e$ can be treated symmetrically as $L_e$ as an exit quantity. Furthermore, the estimate of radiance measurement (Eq. (3.11)) does not depend on the way a path sample is generated; the estimate is unbiased as long as the path is sampled according to its distribution. It results the *adjoint transport equation* also called *importance transport equation* has a form similar to the light transport equation (Eq. (3.1)):

$$W(r'{\to}r'') = W_e(r'{\to}r'') + \int_A W(r{\to}r') \cdot f_s{}^*(r{\to}r'{\to}r'') \cdot G(r{\leftrightarrow}r')dA(r) \qquad (3.12)$$

The exit importance $W(r'{\to}r'')$ quantifies the potential contribution of incident radiation to the radiance measurement. Eq. (3.12) stresses that $W(r'{\to}r'')$ is the sum of the emitted importance $W_e(r' \to r'')$ and importance due to the scattering of all incident importance $W(r \to r')$. The *adjoint bidirectional scattering distribution function* $f_s{}^*(r \to r' \to r'')$ is equal to $f_s(r \to r' \to r'')$ if the reciprocity is verified, *i.e.*, BSDF is constant if the incident and exit radiation directions are interchanged. Otherwise, it is corrected to be equal to $f_s(r'' \to r' \to r)$.

### 3.2.2 Bidirectional path tracing

Although both the forward ray tracing and the backward path tracing are commonly used in 3D radiative transfer modelling and perform well for most scenarios, these unidirectional path samplings can introduce large variance. Figure 3.4 shows two examples. 1) Daylight sensor with a small FOV compared to the simulated environment: the forward ray tracing can generate many paths that do not contribute to the radiance measurement. The resulting image is unbiased, but very noisy. 2) Night time sensor with wide FOV compared to the light source (*i.e.*, fire): the backward path tracing can create many useless paths. These inefficiencies are explained below.

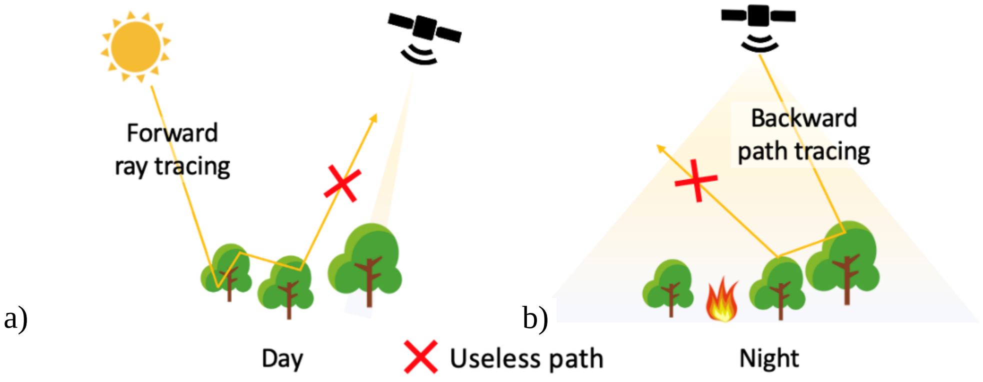

Figure 3.4. Scenarios for which the unidirectional path sampling is inefficient. a) Narrow FOV sensor: the forward ray tracing can generate a lot of paths that do not contribute to the measurement. b) Wide FOV sensor: the backward path tracing can generate many useless paths if the size of the light source is small such as the fire.

Because the distribution of the contribution function $f^{(j)}(\bar{r})$ greatly depends on experimental and instrumental configurations, it is nearly impossible to get the distribution of $f^{(j)}(\bar{r})$ when we formulate the probability density function, except for very simple scenarios (*e.g.*, specular ground illuminated by a parallel distant light). Therefore, the use of a unique sampling strategy to evaluate the measurement is not optimal: it cannot ensure that the sample distribution is close to the distribution of $f^{(j)}(\bar{r})$ for a wide variety of scenarios. A robust algorithm should combine all possible sampling strategies and weight their contributions according to the probability density of the sample. It stresses the interest of the bidirectional path tracing (Figure 3.5). It effectively generates a group of paths by connecting two sub-paths, one starting from the light source and another from the sensor. More precisely, a random walk starts from the light source and gives a light sub-path:

$$\bar{p}_{N_v} = p_0, p_1, \dots, p_{N_v-1}$$

with vertex $p_0$ on the light source and other vertices in the environment. $N_v$ is the sub-path depth (*i.e.*, $N_v$ is the total number of vertices).

A second one starts from the sensor and gives a sensor sub-path:

$$\bar{q}_{N_v} = q_0, q_1, \dots, q_{N_v-1}$$

with vertex $q_0$ on the sensor lens and other vertices in the environment.

An end-to-end path $\bar{r}_{s,t}$ is generated by connecting the light sub-path $\bar{p}_s = p_0, p_1, \dots, p_{s-1}$ and the sensor sub-path $\bar{q}_t = q_0, q_1, \dots, q_{t-1}$ with $s, t \in [0,\ N_v]$:

$$\bar{r}_{s,t} = \bar{p}_s, \bar{q}_t = p_0, p_1, \dots, p_{s-1}, q_{t-1}, q_{t-2}, \dots, q_0$$

Vertex $q_{t-1}$ is on the light source if $s = 0$. Vertex $p_{s-1}$ is on the sensor lens if $t = 0$. Any path of length $n$ (*i.e.*, $s + t = n + 1$ vertices) can be created in $n + 2$ ways. For example, Figure 3.6 shows how a path of length 3 can be created in five ways.

Because a path of length $n$ can be created by $n$+2 different ways, $n$+2 different sampling strategies can evaluate the contribution $C_{\mathcal{D}_{n\text{-}1}}$ (Eq. (3.10)) using the importance sampling (Eq. (3.11)). For example, the backward path tracing applies the “connect to light” way (Figure 3.6.b), and the forward ray tracing applies the “connect to sensor” way (Figure 3.6.d). As mentioned above, the use of a unique strategy risks to produce defects in some scenarios. The bidirectional path tracing sums and weights all possible sampling strategies possibly for a wide variety of scenarios. It results the multiple importance sampling (Eq. (C.15)) with only one sample per sampling strategy. An estimate of the radiance measurement takes the form:

$$F_{\mathrm{MIS}}^{(j)} = \sum_{s\geq 0}\sum_{t\geq 0} w_{s,t}(\bar{r}_{s,t}) \cdot \frac{f^{(j)}(\bar{r}_{s,t})}{p(\bar{r}_{s,t})} \tag{3.13}$$

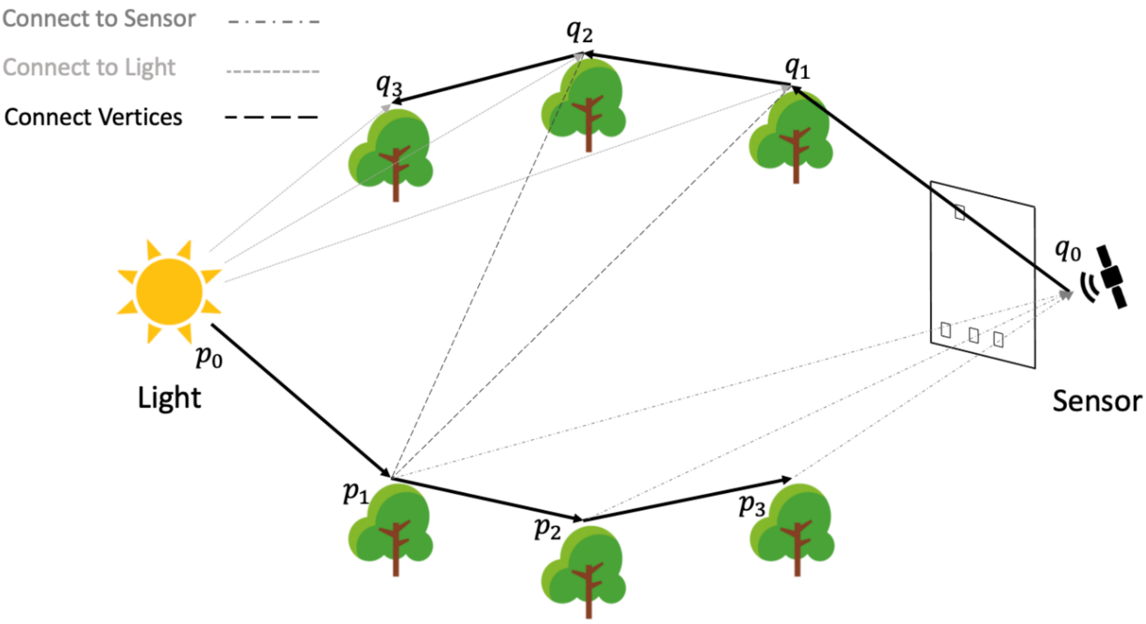

Figure 3.5. DART-Lux bidirectional path tracing with $N_v = 4$ vertices (maximal scattering order 3). The “random walk” process creates two sub-paths: a light sub-path $\bar{p}_4$=$p_0, p_1, p_2, p_3$ from the light source, and a sensor sub-path $\bar{q}_4 = q_0, q_1, q_2, q_3$ from the sensor. A path is created by connecting a vertex of light sub-path and a vertex of sensor sub-path, using an intersection test at each connection. Three connecting methods are used. 1) Connect to light: a sensor sub-path vertex is connected to a new sampled vertex on the light source. 2) Connect to sensor: a light sub-path vertex is connected to a new sampled vertex on the sensor lens and mapped to the image plane. 3) Connect vertices: a light sub-path vertex and a sensor sub-path vertex are connected. A light sub-path can randomly hit the sensor lens, and a sensor sub-path can randomly hit the light source. All above mentioned processes are repeated.

Eq. (3.8) and Eq. (3.10) gives the expression of the measured radiance at an infinite scattering order although infinite scattering order cannot be simulated explicitly. Usually, the contribution $C_{\mathcal{D}_n}$ decreases exponentially with the scattering order (Kallel, 2018). After a scattering order

$M_0$ that depends on the optical and structural properties of the environment, the contribution of higher scattering orders is negligible, *i.e.*, $\sum_{n=M_0+2}^{\infty} C_{\mathcal{D}_n} \ll L^{(j)}$, we use the approximation:

$$L^{(j)} \approx C_{\mathcal{D}_1} + C_{\mathcal{D}_2} + \cdots + C_{\mathcal{D}_{M_0+1}} \tag{3.14}$$

and

$$F_{\mathrm{MIS}}^{(j)} \approx \sum_{n=1}^{M_0+1} \sum_{s=0}^{n+1} w_{s,t}(\bar{r}_{s,t}) \cdot \frac{f^{(j)}(\bar{r}_{s,t})}{p(\bar{r}_{s,t})} \tag{3.15}$$

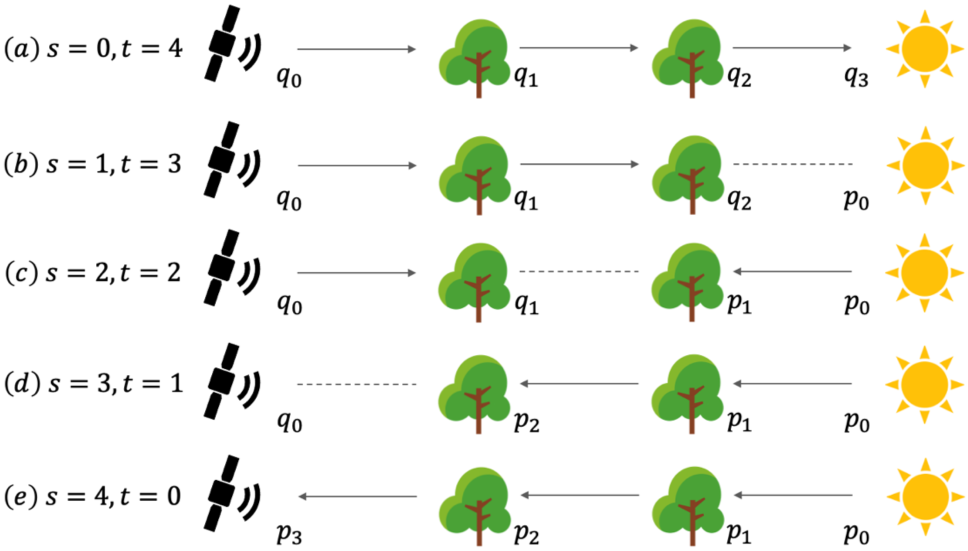

Figure 3.6. Five ways to create a path of length 3. (a) Hit light: a ray starts from a sensor, is scattered twice, then hits a light source. (b) Connect to light: a ray starts from a sensor, is scattered once, then intersects a scene element from which a path is created using an intersection test to a light source. (c) Connect vertices: 2 rays start from a sensor and light source, are intercepted by scene elements, then a path is created between the two intersect vertices, using an intersection test. (d) Connect to sensor: a ray starts from a light source, is scattered once, then intersects a scene element from which a connecting path to the sensor is created using an intersection test. (e) Hit sensor: a ray starts from a light source, is scattered twice, then hits a sensor.

### 3.2.3 Measurement evaluation

The contribution function can be straightforwardly computed once the path is generated:

$$f^{(j)}(\bar{r}_{s,t}) = L_e(p_0{\to}p_1){\cdot}\prod_{k=1}^{s-1}[f_s(p_{k\text{-}2}{\to}p_{k\text{-}1}{\to}p_k){\cdot}G(p_{k\text{-}1}{\leftrightarrow}p_k)]{\cdot}f_s(p_{s\text{-}2}{\to}p_{s\text{-}1}{\to}q_{t\text{-}1})$$
$$\cdot G(p_{s\text{-}1}{\leftrightarrow}q_{t\text{-}1}){\cdot}f_s^{\,*}(q_{t\text{-}2}{\to}q_{t\text{-}1}{\to}p_{s\text{-}1}){\cdot}\prod_{k=1}^{t-1}[f_s^{\,*}(q_{k\text{-}2}{\to}q_{k\text{-}1}{\to}q_k){\cdot}G(q_{k\text{-}1}{\leftrightarrow}q_k)]\,{\cdot}W_e^{(j)}(q_0{\to}q_1) \quad (3.16)$$

The virtual BSDFs $f_s(p_{\text{-}2}{\to}p_{\text{-}1}{\to}p_0)$ and $f_s(p_{\text{-}1}{\to}p_0{\to}p_1)$, the virtual adjoint BSDFs $f_s^{\,*}(q_{\text{-}2}{\to}q_{\text{-}1}{\to}q_0)$ and $f_s^{\,*}(q_{\text{-}1}{\to}q_0{\to}q_1)$, and the virtual geometric terms $G(p_{\text{-}1}{\leftrightarrow}q_{t\text{-}1})$ and $G(p_{s\text{-}1}{\leftrightarrow}q_{\text{-}1})$ are introduced to simplify the mathematical formulation. They are all set to one.

The path probability density function is computed incrementally along each random walk. For the light sub-path, a vertex $p_0$ and an emission direction $\Omega_0$ are sampled. $p_1$ is determined using an intersection test in the emission direction. We define the probability density as:

$$\vec{p}(p_0) = p(p_0)$$
$$\vec{p}(p_1) = p(p_1|p_0)$$

The successive vertices are sampled according to the surface optical properties and the local incident direction. In particular, the next vertex is directly derived by an intersection test along the sampled direction. We have:

$$\vec{p}(p_k) = p(p_k|p_{k-1}, p_{k-2}), \forall\ k > 1$$

Similarly, for the sensor sub-path, $\overleftarrow{p}(q_0){=}p(q_0)$, $\overleftarrow{p}(q_1){=}p(q_1|q_0)$ and $\overleftarrow{p}(q_k){=}p(q_k|q_{k\text{-}1}, q_{k\text{-}2})$ $\forall\ k{>}1$. The overall probability density is formulated as:

$$p(\bar{r}_{s,t}) = p(\bar{p}_s)\cdot p(\bar{p}_t) = \prod_{k=0}^{s-1}\vec{p}(p_k)\cdot\prod_{k=0}^{t-1}\overleftarrow{p}(q_k) \quad 3.17)$$

The weight function $w_{s,t}$ is crucial for the performance of the multiple importance sampling. It can be defined in many ways (*cf.* Annex C.3.2). For example, each sampling strategy can have the same weight $w_{s,t}(\bar{r}_{s,t}){=}1/(s{+}t{+}1)$. Also, $w_{s,t}$ can be set to 1 for the sampling strategy with maximum probability of occurring and set to 0 otherwise. A good choice is a power heuristic weight function $w_{s,t}$ proportional to the probability density of each strategy, which effectively reduces the variance in practical applications. The power heuristic weight function for a fixed path length $n$ ($s{+}t{=}s'{+}t'{=}n{+}1$) is:

$$w_{s,t}(\bar{r}_{s,t}) = \frac{\left(p(\bar{r}_{s,t})\right)^2}{\sum_{s'=0,t'=n-s'+1}^{n+1} \left(p(\bar{r}_{s',t'})\right)^2} \tag{3.18}$$

where the *virtual path* $\bar{r}_{s',t'}$ with $(s',t') \neq (s,t)$ has the same vertices as the sampled path $\bar{r}_{s,t}$, but is created in another sampling way (Figure 3.6). It is called “virtual” because it is only used to evaluate the MIS weight $w_{s,t}(\bar{r}_{s,t})$. Eq. (3.18) is unbiased for any path of length $n$ provided that: $\sum_{s=0,t=n-s+1}^{n+1} w_{s,t}(\bar{r}_{s,t}) = 1$ if $f^{(j)}(\bar{r}_{s,t}) \neq 0$, and $w_{s,t}(\bar{r}_{s,t}) = 0$ if $p(\bar{r}_{s,t}) = 0$.

Finally, the estimate of the radiance measurement is:

$$\begin{aligned} F_{\mathrm{MIS}}^{(j)} &\approx \sum_{n=1}^{M_0+1} \sum_{s=0}^{n+1} w_{s,t}(\bar{r}_{s,t}) \cdot \frac{f^{(j)}(\bar{r}_{s,t})}{p(\bar{r}_{s,t})} \\ &= \sum_{n=1}^{M_0+1} \sum_{s=0}^{n+1} \left\{ \frac{\left(p(\bar{r}_{s,t})\right)^2}{\sum_{s'=0,t'=n-s'+1}^{n+1} \left(p(\bar{r}_{s',t'})\right)^2} \cdot \left[T(\bar{p}_s) \cdot C_{s,t} \cdot T(\bar{q}_t)\right] \right\} \end{aligned} \tag{3.19}$$

with *throughputs* $T(\bar{p}_s)$ and $T(\bar{q}_t)$ computed incrementally along the random walks:

$$\begin{aligned} T(\bar{p}_s) &= \frac{L_e(p_0 \to p_1)}{\vec{p}(p_0)} \prod_{k=1}^{s-1} \frac{f_s(p_{k-2} \to p_{k-1} \to p_k) \cdot G(p_{k-1} \leftrightarrow p_k)}{\vec{p}(p_k)} \\ T(\bar{q}_t) &= \frac{{W_e}^{(j)}(q_0 \to q_1)}{\overleftarrow{p}(q_0)} \prod_{k=1}^{t-1} \frac{{f_s}^*(q_{k-2} \to q_{k-1} \to q_k) \cdot G(q_{k-1} \leftrightarrow q_k)}{\overleftarrow{p}(q_k)} \end{aligned} \tag{3.20}$$

and the *connection term* defined by:

$$C_{s,t} = f_s(p_{s-2} \to p_{s-1} \to q_{t-1}) \cdot G(p_{s-1} \leftrightarrow q_{t-1}) \cdot {f_s}^*(q_{t-2} \to q_{t-1} \to p_{s-1}) \tag{3.21}$$

## 3.3 Light, sensor, and BSDF models

The Monte Carlo method is flexible to integrate a variety of light sources (*e.g.*, sun, sky, moon, LiDAR, *etc.*), sensors (*e.g.*, pinhole camera, orthographic camera, fisheye camera, *etc.*) and surface BSDF models (*e.g.*, Lambertian, specular, RPV, *etc.*). This section presents some light, sensor and BSDF models commonly used in 3D radiative transfer modelling. All of them have been implemented in DART-Lux.

### 3.3.1 Light sources

Here, the sun and the atmosphere are the only light sources. The other light sources (*i.e.*, thermal emission in the atmosphere and land surfaces, and sun-induced fluorescent sources) will be presented in Regaieg (2023)[1]. If more than one light source is simulated, the light sources are sampled with the probability distribution depending on their radiant power. Sunlight can be parallel or within a cone, and sky light can be isotropic or anisotropic. In both cases, light is uniformly emitted from a virtual disk $A_{\text{disk}}$ that is the projection of the *scene sphere* along the illumination direction. The probability density function of the first vertex on the light source is:

$$p(p_0) = 1/A_{\text{disk}}$$

The so-called scene sphere is the sphere with minimum radius $R$ that encloses the scene (Figure 3.7). The light direction is sampled according to the energy angular distribution of the source. The emitted radiance $L_e(p_0, \Omega_0)$ is always determined by:

$$E_{\text{BOA}} = \int L_e(p_0, \Omega_0) \cdot \cos\theta_0 \, d\Omega_0$$

with $E_{\text{BOA}}$ the BOA irradiance of a horizontal surface due to the light source. This strategy is more robust than the usual strategy that illuminates the scene with rays from the horizontal plane above the scene (North, 1996; Thompson and Goel, 1998). Indeed, it ensures that the scene can be fully illuminated in any direction even for strong sloping topography.

**Sunlight.** If it is parallel (solar direction $\Omega_s$), the probability density function of the light direction is interpreted as a Dirac delta function:

$$p(\Omega_0) = \delta(\Omega_0 - \Omega_s)$$

with BOA direct irradiance $E_{\text{BOA}}^{\text{dir}}$, the incident radiance is:

$$L_e(p_0, \Omega_0) = \frac{E_{\text{BOA}}^{\text{dir}}}{\cos\theta_s} \cdot \delta(\Omega_0 - \Omega_s)$$

The penumbra phenomena can be simulated. Then, the direction $\Omega_0$ is uniformly sampled in the solid angle $\Delta\Omega_s = A_{\text{sun}}/(1\ AU)^2$, with $A_{\text{sun}}$ the solar disk area and $1\ AU$ the distance from the Earth to the sun. The incident radiance is:

---

[1] Regaieg, O., Lauret, N., Wang, Y., et al., 2023. DART Monte-Carlo based modelling of chlorophyll solar-induced fluorescence images of 3D canopies. [ready to submit].

$$L_e(p_0, \Omega_0) = \frac{E_{\mathrm{BOA}}^{\mathrm{dir}}}{\cos\theta_s \cdot \Delta\Omega_s}$$

**Light of the sky.** If it is isotropic, the incident radiance is $L_e(p_0, \Omega_0) = \frac{E_{\mathrm{BOA}}^{\mathrm{diff}}}{\pi}$, with $E_{\mathrm{BOA}}^{\mathrm{diff}}$ the BOA diffuse irradiance. Its probability density function follows a cosine distribution:

$$p(\Omega_0) = \frac{\cos\theta_o}{\pi}$$

If it is anisotropic: $E_{\mathrm{BOA}}^{\mathrm{diff}} = \int_0^{2\pi}\int_{\pi/2}^{\pi} L(\theta,\varphi) \cdot \cos\theta \cdot \sin\theta \, d\theta d\varphi$ with $L(\theta,\varphi)$ the radiance in the downward direction $\Omega(\theta, \varphi)$ and the light direction probability density function is:

$$p(\Omega_0) = \frac{p(\theta) \cdot p(\varphi|\theta)}{\sin\theta}$$

with $p(\theta) = \frac{\int_0^{2\pi} L(\theta,\varphi) d\varphi}{E_{\mathrm{BOA}}^{\mathrm{diff}}}$ and $p(\varphi|\theta) = \frac{p(\theta,\varphi)}{p(\theta)} = \frac{L(\theta,\varphi)}{\int_0^{2\pi} L(\theta,\varphi) d\varphi}$.

The illumination radiance is computed according to the sampled zenith and azimuth angle:

$$L_e(p_0, \Omega_0) = L(\theta, \varphi)$$

The radiance distribution $L(\theta,\varphi)$ can also come from a parametric model (*e.g.*, CIE model) or discrete values from an atmospheric radiative transfer model (*e.g.*, MODTRAN, DISORT).

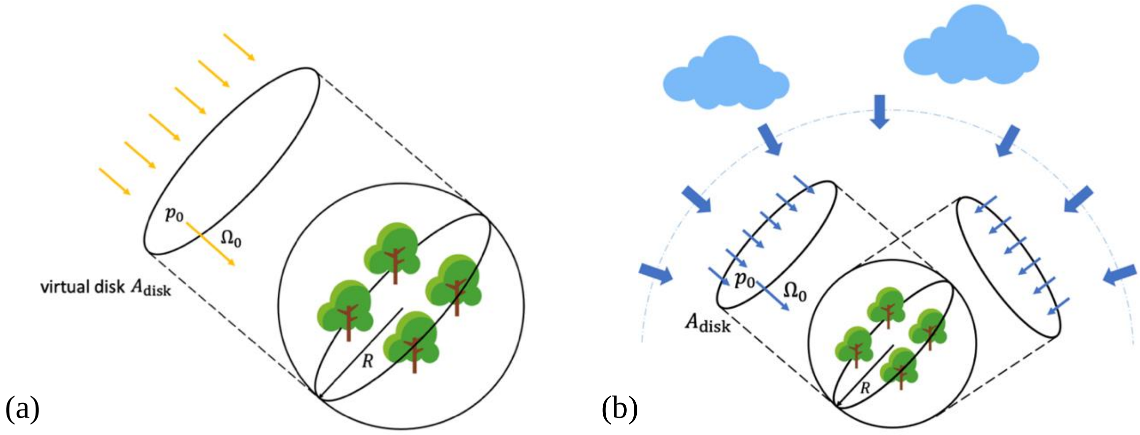

Figure 3.7. Scene illumination. a) Sunlight. b) Diffuse light from the sky. The scene sphere is the smallest sphere that contains the scene. Any ray from the sun or the sky originates from a virtual disk that is the projection of the scene sphere in the illumination direction.

### 3.3.2 Sensors

Two common sensors, *i.e.*, pinhole camera and orthographic camera, have been implemented. The pinhole camera has an infinitesimal lens. It is used to simulate airborne and in-situ observations with infinite depth of field. The orthographic camera has an infinitesimal FOV. It is used to simulate satellite images. For both cameras, the random walk starts by sampling a random vertex on the lens $A_0$ and a direction in the FOV. In addition, a special camera, called *BRF camera*, has been implemented for an efficient simulation of scene albedo, BRF and DBT.

**Pinhole camera (**Figure 3.3**).** It is at a distance $f$ in front of the image plane $A_{\mathrm{img}}$. The vertex on the lens is sampled by a Dirac delta function:

$$p(q_0) = \delta(q_0 - q_{\mathrm{d}})$$

with $q_{\mathrm{d}}$ the pinhole position. The direction is obtained by uniformly sampling a vertex $q_{\mathrm{img}}^{(j)}$ on the pixel support ($p\left(q_{\mathrm{img}}^{(j)}\right)=1/A_{\mathrm{img}}^{(j)}$) and connecting $q_0$ on the lens. Since the lens does not refract rays, the probability density function of the importance direction is derived from:

$$p\left(\Omega_0^{(j)}\right) = \mathcal{J}_T \cdot p\left(q_{\mathrm{img}}^{(j)}\right) = \frac{f^2}{A_{\mathrm{img}}^{(j)} \cdot \cos^3 \theta_i^{q_0}}$$

with Jacobian determinant $\mathcal{J}_T = \left(f/\cos\theta_i^{q_0}\right)^2/\cos\theta_i^{q_0}$. Eq. (3.5)gives the corresponding emitted importance ${W_e}^{(j)}$ for pixel $j$. In DART-Lux implementation, we often sample a vertex $q_{\mathrm{img}}$ on the image plane instead of sampling on the support of a specific pixel. Then, the mathematically equivalent importance function $W_e(q_0, \Omega_0)$ applied to any pixel is:

$$W_e(q_0, \Omega_0) = \frac{f^2 \cdot \delta(r_0 - r_{\mathrm{d}})}{A_{\mathrm{img}} \cdot \left(\cos\theta_i^{r_0}\right)^4} \tag{3.22}$$

The term “mathematically equivalent” means that the estimate by sampling a vertex $q_{\mathrm{img}}^{(j)}$ on a specific pixel *j* and the importance function in Eq. (3.5) is identical to the estimate by sampling a vertex $q_{\mathrm{img}}$ on the image plane and the importance function in Eq. (3.22).

**Orthographic camera (**Figure 3.8**).** It captures parallel radiation perpendicular to the image plane. Hence, the lens has the same shape as the image ($A_0 \equiv A_{\mathrm{img}}$). The vertex on the lens corresponding to pixel $j$ is uniformly sampled with the probability density function:

$$p\left(q_0^{(j)}\right) = \frac{1}{A_{\mathrm{img}}^{(j)}}$$

The importance direction is sampled by the Dirac delta function:

$$p(\Omega_0) = \delta(\Omega_0 - \Omega_{\mathrm{d}})$$

with -$\Omega_{\mathrm{d}}$ the camera orientation. The corresponding emitted importance ${W_e}^{(j)}$ is computed by Eq. (3.6). In DART-Lux implementation, $q_0$ is often uniformly sampled on the lens support with $p(q_0)$=$1/A_{\mathrm{img}}$ and the mathematically equivalent importance function:

$$W_e(q_0, \Omega_0) = \frac{\delta(\Omega_0 - \Omega_{\mathrm{d}})}{A_{\mathrm{img}}} \tag{3.23}$$

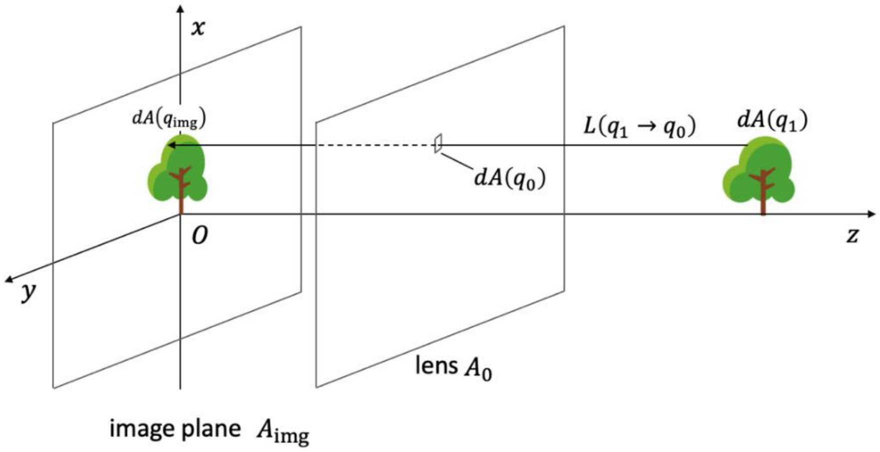

Figure 3.8. Orthographic camera. The lens (area $A_0$) is in front of the image plane $A_{\mathrm{img}}$ ($A_0 \equiv A_{\mathrm{img}}$). Radiation from a scene differential surface $dA(q_1)$ in direction $q_1$→$q_0$ is focused by the lens onto the differential surface $dA(q_{\mathrm{img}})$ at the image plane.

**BRF camera (**Figure 3.9**).** It is designed for assessing the directional radiance from the simulated scene, for an illumination configuration. The mean scene radiance in any direction $\Omega_0$ is captured by an orthographic camera (Figure 3.9) that has a lens area equal to the projected area $A_{\mathrm{ortho}}(\Omega_0)$ of the environment, *i.e.*, $A_0 \equiv A_{\mathrm{img}} = A_{\mathrm{ortho}}(\Omega_0)$. This specific orthographic camera has only one pixel. The sensor of the BRF camera is a hemispheric dome with infinite radius (Figure 3.9.b). The pixel array has equal zenith $\Delta\theta$ and azimuth $\Delta\varphi$ steps. The corresponding solid angle of pixel $j$ viewing from the environment is:

$$\Delta\Omega^{(j)} = \int_{\Delta\varphi}\int_{\Delta\theta} \sin\theta^{(j)}\, d\theta d\varphi$$

Each pixel stores the mean scene radiance over $\Delta\Omega^{(j)}$. It is an average of measurements of orthographic cameras with direction angles in $\theta^{(j)}\pm\Delta\theta/2$ and $\varphi^{(j)}\pm\Delta\varphi/2$.

The direction of the exit importance is uniformly sampled with the probability density:

$$p(\Omega_0) = \frac{p(\theta,\varphi)}{\sin\theta} = \frac{p(\theta)\cdot p(\varphi)}{\sin\theta}$$

with $p(\theta) = \frac{1}{\pi/2}$ and $p(\varphi) = \frac{1}{2\pi}$

Once the exit direction is sampled, the vertex is uniformly sampled on the lens area:

$$p(q_0) = \frac{1}{A_0} = \frac{1}{A_{\text{ortho}}(\Omega_0)}$$

and the corresponding mathematically equivalent importance is computed by:

$$W_e(q_0,\Omega_0) = \frac{1}{\pi^2\cdot A_{\text{ortho}}(\Omega_0)} \tag{3.24}$$

Compared to the photon spread method (Thompson and Goel, 1998) commonly used in forward ray tracing codes (*e.g.*, SPRINT and Rayspread), the BRF camera has two advantages: (1) it is easy to implement in Monte Carlo codes (*e.g.*, forward, backward and bi-directional algorithm), and (2) the mean radiance/reflectance of any direction with any solid angle can be derived in a postprocess once the BRF camera pixel values are computed.

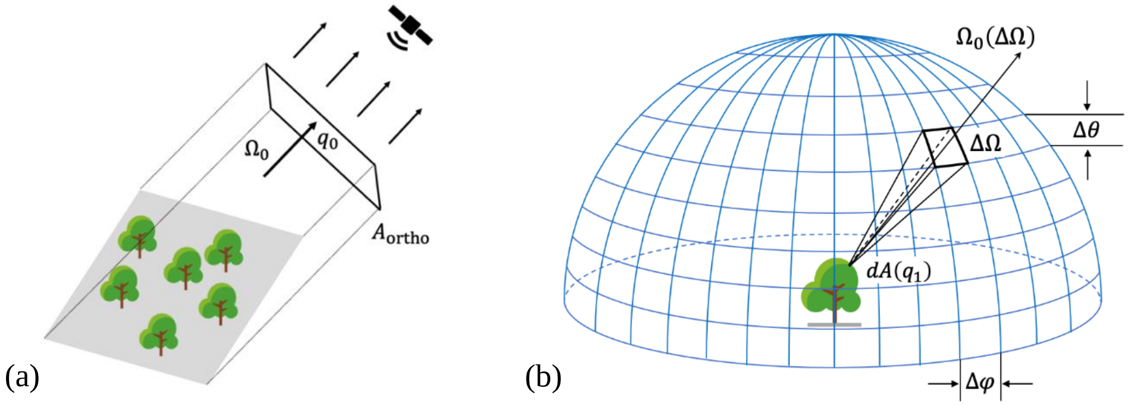

Figure 3.9. a) Scene exit radiation in direction $\Omega_0$ captured by a “single pixel” orthographic camera with image plane $A_{\text{ortho}}(\Omega_0)$. b) The hemispheric image plane of the BRF camera.

### 3.3.3 BSDF models

BSDF models (*cf.* section 1.4) define surface scattering events (*i.e.*, reflection, transmission). Scattered radiation and importance (adjoint transport) depend on the surface optical properties and the distribution of incident radiation (Eq. (1.39)) or importance (Eq. (3.12)). Because the distribution of incident radiation or importance is not known when the sampling probability density function $p(\Omega_o|\Omega_i)$ is needed, $p(\Omega_o|\Omega_i)$ is usually derived assuming isotropic incident quantities $L_i$ or $W_i$. For an incident direction $\Omega_i$ in the surface local coordinate (*i.e.*, radiation direction in light transport and importance direction in adjoint transport):

$$p(\Omega_o|\Omega_i) = \frac{f_s(r, \Omega_i \to \Omega_o) \cdot \cos\theta_o}{\int_{4\pi} f_s(r, \Omega_i \to \Omega'_o) \cdot \cos\theta'_o \, d\Omega'_o} \tag{3.25}$$

Eq. (3.25) is valid even if the reciprocity is not verified. To optimize the calculation of $p(\Omega_o|\Omega_i)$, reflection and transmission are separated using a constant probability of reflection $\mathrm{P}^*$:

$$p(\Omega_o|\Omega_i) = \begin{cases} \mathrm{P}^* \cdot \dfrac{f_r(r, \Omega_i \to \Omega_o) \cdot \cos\theta_o}{\int_{2\pi^+} f_r(r, \Omega_i \to \Omega'_o) \cdot \cos\theta'_o \, d\Omega'_o}, & \text{if } (\vec{n} \cdot \Omega_o) \cdot (\vec{n} \cdot \Omega_i) \geq 0 \\ (1 - \mathrm{P}^*) \cdot \dfrac{f_t(r, \Omega_i \to \Omega_o) \cdot \cos\theta_o}{\int_{2\pi^-} f_t(r, \Omega_i \to \Omega'_o) \cdot \cos\theta'_o \, d\Omega'_o}, & \text{otherwise} \end{cases} \tag{3.26}$$

In DART-Lux, $\mathrm{P}^*$ is 1 for opaque surfaces (transmittance is zero), 0 for non-reflective surfaces (reflectance is zero), and 0.5 for non-zero transmittance and reflectance which reduces the dependence of sampling on spectral properties. Once a scattering direction is sampled, an intersection test along the sampled direction determines the next path vertex.

**Lambertian model.** It has constant BRDF (Eq. (1.22)) and BTDF (Eq. (1.33)):

$$f_r(r, \Omega_i \to \Omega_o) = \frac{\rho}{\pi}, \;\; f_t(r, \Omega_i \to \Omega_o) = \frac{\tau}{\pi}$$

Plugging $f_r(r, \Omega_i \to \Omega_o)$ and $f_t(r, \Omega_i \to \Omega_o)$ into Eq. (3.26), we get:

$$p(\Omega_o|\Omega_i) = \begin{cases} \mathrm{P}^* \cdot \dfrac{\cos\theta_o}{\pi}, & \text{if } (\vec{n} \cdot \Omega_o) \cdot (\vec{n} \cdot \Omega_i) \geq 0 \\ (1 - \mathrm{P}^*) \cdot \dfrac{\cos\theta_o}{\pi}, & \text{otherwise} \end{cases}$$

**Specular model.** The BRDF (Eq. (1.27)) and BTDF (Eq. (1.36)) are based on the Fresnel's law:

$$f_r(r,\Omega_i \to \Omega_o) = \mathcal{R}_s(r,\Omega_i \to \Omega_o) \cdot \frac{\delta(\Omega_i - \Omega_i^*)}{\cos\theta_i}$$

$$f_t(r,\Omega_i \to \Omega_o) = \mathcal{T}_s(r,\Omega_i \to \Omega_o) \cdot \frac{\left(\frac{n_o}{n_i}\right)^3 \cdot \delta(\Omega_i - \Omega_i^*)}{\cos\theta_i}$$

Substituting $f_r(r,\Omega_i \to \Omega_o)$ and $f_t(r,\Omega_i \to \Omega_o)$ into Eq. (3.26), we get:

$$p(\Omega_o|\Omega_i) = \begin{cases} \mathrm{P}^* \cdot \dfrac{\delta(\Omega_i - \Omega_i^*) \cdot \cos\theta_o}{\cos\theta_i}, & \text{if } (\vec{n} \cdot \Omega_o) \cdot (\vec{n} \cdot \Omega_i) \geq 0 \\ (1 - \mathrm{P}^*) \cdot \dfrac{\frac{n_o}{n_i} \cdot \delta(\Omega_i - \Omega_i^*) \cdot \cos\theta_o}{\cos\theta_i}, & \text{otherwise} \end{cases}$$

**Microfacet model.** The rough surface is modelled as a collection of microfacets that represent the roughness. The microfacets distribution and the masking-shadowing function are described by $D_{\mathrm{m}}(\Omega_{\mathrm{f}})$ (Eq. (1.28)) and $G_{\mathrm{m}}(\Omega_i,\Omega_o)$ (Eq. (1.29)), respectively. The BRDF (Eq. (1.30)) and BTDF (Eq. (1.37)) of rough surface is computed by:

$$f_r(r,\Omega_i \to \Omega_o) = \frac{\mathcal{R}_s(r,\Omega_i \to \Omega_o) \cdot D_{\mathrm{m}}(\Omega_{\mathrm{f}}) \cdot G_{\mathrm{m}}(\Omega_i,\Omega_o)}{4\cos\theta_i\cos\theta_o}$$

$$f_t(r,\Omega_i \to \Omega_o) = \frac{|\Omega_i \cdot \Omega_{\mathrm{f}}| \cdot |\Omega_o \cdot \Omega_{\mathrm{f}}|}{\cos\theta_i\cos\theta_o} \cdot \frac{\left(\frac{n_o}{n_i}\right)^3 \cdot \mathcal{T}_s(r,\Omega_i \to \Omega_o) \cdot D_{\mathrm{m}}(\Omega_{\mathrm{f}}) \cdot G_{\mathrm{m}}(\Omega_i,\Omega_o)}{\left(|\Omega_i \cdot \Omega_{\mathrm{f}}| - \frac{n_o}{n_i}|\Omega_o \cdot \Omega_{\mathrm{f}}|\right)^2}$$

The BRDF and BTDF cannot be analytically integrated. Therefore, their numeric integration is done by random sampling a microfacet normal $\Omega_{\mathrm{f}}$ over the facet distribution $D_{\mathrm{m}}(\Omega_{\mathrm{f}})$:

$$p(\Omega_{\mathrm{f}}) = D_{\mathrm{m}}(\Omega_{\mathrm{f}}) \cdot \cos\theta_{\mathrm{f}}$$

For a unique incident direction $\Omega_i$ (i.e., infinitesimal incident solid angle) and for $\Omega_{\mathrm{f}}$ variable in a small solid angle $d\Omega_{\mathrm{f}}$, the geometric optics shows that the reflected direction is in:

$$d\Omega_o = 4 \cdot |\Omega_i \cdot \Omega_{\mathrm{f}}| d\Omega_{\mathrm{f}}$$

and the transmitted direction is in:

$$d\Omega_o = \frac{\left(|\Omega_i \cdot \Omega_{\mathrm{f}}| - \frac{n_o}{n_i}|\Omega_o \cdot \Omega_{\mathrm{f}}|\right)^2}{\left(\frac{n_o}{n_i}\right)^2 |\Omega_o \cdot \Omega_{\mathrm{f}}|} d\Omega_{\mathrm{f}}$$

Because $p(\Omega_o|\Omega_i) = p(\Omega_{\mathrm{f}}) d\Omega_{\mathrm{f}} / d\Omega_o$, we have:

$$p(\Omega_o|\Omega_i) = \begin{cases} \mathrm{P}^* \cdot \dfrac{D_\mathrm{m}(\Omega_\mathrm{f}) \cdot \cos\theta_\mathrm{f}}{4 \cdot |\Omega_i \cdot \Omega_\mathrm{f}|}, & \text{if } (\boldsymbol{n} \cdot \Omega_o) \cdot (\boldsymbol{n} \cdot \Omega_i) \geq 0 \\ (1 - \mathrm{P}^*) \cdot \dfrac{\left(\frac{n_o}{n_i}\right)^2 \cdot D_\mathrm{m}(\Omega_\mathrm{f}) \cdot |\Omega_o \cdot \Omega_\mathrm{f}| \cdot \cos\theta_\mathrm{f}}{\left(|\Omega_i \cdot \Omega_\mathrm{f}| - \frac{n_o}{n_i}|\Omega_o \cdot \Omega_\mathrm{f}|\right)^2}, & \text{otherwise} \end{cases}$$

**Parametric models and measurements.** Some parametric BSDF models such as the RPV model (Eq. (1.23)) and the Hapke model (Eq. (1.24)) cannot be integrated analytically to derive the probability density function using Eq. (3.25). Also, they cannot be approximated by a simpler integrable form. In some cases, the BSDF may be known for only a limited number of directions. To adapt these parametric models and measurements, we compute or interpolate a 2D piecewise-constant BSDF for a set of discrete incident and exit directions and then, derive the probability density based on this new BSDF using Eq. (C.9).

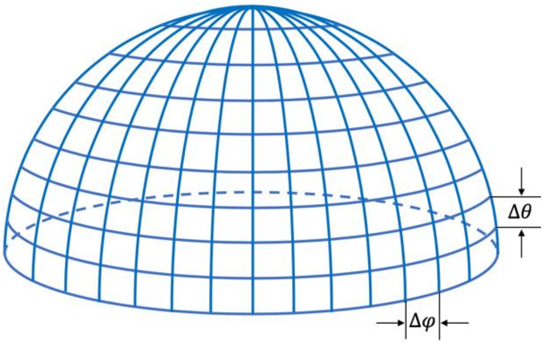

Figure 3.10. Resampled equal angle step directions on the hemisphere with constant $\Delta\theta$ and $\Delta\varphi$ for each solid angle.

Here, we present how a 2D piecewise-constant BRDF is constructed; its associate BTDF can be similarly constructed. The $2\pi$ hemispheric space is discretized into $N_\theta \cdot N_\varphi$ solid angles ($N_\theta = \pi/2\Delta\theta$, $N_\varphi = 2\pi/\Delta\varphi$) with constant zenith step $\Delta\theta$ and azimuth step $\Delta\varphi$ (Figure 3.10). $\Omega^{(x,y)}(\theta_x, \varphi_y)$, with $\theta_x$, $\varphi_y$ ($x = 1, \cdots, N_\theta$, $y = 1, \cdots, N_\varphi$) its zenith and azimuth angles, is the central direction of the solid angle $\Delta\Omega^{(x,y)} = [\theta_x - \Delta\theta/2, \theta_x + \Delta\theta/2] \times [\varphi_y - \Delta\varphi/2, \varphi_y + \Delta\varphi/2]$. For an incident direction $\Omega_i^{(x_i,y_i)}$ and a reflected direction $\Omega_o^{(x_o,y_o)}$, the BRDF is:

$$f_r(r, \Omega_i \to \Omega_o) = c_{x_o,y_o|x_i,y_i}, \forall\ \Omega_i \in \Delta\Omega_i^{(x_i,y_i)}, \Omega_o \in \Delta\Omega_o^{(x_o,y_o)}$$

The corresponding probability density function for $\Omega_i \in \Delta\Omega_i^{(x_i,y_i)}$ and $\Omega_o \in \Delta\Omega_o^{(x_o,y_o)}$ is:

$$\begin{aligned}
p(\Omega_o|\Omega_i) &= \frac{\frac{1}{\Delta\Omega_o^{(x_o,y_o)}} \int_{\Delta\Omega_o^{(x_o,y_o)}} f_r(r, \Omega_i \to \Omega_o) \cdot \cos\theta_o \, d\Omega_o}{\int_{2\pi^+} f_r(r, \Omega_i \to \Omega_o) \cdot \cos\theta_o \, d\Omega_o} \\
&= \frac{\frac{1}{\int_{\varphi_{y_o}-\Delta\varphi/2}^{\varphi_{y_o}+\Delta\varphi/2} \int_{\theta_{x_o}-\Delta\theta/2}^{\theta_{x_o}+\Delta\theta/2} \sin\theta \, d\theta d\varphi} \int_{\varphi_{y_o}-\Delta\varphi/2}^{\varphi_{y_o}+\Delta\varphi/2} \int_{\theta_{x_o}-\Delta\theta/2}^{\theta_{x_o}+\Delta\theta/2} c_{x_o,y_o|x_i,y_i} \cos\theta \sin\theta \, d\theta d\varphi}{\sum_{x=1}^{N_\theta} \sum_{y=1}^{N_\varphi} \int_{\varphi_y-\Delta\varphi/2}^{\varphi_y+\Delta\varphi/2} \int_{\theta_x-\Delta\theta/2}^{\theta_x+\Delta\theta/2} c_{x,y|x_i,y_i} \cos\theta \sin\theta \, d\theta d\varphi} \\
&= \frac{c_{x_o,y_o|x_i,y_i} \cos\theta_{x_o} \sin\Delta\theta}{2\sin\frac{\Delta\theta}{2} \sum_{x=1}^{N_\theta} \sum_{y=1}^{N_\varphi} c_{x,y|x_i,y_i} \sin\theta_x \cos\theta_x \sin\Delta\theta \, \Delta\varphi} \\
&= \frac{c_{x_o,y_o|x_i,y_i} \cos\theta_{x_o}}{2\sin\frac{\Delta\theta}{2} \Delta\varphi \sum_{x=1}^{N_\theta} \sum_{y=1}^{N_\varphi} c_{x,y|x_i,y_i} \sin\theta_x \cos\theta_x}
\end{aligned}$$

using: $\int_{\varphi-\Delta\varphi/2}^{\varphi+\Delta\varphi/2} \int_{\theta-\Delta\theta/2}^{\theta+\Delta\theta/2} \sin\theta \, d\theta d\varphi = 2\sin\theta \sin\frac{\Delta\theta}{2} \Delta\varphi$

$\int_{\varphi-\Delta\varphi/2}^{\varphi+\Delta\varphi/2} \int_{\theta-\Delta\theta/2}^{\theta+\Delta\theta/2} \cos\theta \sin\theta \, d\theta d\varphi = \sin\theta \cos\theta \sin\Delta\theta \, \Delta\varphi$

**Mixed model.** It combines two BSDF models with specific mixture ratio $a$ to simulate several scattering effects (*e.g.*, specular and diffuse reflection) without the effort to create a new BSDF model. It is characterized by:

Mixed BSDF: $f_s(r, \Omega_i \to \Omega_o) = a \cdot f_{s1}(r, \Omega_i \to \Omega_o) + (1 - a) \cdot f_{s2}(r, \Omega_i \to \Omega_o)$

Mixed probability density: $p(\Omega_o|\Omega_i) = a \cdot p_1(\Omega_o|\Omega_i) + (1 - a) \cdot p_2(\Omega_o|\Omega_i)$

Mixed models can be mixed to represent more than two scattering effects. It is useful in radiative transfer modelling if the scattering behaviour of a surface can be decomposed into several scattering behaviours that can be represented by an analytical BSDF.

The mathematical descriptions of the light sources, sensors, and surfaces presented in Section 3.3 can be evaluated once the vertex location and light geometry is determined. Then, using these values in Eq. (3.19) gives the radiance measurement. However, the straightforward evaluation of Eq. (3.19) is computationally very expensive. Here we present an algorithm to evaluate Eq. (3.19) with a reduced number of computations.

# 3.4 Practical implementation

## 3.4.1 Computation of throughput

The throughput (Eq. (3.20)) is evaluated incrementally along the random walk:

$$T(\bar{p}_0) = L_e(p_0 \to p_1) \qquad T(\bar{q}_0) = W_e{}^{(j)}(q_0 \to q_1)$$

$$T(\bar{p}_1) = \frac{L_e(p_0 \to p_1)}{\vec{p}(p_0)} \cdot \frac{\cos\theta_o^{p_0}}{p(p_0 \to p_1)} \qquad T(\bar{q}_1) = \frac{W_e{}^{(j)}(q_0 \to q_1)}{\overleftarrow{p}(q_0)} \cdot \frac{\cos\theta_i^{q_0}}{p(q_0 \to q_1)}$$

$$\dots \qquad \dots$$

$$T(\bar{p}_k) = T(\bar{p}_{k-1}) \cdot \frac{f_s(p_{k-2} \to p_{k-1} \to p_k) \cdot \cos\theta_o^{p_{k-1}}}{p(p_{k-1} \to p_k)} \quad T(\bar{q}_k) = T(\bar{q}_{k-1}) \cdot \frac{f_s{}^*(q_{k-2} \to q_{k-1} \to q_k) \cdot \cos\theta_i^{q_{k-1}}}{p(q_{k-1} \to q_k)}$$

with $\frac{G(p_{k-1} \leftrightarrow p_k)}{\vec{p}(p_k)} = \frac{\cos\theta_o^{p_{k-1}}}{p(p_{k-1} \to p_k)}$ and $\frac{G(q_{k-1} \leftrightarrow q_k)}{\overleftarrow{p}(q_k)} = \frac{\cos\theta_i^{q_{k-1}}}{p(q_{k-1} \to q_k)}$

These throughputs are stored in memory and can be directly used to compute the contribution function of any sub-path combinations (*cf.* section 3.2.2).

## 3.4.2 Computation of the weight function

The division of Eq. (3.18) by its numerator gives

$$w_{s,t}(\bar{r}_{s,t}) = \frac{1}{w_{s-1}^{\text{light}} + 1 + w_{t-1}^{\text{sensor}}}$$

with $w_{s-1}^{\text{light}} = \sum_{s'=0}^{s-1} \left(\frac{p(\bar{r}_{s',t'})}{p(\bar{r}_{s,t})}\right)^2$ and $w_{t-1}^{\text{sensor}} = \sum_{t'=0}^{t-1} \left(\frac{p(\bar{r}_{s',t'})}{p(\bar{r}_{s,t})}\right)^2$.

The overall probability density (Eq. 3.17))leads to the probability density of a virtual path $\bar{r}_{s',t'}$:

$$p(\bar{r}_{s',t'}) = \begin{cases} \prod_{k=0}^{s'-1} \vec{p}(p_k) \cdot \prod_{k=s'}^{s-1} \overleftarrow{p}(p_k) \cdot \prod_{k=0}^{t-1} \overleftarrow{p}(q_k), s' < s \\ \prod_{k=0}^{s-1} \vec{p}(p_k) \cdot \prod_{k=t'}^{t-1} \vec{p}(q_k) \cdot \prod_{k=0}^{t'-1} \overleftarrow{p}(q_k), s' > s \end{cases}$$

Then, the weights $w_{s-1}^{\text{light}}$ and $w_{t-1}^{\text{sensor}}$ are expressed by:

$$w_{s-1}^{\text{light}} = \sum_{s'=0}^{s-1} \left( \frac{\prod_{k=0}^{s'-1} \vec{p}(p_k) \cdot \prod_{k=s'}^{s-1} \overleftarrow{p}(p_k) \cdot \prod_{k=0}^{t-1} \overleftarrow{p}(q_k)}{\prod_{k=0}^{s-1} \vec{p}(p_k) \cdot \prod_{k=0}^{t-1} \overleftarrow{p}(q_k)} \right)^2 = \sum_{s'=0}^{s-1} \left( \prod_{k=s'}^{s-1} \frac{\overleftarrow{p}(p_k)}{\vec{p}(p_k)} \right)^2$$

$$w_{t-1}^{\text{sensor}} = \sum_{t'=0}^{t-1} \left( \frac{\prod_{k=0}^{s-1} \vec{p}(p_k) \cdot \prod_{k=t'}^{t-1} \vec{p}(q_k) \cdot \prod_{k=0}^{t'-1} \overleftarrow{p}(q_k)}{\prod_{k=0}^{s-1} \vec{p}(p_k) \cdot \prod_{k=0}^{t-1} \overleftarrow{p}(q_k)} \right)^2 = \sum_{t'=0}^{t-1} \left( \prod_{k=t'}^{t-1} \frac{\vec{p}(q_k)}{\overleftarrow{p}(q_k)} \right)^2$$

Both weights can be incrementally evaluated after some mathematical inductions. For example:

$$w_{-1}^{\text{light}} = 0$$

$$w_0^{\text{light}} = \left( \frac{\overleftarrow{p}(p_0)}{\vec{p}(p_0)} \right)^2$$

$$w_1^{\text{light}} = \left( \frac{\overleftarrow{p}(p_1)}{\vec{p}(p_1)} \cdot \frac{\overleftarrow{p}(p_0)}{\vec{p}(p_0)} \right)^2 + \left( \frac{\overleftarrow{p}(p_1)}{\vec{p}(p_1)} \right)^2$$

$$w_2^{\text{light}} = \left( \frac{\overleftarrow{p}(p_2)}{\vec{p}(p_2)} \cdot \frac{\overleftarrow{p}(p_1)}{\vec{p}(p_1)} \cdot \frac{\overleftarrow{p}(p_0)}{\vec{p}(p_0)} \right)^2 + \left( \frac{\overleftarrow{p}(p_2)}{\vec{p}(p_2)} \cdot \frac{\overleftarrow{p}(p_1)}{\vec{p}(p_1)} \right)^2 + \left( \frac{\overleftarrow{p}(p_2)}{\vec{p}(p_2)} \right)^2$$

$$\dots$$

After some mathematical inductions, we finally derive the expression of $w_k^{\text{light}}$ and $w_k^{\text{sensor}}$ that can be evaluated incrementally and be stored in memory to compute the weight for any sub-path combinations (*cf*. section 3.2.2):

$$w_k^{\text{light}} = [\overleftarrow{p}(p_k)]^2 \left( \frac{1}{[\vec{p}(p_k)]^2} + \frac{w_{k-1}^{\text{light}}}{[\vec{p}(p_k)]^2} \right)$$

$$w_k^{\text{sensor}} = [\vec{p}(q_k)]^2 \left( \frac{1}{[\overleftarrow{p}(q_k)]^2} + \frac{w_{k-1}^{\text{sensor}}}{[\overleftarrow{p}(q_k)]^2} \right)$$

### 3.4.3 Computer programming

The computer graphics community develops increasingly efficient physically based renderers (*e.g.*, *LuxCoreRender*: https://luxcorerender.org, Mitsuba 3: https://mitsuba-renderer.org, Cycles: https://cycles-renderer.org) that simulate very fast and visually pleasing colour images or videos of 3D artificial world. They provide well modularized program architecture to facilitate the implementation of a large variety of light transport algorithms, light sources, sensors, surface and volume materials, and sampling methods. However, they work with three colour bands and usually low radiometric accuracy, and neglect important radiative processes (*e.g.*, polarization and SIF emission). Therefore, they are not adapted to land surface modelling and remote sensing applications that need radiometric quantities (*e.g.*, reflectance and radiative budget) in various ranges of spectral bands, for specific radiation processes (*e.g.*, dependence of leaf reflectance to its chlorophyll content), and with an appropriate radiometric accuracy. Therefore, a current trend in the 3D RTM community is to adapt and further develop the efficient light transport algorithms. DART-Lux is the result of the implementation and great adaptation in DART (Figure 2.4) of the bidirectional path tracing architecture of the renderer *LuxCoreRender*, and a variety of light sources, sensors, and BSDFs (*cf.* section 3.3).

Due to its flexible algorithm and modularized program, DART-Lux can be extended to many uses. Three types of extension, some of which are already implemented, are indicated here. (1) Physical modelling: SIF and thermal emission, spherical atmosphere with 3D clouds, any surface / volume scattering function, polarization, radiative budget, *etc*. (2) Products: spectral radiance / reflectance / brightness temperature / solar induced fluorescence images, 3D radiative budget, images per type of land cover (*e.g.*, tree, ground), LiDAR waveform, point cloud and photon counting, polarized components, look-up-tables for inversion and sensitivity work, *etc*. (3) Computer science: accurate ray-object intersection to avoid self-intersection and watertight intersection issues (Woo et al., 1996; Woop et al., 2013)), GPU acceleration, distributed computing, *etc*.

## 3.5 Evaluation of DART-Lux

Here, DART-Lux accuracy for reflectance and remote sensing images is assessed using the classic DART discrete ordinates mode (referred to DART-FT). The idea here is double. (1) Having already been validated by measurements and model comparison (*cf.* section 2.3.1), DART-FT can be used as a reference, even if for doing so, DART-FT must be run with input parameters that imply very large computer resources. (2) DART-FT and DART-Lux use two totally different radiative transfer modelling methods, while using the same representations of 3D landscapes. Therefore, there is a high probability that the two models are exact if they give the same results. Three scenes are considered: schematic scene, urban scene, and forest scene.

### 3.5.1 Schematic scene

The schematic scene (Figure 3.11) has seven cherry trees with different sizes and a DART-created house with gable roof to assess DART-Lux accuracy in presence of slopes. Its mock-up consists of 0.137 million facets. Table 3.1 and Table 3.2 give DART input parameters. Its BOA images are simulated for four spectral bands (blue B: 0.44 $\mu$m; green G: 0.56 $\mu$m; red R: 0.66 $\mu$m; near infrared NIR: 0.87 $\mu$m) at 0.125m spatial resolution, for three light conditions (*i.e.*, single and multiple light sources) with $\mathrm{SKYL} = \frac{\text{BOA sky diffuse irradiance}}{\text{BOA total irradiance}}$ equal to 0 (direct sun), 1 (diffuse sky) and 0.5 (direct sun + diffuse sky).

Table 3.1. Schematic scene: input parameters for the mock-up, light source and spectral band.

| **Parameters** | | **Value** |
|---|---|---|
| **DART scene** | Scene dimension | X=Y=32 m |
| | Spatial resolution | $\Delta$x=$\Delta$y=0.125 m |
| | Tree model | Cherry tree |
| | Building model | DART classic house |
| | Neighbourhood effect | Repetitive mode |
| **Sunlight** | Direction | Zenith $\theta_{\mathrm{sun}}$=30°, Azimuth $\varphi_{\mathrm{sun}}$=225° |
| | TOA irradiance | THKUR (Berk et al., 2008) |
| **Sky light** | SKYL | 0, 0.5 or 1 |
| **Spectral band** | Spectral band | 0.44 $\mu$m, 0.56 $\mu$m, 0.66 $\mu$m, 0.87 $\mu$m |
| | Bandwidth | 0.02 $\mu$m |

Table 3.2. Configurations of DART-Lux and DART-FT radiative transfer methods.

| DART-Lux | | DART-FT | |
|---|---|---|---|
| Samples/pixel | 400 | Discrete direction | 1000 |
| Max scattering order | 6 | Max scattering order | 6 |
| Number of threads | 8 | Number of threads | 8 |
| | | Illumination rays per pixel | 169 |

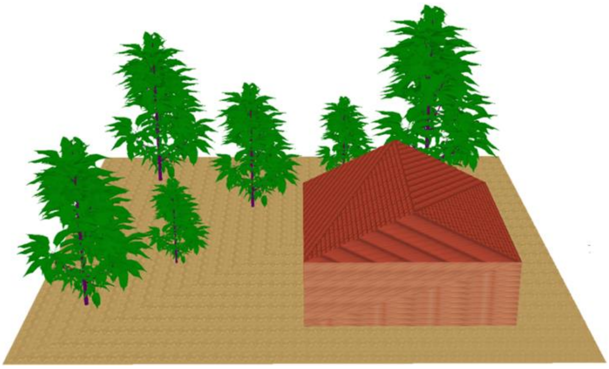

Figure 3.11. schematic scene: mock-up with its seven cherry trees of different sizes and DART classic house.

The consistency of DART-Lux and DART-FT images is illustrated by visually comparing their RGB colour composite images (Figure 3.12) and their scatter plots of NIR reflectance (Figure 3.13) for the three BOA illumination conditions. Degrading the image resolution from 0.125m to 0.5 m greatly improves the pixelwise comparison from {$R^2 > 0.968$, bias $< 0.006$} to {$R^2 > 0.995$, bias $< 0.0004$} because it mitigates the noise and discretization effects. Figure 3.14 shows the BRF profiles in the solar plane for the four spectral bands (B, G, R, NIR), with viewing zenith angle step $\Delta\theta_v$=5°. Differences are quantified by the average absolute relative difference:

$$\bar{\varepsilon} = \frac{1}{N_{\theta_v}} \sum\nolimits_{\theta_v} \left| \frac{\rho_{\text{DART-Lux}}(\theta_v) - \rho_{\text{DART-FT}}(\theta_v)}{\rho_{\text{DART-FT}}(\theta_v)} \right| \cdot 100\%$$

with $N_{\theta_v}$ the number of viewing directions.

Usually, $\bar{\varepsilon} \approx 0.4\%$ (Table 3.3) and maximal $\bar{\varepsilon}_{\max} \approx 0.6\%$. The slight differences in the scatter plot and the BRF profile are mostly due to DART-Lux Monte Carlo noise and DART-FT discretization processes. Indeed, even with 1000 discrete directions, the DART-FT “atmosphere shadows” (*i.e.*, SKYL = 1) have a discrete aspect less realistic than that with DART-Lux.

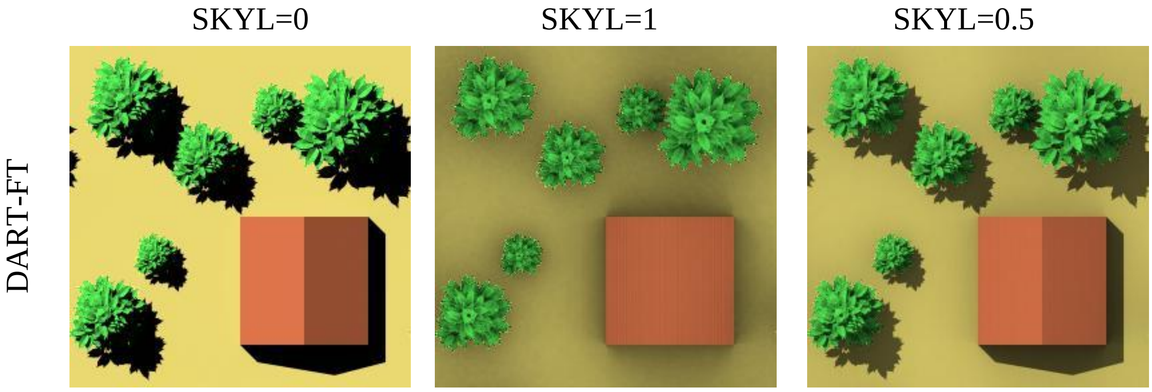

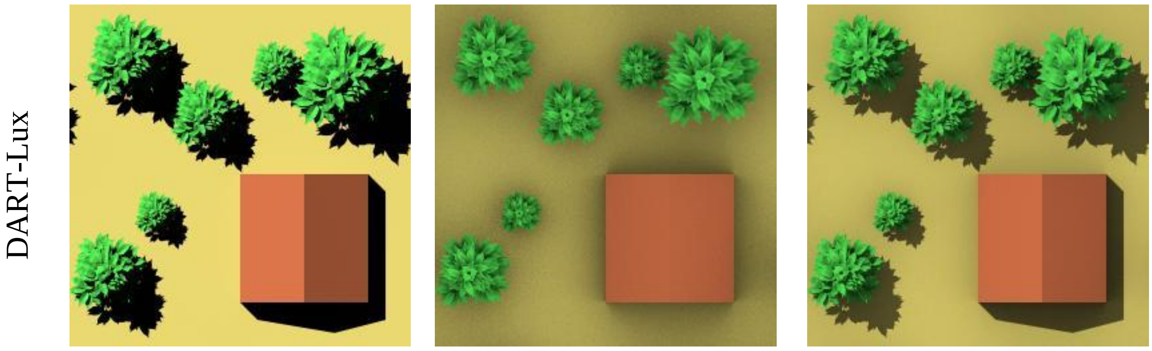

Figure 3.12. DART-FT (top) and DART-Lux (bottom) RGB images for three light conditions: SKYL = 0 (left), SKYL = 1 (centre) and SKYL = 0.5 (right).

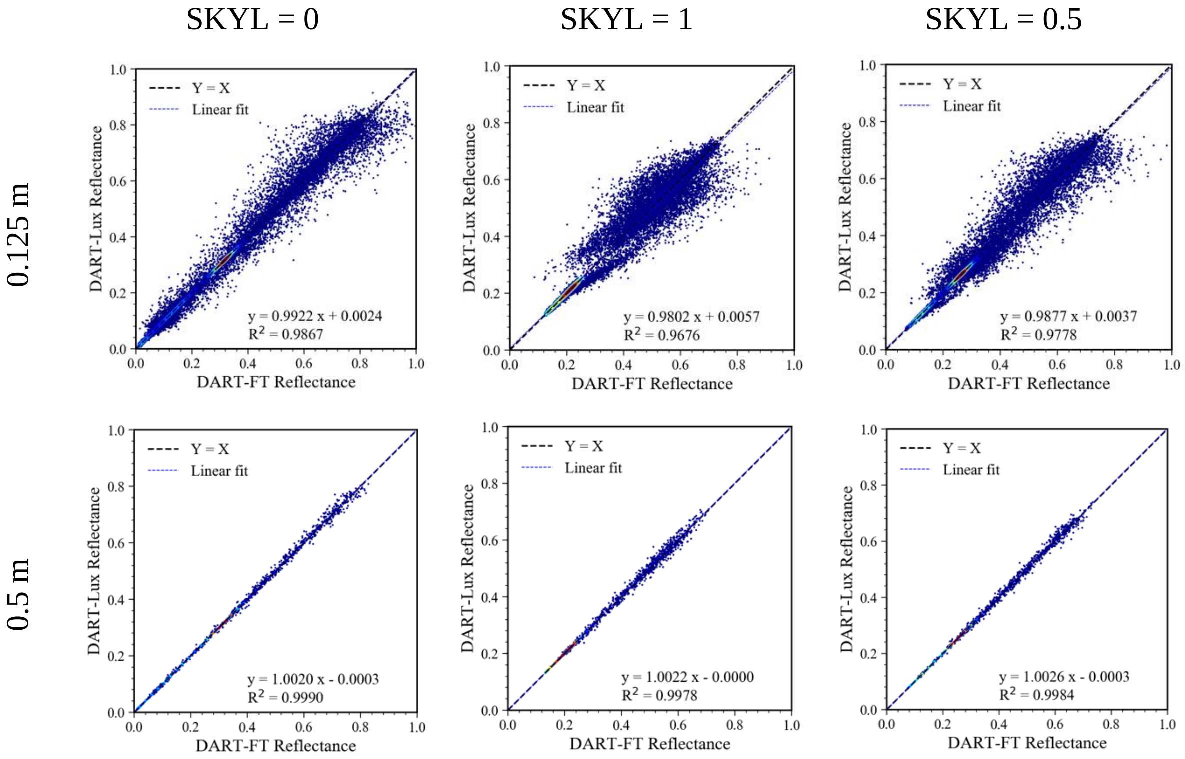

Figure 3.13. Pixelwise comparison of DART-FT and DART-Lux NIR reflectance. Pixel values at 0.5 m resolution result from the degradation of the initial image at 0.125 m resolution.

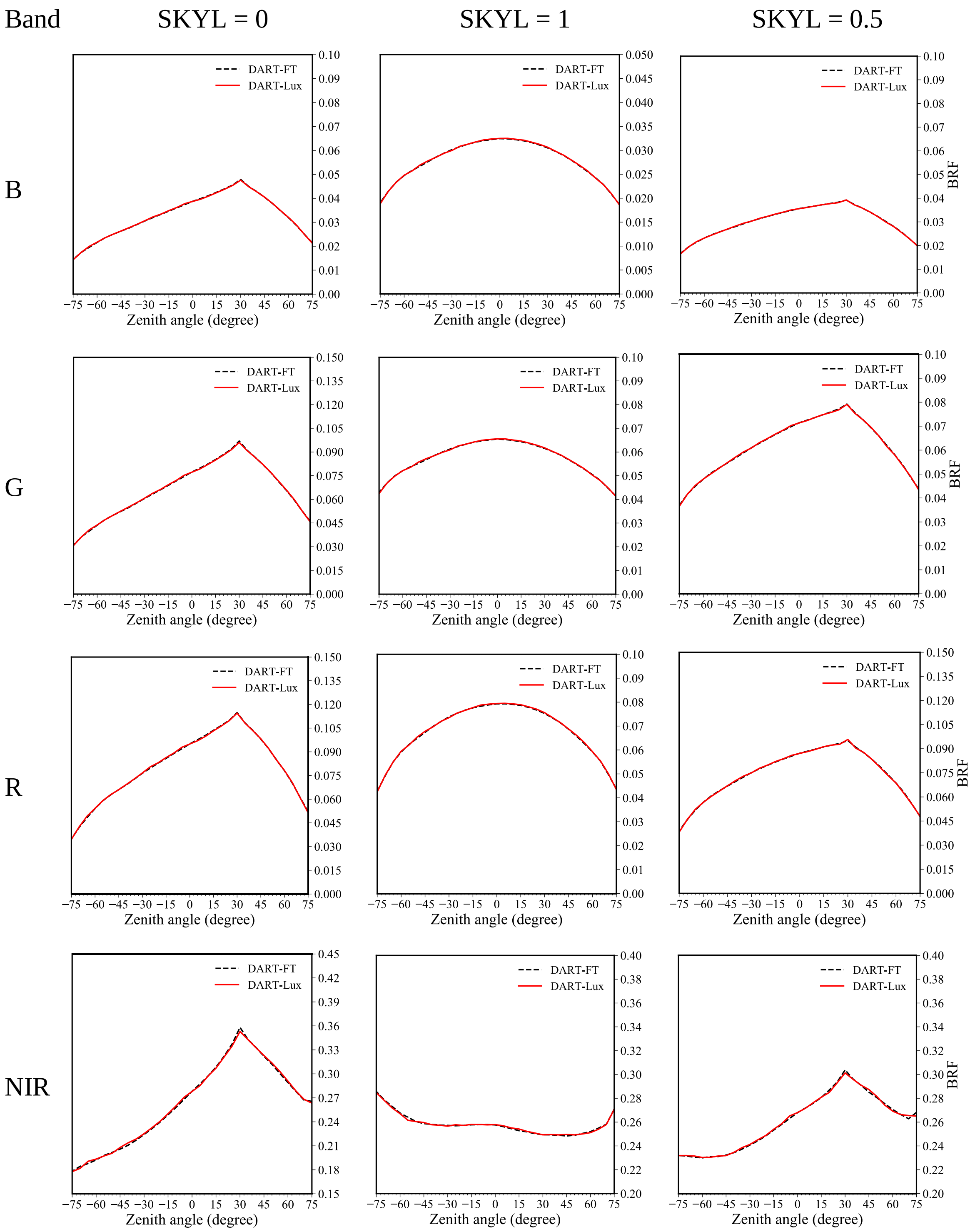

Figure 3.14. DART-FT and DART-Lux solar plane reflectance ($\Delta\theta_v = 5°$) in four spectral bands (R, G, B, NIR) for three illuminations (SKYL=0, SKYL=1, SKYL=0.5).

Table 3.3. Summary of average absolute relative difference $\bar{\varepsilon}$ of BRF in Figure 3.14.

| Band | SKYL = 0 | SKYL = 1 | SKYL = 0.5 |
|---|---|---|---|
| B | 0.443% | 0.335% | 0.360% |
| G | 0.467% | 0.336% | 0.359% |
| R | 0.445% | 0.349% | 0.404% |
| NIR | 0.605% | 0.226% | 0.338% |

## 3.5.2 Urban scene

The urban scene is the Brienne district (1400 m × 750 m) of Toulouse, France. Its 3D mock-up (Figure 3.15.a) was provided by the Toulouse town hall (Wang et al., 2022). It contains 953 buildings, 2433 trees, 3 grasslands, 1 river, 1 canal and other city facilities, represented by 8 million facets. DART-FT and DART-Lux are configured with direct sunlight ($\theta_{\text{sun}} = 20°, \varphi_{\text{sun}} = 180°, \text{SKYL} = 0$), 0.5 m spatial resolution, four spectral bands (B: 0.44 $\mu$m, G: 0.55 $\mu$m, R: 0.66 $\mu$m, NIR: 0.87 $\mu$m), maximal scattering orders six, no topography, and no atmosphere. Common optical properties are assigned per type of urban element (*e.g.*, roof, vegetation). DART-FT is run with 100 discrete directions and 100 illumination rays per pixel. DART-Lux is run with 60 samples per pixel.

DART-FT and DART-Lux RGB images are very close as illustrated by their RGB colour composites (Figure 3.16) and scatter plot of pixel reflectance in R band at 0.5m resolution (Figure 3.16.a): {$R^2 > 0.99$ and bias ~ 0.0001}. Degrading image resolution down to 2.0 m improves their similarity: {$R^2 > 0.999$ and bias < 0.0001} (Figure 3.16.b). Figure 3.16.c shows the R band BRF in the solar plane with zenith angle step $\Delta\theta_v = 2°$. Its average absolute relative difference $\bar{\varepsilon}$ is 0.24%.

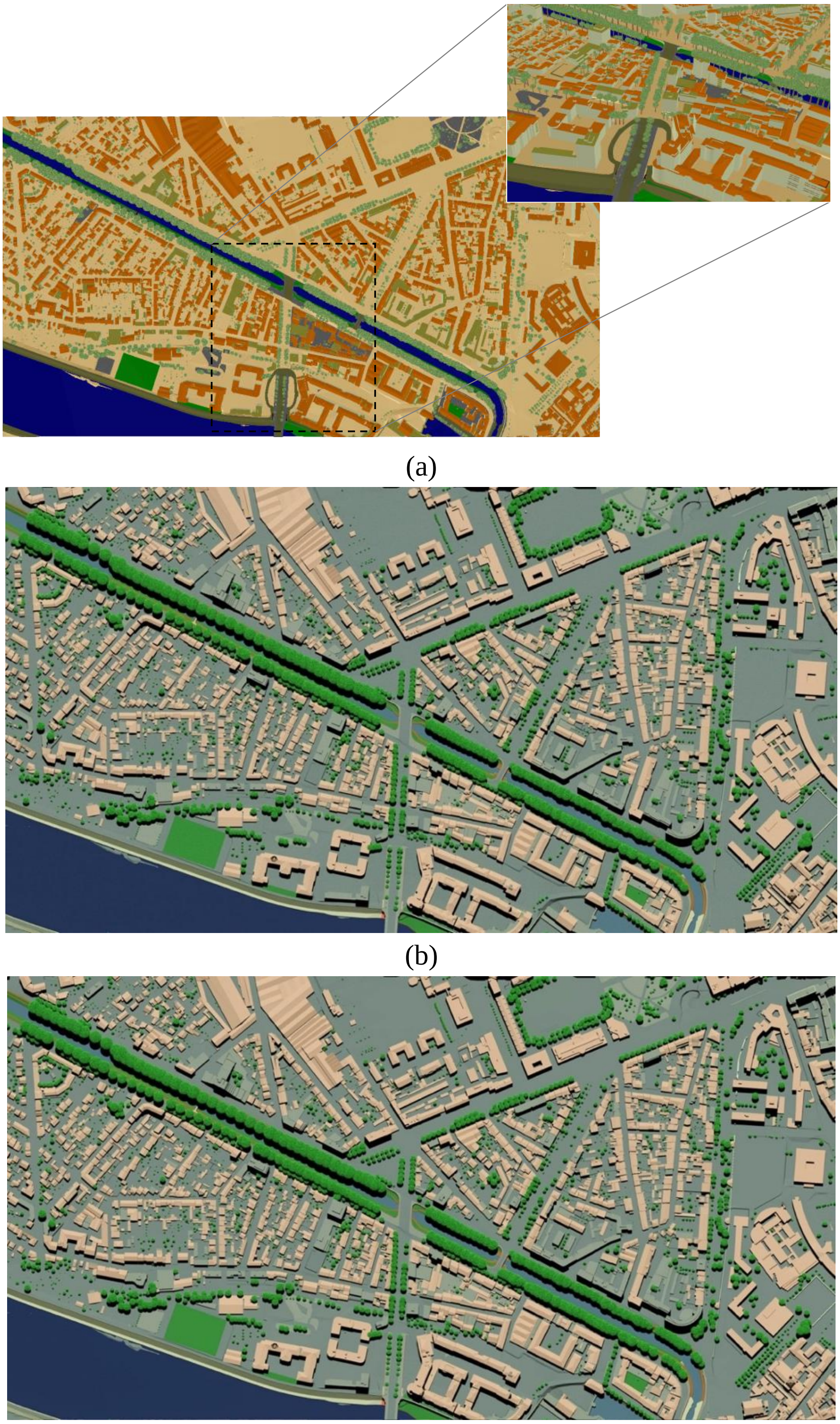

(a)

(b)

(c)

Figure 3.15. Brienne district: 3D mock-up (1400 m × 750 m) (a) and its DART-FT (b) and DART-Lux (c) RGB images.

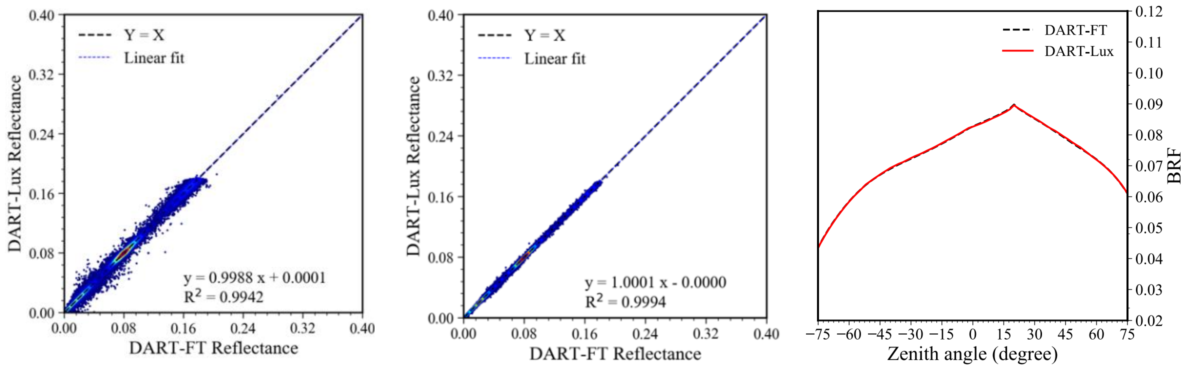

(a) (b) (c)

Figure 3.16. DART-Lux and DART-FT reflectance in R band. Scatter plot of pixel reflectance for 0.5 m (a) and 2.0 m (b) spatial resolution. c) Reflectance in the solar plane.

### 3.5.3 Forest scene

The forest scene is the Järvselja summer birch forest (summer, HET09_JBS_SUM) of RAMI4 experiment (https://rami-benchmark.jrc.ec.europa.eu). It has 1029 realistic trees with 465 birch trees, 196 common alder trees, 185 aspen trees, 78 linden trees, 39 spruce trees, and 46 ash and maple trees (Figure 3.17.a). Its mock-up is created by repeating and/or rotating 18 individual 3D tree objects. For example, the 465 birch trees are generated by cloning and/or rotating 4 birch tree objects at different growing stages. This forest stand is very challenging for 3D RT models (Figure 3 in (Widlowski et al., 2015)) because it consists of more than 550 million facets.

Simulations are for direct sun illumination ($\theta_{\mathrm{sun}} = 36.6°, \varphi_{\mathrm{sun}} = 270.69°$, SKYL=0), 0.125 m spatial resolution, four spectral bands (B: 0.44 $\mu$m, G: 0.55 $\mu$m, R: 0.66 $\mu$m, NIR: 0.87 $\mu$m), maximal scattering order 6. Specific optical properties are assigned per tree species. DART-Lux is run with 200 samples per pixel. DART-FT is run with 62500 illumination rays per pixel, and 80 discrete directions. Figure 3.17.b shows DART-FT and DART-Lux RGB colour composite images. As for the schematic and urban cases, the scatter plots of pixel NIR reflectance indicate that the pixelwise comparison greatly improves from 0.125 m spatial resolution (Figure 3.17.d): {$R^2$ > 0.93, bias ≈ 0.01} to 1 m spatial resolution (Figure 3.17.e): {$R^2$ > 0.997, bias < 0.002}.

Figure 3.17.f shows DART-FT and DART-Lux NIR reflectance in the solar plane, at first order scattering. DART-FT is run with and without an acceleration technique: rays that exit a cell face along a same direction are not merged (approximate case called DART-FT) or merged (accurate case called DART-FT-REF, used as a reference). DART-Lux average absolute relative difference is $\bar{\varepsilon}$ = 0.5% for DART-FT-REF and 0.7% for DART-FT. Larger differences occur at the hot spot direction. DART-FT underestimates the hot spot (Figure 3.17.f) because its merging technique reduces the exactly backscattered rays. Multiple scattering is only simulated with DART-FT and DART-Lux because DART-FT-REF is very time and memory consuming. The average absolute difference $\bar{\varepsilon}$ between DART-Lux and DART-FT is 1.0% (Figure 3.17.g).

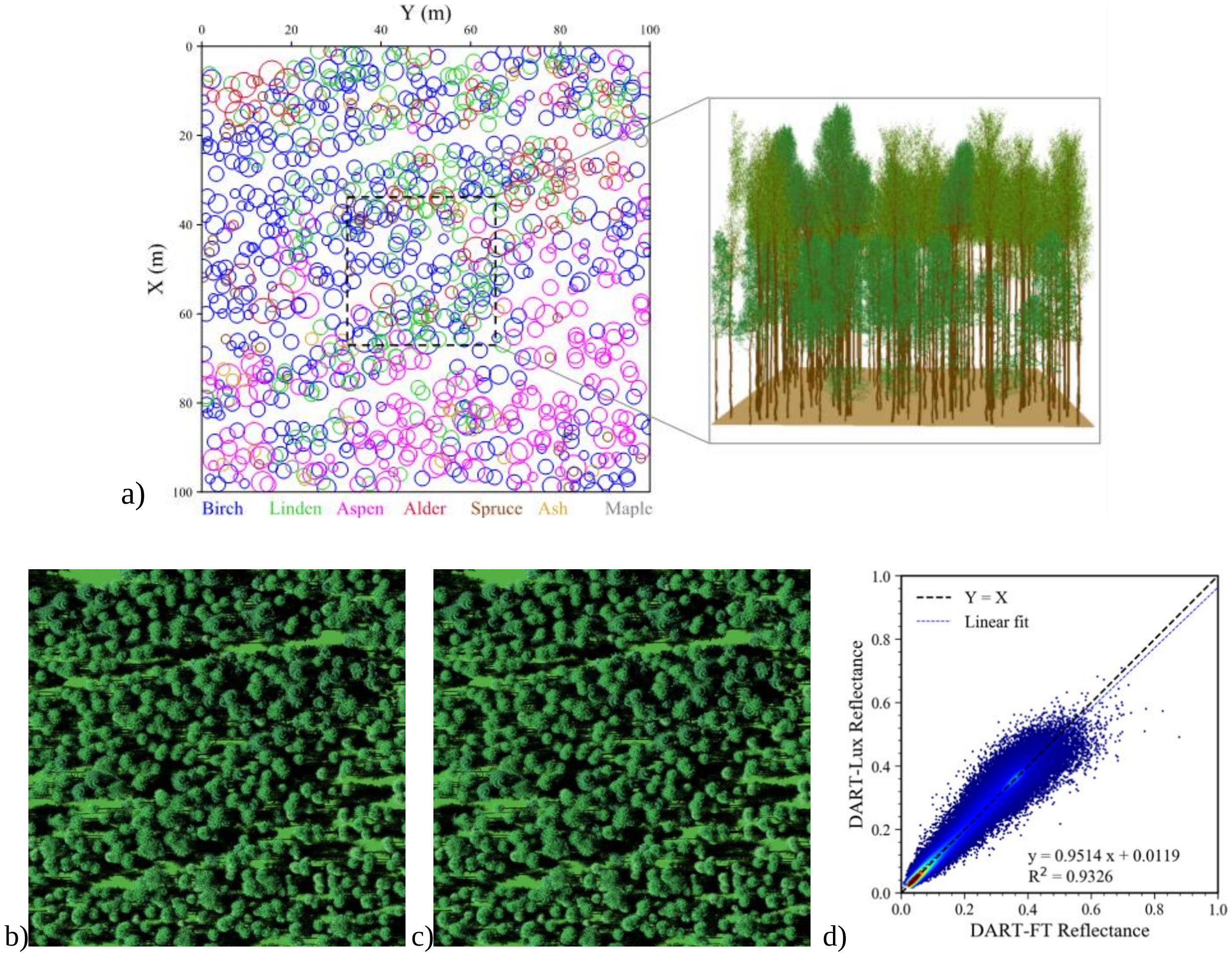

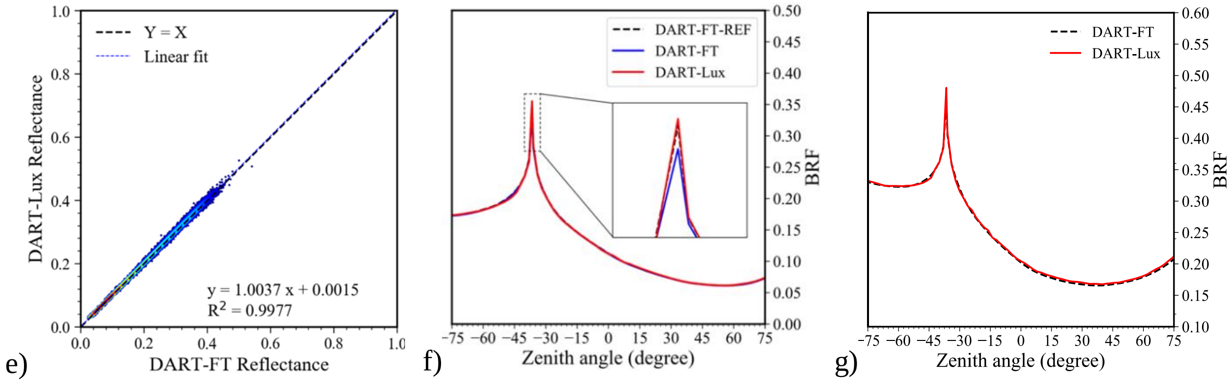

Figure 3.17. Järvselja birch forest. a) Location of trees and 3D mock-up of the centre region. DART-FT (b) and DART-Lux (c) RGB images at resolution 0.125 m. Scatter plot of pixel NIR reflectance at resolution 0.125 m (d) and 1.0 m (e). DART-FT and DART-Lux NIR reflectance in the solar plane with zenith angle step $\Delta\theta_v = 2°$: f) single scattering reflectance, g) total reflectance.

# 3.6 Discussion

## 3.6.1 Correlation of path samples

The bidirectional path tracing algorithm (*cf.* section 3.2.2) with $N_v$ vertices per random walk is very efficient because it creates $N_v^2$ paths with only $N_v^2$+2($N_v$-1) intersection tests, compared to $N_v^3$ if each path is created independently. Knowing that the intersection test is the most computational expensive process in 3D radiative transfer modelling, this algorithm almost reduces the simulation time by a factor of:

$$\frac{N_v^3}{N_v^2 + 2(N_v - 1)}$$

However, it increases the covariance (*i.e.*, Monte Carlo noise) between path samples, because they are created with the same light and sensor sub-paths. Although the estimate of radiance measurement Eq. (3.15) gives unbiased results (*cf.* 3.Appendix A), compared to estimates with independent path samples, the path sample correlation can increase the overall variance by a maximal factor $f(\tau)$ (Eq. (3.27)). With $C_{\mathcal{D}_{n+1}}/C_{\mathcal{D}_n} \approx \tau, \forall\, n$ $(0 \leq \tau < 1)$ the average ratio of contributions of successive scattering orders (*cf.* 3.Appendix B), we have:

$$f(\tau) = \frac{(1+\tau)\cdot\left(2+\tau\left(\frac{\sqrt{2}}{2}-\tau\right)(3-\tau)\right)}{(1-\tau)^2} \tag{3.27}$$

Figure 3.18.a shows the decrease in the contribution of the scene average nadir radiance of scattering order $n = 1, \cdots, 6$, relative to the contribution of first order scattering, for the three scenes studied in section 3.5. The trendiness is an exponentiation

$$g(n) = \tau^{-(n-1)}$$

with $\tau$ usually in [0, 0.1] for visible bands and in [0.4, 0.6] for NIR bands. $f(\tau)$ of Eq. (3.27) (Figure 3.18.b) is less than 2.4 for simulations in visible bands, and in [9, 22] for most simulations in the NIR band. It highlights the usual faster convergence of DART-Lux in visible bands than in NIR bands. This is also underlined by the BRF profiles (Figure 3.14): NIR BRFs are noisier than VIS BRFs if the same number of samples per pixel is used.

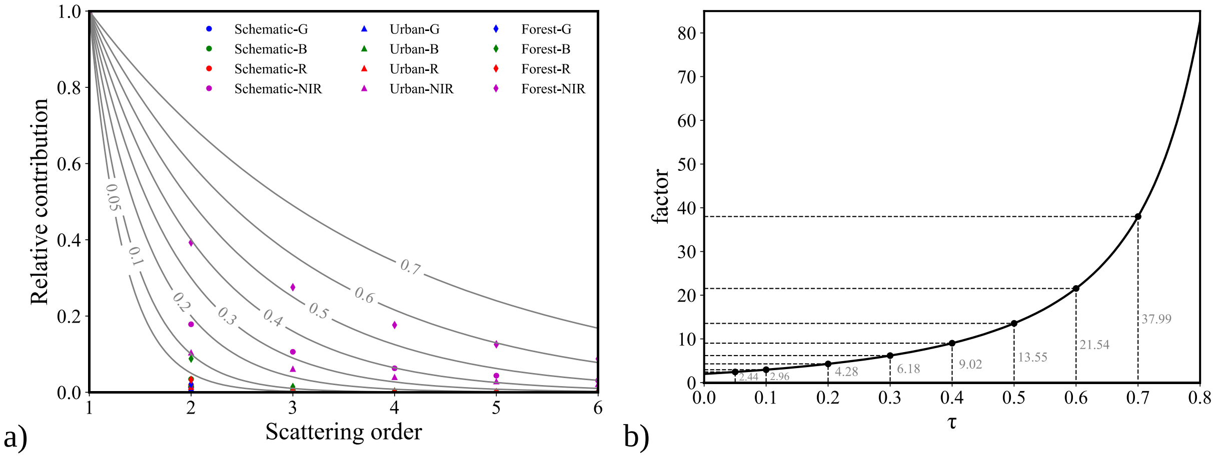

Figure 3.18. Contribution $g(n)$ of scene radiance for scattering order $n$ = 1 to 6, relative to the contribution of first order scattering, for the three studied scenes: schematic, urban and forest. a) Trendlines $g(n)=\tau^{-(n-1)}$. b) Factor $f(\tau)$ in function of $\tau$ value (Eq. (3.27)).

Recall the efficiency $\epsilon$ of a Monte Carlo method (Eq. (C.14)) defined by its variance $\mathbb{V}$ and computation time $\mathbb{T}$:

$$\epsilon = \frac{1}{\mathbb{V}\cdot\mathbb{T}}$$

Compared to an algorithm that uses independent paths, DART-Lux appears to be more efficient despite the correlation of its path samples. The efficiency gains $\eta$ of DART-Lux over the method that uses independent path samples is:

$$\eta = \left(\frac{\epsilon_{\text{DART-Lux}}}{\epsilon_{\text{independent path}}} - 1\right) = \left(\frac{1}{f(\tau)} \cdot \frac{{N_v}^3}{{N_v}^2 + 2(N_v - 1)} - 1\right)$$

In VIS bands, usually $N_v$=5, $f(\tau)\leqslant 2.5$, then $\eta > 50\%$. In NIR bands, usually $N_v \geqslant 40$, $f(\tau) \leqslant 22$, then $\eta > 70\%$. Actually, $\eta$ is even larger because the variance is usually smaller than the upper boundary variance.

### 3.6.2 Advantages of DART-Lux for simulating images

Compared to DART-FT, DART-Lux has great advantages for simulating remote sensing images and BRF, especially for complex environments with millions of facets. Table 3.4 summarizes the memory allocation and computation time of simulations in section 3.5. For the Järvselja birch forest, DART-Lux reduces the simulation time by 715 times, and the memory by 142 times. Four factors explain DART-Lux efficiency. 1) End-to-end simulation: DART-Lux samples the paths that contribute only to the simulated image whereas DART-FT tracks all possible paths. 2) Efficient path generating strategy: bi-directional random walk and vertex connection ways can generate a group of paths with less time cost. Despite the potential increase of variance since path samples can be correlated, the overall efficiency increases (*cf.* section 3.6.1). 3) Depth-first strategy: the random walk requires much less memory compared to the breadth-first strategy of DART-FT whose memory demand greatly increases with scattering order. Although DART-FT applies an acceleration technique by merging rays that come out of a cell face for each discrete direction (*cf.* section 3.5.3), its memory usage is still very high for modelling large-scale landscapes. 4) Data organisation: for a scene with $N$ instances of a 3D object, DART-Lux cloning technique stores a unique 3D object and $N$ rotation – scaling matrices whereas DART-FT stores $N$ 3D objects in the memory for simulating the 3D radiative budget. Therefore, DART-Lux uses much less memory and time than DART-FT.

Two points must be noted here, (1) single direction image simulation: although DART-Lux is much more efficient than DART-FT for simulating complex scenarios, it is slower to simulate simple scenarios, such as the bare ground, the simple building arrays; (2) multi-angle image simulation: a single DART-FT simulation can give many directional image, that is to say, the computation time of 1000 images is nearly the same as for one image. Presently, for DART-Lux, the simulation time for N images is nearly N times the simulation time of one image.

Table 3.4. Simulation time and memory demand for the three cases of section 3.5. Cases 1 and 2 are simulated on a personal computer (Intel Xeon E5-1620 @ 3.5 GHz, 8 cores, 64 Gb memory). Case 3 is simulated on a server (Intel Xeon E5-2687W @ 3.1 GHz, 40 cores, 560 Gb memory).

| Scene | DART-FT | | DART-Lux | |
|---|---|---|---|---|
| | Time (min) | Memory (Gb) | Time (min) | Memory (Gb) |
| Case 1: Schematic | 70.8 | 1.25 | 1.38 | 0.07 |
| Case 2: Urban | 571 | 40.0 | 10.86 | 2.60 |
| Case 3: Forest | 4962 | 469.0 | 6.93 | 3.30 |

### 3.6.3 Accuracy of DART-Lux

In theory, the Monte Carlo method is more accurate than the discrete ordinates method, because it does not need to simplify the 3D mock-up and radiation processes. The underestimation of the hot-spot in Figure 3.17.f illustrates this point. However, because Monte Carlo methods need many samples to reach convergence, there is a trade-off between accuracy and number of samples. Fortunately, DART-Lux accuracy and efficiency is less dependent than DART-FT on the complexity of the radiative transfer problem. For example, the forest scene has an average computation time per sample (*i.e.*, $\frac{\text{Simulation time}}{\text{Number of samples}}$) that is only 7 times longer than for the schematic scene, although it is 4000 times more complex than the schematic scene in terms of number of facets (Table 3.5). Table 3.6 shows the accuracy of DART-Lux forest reflectance for six values of samples/m$^2$: difference $\varepsilon_{\text{mean}}$ of image mean reflectance, and RMSE $\varepsilon_{\text{pixel}}$ of image pixel reflectance relative to the reference values computed with a huge number of samples/m$^2$. Results stress that DART-Lux configuration can be optimized according to the application and accuracy requirements. 1) Convergence is much faster for low reflectance bands than for high reflectance bands, which is consistent with discussion in section 3.6.1. 2) $\varepsilon_{\text{mean}}$

and $\varepsilon_{\text{pixel}}$ decrease with the increase of samples/m$^2$, with a much faster convergence for $\varepsilon_{\text{mean}}$ than for $\varepsilon_{\text{pixel}}$.

Table 3.5. Average time cost per sample $\frac{\text{Simulation time}}{\text{Number of samples}}$ of the schematic and forest scenes in section 3.5. Intel Xeon E5-2687W server (3.1 GHz, 40 cores, 560 Gb memory).

| Scene | Nb facet | Nb pixels | Samples/pixel | Time (min) | Time/sample ($\mu$s) |
|---|---|---|---|---|---|
| Case 1: Schematic | 0.137 $10^6$ | 65536 | 400 | 0.20 | **0.45** |
| Case 3: Forest | 558.2 $10^6$ | 640000 | 200 | 6.93 | **3.25** |

Table 3.6. Absolute nadir reflectance error $\varepsilon_{\text{mean}}$ and pixel RMSE $\varepsilon_{\text{pixel}}$ of the forest scene in G and NIR bands for six samples/m$^2$ values. Reference images are simulated with 128000 samples/m$^2$.

| | **Samples/m$^2$** | **640** | **3200** | **6400** | **12800** | **25600** | **51200** |
|---|---|---|---|---|---|---|---|
| **G** | $\varepsilon_{\text{mean}}$ | 3.8E-6 | 9.7E-6 | 4.0E-7 | 2.4E-6 | 1.5E-6 | 2.1E-6 |
| | $\varepsilon_{\text{pixel}}$ | 0.010 | 0.005 | 0.003 | 0.002 | 0.002 | 0.001 |
| **NIR** | $\varepsilon_{\text{mean}}$ | 3.0E-6 | 4.1E-5 | 1.2E-5 | 4.9E-6 | 1.3E-5 | 1.1E-5 |
| | $\varepsilon_{\text{pixel}}$ | 0.075 | 0.034 | 0.024 | 0.018 | 0.013 | 0.010 |

## 3.7 Conclusions

The unbiased, rapid and robust DART-Lux is a new Monte Carlo radiative transfer mode in DART. Its physical modelling relies on a bidirectional path tracing algorithm that efficiently samples a group of paths between the light source and the sensor to estimate radiance measurements. The algorithm is flexible to incorporate multi light sources (*e.g.*, sun and sky), multi sensors (perspective camera, orthographic camera, BRF camera) and multi surface scattering distribution (Lambertian, specular). It greatly improves the computational efficiency of DART to simulate spectral images and BRF. Its accuracy and efficiency are assessed by the classic DART-FT mode for three landscapes (*i.e.*, schematic scene, urban scene, forest scene).

Compared to DART-FT, DART-Lux gives consistent results (relative difference < 1%) while reducing the computation time by up to a factor of 700. A better consistency can be achieved if DART-FT is configured with much more discrete directions and without the above-mentioned acceleration technique. However, in this case, the simulation time and demand in computer memory of DART-FT hugely increase. In addition, DART-Lux is nearly independent on the land surface complexity conversely to DART-FT, which greatly eases the simulation of complex landscapes.

A theoretical demonstration gives analytical expressions of the computation time and the upper boundary variance. It appears that DART-Lux algorithm improves efficiency $\epsilon$ even if it creates correlated path samples. It also has great advantages for simulating remote sensing images due to end-to-end modelling, efficient path sampling and depth-first strategy. Finally, a sensitivity study shows that (1) DART-Lux error decreases with the number of samples, (2) image mean values converge much faster than image pixel values, and (3) the convergence is faster for low reflectance bands than for high reflectance bands.

The high-performance DART-Lux addresses the requirements for simulating large-scale and complex landscapes and massive remote sensing data, as well as the trends in RTM development. The Monte Carlo approach is potentially better adapted than discrete ordinates method for designing and implementing complex physical phenomena such as adjacency effects and clouds scattering and shadowing. DART-Lux opens new avenues for many remote sensing applications: design of satellite missions; correction of directional effects; inversion of remote sensing images; training machine learning models with many images; studying the impact of complex 3D architecture, *etc*. DART-Lux modelling development is still underway to expand its functionality, including solar induced fluorescence and thermal emission, LiDAR, atmospheric radiative transfer, polarization, and 3D radiative budget.

## 3.Appendix A Upper boundary variance of the radiance estimate (Part I)

The estimation of the upper boundary variance of the radiance estimate gives a good insight into the performance of an estimator. Here we analyse the increase of the variance due to the path sample correlation in the bidirectional path tracing algorithm.

Recall the estimate of contribution of $n$-1 scattering order $C_{\mathcal{D}_n}$ (Eq. (3.10)):

$$F_{\mathcal{D}_n}^{(j)} = \sum_{s=0}^{n+1} w_{s,t}(\bar{r}_{s,t}) \cdot \frac{f^{(j)}(\bar{r}_{s,t})}{p(\bar{r}_{s,t})} = \sum_{s=0}^{n+1} F_{s,t}$$

where $\bar{r}_{s,t} \in \mathcal{D}_n$, and $s + t = n + 1$. The corresponding variance is computed by:

$$\mathbb{V}\left(F_{\mathcal{D}_n}^{(j)}\right) = \sum_{s=0}^{n+1} \sum_{s'=0}^{n+1} Cov(F_{s,t}, F_{s',t'}) = \sum_{s=0}^{n+1} \mathbb{V}(F_{s,t}) + \sum_{s=0}^{n+1} \sum_{s'=0,\, s' \neq s}^{n+1} Cov(F_{s,t}, F_{s',t'})$$

If all path samples are independent, we have: $\mathbb{V}\left(F_{\mathcal{D}_n}^{(j)}\right) = \sum_{s=0}^{n+1} \mathbb{V}(F_{s,t}) = \sigma_n^2$.

Because the bidirectional path tracing algorithm uses the same light and sensor random walk to get path samples, the later ones can be dependent (*i.e.*, $\sum_{s=0}^{n+1} \sum_{s'=0,\, s' \neq s}^{n+1} Cov(F_{s,t}, F_{s',t'}) \neq 0$) and the overall variance can increase. For a path of length $n$=1, we always have: $\mathbb{V}\left(F_{\mathcal{D}_1}^{(j)}\right) = \sigma_1^2$.

For a path of length $n$>1, we resample vertices on light source or sensor (*i.e.*, no re-use of already sampled vertex), and use the "connect to light" and "connect to sensor" methods (Figure 3.6) to reduce path correlation. It leads to:

$$Cov(\bar{r}_{0,n+1}, \bar{r}_{n+1,0})=0, \quad Cov(\bar{r}_{1,n}, \bar{r}_{n,1})=0, \quad Cov(\bar{r}_{0,n+1}, \bar{r}_{n,1})=0, \quad Cov(\bar{r}_{1,n}, \bar{r}_{n+1,0})=0$$

The inequalities $\sqrt{\mathbb{V}(\mathrm{X}) \cdot \mathbb{V}(\mathrm{Y})} \leq [\mathbb{V}(\mathrm{X}) + \mathbb{V}(\mathrm{Y})]/2$ and $Cov(\mathrm{X}, \mathrm{Y}) \leq \sqrt{\mathbb{V}(\mathrm{X}) \cdot \mathbb{V}(\mathrm{Y})}$ (Cauchy-Schwarz) lead to the expression of the upper boundary variance of the estimate $F_{\mathcal{D}_n}^{(j)}$:

$$\mathbb{V}\left(F_{\mathcal{D}_n}^{(j)}\right) \leq \sum_{s=0}^{n+1} \sum_{s'=0}^{n+1} \frac{\mathbb{V}(F_{s,t}) + \mathbb{V}(F_{s',t'})}{2} - 2[\mathbb{V}(F_{0,n+1}) + \mathbb{V}(F_{1,n}) + \mathbb{V}(F_{n+1,0}) + \mathbb{V}(F_{n,1})]$$
$$= (n+2)\delta_{\mathcal{D}_n}^2 - 2[\mathbb{V}(F_{0,n+1}) + \mathbb{V}(F_{1,n}) + \mathbb{V}(F_{n+1,0}) + \mathbb{V}(F_{n,1})]$$

Finally, we derive: $\begin{cases} \mathbb{V}\left(F_{\mathcal{D}_1}^{(j)}\right) = \sigma_1^2, \\ \mathbb{V}\left(F_{\mathcal{D}_2}^{(j)}\right) \leq 2\sigma_2^2, \\ \mathbb{V}\left(F_{\mathcal{D}_n}^{(j)}\right) \leq (n+2)\sigma_n^2, \;\; \forall\, n > 2 \end{cases}$

## 3.Appendix B Upper boundary variance of the radiance estimate (Part II)

The methodology in 3.Appendix A can be extended to evaluate the upper boundary variance of

$$F_{\mathrm{MIS}}^{(j)} = \sum_{n=1}^{\infty} \sum_{s=0}^{n+1} w_{s,t}\left(\bar{r}_{s,t}\right) \cdot \frac{f^{(j)}\left(\bar{r}_{s,t}\right)}{p\left(\bar{r}_{s,t}\right)}$$

Since in most optical Earth observation missions, the sensor does not see the light source (*e.g.*, sun) directly, contribution $C_{\mathcal{D}_1}$ is null. Besides, the path correlation does not increase the variance of $F_{\mathcal{D}_1}^{(j)}$ (Eq. (C.2)). Therefore, we analyse the impact of path correlation on $C_{\mathcal{D}_2}, \cdots, C_{\mathcal{D}_{M_0+1}}$.

We rewrite $F_{\mathrm{MIS}}^{(j)}$ as $F_{\mathrm{MIS}}^{(j)} = \sum_{n=2}^{\infty} F_{\mathcal{D}_n}^{(j)}$. Its variance is $\mathbb{V}\left(F_{\mathrm{MIS}}^{(j)}\right) = \sum_{n_1=2}^{\infty} \sum_{n_2=2}^{\infty} Cov\left(F_{\mathcal{D}_{n_1}}^{(j)}, F_{\mathcal{D}_{n_2}}^{(j)}\right)$. (Kallel, 2018) shows that the contribution $C_{\mathcal{D}_n}$ decreases exponentially with the scattering order. We can suppose $C_{\mathcal{D}_{n+1}} \approx \tau \cdot C_{\mathcal{D}_n}, \forall\, n$, $\tau$ is a constant, $0 \leq \tau \leq 1$. It is more or less true in most radiative transfer modelling for the Earth observation (Figure 3.18.a). It leads to:

$$\mathbb{V}\left(F_{\mathcal{D}_{n+1}}^{(j)}\right) = \tau^2 \cdot \mathbb{V}\left(F_{\mathcal{D}_n}^{(j)}\right)$$

If all the path samples are independent, the variance $\mathbb{V}(F_{\mathrm{MIS}})$ is the sum of variances $\sigma_n^2$:

$$\mathbb{V}\left(F_{\mathrm{MIS}}^{(j)}\right) = \sum_{n=2}^{\infty} \sigma_n^2 = \sum_{n=2}^{\infty} \tau^{2(n-2)} \cdot \sigma_2^2 = \frac{\sigma_2^2}{1-\tau^2}$$

If path samples are not all independent, the Cauchy-Schwarz inequality and the conclusions in the 3.Appendix A lead to:

$$\begin{aligned}
\mathbb{V}\left(F_{\mathrm{MIS}}^{(j)}\right) &= \sum_{n_1=2}^{\infty} \sum_{n_2=2}^{\infty} Cov\left(F_{\mathcal{D}_{n_1}}^{(j)}, F_{\mathcal{D}_{n_2}}^{(j)}\right) \leq \sum_{n_1=2}^{\infty} \sum_{n_2=2}^{\infty} \sqrt{\mathbb{V}\left(F_{\mathcal{D}_{n_1}}^{(j)}\right) \cdot \mathbb{V}\left(F_{\mathcal{D}_{n_2}}^{(j)}\right)} \\
&= \mathbb{V}\left(F_{\mathcal{D}_2}^{(j)}\right) + 2\sqrt{\mathbb{V}\left(F_{\mathcal{D}_2}^{(j)}\right)} \sum_{n=3}^{\infty} \sqrt{\mathbb{V}\left(F_{\mathcal{D}_n}^{(j)}\right)} + \sum_{n_1=3}^{\infty} \sqrt{\mathbb{V}\left(F_{\mathcal{D}_{n_1}}^{(j)}\right)} \sum_{n_2=3}^{\infty} \sqrt{\mathbb{V}\left(F_{\mathcal{D}_{n_2}}^{(j)}\right)} \\
&\leq 2\sigma_2^2 + 2\sqrt{2}\sigma_2\left[\sum_{n=3}^{\infty} \sqrt{n+2}\,\sigma_n\right] + \sum_{n_1=3}^{\infty} \sqrt{n_1+2} \cdot \sigma_{n_1} \sum_{n_2=3}^{\infty} \sqrt{n_2+2} \cdot \sigma_{n_2} \\
&= \sigma_2^2\left[2+2\sqrt{2}\cdot \sum_{n=3}^{\infty} \sqrt{(n+2)} \cdot \tau^{n-2} + \sum_{n_1=3}^{\infty} \sum_{n_2=3}^{\infty} \sqrt{(n_1+2)(n_2+2)} \cdot \tau^{n_1-2} \cdot \tau^{n_2-2}\right]
\end{aligned}$$

Using the relationships: $\sqrt{(n_1+2)(n_2+2)} \leq \frac{(n_1+2)+(n_2+2)}{2}$

$$\sqrt{(n+2)\cdot 1} \leq \frac{(n+2)+1}{2}, \forall\, n > 0$$

$$\sum_{n=3}^{\infty}(n+i)\cdot\tau^{n-2} = \frac{(3+i)\tau-(2+i)\tau^2}{(1-\tau)^2}, \forall\, i \in \mathbb{N}$$

we get: $\mathbb{V}\left(F_{\text{MIS}}^{(j)}\right) \leq \sigma_2^2\left[\frac{2+(6\sqrt{2}-6)\tau+(11-11\sqrt{2})\tau^2+(5\sqrt{2}-6)\tau^3}{(1-\tau)^3}\right]$

$$= \sigma_2^2\left[\frac{2+\tau\left(\frac{\sqrt{2}}{2}-\tau\right)(3-\tau)}{(1-\tau)^3} + \frac{\left(\frac{9}{\sqrt{2}}-6\right)\tau+\left(14-\frac{21}{\sqrt{2}}\right)\tau^2+\left(5\sqrt{2}-7\right)\tau^3}{(1-\tau)^3}\right]$$

$$\approx \sigma_2^2\cdot\left[\frac{2+\tau\left(\frac{\sqrt{2}}{2}-\tau\right)(3-\tau)}{(1-\tau)^3}\right]$$

The term $\left(\frac{9}{\sqrt{2}}-6\right)\tau+\left(14-\frac{21}{\sqrt{2}}\right)\tau^2+\left(5\sqrt{2}-7\right)\tau^3$ is omitted since it is less than $0.04 \ll 1$ if $\tau \in [0,1]$. Hence, the variance will increase maximally by a factor of

$$f(\tau) = \frac{\sigma_2^2\cdot\left[\frac{2+\tau\left(\frac{\sqrt{2}}{2}-\tau\right)(3-\tau)}{(1-\tau)^3}\right]}{\frac{\sigma_2^2}{1-\tau^2}} = \frac{(1+\tau)\cdot\left[2+\tau\left(\frac{\sqrt{2}}{2}-\tau\right)(3-\tau)\right]}{(1-\tau)^2}$$

In the short waves, a sensor does not usually see the light source, conversely to the long waves where the observed environment is a light source, which implies that the contribution $C_{\mathcal{D}_1}$ to the measured radiance is usually large. Then, the same method as above shows that the variance maximally increases by a factor of

$$f(\tau) = \frac{(1+\tau)\cdot\left(1+\tau^2\cdot(1-\tau^2)\cdot(2-\tau)\right)}{(1-\tau)^2}$$

# *CHAPTER 3 APPENDIX*

# Chapter 4

# Modelling of atmospheric effects

Chapter 3 describes a newly developed DART-Lux mode in DART based on the bidirectional path tracing algorithm. It efficiently samples a group of stochastic paths that connect the light source and the sensor and estimates the unbiased radiance measurement using the weighted contribution of these path samples. However, it works with only the environment represented by a collection of surfaces without the consideration of fluids and their volume absorption, emission and scattering mechanisms. This chapter generalizes DART-Lux modelling to scenes made of surfaces and fluids. Regaieg (2023) will present the case of scenes with 3D distribution of turbid medium used to represent vegetation statistically.

We first propose a uniform formulation of the radiance measurement:

$$L^{(j)} = \int_{\mathcal{D}} f^{(j)}(\bar{r})\, d\mu(\bar{r})$$

$L^{(j)}$ is an integral over the generalized path space $\mathcal{D}$ with path vertices at a surface or in a medium. It is evaluated by sampling stochastic paths and an uniform bidirectional path tracing algorithm. In its practical implementation, we have designed an innovative Earth-Atmosphere system to simulate remote sensing observations with atmospheric effects. The accuracy of the atmospheric radiative transfer modelling is assessed by the atmosphere model MODTRAN.

Finally, based on this new modelling, we conduct a virtual experiment to analyse the driving factors that create and influence neighbourhood effects in remote sensing images.

The atmosphere in our implementation is abstracted as plane-parallel and horizontally homogeneous layers. Considering this simple structure, the discrete ordinates method is more efficient, but less accurate, than the Monte Carlo method. Therefore, we also propose an alternative fast hybrid method that combines discrete ordinates radiative transfer in the atmosphere and the Monte Carlo radiative transfer at land surfaces. Its theory, algorithm and accuracy are presented in Annex B.

## 4.1 Theoretical background

### 4.1.1 The three-point form of the radiative transfer equation

The formal solution of the radiative transfer equation (Eq. (1.18)) describes the exit radiation in direction Ω as the radiation transmitted from the nearest surface "seen" in direction Ω, plus the radiation scattered and emitted in direction Ω. In the absence of surfaces (*e.g.*, surfaces are infinitely far from the location where radiance is measured), we can derive an alternative expression using the source function (Eq. (1.19)) as the exit quantity $dL_o/ds$:

$$\frac{dL_o(r,\Omega)}{ds}=\frac{dL_e(r,\Omega)}{ds}+\int_{4\pi}\frac{\alpha_s(r,\Omega')}{4\pi}\cdot P(r,\Omega'\to\Omega)\cdot\left[\int_0^\infty\frac{dL_o(r',\Omega)}{ds}\cdot\mathcal{T}(r\leftrightarrow r')ds'\right]d\Omega' \quad (4.1)$$

As the light transport equation (section 3.1.1), Eq. (4.1) can be represented by a three-point form:

$$\begin{aligned}\frac{dL_o(r'\to r)}{ds}&=\frac{dL_e(r'\to r)}{ds}\\&+\int_V\frac{dL_o(r''\to r')}{ds'}\cdot\frac{\alpha_s(r''\to r')\cdot P(r''\to r'\to r)}{4\pi}\cdot\frac{V(r''\leftrightarrow r')\cdot T(r''\leftrightarrow r')}{\|r''-r'\|^2}dV(r'')\end{aligned} \quad (4.2)$$

with $V(r''\leftrightarrow r')$ the visibility function and $V$ all scene volumes $dV(r'')=dA(r'')ds=\|r''-r'\|^2 d\Omega ds$.

### 4.1.2 The unified light transport equation

The three-point form of the light transport equation (Eq. (3.1)) and the three-point form of the radiative transfer equation (Eq. (4.2)) can be included in a unified formulation:

$$\tilde{L}_o(r'{\to}r) = \tilde{L}_e(r'{\to}r) + \int_{\mathcal{M}} \tilde{L}_o(r''{\to}r') \cdot \tilde{f}_s(r''{\to}r'{\to}r) \cdot \tilde{G}(r'{\leftrightarrow}r'') d\mathcal{M}(r'') \qquad (4.3)$$

with $\mathcal{M}$ a surface $A$ or volume $V$ depending on the present material. The effective exit radiance $\tilde{L}_o$ and the effective source emission radiance $\tilde{L}_e$ are radiance terms for a surface, and radiance per unit distance for a volume:

$$\tilde{L}(r' \to r'') = \begin{cases} L(r' \to r''), & \forall\, r' \in A \\ \dfrac{\partial L(r' \to r'')}{\partial r}, & \forall\, r' \in V \end{cases}$$

Then, the scattering distribution function $\tilde{f}_s$ is BSDF for the surface, and is the product of the scattering coefficient by the scattering phase function for the volume:

$$\tilde{f}_s(r'' \to r' \to r) = \begin{cases} f_s(r'' \to r' \to r), & \forall\, r' \in A \\ \alpha_s(r'' \to r') \cdot \dfrac{P(r'' \to r' \to r)}{4\pi}, & \forall\, r' \in V \end{cases}$$

The generalized geometric term $\tilde{G}$ is: $\tilde{G}(r' \leftrightarrow r'') = V(r' \leftrightarrow r'') \cdot \mathcal{T}(r'' \leftrightarrow r') \cdot \frac{\mu_o^{r'} \cdot \mu_i^{r''}}{\|r'' - r'\|^2}$ with

$$\mu_o^{r'} = \begin{cases} \cos\theta_o^{r'}, & r' \in A \\ 1, & r' \in V \end{cases} \text{ and } \mu_i^{r''} = \begin{cases} \cos\theta_i^{r''}, & \forall\, r'' \in A \\ 1, & \forall\, r'' \in V \end{cases}$$

### 4.1.3 Path integral formulation

In an interaction, $\tilde{L}_o$ is contributed by the $\tilde{L}_o$ from the previous interaction. As a result, Eq. (4.3) can be iteratively expanded to an infinite sum of multi-dimensional integral

$$\begin{aligned} \tilde{L}_o(r_1 \to r_0) = {} & \tilde{L}_e(r_1 \to r_0) + \int_{\mathcal{M}} \tilde{L}_e(r_2 \to r_1) \cdot \tilde{f}_s(r_2 \to r_1 \to r_0) \cdot \tilde{G}(r_1 \leftrightarrow r_2) d\mathcal{M}(r_2) \\ & + \int_{\mathcal{M}} \int_{\mathcal{M}} \tilde{L}_e(r_3{\to}r_2) \cdot \tilde{f}_s(r_3{\to}r_2{\to}r_1) \cdot \tilde{G}(r_2{\leftrightarrow}r_3) \cdot \tilde{f}_s(r_2{\to}r_1{\to}r_0) \cdot \tilde{G}(r_1{\leftrightarrow}r_2) d\mathcal{M}(r_3) d\mathcal{M}(r_2) + \ldots \end{aligned}$$

with each multi-dimensional integral being the contribution of a scattering order to $\tilde{L}_o(r_1 \to r_0)$.

$r_1 \to r_0$ being the direction to the sensor, the radiance measurement $L^{(j)}$ can be computed by integrating and weighting $\tilde{L}_o(r_1 \to r_0)$ using the importance function ${W_e}^{(j)}(r_0 \to r_1)$:

$$L^{(j)} = \int_A \int_{\mathcal{M}} {W_e}^{(j)}(r_0 \to r_1) \cdot \tilde{L}_o(r_1 \to r_0) \cdot \tilde{G}(r_0 \leftrightarrow r_1) \cdot d\mathcal{M}(r_1) \cdot dA(r_0) \tag{4.4}$$

Eq. (4.4) can still be represented by a Lebesgue integration over the space measure $\mu$ that represents the measurement radiance of the set of paths $\mathcal{D}$:

$$L^{(j)} = \int_{\mathcal{D}} f^{(j)}(\bar{r}) \cdot d\mu(\bar{r}) \tag{4.5}$$

with $\mathcal{D}_n$ and $\mu(\mathcal{D}_n)$ generalized to the paths that intersect surfaces and volumes. Because a vertex is either in a volume $V$ or on a surface $A$, the new $\mathcal{D}_n$ is the multiple Cartesian product of the space set $\{A, V\}$. Integration over it is the sum of $2^n$ $(n+1)$-dimensional integrals.

$$\mathcal{D}_n = \bigcup_{c \in \{0,1\}^n} (A \times \mathcal{M}_1 \times \cdots \times \mathcal{M}_n)\, , \text{with } \mathcal{M}_k = \begin{cases} A, c_k = 0 \\ V, c_k = 1 \end{cases}$$

$$\mu(\mathcal{D}_n) = \int_{\mathcal{D}_n} d\mu(\bar{r}_n) = \sum_{c \in \{0,1\}^n} \int_{(A \times \mathcal{M}_1 \times \cdots \times \mathcal{M}_n)} dA(r_0) \cdot \prod_{k=1}^{n} \begin{cases} dA(r_k), & c_k = 0 \\ dV(r_k), & c_k = 1 \end{cases}$$

with the Cartesian product $\{0, 1\}^n = \left\{(c_1, c_2, \cdots, c_k, \cdots, c_n) | c_k \in \{0, 1\}\ \forall k \in \{1, 2, \cdots, n\}\right\}$.

The re-defined contribution function $f^{(j)}(\bar{r}_n)$ using the unified surface and volume terms is:

$$f^{(j)}(\bar{r}_n) = \tilde{L}_e(r_n \to r_{n-1}) \cdot \tilde{G}(r_0 \leftrightarrow r_1) \cdot {W_e}^{(j)}(r_0 \to r_1) \cdot \prod_{k=2}^{n} \tilde{f}_s(r_k \to r_{k-1} \to r_{k-2}) \cdot \tilde{G}(r_{k-1} \leftrightarrow r_k) \tag{4.6}$$

## 4.2 Radiative transfer modelling

Eq. (4.6) has the same formulation as Eq. (3.9). It stresses that a unified algorithm (*cf.* section 3.2) can be used to treat the interactions with both surfaces and media. The only difference is that the evaluation of the effective source emission, the scattering distribution function and the geometric term depend on the present material. The bidirectional path tracing algorithm is still efficient for small environment that is a mixture of surfaces and media, for example, to simulate a cloud of smoke over a city building. However, with the usual representation of the atmosphere

(Figure 4.1) with an infinite horizontal dimension, the forward random walk from the light source is very inefficient. For example, a random walk from the light source can be 200 km away from the target has very small probability to give a ray that is scattered into the FOV of a sensor. Also, its intersection with an object (*e.g.*, leaf) is not accurate at all due to the computer decimal imprecision. Therefore, the forward random walk can waste time and be a source of inaccuracy. Consequently, the forward random walk is disactivated if one simulates the remote sensing observations in the new Earth-Atmosphere system (Figure 4.1). In short, a random virtual ray is emitted from the sensor, and is connected to the light source after each interaction with a medium or a surface (*cf.* Figure 3.6.b). The estimator in Eq. (3.13) is then reduced to

$$F_{\mathrm{IS}}^{(j)} = \sum_{n=1}^{\infty} \frac{f^{(j)}(\bar{r}_n)}{p(\bar{r}_n)} \tag{4.7}$$

Because the infinite scattering order cannot be explicitly simulated, a user defined maximal scattering order $M_0$ is usually set to limit the path length as in Eq. (3.15).

### 4.2.1 The proposed Earth-Atmosphere system

Usually, the ground area imaged by the instantaneous FOV of the sensor is much smaller compared to the dimension of the atmosphere and Earth surfaces. Therefore, because of atmospheric scattering, the radiance of a pixel in a remote sensing image depends on the radiance of the surfaces that neighbour the land surface geometrically associated to the considered pixel. This is the so-called *adjacency effect*. It emphasizes the need to consider the near-infinity of the surrounding surface and atmosphere in modelling radiative transfer. Therefore, we designed a new Earth-Atmosphere system (Figure 4.1) in which the target 3D landscape (also called scene) is in its bottom centre and is surrounded by a quasi-infinite background and atmosphere. In presence of topography on the target scene boundary with the background, a smooth connection is done using the Bézier triangle (Farin, 2014; Wang et al., 2020). The atmosphere (*i.e.*, gases, aerosols, clouds) is simulated as horizontally homogeneous layers with continuous vertical properties (*e.g.*, extinction coefficient, temperature). The default atmosphere geometry is 1 km vertical step from 0 to 15 km and 5 km step from 15 to 50 km. In each layer, vertical variations are represented by polynomials. The default dimension of the horizonal cross section of the system is X × Y = 500 km × 500 km. This configuration is chosen because most atmospheric constituents are concentrated below 50 km altitude and the impact of the environment at 250 km away is usually negligible. Experiments in 4.Appendix A prove that the default choice gives relative differences less than 0.1% compared to an atmosphere up to 100 km in altitude and up to 10000 km in horizontal size. One can also define the atmosphere geometry according to the experiment requirement. Six standard atmosphere models (*i.e.*, TROPICAL, MIDLATSUM, MIDLATWIN, SUBARCSUM, SUBARCWIN and USSTD76 (Anderson et al., 1986)) and five standard aerosol models (*i.e.*, Rural, Urban, Maritime, Tropospheric and Fog (Shettle and Fenn, 1979)) are provided (note that the fog is not a type of aerosol, but its modelling is treated similarly as aerosols). One can adjust them with multiplicative factors or import external measurements. The methods to compute the vertical properties at each altitude are detailed in 4.Appendix B and 4.Appendix C. Sensors in the system can be placed at an arbitrary position with an arbitrary orientation and FOV. This innovative concept allows one to simulate atmospheric and adjacency effects.

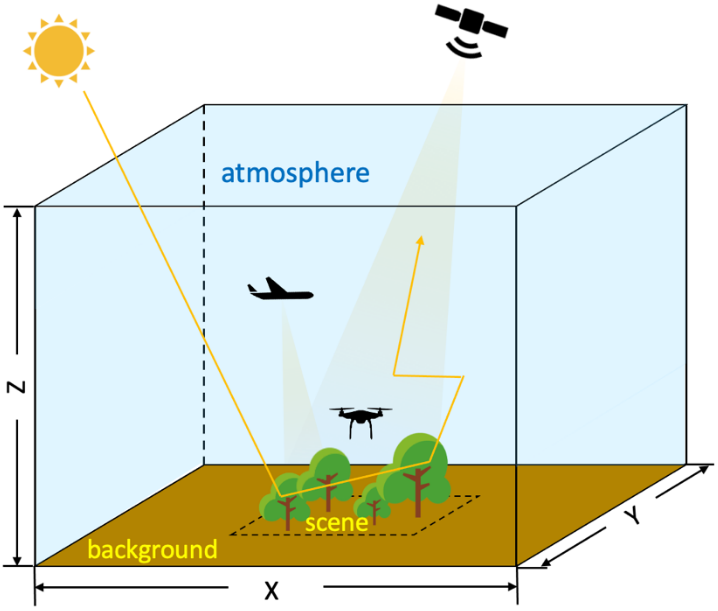

Figure 4.1. DART-Lux Earth-Atmosphere system (default dimension: X × Y × Z = 500 km × 500 km × 50 km). The atmosphere is in a rectangular parallelepiped. The target scene is at the bottom centre and is surrounded by a horizontal bare ground (background).

### 4.2.2 Light transmission in the atmosphere

Radiation $L(r,\Omega)$ in a medium is attenuated due to absorption and scattering (*cf.* section 1.3.2):

$$\frac{dL(r,\Omega)}{ds} = -\alpha_e(r,\Omega)\cdot L(r,\Omega)$$

Therefore, the longer the radiation propagates, the more likely it is intercepted by a molecule or a particle. The probability that a free path $S$ that terminates before a distance $s$ is:

$$\mathbb{P}(S \le s) = 1 - \mathcal{T}(s)$$

with $\mathcal{T}(s)$ the transmittance of the line of sight from a location $r$ to $r+s\cdot\Omega$ in direction $\Omega$.

Based on this definition, it is convenient to derive the cumulative distribution function $P_S(s)$ and the probability density function of the free path $p(s)$:

$$P_S(s) = \mathbb{P}(S \le s) = 1 - \mathcal{T}(s) \quad \text{and} \quad p(s) = \frac{dP_S(s)}{ds} = \alpha_e(s, \Omega) \cdot \mathcal{T}(s) \tag{4.8}$$

with $\alpha_e(s,\Omega)$ the extinction coefficient at location $r+s\cdot\Omega$ (Figure 4.2). Note that $\alpha_e$ is the spectral average quantity if the spectral signal is modelled.

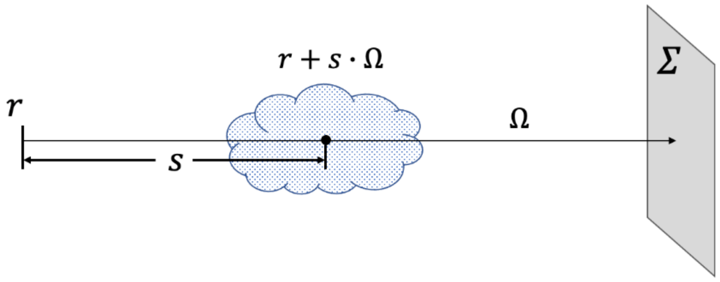

Figure 4.2. Distance sampling scheme. $s$ is the distance from the start location $r$ to the location $r+s\cdot\Omega$ in direction $\Omega$. $\Sigma$ is the nearest surface in the propagation direction.

The probabilistic free path $S$ is derived from a random variable $\xi \in [0,1)$ and an inversion function:

$$S = P_S^{-1}(\xi) \tag{4.9}$$

$S$ has an analytic solution if the medium is homogeneous (*i.e.*, constant $\alpha_e$ in the line of sight):

$$S = P_S^{-1}(\xi) = -\frac{\ln(1-\xi)}{\alpha_e}$$

If $\alpha_e$ varies along the line of sight, which is the most common situation in the atmosphere, $P_S^{-1}(\xi)$ cannot be derived analytically. Then, we represent the heterogeneous medium by discrete layers or cells and implement a so-called *Regular Tracking* method (Amanatides and

Woo, 1987) to sample the free path. For example, for a series of homogeneous segment medium each one with extinction coefficient $\alpha_i$ and segment length $\Delta s_i$ along the line of sight:

$$\begin{aligned} P_S(s) &= 1 - e^{-\sum_{k=0}^{i-1} \alpha_k \cdot \Delta s_k + \alpha_i \cdot \left(s - \sum_{k=0}^{i-1} \Delta s_k\right)}, \quad \forall\, s \in [\sum_{k=0}^{i-1} \Delta s_k, \sum_{k=0}^{i} \Delta s_k) \\ p(s) &= \alpha_i \cdot e^{-\sum_{k=0}^{i-1} \alpha_k \cdot \Delta s_k + \alpha_i \cdot \left(s - \sum_{k=0}^{i-1} \Delta s_k\right)}, \quad \forall\, s \in [\sum_{k=0}^{i-1} \Delta s_k, \sum_{k=0}^{i} \Delta s_k) \end{aligned} \tag{4.10}$$

The free path equation $s = F_S^{-1}(\xi)$ can be recursively solved until we reach the equality:

$$-\ln(1-\xi) = \sum_{k=0}^{i-1} \alpha_k \cdot \Delta s_k + \alpha_i \cdot \left(s - \sum_{k=0}^{i-1} \Delta s_k\right)$$

Once the free path is sampled, we compare it to the distance to the nearest surface (Figure 4.2). If it does not reach the surface, the sampled vertex is in a medium. Otherwise, the sampled vertex is on the nearest surface and the path probability is multiplied by the probability $\mathbb{P}(S>s_0)=\int_{s_0}^{\infty} p(s)ds$, with $s_0$ the distance to the nearest surface.

### 4.2.3 Light scattering in the atmosphere

Radiation attenuation in the line of sight is described by two mechanisms. (1) Absorption of (1-$\omega$) times its incident energy (*i.e.*, increases of the medium internal energy), with $\omega=\alpha_s/\alpha_e$ the single scattering albedo (*cf.* Annex A.1). (2) Redirection of $\omega$ times the incident energy to another line of sight, which is described by the scattering phase function $P(r, \Omega' \to \Omega)$. Usually, absorption is not explicitly modelled as it does not contribute directly to observations.

The general expression of the probability density function of scattering is formulated by:

$$p(\Omega|\Omega') = \frac{P(r, \Omega' \to \Omega)}{\int_{4\pi} P(r, \Omega' \to \Omega) d\Omega} = \frac{P(r, \Omega' \to \Omega)}{4\pi} \tag{4.11}$$

$p(\Omega|\Omega')$ is not proportional to $P(r, \Omega' \to \Omega)$ if the scatterers are not macroscopically isotropic and mirror-symmetric, as if the scattering coefficient $\alpha_s(r, \Omega')$ depends on the incident direction (Mishchenko et al., 2006). More generally, $p(\Omega|\Omega')$ should be formulated by:

$$p(\Omega|\Omega') = \frac{\alpha_s(r,\Omega') \cdot P(r,\Omega' \to \Omega)}{\int_{4\pi} \alpha_s(r,\Omega') \cdot P(r,\Omega' \to \Omega) d\Omega}$$

Two scattering phase functions are implemented in DART-Lux:

- **Rayleigh scattering phase function.** It considers the impact of the molecule anisotropy.

$$P(r,\Omega' \to \Omega) = \frac{3}{2} \cdot \frac{1-\delta}{2+\delta} \cdot \left(\frac{1+\delta}{1-\delta} + \cos^2\gamma\right) \tag{4.12}$$

with scattering phase angle $\gamma$ ($\cos\gamma = \Omega' \cdot \Omega$) and depolarization factor $\delta$.

- **Double Henyey-Greenstein scattering phase function.** It often represents the scattering of particles (*e.g.*, aerosols) with strong forward ($\mathrm{g}_1 > 0$) and smaller backward ($\mathrm{g}_2 < 0$) peaks, using the asymmetry factor g and a constant $a$ that describes the degree of forward scattering.

$$P(r,\Omega' \to \Omega) = \frac{a \cdot (1-\mathrm{g}_1{}^2)}{(1+\mathrm{g}_1{}^2 - 2\mathrm{g}_1 \cdot \cos\gamma)^{1.5}} + \frac{(1-a) \cdot (1-\mathrm{g}_2{}^2)}{(1+\mathrm{g}_2{}^2 - 2\mathrm{g}_2 \cdot \cos\gamma)^{1.5}} \tag{4.13}$$

### 4.2.4 Measurement evaluation

Starting from the sensor, a complete path is created by repeatedly sampling a vertex and free path. In detail, a vertex $r_0$ on the lens and an emitted virtual ray direction $\Omega_0$ are first sampled using sensor characteristics. Then, a vertex $r_k$ is generated by sampling a stochastic exit direction $\Omega_{k\text{-}1}$ at the vertex $r_{k\text{-}1}$. This sampling depends only on the local incident direction $r_{k\text{-}2} \to r_{k\text{-}1}$. The free path is always sampled after each bounce. Finally, the last vertex $r_n$ on the light source is generated by uniformly sampling the solid angle subtended by the light source at the previous vertex $r_{n\text{-}1}$. Here the free path is not sampled; instead, we force the radiation to connect the light source to increase the efficiency. We have:

$$\overleftarrow{p}(r_0) = p(r_0)$$

and $\overleftarrow{p}(r_1) = p(r_1|r_0) = \begin{cases} p(\Omega_0) \cdot \frac{\mathcal{T}(r_0 \leftrightarrow r_1) \cdot \cos\theta_o^{r_1}}{\|r_0 - r_1\|^2}, & \forall\, r_1 \in A \\ p(\Omega_0) \cdot \frac{\alpha_e(r_0 \to r_1) \cdot \mathcal{T}(r_0 \leftrightarrow r_1)}{\|r_0 - r_1\|^2}, & \forall\, r_1 \in V \end{cases}$

After the vertex $r_1$, the next vertex $r_k$ ($k>1$) usually depends on the direction decided by the previous two vertices except the last one $r_n$. Therefore:

$$\overleftarrow{p}(r_k) = p(r_k|r_{k-1}, r_{k-2}) = \begin{cases} p(\Omega_{k-1}|\Omega_{k-2}) \cdot \dfrac{\mathcal{T}(r_{k-1} \leftrightarrow r_k) \cdot \cos\theta_o^{r_k}}{\|r_{k-1} - r_k\|^2}, & \forall\, r_k \in A \\ p(\Omega_{k-1}|\Omega_{k-2}) \cdot \dfrac{\alpha_e(r_{k-1} \to r_k) \cdot \mathcal{T}(r_{k-1} \leftrightarrow r_k)}{\|r_{k-1} - r_k\|^2}, & \forall\, r_k \in V \end{cases}$$

$$\overleftarrow{p}(r_n) = p(r_n|r_{n-1}) = p(\Omega_{n-1}) \cdot \frac{\mathcal{T}(r_{n-1} \leftrightarrow r_n) \cdot \cos\theta_o^{r_n}}{\|r_{n-1} - r_n\|^2}$$

The resulting path probability density is:

$$p(\bar{r}_n) = \prod_{k=0}^{n} \overleftarrow{p}(r_k) \tag{4.14}$$

Considering the contribution function in Eq. (4.6), the estimate (Eq. (4.7)) can be rewritten as:

$$F_{\mathrm{IS}}^{(j)} = \sum_{n=1}^{\infty} \left[ \frac{\tilde{L}_e(r_n \to r_{n\text{-}1}) \cdot \tilde{G}(r_0 \leftrightarrow r_1) \cdot W_e^{(j)}(r_0 \to r_1)}{\overleftarrow{p}(r_0) \cdot \overleftarrow{p}(r_1)} \cdot \prod_{k=2}^{n} \frac{\tilde{f}_s(r_k \to r_{k\text{-}1} \to r_{k\text{-}2}) \cdot \tilde{G}(r_{k\text{-}1} \leftrightarrow r_k)}{\overleftarrow{p}(r_k)} \right] \tag{4.15}$$

Eq. (4.15) is analysed in 4.Appendix D for a specific environment that is a semi-infinite plane parallel atmosphere, illuminated by parallel sunlight and observed by a TOA orthographic camera. Results are consistent with the familiar SSA method (Spada et al., 2006).

## 4.3 Accuracy evaluation

For land surfaces, DART-Lux has already been shown to be consistent (relative difference < 1%) with classic DART-FT that agrees within 1% with Monte Carlo models of the RAMI experiment and has a reflectance accuracy ≈ 0.02 compared to measurements (Janoutová et al., 2019; Widlowski et al., 2007). This section presents the evaluation of DART-Lux accuracy of atmospheric radiative transfer modelling using the atmosphere model MODTRAN (Berk et al., 2005, 1987) as a reference. For both models, we consider a USSTD76 atmosphere (Anderson et al., 1986), without aerosols, a nadir sun illumination, a TOA sensor with a viewing zenith angle $\theta_v$ from nadir to 60°, and a flat Lambertian ground with albedo equal to 0.5 for all 2721 spectral bands from 0.32 to 2.5 $\mu$m (10 cm$^{-1}$ interval). DART-Lux and MODTRAN agree very well (Figure 4.3), using the average absolute relative difference as the measure of difference:

$$\varepsilon = \frac{1}{N} \sum_{\lambda=1}^{N} \left| \frac{\rho_{\mathrm{DART-Lux}}(\lambda) - \rho_{\mathrm{MODTRAN}}(\lambda)}{\rho_{\mathrm{MODTRAN}}(\lambda)} \right|$$

We have: $\varepsilon = 0.38\%$ for $\theta_v = 0°$, $\varepsilon = 0.40\%$ for $\theta_v = 30°$ and $\varepsilon = 0.91\%$ for $\theta_v = 60°$. For nadir or near nadir viewing angle (*i.e.*, $\theta_v \leq 30°$), the small differences between DART-Lux and MODTRAN are mainly due to the modelling of multiple scattering. Indeed, DART-Lux samples random scattering directions in the $4\pi$ space whereas MODTRAN couples the DISORT model (Stamnes et al., 2000) that uses the *N*-streams approximation (note that with current version 5 of MODTRAN, the maximum number of streams is 32). As the viewing zenith increases, the difference slightly increases because of two factors: (1) Earth and atmosphere curvature. DART-Lux currently models parallel atmosphere layers without refraction at interfaces while MODTRAN considers both the curvature of the Earth surface and atmosphere refraction. (2) Radiation transmission. DART-Lux uses the monochromatic assumption to compute the atmosphere absorption transmittance (i.e., absorption is spectrally constant in each spectral band of the atmosphere spectral database), whereas MODTRAN considers that absorption is spectrally variable within bands. It causes slight difference for very oblique viewing directions for bands where absorption is spectrally very variable.

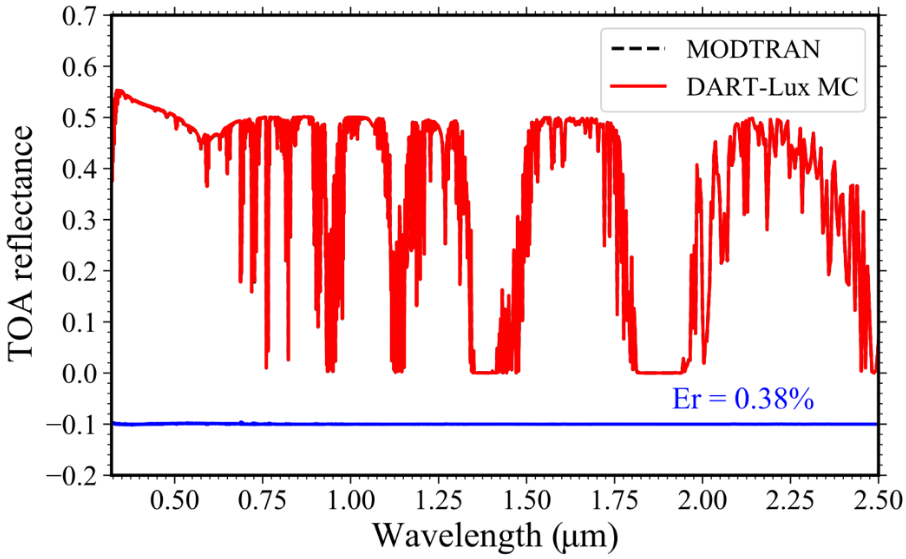

(a)

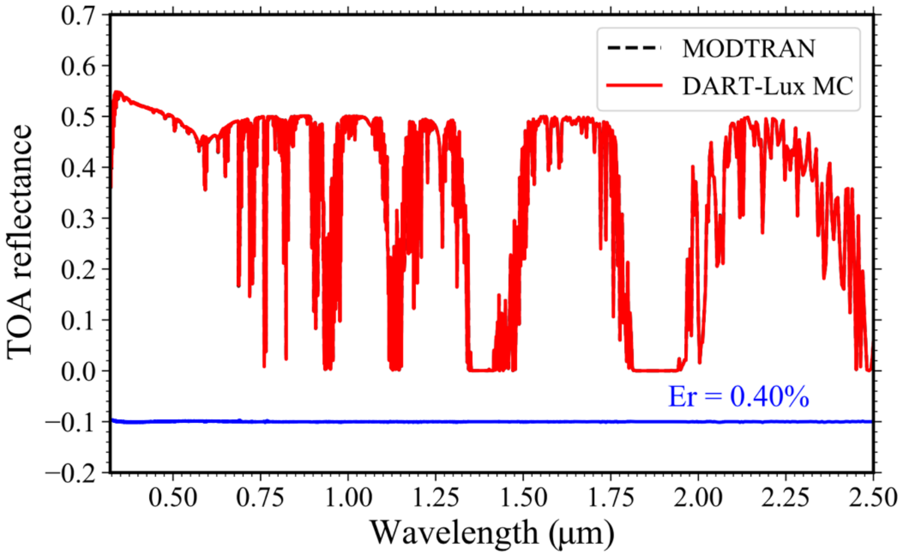

(b)

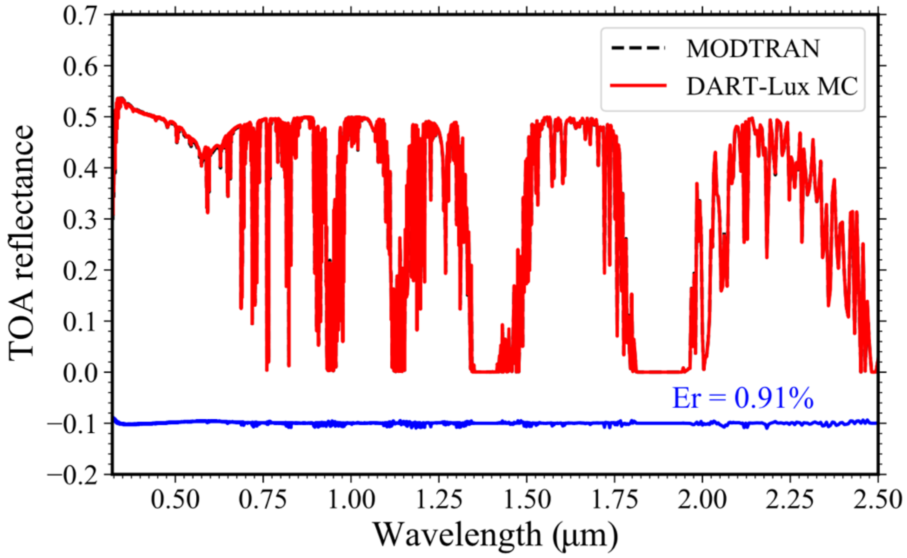

(c)

Figure 4.3. MODTRAN (black dashes) and DART-Lux (red line) TOA reflectance over [0.32 2.5 $\mu$m] with 10 cm$^{-1}$ spectral interval for viewing zenith at nadir (a), 30° (b) and 60 ° (c). Solar zenith $\theta_s$=0°. USSTD76 atmosphere. DART-Lux - MODTRAN residual is plotted (blue line) with indication of the average absolute relative difference.

## 4.4 Modelling and studying the adjacency effect

The adjacency effect is defined as the atmospheric scattering of the reflected radiation from the surrounding pixels into the line of sight of the pixel of interest. It is one of the most challenging sources of inaccuracy in the interpretation of remote sensing images since the advent of high-resolution Earth observation satellite (Borel and Gerstl, 1992; Bulgarelli and Zibordi, 2018; Feng and Hu, 2017; Pearce, 1977; Sterckx et al., 2015; Tanré et al., 1979). It depends on the atmospheric condition (Reinersman and Carder, 1995), the heterogeneity and the anisotropic scattering of the land surface (Bulgarelli and Zibordi, 2018), the light source and the sensor configuration (Vermote et al., 1997), the spectral region (Dave, 1980), *etc*. According to (Bulgarelli and Zibordi, 2018; Sterckx et al., 2015; Tanre et al., 1981; Tanré et al., 1979), it can account for more than 30% of the observed TOA signals. Ground reflectance can be greatly overestimated if we neglect the adjacency effect. Below, we quantify the influence of 3D structure, sensor altitude, and atmosphere absorption attenuation on the adjacency effect using DART-Lux based virtual experiment for the visible and near infrared bands of Sentinel-2A.

### 4.4.1 Design of experiment

The target is a city of 2 km radius surrounded by a forest of dimension 10 km × 10 km (Figure 4.4),which is itself surrounded by flat Lambertian background as shown in Figure 4.1. The city consists of 55828 regularly aligned houses and streets between houses. The house model is created by the DART object module. The optical properties of the roof, the wall and the street are from the DART database. The forest consists of 1553504 quasi-randomly distributed Tilia cordata trees at five growing stages with a homogeneous understory. The geometry and optical properties of the trees as well as the optical properties of the understory are from the RAMI experiment (https://rami-benchmark.jrc.ec.europa.eu/_www/index.php). The albedo of the background (Table 4.1) is equal to that of the forest. It was computed using DART simulations of a 3 km × 3 km forest subzone of the considered scene (Figure 4.4). The atmosphere model is USSTD76 with both gases and aerosols. Its mean single scattering albedo ($\omega$=$\tau_s/\tau_e$, with $\tau_s$ and $\tau_e$ the atmosphere scattering and total optical depths, respectively) is computed in Table 4.1. The solar zenith and azimuth angles are $\theta_s$=30° and $\varphi_s$=225°, respectively. The focus of the sensor is at 80 km altitude and is centred at the midpoint of the target (nadir observation). In this experiment, we consider four spectral bands of Sentinel-2A: blue (B: $\lambda = 0.4924\ \mu$m, $\Delta\lambda = 0.066\ \mu$m), green (G: $\lambda = 0.5598\ \mu$m, $\Delta\lambda = 0.036\ \mu$m), red (R: $\lambda = 0.6646\ \mu$m, $\Delta\lambda = 0.031\ \mu$m) and near infrared (NIR: $\lambda = 0.8328\ \mu$m, $\Delta\lambda = 0.106\ \mu$m).

The adjacency effect is the difference of two simulations, one with the defined neighbourhood and another one without it (set as black ground). Here, we quantify it by:

- The horizontal profile of the *adjacency radiance* $L_{\mathrm{adj}}(r)$ (the additional radiance due to the adjacency effect) as a function of distance $r$ from the centre to the target boundary. $L_{\mathrm{adj}}(r)$ is the average for all pixels in the ring $[r, r+\Delta r]$ (Figure 4.4).
- The *adjacency perturbation* $\zeta_{\mathrm{adj}} = \bar{L}_{\mathrm{adj}}/\bar{L}_{\mathrm{tot}}$. It is defined as the ratio of the average adjacency radiance $\bar{L}_{\mathrm{adj}}$ and the average total radiance of the target $\bar{L}_{\mathrm{tot}}$.

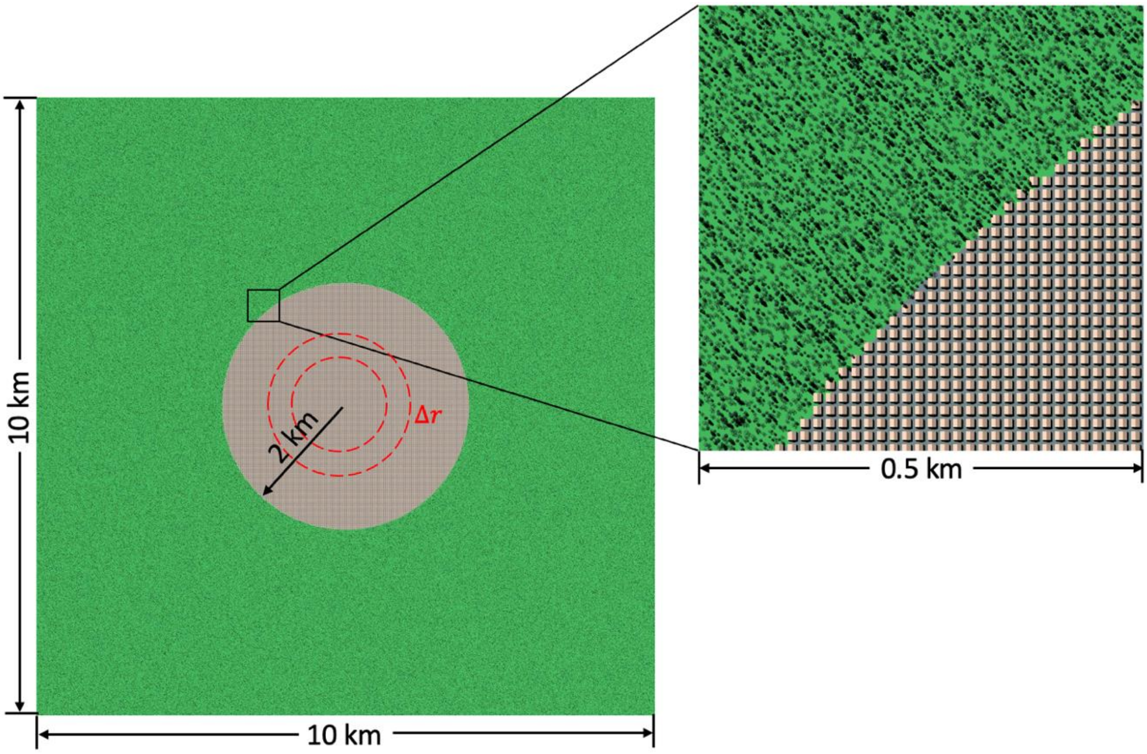

Figure 4.4. Mock-up for studying the adjacency effect. The target scene is a circular city (2 km radius; 55828 houses with gable roof and ≈ 15 m average building distance) surrounded by a square 10 × 10 km forest (1553504 quasi-randomly distributed Tilia cordata trees at five growing stages, derived from the RAMI experiment: https://rami-benchmark.jrc.ec.europa.eu/_www/index.php; the average tree distance is ≈5 m). The evaluation of the average radiance at distance $r$+$\Delta r/2$ from the target centre is computed by averaging all the pixels within the red dashed ring from $r$ to $r$+$\Delta r$.

In order to configure a simulation with no impact of the 3D structure of the forest and the city, we simulated the nadir reflectance of the target and the albedo of the surrounding forest. These optical properties (Table 4.1) are chosen because the direct radiation from the target and the diffuse radiation from the surrounding forest are the quantities that contribute most to the observation of the target. We calculated them by simulating a subzone (*i.e.*, city or forest) of the target scene under BOA direct and diffuse illuminations that were precomputed by DART-FT (i.e., discrete ordinates radiative transfer mode) using 1000 discrete directions in the $4\pi$ space and the previously mentioned solar direction and atmosphere model. All simulations were run with 100 scattering orders to mimic the results of infinite scattering orders since the contribution after 100 scattering order is negligible compared to the total signal.

Table 4.1. Average single scattering albedo of the USSTD76 atmosphere, target (city) nadir reflectance and albedo of the neighbourhood (forest), for four Sentinel-2A bands.

| Band | Wavelength ($\mu$m) | Scattering albedo | Target reflectance | Neighbour albedo |
|---|---|---|---|---|
| B | 0.4924 | 0.9437 | 0.064 | 0.033 |
| G | 0.5598 | 0.8716 | 0.073 | 0.067 |
| R | 0.6646 | 0.8881 | 0.096 | 0.032 |
| NIR | 0.8328 | 0.8090 | 0.101 | 0.419 |

### 4.4.2 Impact of the 3D structure of land surfaces

The impact of the 3D structure is evaluated by comparing the results simulated with the exact 3D surrounding forest (Figure 4.5.b) and those simulated with the 1D neighbourhood (Figure 4.5.a). The flat Lambertian neighbourhood in Figure 4.5.a is configured with the neighbour albedo in Table 4.1. Figure 4.6 shows that the adjacency radiance $L_{\mathrm{adj}}(r)$ increases from the target centre to the border. This trend is similar for both 1D and 3D cases, as the influence of the neighbouring surface decreases with the distance that is independent of the land structure. Table 4.2 summarizes the average adjacency radiance $\bar{L}_{\mathrm{adj}}$ of the target and the adjacency perturbation $\zeta_{\mathrm{adj}}$ for the four Sentinel-2A bands. Due to the impact of the 3D structure, $\zeta_{\mathrm{adj}}$ can differ by up to 0.5% in absolute and by up to 9.2% in relative (green band). The difference between 1D and 3D is mostly due to the adjacent anisotropic scattering linked to the 3D structure. For example, there is a strong backward reflectance of the canopy due to the hot spot effect and there is a decrease of forward reflectance due to shadows.

Besides, it can be noticed that both $\overline{L}_{\mathrm{adj}}$ and $\zeta_{\mathrm{adj}}$ increase with the scattering albedo of the neighbouring surface and the atmosphere. For example, $\zeta_{\mathrm{adj}}$ at near infrared band is ≈ 7 times larger than that at red band because the neighbour albedo at near infrared band is ≈ 13 times larger; $\zeta_{\mathrm{adj}}$ at blue band is ≈ 1.5 times larger than that at red band although they have similar neighbour albedo, because the atmospheric scattering albedo at blue band is larger.

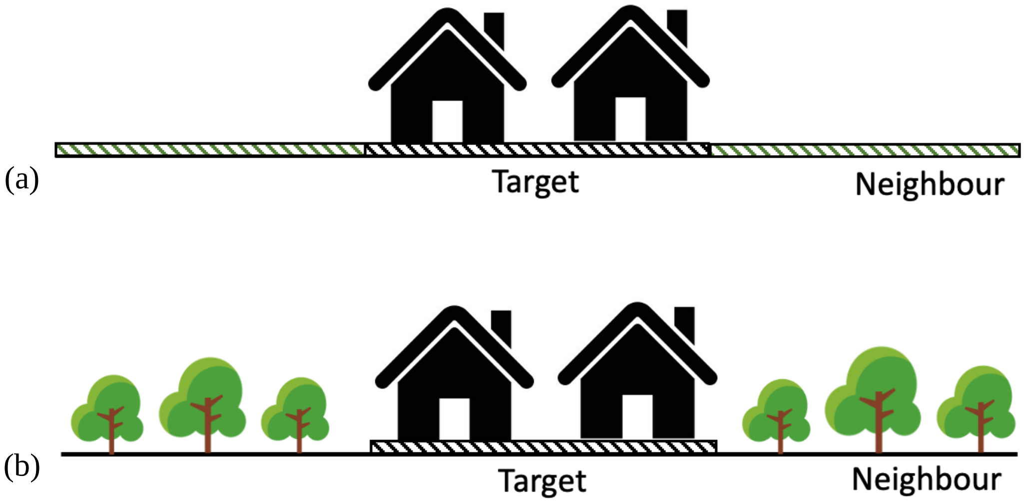

Figure 4.5. The 1D (a) and 3D (b) cases. They have a same target, but the neighbourhood is a Lambertian ground for the 1D case (a) and a realistic forest for the 3D case (b).

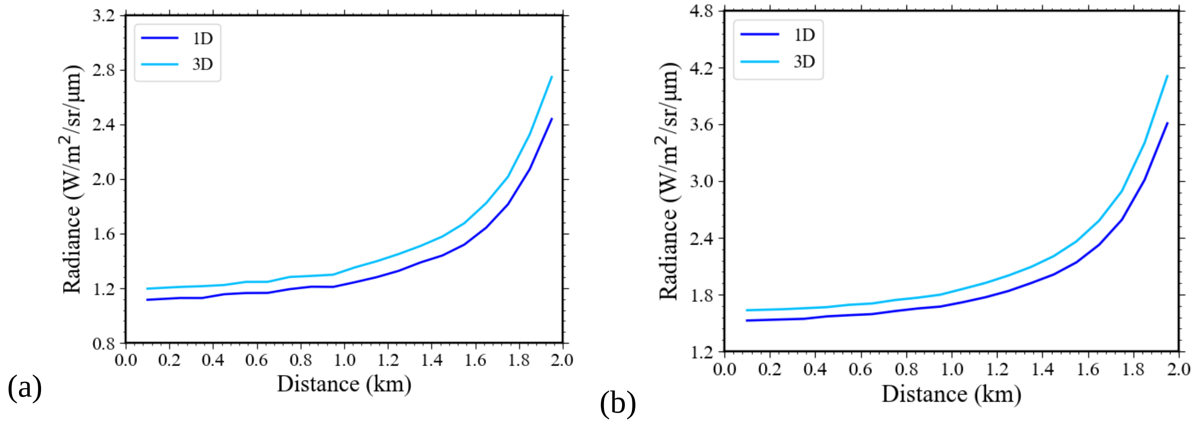

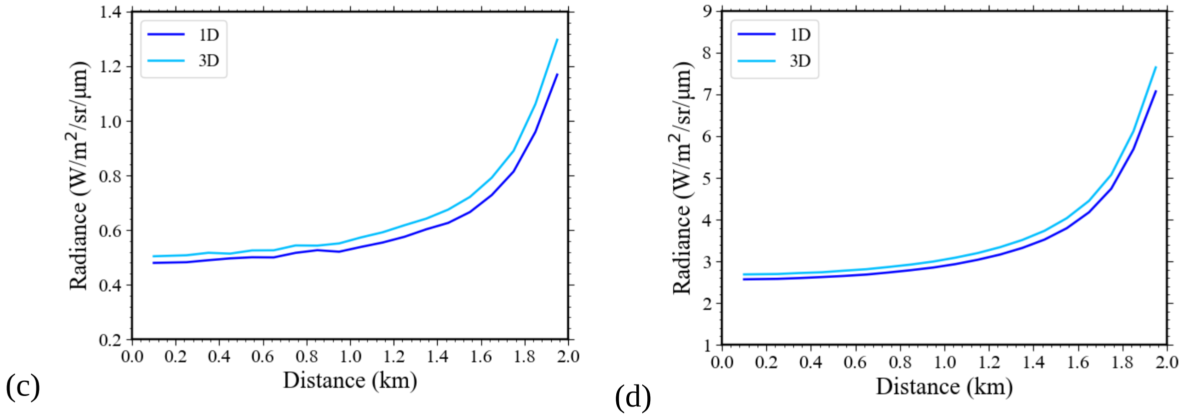

Figure 4.6. The adjacency radiance $L_{\mathrm{adj}}(r)$ as a function of distance $r$ away from the target centre for 1D (Figure 4.5.a) and 3D (Figure 4.5.b) cases, for the blue (a), green (b), red (c) and near infrared (d) bands of Sentinel-2A satellite.

Table 4.2. The average adjacency radiance $\bar{L}_{\mathrm{adj}}$ (W/m$^2$/sr/$\mu$m) of the target city and the adjacency perturbation $\zeta_{\mathrm{adj}}(\%) = \bar{L}_{\mathrm{adj}}/\bar{L}_{\mathrm{tot}}$ for 1D and 3D cases.

| Band | 1D | | 3D | |
|---|---|---|---|---|
| | $\bar{L}_{\mathrm{adj}}$ | $\zeta_{\mathrm{adj}}$ | $\bar{L}_{\mathrm{adj}}$ | $\zeta_{\mathrm{adj}}$ |
| B | 1.6 | 2.8% | 1.8 | 3.0% |
| G | 2.3 | 4.9% | 2.6 | 5.4% |
| R | 0.7 | 1.8% | 0.8 | 1.9% |
| NIR | 4.4 | 13.7% | 4.7 | 14.6% |

### 4.4.3 Impact of the sensor altitude

To study the impact of the sensor altitude on the adjacency effect, we eliminate the anisotropic scattering due to the 3D structure and to keep the same viewing direction for every pixel. For that, the 3D mock-up in Figure 4.4 is simplified as a flat disk target surrounded by the flat neighbour. The target has the nadir reflectance of the city, and the environment has the albedo of the forest (Table 4.1). The focus of FOV is fixed at altitude 80 km while the sensor altitude (*i.e.*, image plane) varies from 0.5 km, 1 km, 5 km, 10 km to 50 km (Figure 4.7).

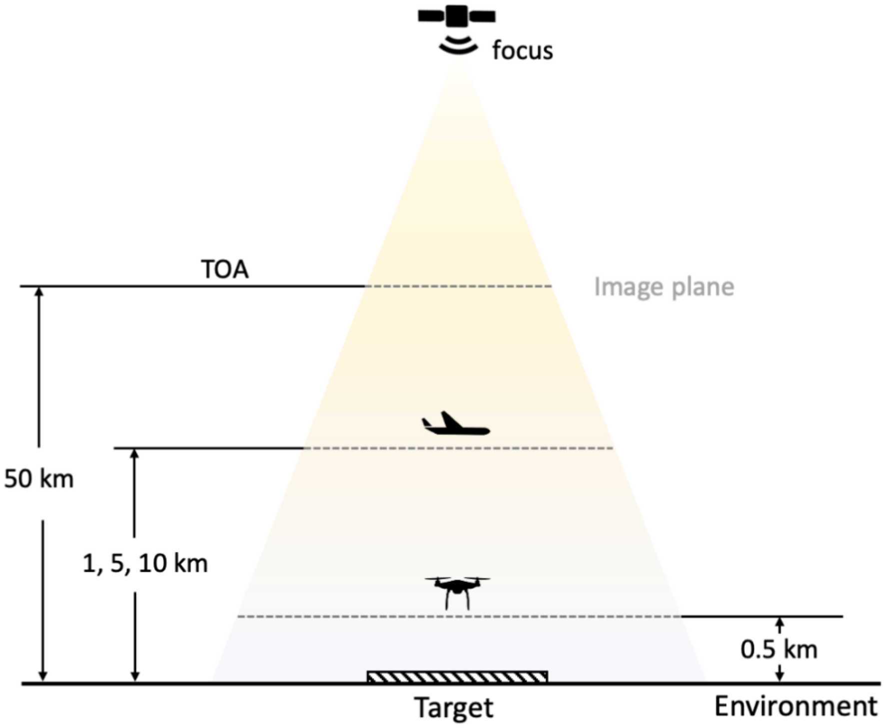

Figure 4.7. Sensors at five altitudes (0.5 km, 1 km, 5 km, 10 km, 50 km). The focus of the sensor is set at altitude 80 km to eliminate differences due to the change of sensor FOV.

Figure 4.8 shows that the adjacency radiance increases with the sensor altitude, which is consistent with the increase of atmosphere amount in the sensor FOV. Table 4.3 shows the average adjacency radiance $\bar{L}_{\mathrm{adj}}$ of the target and the adjacency perturbation $\zeta_{\mathrm{adj}}$ for each altitude. At near infrared band, $\zeta_{\mathrm{adj}}$ is 4.5% for the sensor at 0.5 km while it increases more than two times to 14.7% for the sensor at 50 km. The average $\zeta_{\mathrm{adj}}$ of the four Sentinel-2A bands for the sensor at 50 km is around 3 times larger than that of the sensor at 0.5 km. It is interesting to note that the difference of the adjacency effect between 1 km and 5 km (1.1% at blue band) is larger than that from 5 km to 50 km (0.4% at blue band) although the altitude difference of the latter is much larger. This is because the atmospheric scattering between 1 km and 5 km is stronger than that from 5 km to 50 km. This non-linear relationship also stresses that using the same parameters (*e.g.*, (Reinersman and Carder, 1995) suggest the PSF generated for a sensor at 20 km is applicable to the analysis of images acquired by satellite) to correct the adjacency effect presenting in different remote sensing platforms can introduce errors. This error increases with the scattering albedo of the neighbouring surface and the atmosphere.

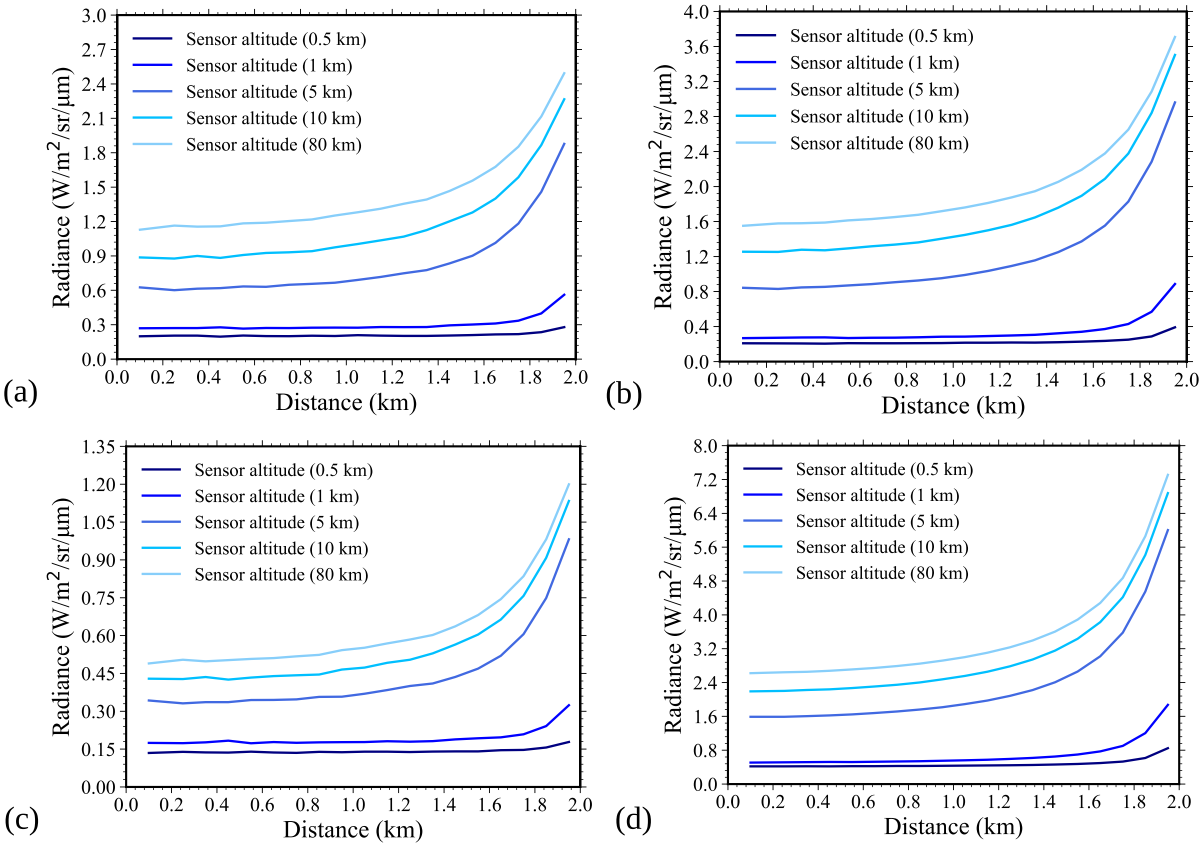

Figure 4.8. The adjacency radiance at five sensor altitudes (0.5 km, 1 km, 5 km, 10 km, 50 km) for four bands (blue: a), green: b), red: c), near infrared: d) of Sentinel-2A satellite.

Table 4.3. The average adjacency radiance $\bar{L}_{\mathrm{adj}}$ (W/m$^2$/sr/$\mu$m) and the adjacency perturbation $\zeta_{\mathrm{adj}}$ (%) for the sensor at altitude 0.5 km, 1 km, 5 km, 10 km, and 50 km.

| Band | 0.5 km | | 1 km | | 5 km | | 10 km | | 50 km | |
|---|---|---|---|---|---|---|---|---|---|---|
| | $\bar{L}_{\mathrm{adj}}$ | $\zeta_{\mathrm{adj}}$ | $\bar{L}_{\mathrm{adj}}$ | $\zeta_{\mathrm{adj}}$ | $\bar{L}_{\mathrm{adj}}$ | $\zeta_{\mathrm{adj}}$ | $\bar{L}_{\mathrm{adj}}$ | $\zeta_{\mathrm{adj}}$ | $\bar{L}_{\mathrm{adj}}$ | $\zeta_{\mathrm{adj}}$ |
| B | 0.35 | 1.1% | 0.47 | 1.4% | 1.07 | 2.5% | 1.41 | 2.7% | 1.67 | 2.9% |
| G | 0.46 | 1.4% | 0.61 | 1.8% | 1.65 | 4.1% | 2.13 | 4.8% | 2.41 | 5.1% |
| R | 0.26 | 0.7% | 0.32 | 0.8% | 0.60 | 1.5% | 0.71 | 1.8% | 0.78 | 1.9% |
| NIR | 1.28 | 4.5% | 1.58 | 5.5% | 3.58 | 11.7% | 4.31 | 13.7% | 4.75 | 14.7% |

### 4.4.4 Impact of the absorption attenuation

The adjacency effect in satellite images is often corrected by a convolution with the PSF $PSF(\mathrm{P}_0, \mathrm{P})$, that is, the probability that a photon reflected by a point P is scattered into the instantaneous FOV of a point $\mathrm{P}_0$. However, some approaches (Mekler and Kaufman, 1980) and

(Reinersman and Carder, 1995) neglect the atmosphere absorption attenuation when deriving $PSF(\mathrm{P_0}, \mathrm{P})$. Here, we study the impact of absorption attenuation using the case of the sensor at 50 km in section 0. To simulate the result without absorption attenuation, we set the single scattering albedo of both aerosols and molecules as 1. Figure 4.9 confirms that the neglect of the absorption leads to overestimate the adjacency effect. Here, the overestimate of the adjacency perturbation is 0.1%, 0.6%, 0.2%, 2.0% in absolute and 3%, 12%, 11%, 14% in relative respectively for the blue, green, red and near infrared bands (Table 4.4).

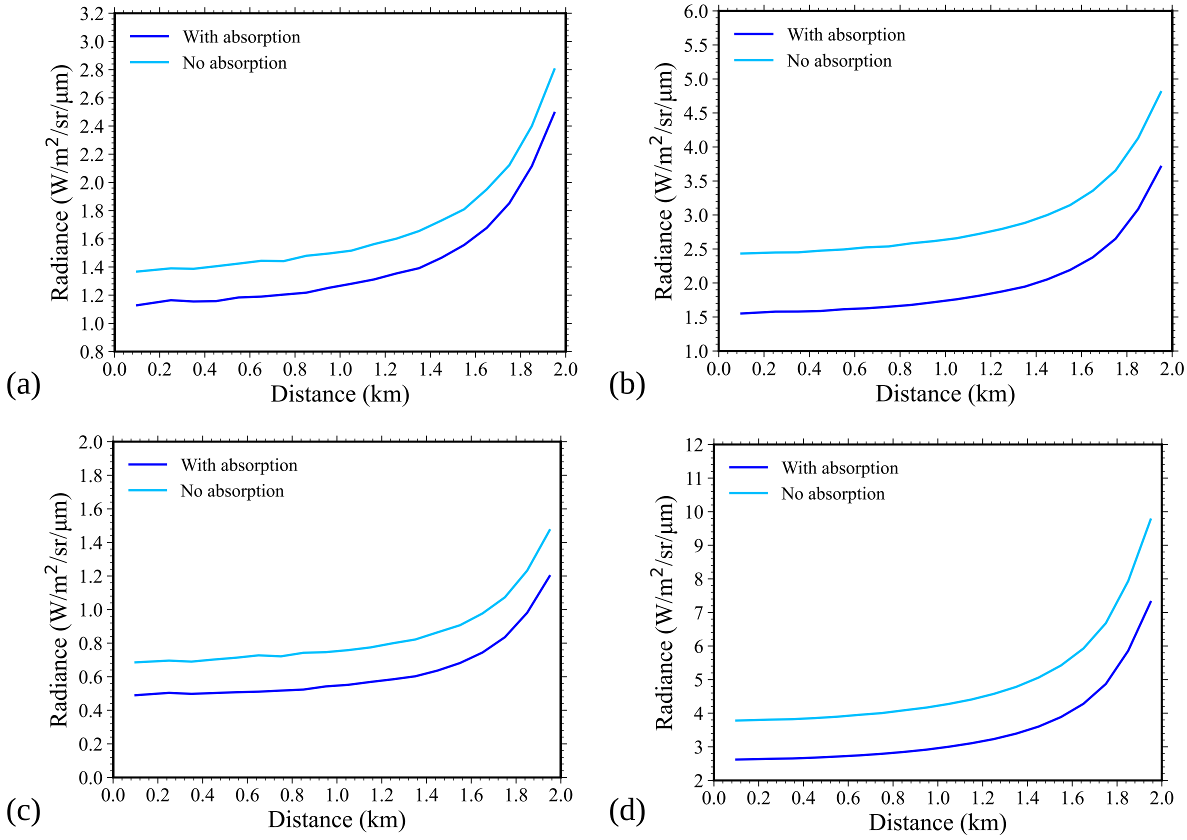

Figure 4.9. The adjacency radiance simulated with and without absorption attenuation for the blue (a), green (b), red (c), and near infrared (d) bands of Sentinel-2A satellite.

Table 4.4. Average adjacency radiance $\bar{L}_{\text{adj}}$ (W/m²/sr/$\mu$m) of the target city and adjacency perturbation $\zeta_{\text{adj}}(\%)=\bar{L}_{\text{adj}}/\bar{L}_{\text{tot}}$ for cases with and without absorption attenuation.

| Band | No absorption | | With absorption | |
|---|---|---|---|---|
| | $\bar{L}_{\text{adj}}$ | $\zeta_{\text{adj}}$ | $\bar{L}_{\text{adj}}$ | $\zeta_{\text{adj}}$ |
| B | 1.9 | 3.0% | 1.7 | 2.9% |
| G | 3.4 | 5.7% | 2.4 | 5.1% |

| | | | | |
|---|---|---|---|---|
| R | 1.0 | 2.1% | 0.8 | 1.9% |
| NIR | 6.4 | 16.7% | 4.7 | 14.7% |

## 4.5 Conclusions

This work generalizes the DART-Lux radiative transfer theory and implementation for both land surfaces and the atmosphere. We start from the formal solution of the radiative transfer equation in the medium and develop it to get the same path integral formulation as at surfaces. Then, we demonstrate the unified path integral over paths that consist of vertices at surfaces and in media. This integral is further solved in the frame of the bidirectional path tracing algorithm. To simulate the remote sensing observations with atmospheric and adjacency effects, we also propose an Earth-Atmosphere system in which the target scene is placed at the bottom centre and is surrounded by the atmosphere and a neighbouring land surface. The forward random walk is disactivated for this new system because it risks slowing down the computation and introducing bias.

Its atmospheric radiative transfer modelling is assessed by the widely used and validated model MODTRAN. In particular, the simulated TOA spectral reflectance spectra from 0.32 to 2.5 $\mu$m for a standard USSTD76 atmosphere is compared. The average relative difference between DART-Lux and MODTRAN is 0.38% for viewing zenith at nadir, 0.40% for viewing zenith at 30° and increases to 0.91% for viewing zenith at 60°. The slight difference is mainly due to the different methods in modelling the multiple scattering, transmission, atmospheric refraction, and Earth curvature.

Based on this new DART-Lux modelling, we studied the impact of the 3D structure, sensor altitude, and atmosphere absorption attenuation on the adjacency effect. The experiment field is represented by a target city and a surrounding forest. Results show that the adjacency effect increases with the increase of (1) the neighbour albedo, (2) the atmosphere scattering and (3) the sensor altitude. For example, the adjacency perturbation at near infrared band is 7 times of that at red band, because the neighbour albedo at near infrared band is 13 times larger. The adjacency perturbation at blue band is 1.5 times larger than that at red band although they have similar neighbour albedo, because the atmosphere scattering (single scattering albedo) at blue band is 1.1 times stronger. In addition, the average adjacency effect of the four Sentinel-2A bands for the sensor at 50 km is around 3 times larger than that of the sensor at 0.5 km. The impact of the 3D structure and the absorption attenuation is less important compared to the above-mentioned three factors. However, they are not negligible for high accuracy atmospheric correction algorithms. They would be much larger in presence of topography. In our study, with a flat surface, the neglect of the 3D structure can lead to an error of the adjacency perturbation $\zeta_{\mathrm{adj}}$ up to 0.8% in absolute and the neglect of the absorption attenuation can overestimate the adjacency perturbation up to 2.0% in absolute.

The new DART-Lux modelling greatly enhances the usefulness of DART for calibration and validation activities related to Earth observation satellite missions, especially the correction of the adjacency effect due to the atmosphere scattering and land surface heterogeneity. For very homogeneous land surfaces (*e.g.*, dense forest, crop field), a hybrid method is also designed as an alternative fast option (*cf.* Annex B). Its central idea is to couple the discrete ordinates radiative transfer in the atmosphere and the Monte Carlo radiative transfer at land surface to simulate TOA and sensor images.

## 4.Appendix A The default atmosphere dimension

In the current implementation, the default TOA altitude is 50 km, and the default atmosphere horizontal dimension is 500 km × 500 km (*cf.* section 4.2.1). Is the default dimension (X × Y × Z) a good representation of a quasi-infinite atmosphere? To answer this question, we did two sensitivity studies to show the impact of the atmosphere dimension on the simulated radiance. The sensitivity study of TOA altitude is conducted with MODTRAN, a USSTD76 atmosphere with rural aerosols, 0.5 ground albedo for all bands from 0.32 to 2.5 $\mu$m, nadir solar and viewing directions, and sensors at 40 km, 45 km, 50 km, 55 km, 60 km, and 70 km. Figure 4.A.1 shows the closeness of the radiance spectra simulated at all sensor altitudes. Table 4.A.1 shows the average relative errors compared to observation at 100 km. As expected, the error decreases with the increase of sensor altitude, with very accurate results at 50 km altitude, *i.e.*, $\varepsilon = 0.07\%$.

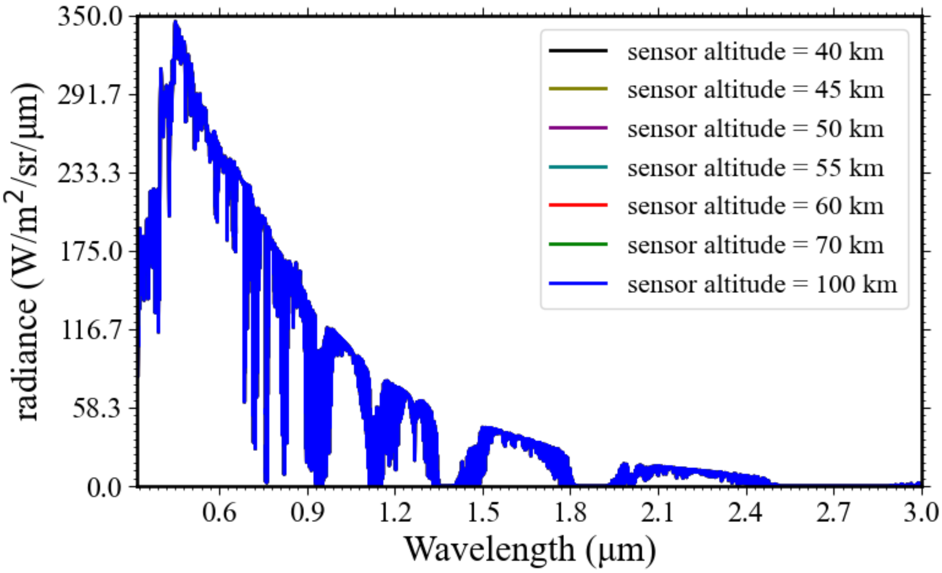

Figure 4.A.1. TOA radiance spectra for the sensor altitude at 40 km, 45 km, 50 km, 55 km, 60 km, 70 km, and 100 km, simulated by MODTRAN. The ground albedo is 0.5. The atmosphere model is USSTD76, with rural aerosols.

Table 4.A.1. The mean relative error $\varepsilon$ of radiance spectra in Figure 4.A.1 compared to the reference spectrum observed at 100 km.

| Sensor altitude | 40 km | 45 km | 50 km | 55 km | 60 km | 70 km |
|---|---|---|---|---|---|---|
| $\varepsilon$ | 0.17% | 0.07% | 0.07% | 0.06% | 0.03% | 0.01% |

The sensitivity study of the impact of the horizontal dimension $\mathrm{D}_{XY}$ of the atmosphere is done with DART-Lux for a 0.5 ground albedo, USSTD76 atmosphere, rural aerosols, and nadir solar and viewing direction. The horizontal dimension is set at 20 km, 50 km, 100 km, 200 km, and 500 km. Figure 4.A.2 indicates that a small value of the horizontal dimension such as 20 km leads to lower TOA reflectance in visible domain. The average relative errors compared to the reference result simulated with $\mathrm{D}_{XY} = 10000$ km are computed in Table 4.A.2. It shows that $\mathrm{D}_{XY} = 500$ km is a good approximation of infinite parallel atmosphere.

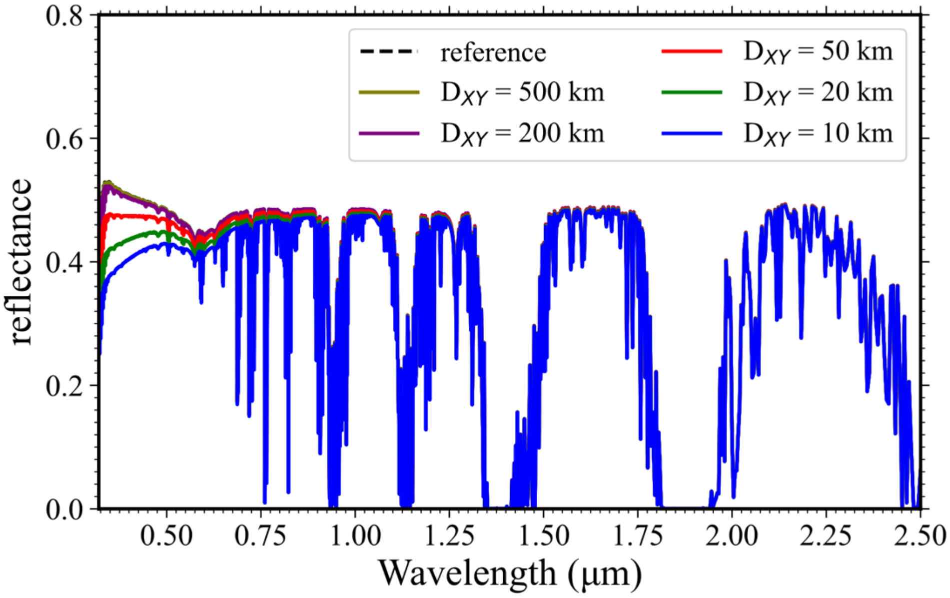

Figure 4.A.2. DART-Lux simulated TOA reflectance with the atmosphere horizontal dimension $\mathrm{D}_{XY}$ setting as 20 km, 50 km, 100 km, 200 km, and 500 km. The ground albedo is 0.5. The atmosphere model is USSTD76, with rural aerosols.

Table 4.A.2. The mean relative error $\varepsilon$ of all reflectance spectrums in Figure A.2 compared to the reference spectrum simulated with $\mathrm{D}_{XY} = 10000$ km.

| $\mathrm{D}_{XY}$ | 20 km | 50 km | 100 km | 200 km | 500 km |
|---|---|---|---|---|---|
| $\varepsilon$ | 7.74% | 3.59% | 0.55% | 0.45% | 0.08% |

# 4.Appendix B Computation of atmospheric properties (Part I)

The DART atmosphere SQL database stores vertical profiles of the atmospheric constituents: temperature $T_{DB}(z)$, pressure $P_{DB}(z)$, number density $N_{m_i,DB}(z)$ per gas $m_i$, relative density $\rho^s_{m,DB}(z)$ of scattering gases to air at standard temperature and pressure, and aerosol extinction coefficient profile $\alpha^e_{p,DB}(z)$ at 550 nm. They are given at 36 altitude levels (0 to 25 km with 1 km interval, 30 to 60 km with 5 km interval and 3 levels at 70 km, 80 km and 100 km) for:

- six standard atmospheres (Anderson et al., 1986): (1) TROPICAL: Tropical (15°N annual average), (2) MIDLATSUM: Mid-Latitude Summer (45°N July), (3) MIDLATWIN: Mid-Latitude Winter (45°N January), (4) SUBARCSUM: Sub-Arctic Summer (60°N July), (5) SUBARCWIN: Sub-Arctic Winter (60°N January), and (6) USSTD76: US Standard 1976.
- five aerosol models (Shettle and Fenn, 1979): (1) Rural, (2) Urban, (3) Maritime, (4) Tropospheric and (5) Fog.

The DART atmosphere SQL database also stores the spectral optical properties of the atmospheric constituents (*i.e.*, gas: vertical absorption transmittance $\mathcal{T}^a_{m_i,DB}(\lambda)$ per gas $m_i$, vertical scattering transmittance $\mathcal{T}^s_{m,DB}(\lambda)$; aerosol: vertical optical depth $\tau_{p,DB}(\lambda)$, single scattering albedo $\omega_{p,DB}(\lambda)$, asymmetry factors of double Henyey-Greenstein phase function) from 10 to 40000 cm$^{-1}$ with a spectral resolution of 1 cm$^{-1}$. They were derived from MODTRAN simulations and LOWTRAN source code for the six standard atmospheres and for the five aerosol models per standard atmosphere. The optical properties and vertical profiles of gases and aerosols derived from reanalysis datasets (*e.g.*, ECMWF reanalysis: https://www.ecmwf.int) and measurements (*e.g.*, Aeronet: https://aeronet.gsfc.nasa.gov) can also be imported into the DART atmosphere database.

The atmospheric properties at any altitude *z* are interpolated by the multi-quadric *radial basis function* (Press et al., 2007) using the vertical profiles and the optical properties in the SQL database. The band (central wavelength $\lambda$, bandwidth $\Delta\lambda$) mean optical properties (*i.e.*, vertical absorption transmittance $\mathcal{T}^a_{m_i}(\lambda)$ of each gas $m_i$, gas vertical scattering transmittance $\mathcal{T}^s_m(\lambda)$, aerosol vertical optical depth $\tau_p(\lambda)$) are computed (trapezoidal integration) using the database spectral vertical transmittance $\mathcal{T}^a_{m_i,DB}(\lambda')$, $\mathcal{T}^s_{m,DB}(\lambda')$ and optical depth $\tau_{p,DB}(\lambda')$ at 1 cm$^{-1}$ spectral resolution in the spectral bin $\Delta\lambda$:

$$\mathcal{T}^a_{m_i}(\lambda) = \frac{\int_{\lambda-\Delta\lambda/2}^{\lambda+\Delta\lambda/2} \mathcal{T}^a_{m_i,DB}(\lambda')\, d\lambda'}{\Delta\lambda}, \quad \mathcal{T}^s_m(\lambda) = \frac{\int_{\lambda-\Delta\lambda/2}^{\lambda+\Delta\lambda/2} \mathcal{T}^s_{m,DB}(\lambda')\, d\lambda'}{\Delta\lambda}$$
$$\tau_p(\lambda) = \frac{\int_{\lambda-\Delta\lambda/2}^{\lambda+\Delta\lambda/2} \tau_{p,DB}(\lambda')\, d\lambda'}{\Delta\lambda} \tag{4.B.1}$$

The extinction coefficient $\alpha$ (*i.e.*, total $\alpha^e$, absorption $\alpha^a$ and scattering $\alpha^s$ extinction coefficient) per layer $j$ is computed such that their use with Beer's law gives the band vertical transmittance and optical depth computed in Eq. (4.B.1).

$$\alpha^a_{j,m_i}(\lambda) = \frac{-\ln\left(\mathcal{T}^a_{m_i}(\lambda)\right)}{z_j - z_{j-1}} \cdot \frac{\int_{z_{j-1}}^{z_j} \sigma^a_{m_i}(\lambda) \cdot N_{m_i,DB}(z)dz}{\int_0^\infty \sigma^a_{m_i}(\lambda) \cdot N_{m_i,DB}(z)dz}$$
$$\alpha^s_{j,m}(\lambda) = \frac{-\ln(\mathcal{T}^s_m(\lambda))}{z_j - z_{j-1}} \cdot \frac{\int_{z_{j-1}}^{z_j} \sigma^s_m(\lambda) \cdot N^s_m(z)dz}{\int_0^\infty \sigma^s_m(\lambda) \cdot N^s_m(z)dz} = \frac{-\ln(\mathcal{T}^s_m(\lambda))}{z_j - z_{j-1}} \cdot \frac{\int_{z_{j-1}}^{z_j} \rho^s_{m,DB}(z)dz}{\int_0^\infty \rho^s_{m,DB}(z)dz} \tag{4.B.2}$$
$$\alpha^e_{j,p}(\lambda) = \frac{\tau_{p,DB}(\lambda)}{z_j - z_{j-1}} \cdot \frac{\int_{z_{j-1}}^{z_j} \alpha^e_{p,DB}(z)dz}{\int_0^\infty \alpha^e_{p,DB}(z)dz}$$

Newton-Cotes integration method (Abramowitz and Stegun, 1948) is used in Eq. (4.B.2) with 10 interpolated equal-distance values per layer assuming that the absorption cross-section $\sigma^a_{m_i}(\lambda)$ of gas $m_i$ only depends on wavelength. The gas scattering cross-section $\sigma^s_m(\lambda)$ only depends on wavelength and gas composition (Bodhaine et al., 1999). Therefore, $\sigma^s_m(\lambda) \cdot N^s_m(z)$, with $N^s_m(z)$ being the number density of scattering gases at altitude $z$, is proportional to the relative density of scattering gases $\rho^s_{m,DB}(z)$.

Then, the total gas extinction coefficient $\alpha^e_{j,m}(\lambda)$, aerosol absorption $\alpha^a_{j,p}(\lambda)$ and scattering $\alpha^s_{j,p}(\lambda)$ extinction coefficient and total extinction coefficient $\alpha^e_j(\lambda)$ are computed per layer:

$$\alpha^e_{j,m}(\lambda) = \alpha^a_{j,m}(\lambda) + \alpha^s_{j,m}(\lambda), \quad \alpha^a_{j,m}(\lambda) = \sum\nolimits_{m_i} \alpha^a_{j,m_i}(\lambda)$$
$$\alpha^a_{j,p}(\lambda) = \alpha^e_{j,p}(\lambda) \cdot \left(1 - \omega_{p,DB}(\lambda)\right), \quad \alpha^s_{j,p}(\lambda) = \alpha^e_{j,p}(\lambda) \cdot \omega_{p,DB}(\lambda)$$
$$\alpha^e_j(\lambda) = \alpha^e_{j,m}(\lambda) + \alpha^e_{j,p}(\lambda)$$

The layer mean temperature is the average of the layer upper boundary temperature $T_j^U$ and the lower boundary temperature $T_j^L$: $T_j = \frac{T_j^U + T_j^L}{2}$

## 4.Appendix C Computation of atmospheric properties (Part II)

The use of constant properties per layer is a good approximation commonly used in the radiative transfer calculations, although there is no discrete atmospheric vertical profiles in nature. Here we present the computation of continuous properties in each atmospheric layer. A polynomial is used because it is invertible (*e.g.*, to compute stochastic free path) and easy to derive.

The optical depth at relative altitude $h$ ($h = 0$ at the bottom of layer $j$ and $h = \Delta z_j$ at the top, Figure 4.C.1) can be described by a three-degree polynomial:

$$\tau_j(\lambda, h) = A_j(\lambda)\cdot h^3 + B_j(\lambda)\cdot h^2 + C_j(\lambda)\cdot h + D_j(\lambda)$$

The corresponding extinction coefficient can be derived through derivation:

$$\alpha_j^e(\lambda, h) = -\frac{d\tau_j(\lambda, h)}{dh} = -3A_j(\lambda)\cdot h^2 - 2B_j(\lambda)\cdot h - C_j(\lambda)$$

The four boundary conditions: $\tau(\lambda, 0) = \Delta\tau_j(\lambda)$, $\tau(\lambda, \Delta z_j) = 0$, $\alpha_j^e(\lambda, 0) = \alpha_{z_{j-1}}^e(\lambda)$, $\alpha_j^e(\lambda, \Delta z_j) = \alpha_{z_j}^e(\lambda)$ with $\Delta\tau_j(\lambda) = \alpha_{z_j}^e(\lambda)\cdot\Delta z_j$ and $\alpha_{z_{j-1}}^e(\lambda)$ and $\alpha_{z_j}^e(\lambda)$ are discrete quantities computed in 4.Appendix B leads to:

$$A_j(\lambda) = \frac{2\Delta\tau_j(\lambda) - \left(\alpha_{z_{j-1}}^e(\lambda) + \alpha_{z_j}^e(\lambda)\right)\Delta z_j}{\Delta z_j^3} \qquad B_j(\lambda) = \frac{-3A_j(\lambda)\Delta z_j^2 + \alpha_{z_{j-1}}^e(\lambda) - \alpha_{z_j}^e(\lambda)}{2\Delta z_j}$$

$$C_j(\lambda) = -\alpha_{z_{j-1}}^e(\lambda) \qquad D_j(\lambda) = \Delta\tau_j(\lambda)$$

Figure 4.C.1. DART horizontally homogeneous atmosphere layer with layer thickness $\Delta z_j$. The upper and lower boundary parameters are marked.

The continuous temperature profile is represented by a linear equation using the upper and bottom boundary temperatures:

$$T_j(h) = T_j^L + \frac{T_j^U - T_j^L}{\Delta z_j}\cdot h$$

## 4.Appendix D Radiance estimate for pure atmospheric environment

For the semi-infinite plane-parallel atmosphere, illuminated by parallel sunlight and observed by an orthographic camera, the radiance estimate $F_{\mathrm{IS}}^{(j)} = \sum_{n=1}^{\infty}\left[\frac{\tilde{L}_e(r_n\to r_{n-1})\cdot\tilde{G}(r_0\leftrightarrow r_1)\cdot {W_e}^{(j)}(r_0\to r_1)}{\overleftarrow{p}(r_0)\cdot\overleftarrow{p}(r_1)}\cdot\prod_{k=2}^{n}\frac{\tilde{f}_s(r_k\to r_{k-1}\to r_{k-2})\cdot\tilde{G}(r_{k-1}\leftrightarrow r_k)}{\overleftarrow{p}(r_k)}\right]$ (Eq. (4.15)) can be simplified.

If all vertices (exclude the vertex at the light source and at the sensor) are in the medium, we have the expressions

$$\frac{\tilde{G}(r_0\leftrightarrow r_1)\cdot {W_e}^{(j)}(r_0\to r_1)}{\overleftarrow{p}(r_0)\cdot\overleftarrow{p}(r_1)} = \frac{\mathcal{T}(r_0\leftrightarrow r_1)\cdot\dfrac{\cos\theta_i^{r_0}}{\|r_0-r_1\|^2}\cdot\dfrac{\delta(\Omega_0-\Omega_{\mathrm{d}})}{A_{\mathrm{img}}}}{\dfrac{1}{A_{\mathrm{img}}}\cdot\dfrac{\delta(\Omega_0-\Omega_{\mathrm{d}})}{\|r_0-r_1\|^2}\cdot\alpha_e(r_0\to r_1)\cdot\mathcal{T}(r_0\leftrightarrow r_1)} = \frac{1}{\alpha_e(r_0\to r_1)}$$

$$\frac{\tilde{f}_s(r_k\to r_{k\text{-}1}\to r_{k\text{-}2})\cdot\tilde{G}(r_{k\text{-}1}\leftrightarrow r_k)}{\overleftarrow{p}(r_k)} = \frac{\alpha_s(r_k\to r_{k\text{-}1})\cdot\dfrac{P(r_k\to r_{k\text{-}1}\to r_{k\text{-}2})}{4\pi}\cdot\dfrac{\mathcal{T}(r_{k\text{-}1}\leftrightarrow r_k)}{\|r_{k\text{-}1}-r_k\|^2}}{\dfrac{P(r_{k\text{-}2}\to r_{k\text{-}1}\to r_k)}{4\pi}\cdot\dfrac{\alpha_e(r_{k\text{-}1}\to r_k)\cdot\mathcal{T}(r_{k\text{-}1}\leftrightarrow r_k)}{\|r_{k\text{-}1}-r_k\|^2}} = \frac{\alpha_s(r_k\to r_{k\text{-}1})}{\alpha_e(r_{k\text{-}1}\to r_k)}\cdot\frac{P(r_k\to r_{k\text{-}1}\to r_{k\text{-}2})}{P(r_{k\text{-}2}\to r_{k\text{-}1}\to r_k)}$$

Besides, the direct connection of the light source indicates

$$\begin{aligned}
&\frac{\tilde{L}_e(r_n\to r_{n-1})\cdot\tilde{f}_s(r_n\to r_{n-1}\to r_{n-2})\cdot\tilde{G}(r_{n-1}\leftrightarrow r_n)}{\overleftarrow{p}(r_n)}\\
&\qquad = \frac{E_s\cdot\delta(\Omega_{n-1}-\Omega_s)\cdot\alpha_s(r_n\to r_{n-1})\cdot\dfrac{P(r_n\to r_{n-1}\to r_{n-2})}{4\pi}\cdot\dfrac{\mathcal{T}(r_{n-1}\leftrightarrow r_n)}{\|r_{n-1}-r_n\|^2}}{\delta(\Omega_{n-1}-\Omega_s)\cdot\dfrac{\cos\theta_o^{r_n}}{\|r_{n-1}-r_n\|^2}}\\
&\qquad = E_s\cdot\alpha_s(r_n\to r_{n-1})\cdot\mathcal{T}(r_{n-1}\leftrightarrow r_n)\cdot\frac{P(r_n\to r_{n-1}\to r_{n-2})}{4\pi}
\end{aligned}$$

with $E_s$ is the solar constant at TOA, $\Omega_s$ is the solar direction.

Under the assumption that the scatterers are isotropic, *i.e.*, the reciprocity is verified $P(r_k\to r_{k-1}\to r_{k-2})=P(r_{k-2}\to r_{k-1}\to r_k)$ and extinction coefficients do not depend on direction. It is usually the case for atmospheric molecules and particles. We finally derive the form that is consistent with the SSA method in (Spada et al., 2006).

$$F_{\mathrm{IS}}^{(j)} = \sum_{n=1}^{\infty}\left[E_s\cdot\mathcal{T}(r_n\leftrightarrow r_{n-1})\cdot\frac{P(r_n\to r_{n-1}\to r_{n-2})}{4\pi}\cdot\prod_{k=1}^{n-1}\frac{\alpha_s(r_k)}{\alpha_e(r_k)}\right]$$

# Chapter 5

# Modelling of polarization

Polarization modelling relies on the wave-like properties of radiation. It improves the accuracy of the simulation of remote sensing signals. It helps us in increasing the information content that can be extracted from remote sensing signals. It is very useful for the interpretation of existing polarimetric satellite missions and for the design of future missions, for example, the GCOM-C satellite (2017) of Japan Aerospace Exploration measures polarimetric radiation with the SGLI polarization imager (Imaoka et al., 2010). The GaoFen-5 satellite (2018) of the Chinese Space Agency is equipped with the DPC polarimetric camera (Li et al., 2018). Both the METOP-SG-A satellite of the European Space Agency and the OTB-2 satellite of the National Aeronautics and Space Administration are scheduled to be launched by 2023. The former is a successor of POLDER mission, equipped with a 3MI polarization imager (Fougnie et al., 2018). The latter is equipped with a MAIA polarization imager (Diner et al., 2018).

After a description of the fundamental principles of light representation and the mathematical description of polarized radiative transfer, this chapter details the modelling of the atmosphere and land surface polarized radiative transfer in DART-Lux. This new modelling is validated with reference atmosphere models of the international polarized radiative transfer (IPRT) intercomparison project. Finally, the impact of atmosphere polarization on radiometric measurements is discussed.

# 5.1 Theoretical background

## 5.1.1 Light representation and the rotation matrix

As stated in section 1.1, the standard representation of the monochromatic plane wave is:

$$\boldsymbol{E} = E_{x_P}\hat{\boldsymbol{x}}_P + E_{y_P}\hat{\boldsymbol{y}}_P$$

with $E_{x_P} = A_{x_P} \cdot e^{-i(kz_P-\omega t-\delta_{x_P})}$ and $E_{y_P} = A_{y_P} \cdot e^{-i(kz_P-\omega t-\delta_{y_P})}$.

The polarization state of a monochromatic plane wave is usually described by the Stokes vector:

$$\boldsymbol{S} = \begin{bmatrix} I \\ Q \\ U \\ V \end{bmatrix} = \frac{1}{2}\sqrt{\frac{\varepsilon}{\mu}} \cdot \begin{bmatrix} E_{x_P}E^*_{x_P} + E_{y_P}E^*_{y_P} \\ E_{x_P}E^*_{x_P} - E_{y_P}E^*_{y_P} \\ E_{x_P}E^*_{y_P} + E_{y_P}E^*_{x_P} \\ i\left(E_{x_P}E^*_{y_P} - E_{y_P}E^*_{x_P}\right) \end{bmatrix} \tag{5.1}$$

$\boldsymbol{S}$ is defined with respect to the wave reference coordinate ($\hat{\boldsymbol{x}}_P$, $\hat{\boldsymbol{y}}_P$, $\hat{\boldsymbol{z}}_P$) with $\hat{\boldsymbol{z}}_P$ always the direction of propagation (Figure 1.1). Radiation interaction transforms $\boldsymbol{S}$ into a new Stokes vector $\boldsymbol{S}'$. The representation of this transformation in an absolute reference system relies on a representation in a local reference system that is derived from the absolute reference system through rotations. The components $I$ and $V$ of a Stokes vector are invariant to any rotation around $\hat{\boldsymbol{z}}_P$ conversely to the linear polarization components $Q$ and $U$. Figure 5.1 illustrates an anticlockwise rotation $\eta \in [0, 2\pi)$ of axes $\hat{\boldsymbol{x}}_P$ and $\hat{\boldsymbol{y}}_P$ around $\hat{\boldsymbol{z}}_P$. It transforms $E_{x_P}\hat{\boldsymbol{x}}_P$ into $E_{x'_P}\hat{\boldsymbol{x}}'_P$, $E_{y_P}\hat{\boldsymbol{y}}_P$ into $E_{y'_P}\hat{\boldsymbol{y}}'_P$, and $\boldsymbol{S}$ into the new Stokes vector $\boldsymbol{S}'$.

$$E_{x'_P} = E_{x_P}\cos\eta + E_{y_P}\sin\eta \quad \text{and} \quad E_{y'_P} = E_{y_P}\cos\eta - E_{x_P}\sin\eta \tag{5.2}$$

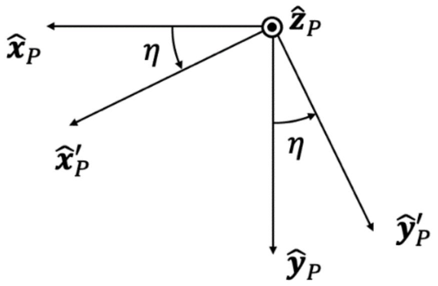

Figure 5.1. Rotation of the wave reference coordinate (Figure 1.1) with respect to the direction of propagation $\hat{\boldsymbol{z}}_P$=$\hat{\boldsymbol{x}}_P$×$\hat{\boldsymbol{y}}_P$. $\eta$>0 indicates anticlockwise rotation around $\hat{\boldsymbol{z}}_P$.

The new rotated Stokes vector is defined by substituting Eq. (5.2) into Eq.(5.1):

$$\boldsymbol{S}' = \mathbf{R}(\eta) \cdot \boldsymbol{S}$$

with

$$\mathbf{R}(\eta) = \begin{bmatrix} 1 & 0 & 0 & 0 \\ 0 & \cos 2\eta & \sin 2\eta & 0 \\ 0 & -\sin 2\eta & \cos 2\eta & 0 \\ 0 & 0 & 0 & 1 \end{bmatrix} \tag{5.3}$$

This rotation matrix verifies: $\mathbf{R}(\eta_1)\cdot\mathbf{R}(\eta_2)=\mathbf{R}(\eta_1+\eta_2)$, $\mathbf{R}(\eta\pm\pi)=\mathbf{R}(\eta)$ and $\mathbf{R}^{-1}(\eta)=\mathbf{R}(-\eta)$.

### 5.1.2 Scattering matrix and phase matrix

A radiative interaction modifies the polarization state of the radiation. The associated change of the Stokes vector is commonly represented by a 4×4 transformation matrix, known as the *Mueller matrix* (Mueller, 1948). Its 16 components result of the essential optical properties of the scattering surface / volume. They can be derived from physical principles (*e.g.*, Fresnel's law), solving Maxwell's equations (*e.g.*, Rayleigh scattering, Mie theory) or measurements.

Here, the change of polarization state due to absorption is neglected and the angular distribution of the polarized scattering is described with two Mueller matrices (Mishchenko et al., 2006):

- *Phase matrix* **P** in the absolute reference system: $\boldsymbol{S}^{(\mathrm{scat})} = \mathbf{P}\cdot\boldsymbol{S}^{(\mathrm{inc})}$, with Stokes vectors $\boldsymbol{S}^{(\mathrm{inc})}$ and $\boldsymbol{S}^{(\mathrm{scat})}$ defined with respect to their respective wave reference coordinate in absolute coordinate system: $(\hat{\boldsymbol{x}}_P^{(\mathrm{inc})}, \hat{\boldsymbol{y}}_P^{(\mathrm{inc})}, \hat{\boldsymbol{z}}_P^{(\mathrm{inc})})$ for $\boldsymbol{S}^{(\mathrm{inc})}$ and $(\hat{\boldsymbol{x}}_P^{(\mathrm{scat})}, \hat{\boldsymbol{y}}_P^{(\mathrm{scat})}, \hat{\boldsymbol{z}}_P^{(\mathrm{scat})})$ for $\boldsymbol{S}^{(\mathrm{scat})}$ (Figure 5.2 and Figure 5.4).
- *Scattering matrix* **M** (Eq. (5.4) in the wave reference system: $\boldsymbol{S}'^{(\mathrm{scat})} = \mathbf{M}\cdot\boldsymbol{S}'^{(\mathrm{inc})}$, with Stokes vectors $\boldsymbol{S}'^{(\mathrm{inc})}$ and $\boldsymbol{S}'^{(\mathrm{scat})}$ defined with respect to their respective wave reference coordinate in local coordinate system: $(\hat{\boldsymbol{x}}_P'^{(\mathrm{inc})}, \hat{\boldsymbol{y}}_P'^{(\mathrm{inc})}, \hat{\boldsymbol{z}}_P'^{(\mathrm{inc})})$ for $\boldsymbol{S}'^{(\mathrm{inc})}$ and $(\hat{\boldsymbol{x}}_P'^{(\mathrm{scat})}, \hat{\boldsymbol{y}}_P'^{(\mathrm{scat})}, \hat{\boldsymbol{z}}_P'^{(\mathrm{scat})})$ for $\boldsymbol{S}'^{(\mathrm{scat})}$ (Figure 5.2 and Figure 5.4).

$$\mathbf{P} = \begin{bmatrix} P_{11} & P_{12} & P_{13} & P_{14} \\ P_{21} & P_{22} & P_{23} & P_{24} \\ P_{31} & P_{32} & P_{33} & P_{34} \\ P_{41} & P_{42} & P_{43} & P_{44} \end{bmatrix} \text{ and } \mathbf{M} = \begin{bmatrix} M_{11} & M_{12} & M_{13} & M_{14} \\ M_{21} & M_{22} & M_{23} & M_{24} \\ M_{31} & M_{32} & M_{33} & M_{34} \\ M_{41} & M_{42} & M_{43} & M_{44} \end{bmatrix} \tag{5.4}$$

### 5.1.3 The vector integral formulation

The transfer of the polarized radiation in a medium can be mathematically described by

$$\frac{d\boldsymbol{L}(r,\Omega)}{ds} = -\alpha_e(r,\Omega)\boldsymbol{L}(r,\Omega) + \int_{4\pi} \mathbf{P}(r,\Omega' \to \Omega)\cdot \boldsymbol{L}(r,\Omega')d\Omega' + \frac{d\boldsymbol{L}_e(r,\Omega)}{ds} \qquad (5.5)$$

where the extinction matrix $\mathbf{K}_e(r,\Omega)$ is reduced to the extinction coefficient $\alpha_e(r,\Omega)$. This approximation is valid for particles that are macroscopically isotropic and mirror-symmetric (Mishchenko et al., 2006). It is less accurate for macroscopically anisotropic particles. Any direction is defined by its unit vector $\Omega(\theta,\varphi)$ in the absolute spherical coordinate; $\Omega(\theta,\varphi) = \hat{\boldsymbol{z}}_P$ if $\Omega$ represents the radiation direction.

At the surface, the corresponding vector form is:

$$\boldsymbol{L}_o(r,\Omega) = \boldsymbol{L}_e(r,\Omega) + \int_{4\pi} \mathbf{P}(r,\Omega' \to \Omega)\cdot \boldsymbol{L}_i(r,\Omega')\,d\Omega' \qquad (5.6)$$

Eq. (5.5) and Eq. (5.6) are similar to their scalar forms (*cf.* section 1.5). They only differ because radiation is represented by the Stokes vector and scattering is represented by the phase matrix $\mathbf{P}(r,\Omega' \to \Omega)$. Therefore, the scalar radiative transfer modelling deduction method (*cf.* Chapter 3 and Chapter 4) can be used to get the integral formulation of the polarimetric measurement:

$$\boldsymbol{L}^{(j)} = \int_{\mathcal{D}} \boldsymbol{f}^{(j)}(\bar{r})\,d\mu(\bar{r}) \qquad (5.7)$$

$\mathcal{D}$ is the generalized path space and $\mu$ is the generalized area- and volume-product measure (*cf.* section 4.1.3). The vector-contribution function $\boldsymbol{f}^{(j)}(\bar{r})$ is defined by:

$$\boldsymbol{f}^{(j)}(\bar{r}_n) = \boldsymbol{W_e}^{(j)}(r_0 \to r_1)\cdot\tilde{G}(r_0 \leftrightarrow r_1)\cdot\left[\prod_{k=2}^{n}\tilde{\boldsymbol{f}}_{\boldsymbol{s}}(r_k \to r_{k\text{-}1} \to r_{k\text{-}2})\cdot\tilde{G}(r_{k\text{-}1} \leftrightarrow r_k)\right]\cdot\tilde{\boldsymbol{L}}_{\boldsymbol{e}}(r_n \to r_{n\text{-}1}) \qquad (5.8)$$

with the importance matrix $\boldsymbol{W_e}^{(j)} = W_e^{(j)}\cdot\mathbf{diag}(1,1,1,1)$ and the vector bidirectional scattering matrix $\tilde{\boldsymbol{f}}_{\boldsymbol{s}}$ equal to the phase matrix.

## 5.2 Surface and volume scattering

Scattering is the major process that changes the polarization state of radiation. This section presents the procedures to compute the phase matrix **P** at surfaces and in media in the absolute coordinate system. It also defines common scattering matrices **M** in local coordinate system.

### 5.2.1 Volume scattering matrix

For volume polarimetric scattering, the scattering matrix **M** is defined in the scattering plane ($\hat{\boldsymbol{z}}_P^{(\mathrm{inc})}$, $\hat{\boldsymbol{z}}_P^{(\mathrm{scat})}$) (Figure 5.2) with the axes $\hat{\boldsymbol{y}}_P^{\prime(\mathrm{inc})}$ and $\hat{\boldsymbol{y}}_P^{\prime(\mathrm{scat})}$ of the incident and exit wave reference systems defined in ($\hat{\boldsymbol{z}}_P^{(\mathrm{inc})}$, $\hat{\boldsymbol{z}}_P^{(\mathrm{scat})}$). The rotation matrix $\mathbf{R}(\pi\text{-}\sigma_1)$ around the axis $\hat{\boldsymbol{z}}_P^{(\mathrm{inc})}$ transforms ($\hat{\boldsymbol{x}}_P^{(\mathrm{inc})}$ $\hat{\boldsymbol{y}}_P^{(\mathrm{inc})}$,$\hat{\boldsymbol{z}}_P^{(\mathrm{inc})}$) into ($\hat{\boldsymbol{x}}_P^{\prime(\mathrm{inc})}$,$\hat{\boldsymbol{y}}_P^{\prime(\mathrm{inc})}$,$\hat{\boldsymbol{z}}_P^{\prime(\mathrm{inc})}$), whereas the rotation matrix $\mathbf{R}(\text{-}\sigma_2)$ around the axis $\hat{\boldsymbol{z}}_P^{(\mathrm{scat})}$ transforms ($\hat{\boldsymbol{x}}_P^{\prime(\mathrm{scat})}$,$\hat{\boldsymbol{y}}_P^{\prime(\mathrm{scat})}$,$\hat{\boldsymbol{z}}_P^{\prime(\mathrm{scat})}$) into ($\hat{\boldsymbol{x}}_P^{(\mathrm{scat})}$, $\hat{\boldsymbol{y}}_P^{(\mathrm{scat})}$, $\hat{\boldsymbol{z}}_P^{(\mathrm{scat})}$). The scattered Stokes vector $\boldsymbol{S}^{(\mathrm{scat})}$ is calculated in three steps from the incident Stokes vector $\boldsymbol{S}^{(\mathrm{inc})}$ (Chandrasekhar, 1960):

1) Calculate the incident Stokes vector in scattering plane reference: $\boldsymbol{S}'^{(\mathrm{inc})}=\mathbf{R}(\pi-\sigma_1)\cdot\boldsymbol{S}^{(\mathrm{inc})}$.
2) Calculate the exit Stokes vector in the scattering plane reference: $\boldsymbol{S}'^{(\mathrm{scat})}=\mathbf{M}\cdot\boldsymbol{S}'^{(\mathrm{inc})}$.
3) Calculate the exit Stokes vector in the absolute reference: $\boldsymbol{S}^{(\mathrm{scat})}=\mathbf{R}(-\sigma_2)\cdot\boldsymbol{S}'^{(\mathrm{scat})}$.

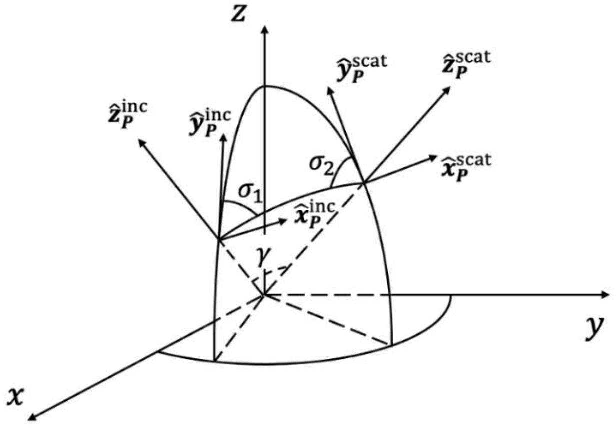

Figure 5.2. Scattering plane ($\hat{\boldsymbol{z}}_P^{(\mathrm{inc})}$, $\hat{\boldsymbol{z}}_P^{(\mathrm{scat})}$) of the incident and scattered radiation, scattering phase angle $\gamma=\arccos(\hat{\boldsymbol{z}}_P^{(\mathrm{inc})}\cdot\hat{\boldsymbol{z}}_P^{(\mathrm{scat})})$, and reference systems of the incident ($\hat{\boldsymbol{x}}_P^{(\mathrm{inc})}$, $\hat{\boldsymbol{y}}_P^{(\mathrm{inc})}$,$\hat{\boldsymbol{z}}_P^{(\mathrm{inc})}$) and scattered ($\hat{\boldsymbol{x}}_P^{(\mathrm{scat})}$,$\hat{\boldsymbol{y}}_P^{(\mathrm{scat})}$,$\hat{\boldsymbol{z}}_P^{(\mathrm{scat})}$) Stokes vectors.

The three-step approach leads to the scattered Stokes vector:

$$\boldsymbol{S}^{(\mathrm{scat})}=\mathbf{R}(-\sigma_2)\cdot\mathbf{M}\cdot\mathbf{R}(\pi-\sigma_1)\cdot\boldsymbol{S}^{(\mathrm{inc})}=\mathbf{P}\cdot\boldsymbol{S}^{(\mathrm{inc})}$$

with the phase matrix:

$$\mathbf{P} = \mathbf{R}(-\sigma_2) \cdot \mathbf{M} \cdot \mathbf{R}(\pi - \sigma_1) \tag{5.9}$$

(Mishchenko et al., 2006) gives the reciprocity relationship of the phase matrix **P**:

$$\mathbf{P}(\Omega' \to \Omega) = \Delta_3 \cdot \mathbf{P}^{\mathrm{T}}(\Omega \to \Omega') \cdot \Delta_3 \tag{5.10}$$

with T the matrix transpose operator, and $\Delta_3$ such that:

$$\Delta_3 = \Delta_3^{\mathrm{T}} = \Delta_3^{-1} = \begin{bmatrix} 1 & 0 & 0 & 0 \\ 0 & 1 & 0 & 0 \\ 0 & 0 & -1 & 0 \\ 0 & 0 & 0 & 1 \end{bmatrix}$$

(Mishchenko et al., 2006) prove that the phase and scattering matrices of medium with macroscopically isotropic and mirror-symmetric properties do not depend on the incident direction and orientation of scattering plane. They only depend on the phase angle between the incident and scattered directions $\gamma = \arccos\left(\hat{\boldsymbol{z}}_P^{(\mathrm{inc})} \cdot \hat{\boldsymbol{z}}_P^{(\mathrm{scat})}\right)$ (Figure 5.2).

The two volume scattering matrices implemented in DART-Lux are given below.

**Rayleigh scattering matrix.** It is expressed in Eq. (5.11) (Mishchenko et al., 2006):

$$\mathbf{M} = \Delta . \begin{bmatrix} \frac{3}{4}(1+\cos^2\gamma) & -\frac{3}{4}(1-\cos^2\gamma) & 0 & 0 \\ -\frac{3}{4}(1-\cos^2\gamma) & \frac{3}{4}(1+\cos^2\gamma) & 0 & 0 \\ 0 & 0 & \frac{3}{2}\cos\gamma & 0 \\ 0 & 0 & 0 & \Delta' \frac{3}{2}\cos\gamma \end{bmatrix} + (1-\Delta) . \begin{bmatrix} 1 & 0 & 0 & 0 \\ 0 & 0 & 0 & 0 \\ 0 & 0 & 0 & 0 \\ 0 & 0 & 0 & 0 \end{bmatrix} \tag{5.11}$$

with $\Delta = \frac{1-\delta}{1+\delta/2}$, $\Delta' = \frac{1-2\delta}{1-\delta}$, and $\delta$ the depolarization factor that considers the potential anisotropy of molecules. We choose $\delta = 0.0279$ following (Young, 1980). The scattering matrix can be expressed as a product of the Rayleigh scattering phase function $M_{11}$ and the so-called *reduced Rayleigh scattering matrix* $\mathbf{M_r}$. Then, we have: $\mathbf{M} = \mathbf{M_r} \cdot M_{11}$.

**Double Henyey-Greenstein scattering matrix.** Following (Adams and Kattawar, 1993; Liu and Weng, 2006; Sun et al., 2016; Tynes et al., 2001), it is the product of the double Henyey-Greenstein scattering phase function (Eq. (4.13)) and the reduced Rayleigh scattering matrix $\mathbf{M_r}$. It is an approximation for simulating polarized scattering of aerosols.

### 5.2.2 Surface scattering matrix

Figure 5.3 shows the geometric configuration in the surface reference system (*i.e.*, index “′”) with indication of the parallel and perpendicular reflectance and transmittance of the amplitude of the parallel and perpendicular electric fields in (a), and the adapted incident and exit wave reference coordinate in (b).

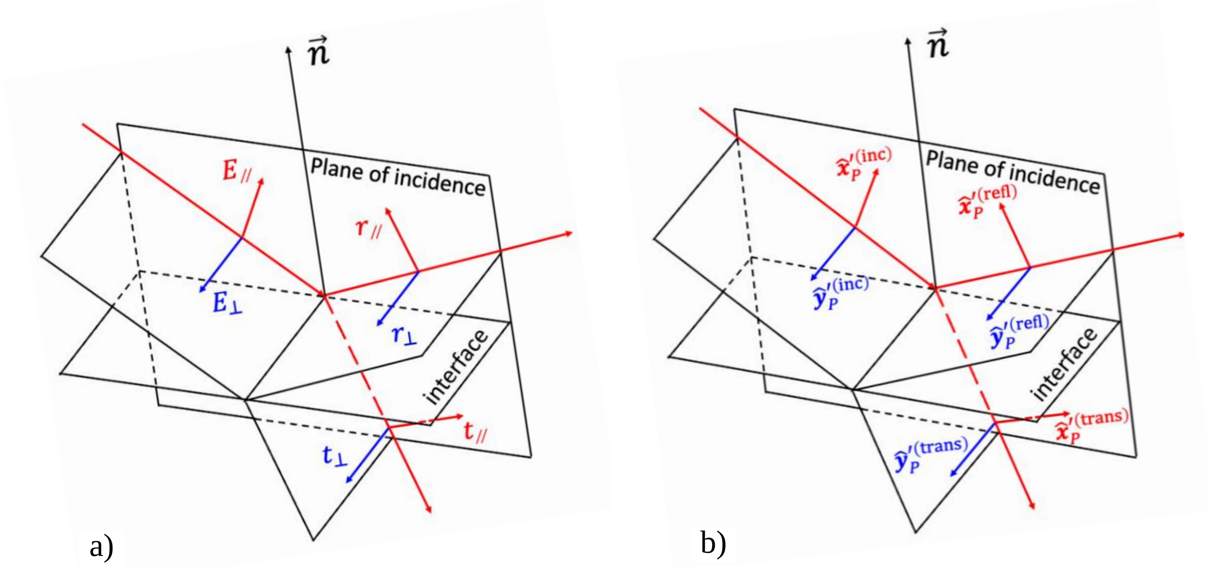

Figure 5.3. (a) Coordinate system at local surface adapted from (Collett, 1971; Hecht, 1987). The parallel (//, red colour) and perpendicular (⊥, blue colour) components of the incident (*E*), reflected (*r*) and transmitted (*t*) radiation are marked. (b) adaptation of coordinate with DART-Lux definition ($\hat{\boldsymbol{z}}'_P = \hat{\boldsymbol{x}}'_P \times \hat{\boldsymbol{y}}'_P$), with incident (inc), reflected (refl) and transmitted (trans) directions marked in the superscript.

The scattering matrix is defined in the surface reference system. The parallel component is in the incidence plane that contains the radiation direction and surface normal (Figure 5.3). $\boldsymbol{S}^{(\mathrm{scat})}$ (Figure 5.4) is computed in three steps:

(1) Calculate the incident Stokes vector in surface reference system: $\boldsymbol{S}'^{(\mathrm{inc})} = \mathbf{R}(\sigma_1) \cdot \boldsymbol{S}^{(\mathrm{inc})}$.

(2) Calculate the exit Stokes vector in surface reference system: $\boldsymbol{S}'^{(\mathrm{scat})} = \mathbf{M} \cdot \boldsymbol{S}'^{(\mathrm{inc})}$.

(3) Calculate the exit Stokes vector in the absolute reference: $\boldsymbol{S}^{(\mathrm{scat})} = \mathbf{R}(-\sigma_2) \cdot \boldsymbol{S}'^{(\mathrm{scat})}$.

It leads to the scattered Stokes vector:

$$\boldsymbol{S}^{(\mathrm{scat})} = \mathbf{R}(-\sigma_2) \cdot \mathbf{M} \cdot \mathbf{R}(\sigma_1) \cdot \boldsymbol{S}^{(\mathrm{inc})} = \mathbf{P} \cdot \boldsymbol{S}^{(\mathrm{inc})}$$

with the phase matrix:

$$\mathbf{P} = \mathbf{R}(-\sigma_2) \cdot \mathbf{M} \cdot \mathbf{R}(\sigma_1) \tag{5.12}$$

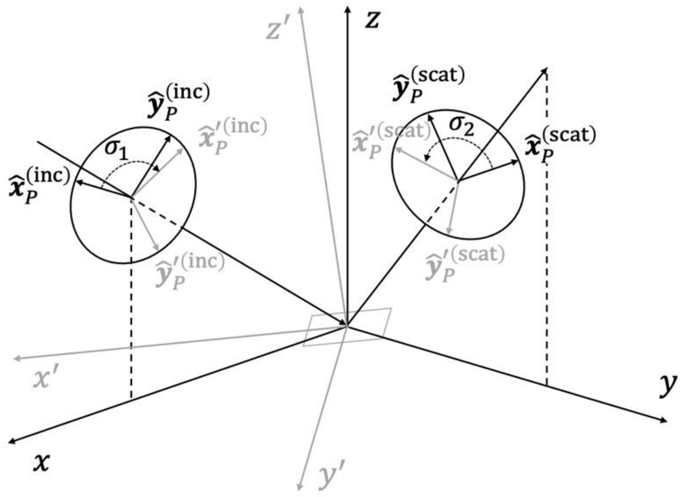

Figure 5.4. Absolute reference system $(x, y, z)$ and surface reference system $(x', y', z')$. $z'$ is the surface normal, noted $\vec{n}$ in Figure 5.3. The wave reference is $(\hat{\boldsymbol{x}}_P^{(\mathrm{rad})}, \hat{\boldsymbol{y}}_P^{(\mathrm{rad})}, \hat{\boldsymbol{z}}_P^{(\mathrm{rad})})$ in the absolute reference system and $(\hat{\boldsymbol{x}}_P'^{(\mathrm{rad})}, \hat{\boldsymbol{y}}_P'^{(\mathrm{rad})}, \hat{\boldsymbol{z}}_P'^{(\mathrm{rad})})$ in the surface reference system (the rotation matrix **R** links them), with (rad) = (inc) for the incident wave and (scat) for the scattered wave.

Two surface scattering matrices implemented in DART-Lux are given below.

**Lambertian scattering.** It is due to perfect diffuse surfaces; *i.e.*, matter where multiple scattering generates isotropic unpolarized radiance. Hence, any radiation, polarized or unpolarized, scattered by a Lambertian surface is unpolarized. Its scattering matrix is:

$$\mathbf{M} = \frac{f_s(r, \Omega' \to \Omega)}{\cos\theta'} \cdot \begin{bmatrix} 1 & 0 & 0 & 0 \\ 0 & 0 & 0 & 0 \\ 0 & 0 & 0 & 0 \\ 0 & 0 & 0 & 0 \end{bmatrix} \tag{5.13}$$

with $f_s(r, \Omega' \to \Omega)$ the Lambertian BSDF and $\theta'$ the zenith angle of the incident direction $\Omega'$.

**Specular scattering.** For an optically smooth surface (*cf.* specular material in section 3.3.3), a strong specular reflection produces or changes the state of polarization. The Fresnel's equation represents this effect. (Collett, 1992, 1971) extends it to a scattering matrix **M** (Eq. (5.14)) for modelling polarized reflection and transmission on specular surfaces. $p_\parallel$ or $p_{x_p}$ is the amplitude coefficient for the electric field vector parallel to the plane of incidence. $p_\perp$ or $p_{y_p}$ is the amplitude coefficient for the electric filed vector perpendicular to the incidence plane (Figure

5.3). They are computed according to the Fresnel's and Snell's laws. For example, we have: $p_{x_p} = \sqrt{\mathcal{R}_{x_p}}$ (Eq. (1.26)) for reflection and $p_{x_p} = \sqrt{\mathcal{T}_{x_p}}$ (Eq. (1.35)) for transmission.

$$\mathbf{M} = \begin{bmatrix} \frac{p_\perp^2+p_\parallel^2}{2} & \frac{p_\perp^2\text{-}p_\parallel^2}{2} & 0 & 0 \\ \frac{p_\perp^2\text{-}p_\parallel^2}{2} & \frac{p_\perp^2+p_\parallel^2}{2} & 0 & 0 \\ 0 & 0 & p_\perp p_\parallel & 0 \\ 0 & 0 & 0 & p_\perp p_\parallel \end{bmatrix} = \begin{bmatrix} \frac{p_{y_p}^2+p_{x_p}^2}{2} & \frac{p_{y_p}^2\text{-}p_{x_p}^2}{2} & 0 & 0 \\ \frac{p_{y_p}^2\text{-}p_{x_p}^2}{2} & \frac{p_{y_p}^2+p_{x_p}^2}{2} & 0 & 0 \\ 0 & 0 & p_{x_p}p_{y_p} & 0 \\ 0 & 0 & 0 & p_{x_p}p_{y_p} \end{bmatrix} \qquad (5.14)$$

## 5.3 Vector bidirectional light transport

Although the consideration of polarization can change the radiation intensity, it almost does not change how radiation propagates in the environment. Therefore, the path sampling method presented in Chapter 3 and Chapter 4 can be applied for polarized radiative transfer. Free path sampling (*cf.* Eq. (4.8)) is used for light transmission. The exit direction is sampled according to Eq. (3.25) and Eq. (4.11) for the light scattering where the related scattering function is replaced by the first element of the corresponding bidirectional scattering matrix $\tilde{\boldsymbol{f}}_{\boldsymbol{s}}$. The major difference between the vector and scalar modelling is the evaluation of the integral estimate. Unlike scalar computation, one cannot change the order of multiplication for vector calculations. Hence, the throughput is computed differently for the light and adjoint transports.

**Light transport.** In the light transport, the contribution function is computed straightforwardly. The emitted radiation from the light source is represented by the Stokes vector. Then, it is multiplied by a phase matrix, which gives a new Stokes vector after each scattering event. The probability is a scalar quantity that is the same for both vector and scalar modelling. Then, the vector throughput (Stokes vector) is computed incrementally as:

$$\begin{aligned} &\boldsymbol{T}(\bar{p}_0) = \tilde{\boldsymbol{L}}_{\boldsymbol{e}}(p_0 \to p_1) \\ &\boldsymbol{T}(\bar{p}_1) = \frac{\tilde{\boldsymbol{L}}_{\boldsymbol{e}}(p_0 \to p_1)}{\vec{p}(p_0)} \cdot \frac{\tilde{G}(p_0 \leftrightarrow p_1)}{\vec{p}(p_1)} \\ &\dots \\ &\boldsymbol{T}(\bar{p}_k) = \frac{\tilde{\boldsymbol{f}}_{\boldsymbol{s}}(p_{k-2} \to p_{k-1} \to p_k) \cdot \tilde{G}(p_{k-1} \leftrightarrow p_k)}{\vec{p}(p_k)} \cdot \boldsymbol{T}(\bar{p}_{k-1}) \end{aligned}$$

**Adjoint transport.** It is a mathematical "trick" because there is no adjoint transport in nature. Although the adjoint bidirectional scattering matrix $\tilde{\boldsymbol{f}}_{\boldsymbol{s}}^{*}$ should be used if reciprocity is not verified, which commonly occurs for vector scattering, $\tilde{\boldsymbol{f}}_{\boldsymbol{s}}$ is used instead because $\tilde{\boldsymbol{f}}_{\boldsymbol{s}}^{*}$ computation is very expensive (Eq. (5.10)). Also, the throughput is stored in a matrix instead of a Stokes vector. It is incrementally evaluated as:

$$\begin{aligned}
&\boldsymbol{T}(\bar{q}_0) = \boldsymbol{W_e}^{(j)}(q_0 \to q_1)\\
&\boldsymbol{T}(\bar{q}_1) = \frac{\boldsymbol{W_e}^{(j)}(q_0 \to q_1)}{\overleftarrow{p}(q_0)} \cdot \frac{\tilde{G}(q_0 \leftrightarrow q_1)}{\overleftarrow{p}(q_1)}\\
&\dots\\
&\boldsymbol{T}(\bar{q}_k) = \boldsymbol{T}(\bar{q}_{k-1}) \cdot \frac{\tilde{\boldsymbol{f}}_{\boldsymbol{s}}(q_k \to q_{k-1} \to q_{k-2}) \cdot \tilde{G}(q_{k-1} \leftrightarrow q_k)}{\overleftarrow{p}(q_k)}
\end{aligned}$$

**Path connection.** Once the two vertices in the bidirectional random walk is mutually visible, the two vertices are connected by a connection matrix:

$$\boldsymbol{C}_{s,t} = \tilde{\boldsymbol{f}}_{\boldsymbol{s}}(q_{s-1} \to q_{t-1} \to p_{t-2}) \cdot \tilde{G}(p_{s-1} \leftrightarrow q_{t-1}) \cdot \tilde{\boldsymbol{f}}_{\boldsymbol{s}}(p_{s-2} \to p_{s-1} \to q_{t-1})$$

and the corresponding estimate of the polarimetric measurement is then computed by:

$$\boldsymbol{F}_{s,t} = \boldsymbol{T}(\bar{q}_t) \cdot \boldsymbol{C}_{s,t} \cdot \boldsymbol{T}(\bar{p}_s)$$

## 5.4 Results

### 5.4.1 Evaluation by intercomparison

DART-Lux modelling of polarization has been validated by comparing it with the benchmark results of the phase A of IPRT (https://meteo.physik.uni-muenchen.de/~iprt/doku.php?id=start) for two study cases (*cf.* case B1 and B2 in (Emde et al., 2015)). Case B1 considers Rayleigh scattering in a standard atmosphere (5.Appendix A), and case B2 considers Rayleigh scattering as well as molecule absorption in a standard atmosphere (5.Appendix B). Both cases model plane parallel multi-layer atmosphere (30 equal-thickness layers from 0 to 30 km) and are given the layer optical depth of the corresponding atmosphere. Ground albedo is zero to emphasize the atmosphere signal. Solar zenith and azimuth angles are $\theta_s$=60° and $\varphi_s$=0°, respectively. Viewing directions are for all the upper hemisphere at TOA level with zenith ($\theta_v \in [0°, 80°]$) and azimuth ($\varphi_v \in [0°, 360°]$) with 5° steps. Benchmark results of the six participant models (*i.e.*, 3DMCPOL, IPOL, MYSTIC, PSTAR, SHDOM, TROPOS) are shown in 5.Appendix A for case B1 and 5.Appendix B for case B2. Differences were assessed with the relative root mean square difference $\Delta_m = \frac{\sqrt{\sum_{i=0}^{N}\left(X_{\text{test}}^i - X_{\text{ref}}^i\right)^2}}{\sqrt{\sum_{i=0}^{N}\left(X_{\text{ref}}^i\right)^2}}$ where $X$ can be a Stokes component and $N$ is the total number of directional observations. We found a high-level consistency with $\Delta_m < 0.6\%$.

DART-Lux results were compared with the average (AVG), minimum (MIN) and maximum (MAX) values of the six participant models in the phase A of IPRT. Figure 5.5 shows the polar plot of the Stokes components of IPRT-AVG and DART-Lux, for case B1, and their differences are also plotted. DART-Lux appears to be consistent with benchmark results in the IPRT project. The relative root mean square difference for the four Stokes components is $\Delta_m(I)$=0.18%, $\Delta_m(Q)$=0.22%, $\Delta_m(U)$=0.17%, and $\Delta_m(V)=NULL$. Figure 5.6 shows the corresponding line plot along a specific viewing azimuth angle $VAA$=$0°, 45°, 90°$. Table 5.1 shows differences. $\Delta_m$ is commonly less than 0.2% with the exception of $\Delta_m(Q)$=0.54% at $VAA$=$0°$.

IPRT-AVG

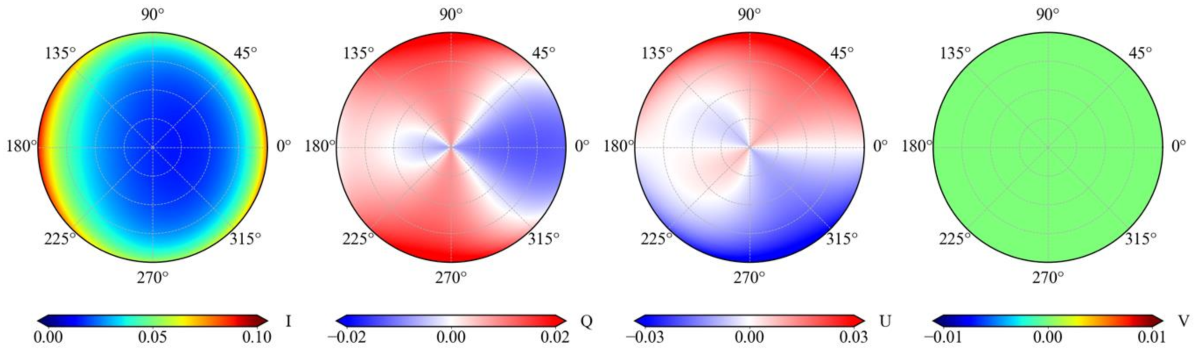

DART-Lux

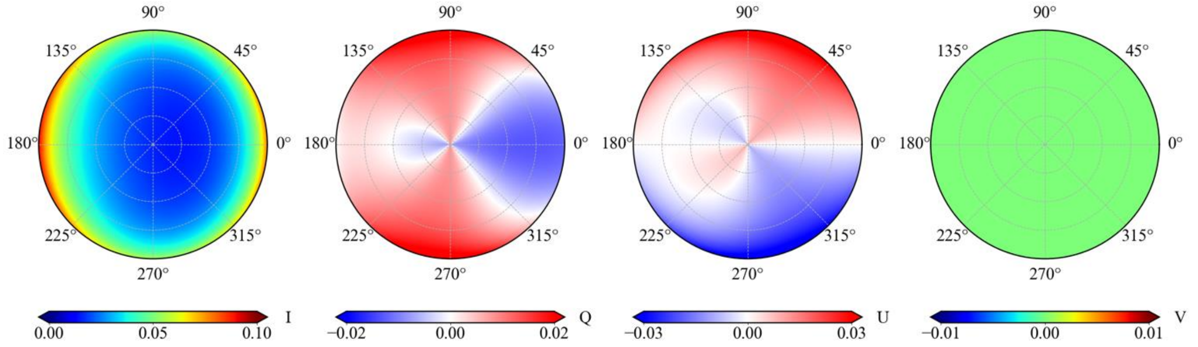

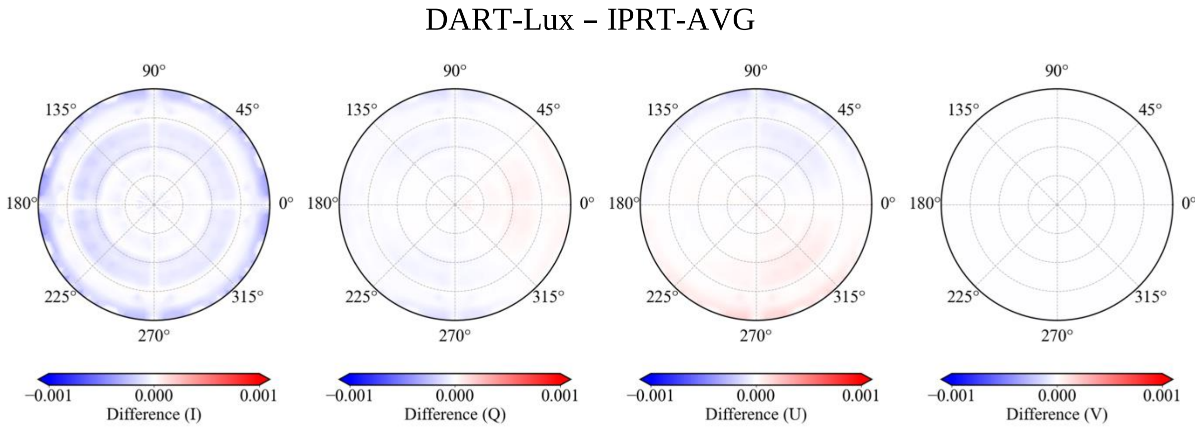

Figure 5.5. Case B1 results of the mean value of the six participant models in IPRT and DART-Lux modelling. The difference is also shown.

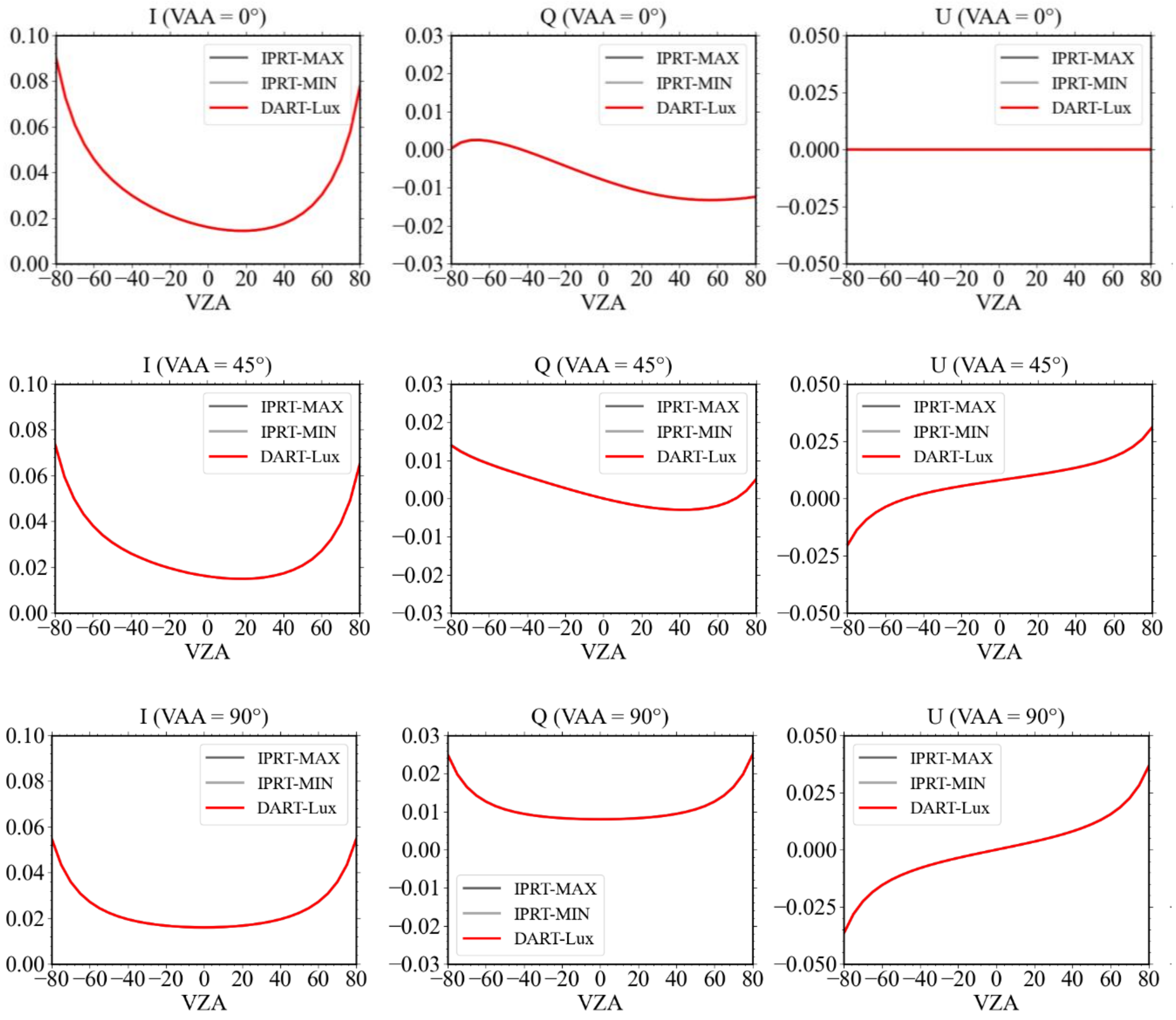

Figure 5.6. DART-Lux and IPRT-AVG Stokes components for three viewing azimuth angles: $VAA$=0°, 45° and 90°. Component $V$ is not shown as there is no circular polarization.

With the same comparisons as in the case B1, the polar plot of Stokes components and the associated difference as well as the line plot for the case B2 are shown in Figure 5.7 and Figure 5.8. Table 5.1 gives the differences. Similar to case B1, the difference $\Delta_m$ is commonly less than 0.2% with exception $\Delta_m(Q)$=0.76% at $VAA$=0°.

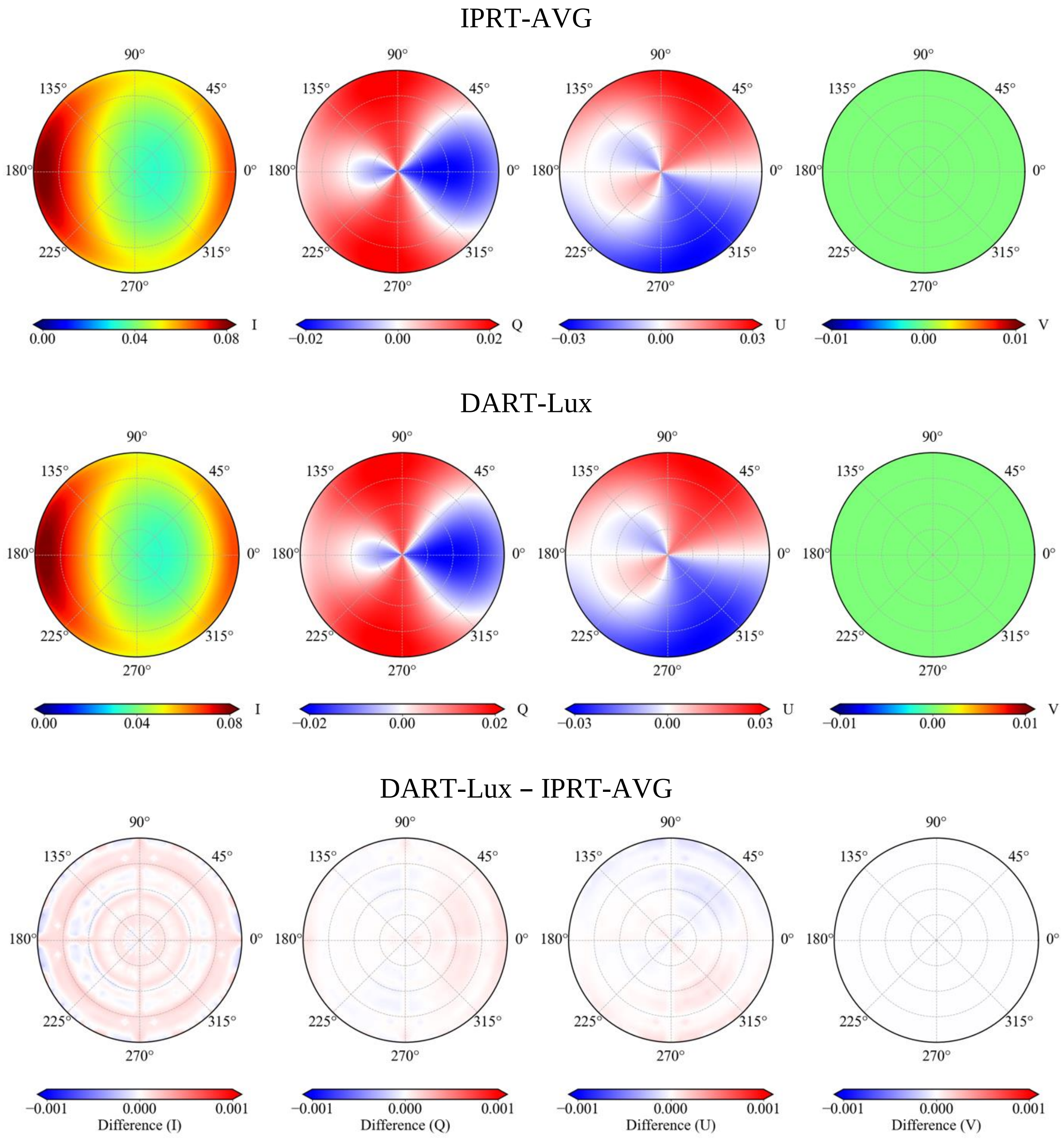
IPRT-AVG

DART-Lux

DART-Lux – IPRT-AVG

Figure 5.7. Case B2 results of the mean value of the six participant models in IPRT project and the DART-Lux modelling. The difference is also displayed.

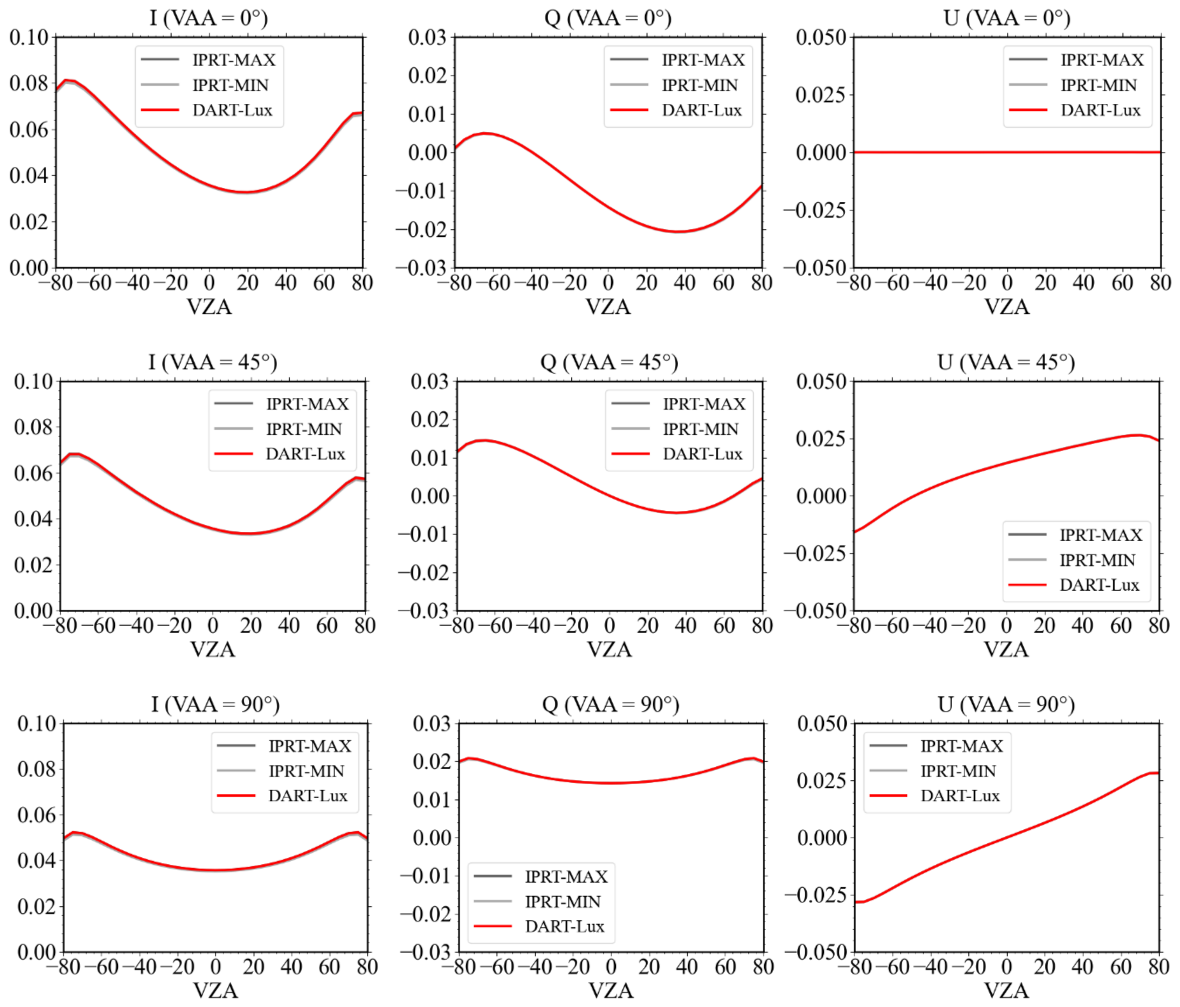

Figure 5.8. Comparison between DART-Lux and IPRT-AVG in for three viewing azimuth angle $VAA = 0°$, $45°$ and $90°$. The profile for component $V$ is not displayed since there is no circular polarization.

Table 5.1. Relative root mean square difference $\Delta_m$ between DART-Lux and IPRT-AVG for Case B1 and B2 of the phase A of IPRT. Both differences for the whole viewing hemisphere and for a specific azimuth angle are evaluated.

| **Region** | **Case B1** | **Case B2** |
|---|---|---|
| Hemisphere | | |
| $I$ | 0.18% | 0.16% |
| $Q$ | 0.22% | 0.22% |
| $U$ | 0.17% | 0.16% |
| $V$ | - | - |
| VAA = 0° | | |

| | | |
|---|---|---|
| $I$ | 0.05% | 0.21% |
| $Q$ | 0.54% | 0.76% |
| $U$ | - | - |
| $V$ | - | - |
| VAA = 45° | | |
| $I$ | 0.16% | 0.15% |
| $Q$ | 0.25% | 0.19% |
| $U$ | 0.15% | 0.17% |
| $V$ | - | - |
| VAA = 90° | | |
| $I$ | 0.04% | 0.26% |
| $Q$ | 0.08% | 0.12% |
| $U$ | 0.05% | 0.05% |
| $V$ | - | - |

### 5.4.2 Impact of polarization on the radiance measurement

Based on this new vector modelling, it is possible to evaluate the impact of polarization on radiance measurement. This quantitative analysis is very useful for the design of Earth observation satellite missions and the retrieval of land surface variables from Earth surface observations. It gives the error of the scalar approximation. The impact on the spectral measurements is evaluated based on the modelling of TOA reflectance spectra from 0.32 to 2.5 $\mu$m of a USSTD76 atmosphere. Figure 5.9 illustrates the comparison between vector DART-Lux and the scalar DART-Lux for three viewing directions (0°, 30°, and 60°) in the solar plane (solar zenith $\theta_s = 60°$). The error varies with the viewing geometry: $\Delta_m(0°)=1.02\%$, $\Delta_m(30°)=2.21\%$ and $\Delta_m(60°)=0.86\%$. The angular impact of polarization is analysed in the following study. Here, we focus on the spectral impact. For all three viewing directions, the error of scalar approximation decreases with the increase of wavelength. For example, for the 30° viewing zenith, the relative error is ≈4.6% at 0.33 $\mu$m, and continuously reduces to 0.1% at 0.7 $\mu$m. Indeed, polarization is only due to scattering and this phenomenon decreases with the increase of wavelength. One can also note a slight decrease of error before 0.33 $\mu$m. This is because, in this spectral region, ozone absorption greatly attenuates the intercepted energy for scattering and thus decreases the polarization. The impact of angular measurements is evaluated based on the modelling of case B1 and B2 in IPRT. Figure 5.10 illustrates the angular variation of the differences between the vector and scalar modelling for the two cases. The scalar approximation tends to underestimate the backscattering and overestimate the forward scattering. Quantitatively, the neglect of polarization leads to a 2.7% average relative error for case B1, and a 4.1% error for case B2. We can also note that the error is the largest in the solar plane ($VAA = 0°$) and decreases for viewing directions away from the solar plane (Table 5.2).

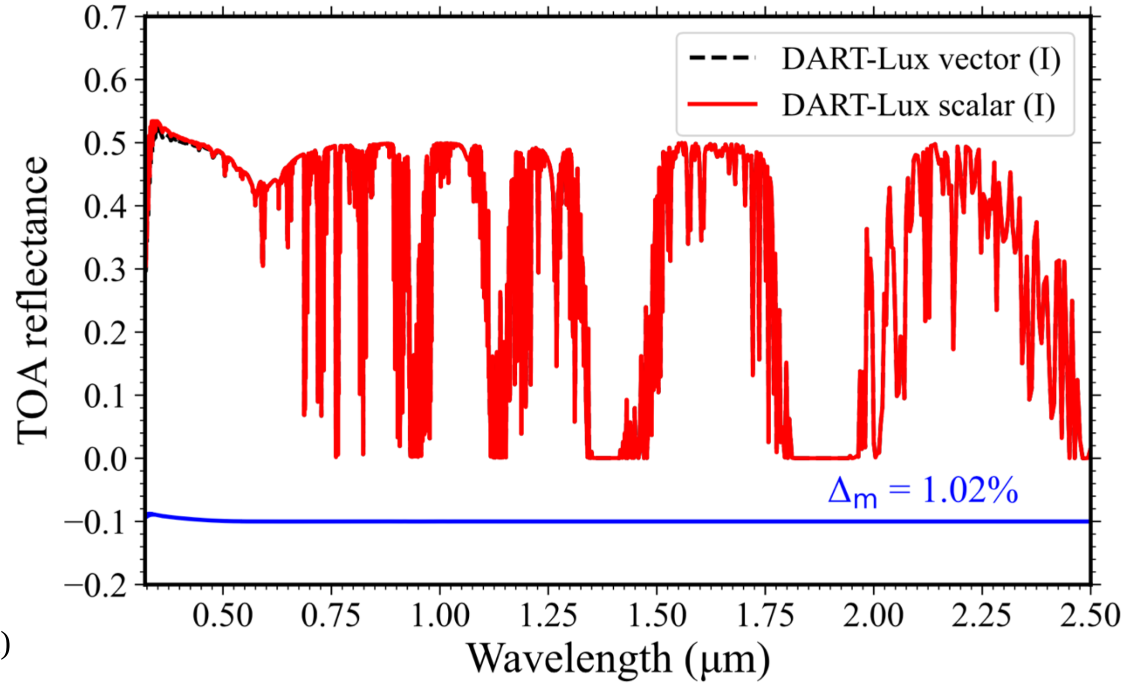

(a)

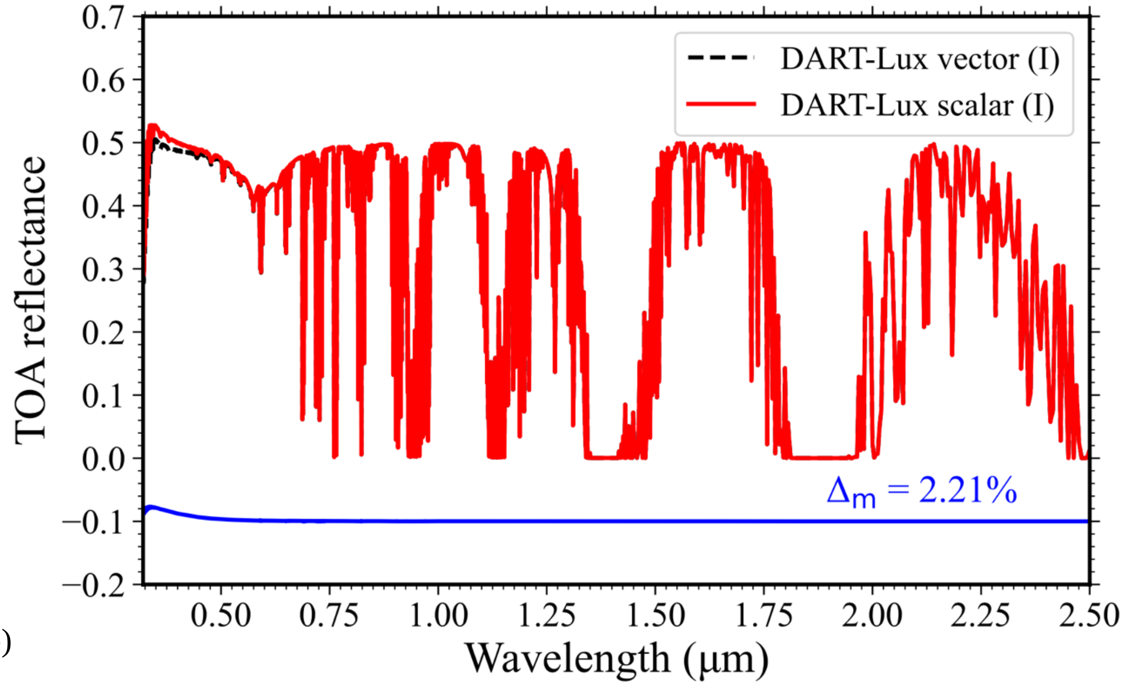

(b)

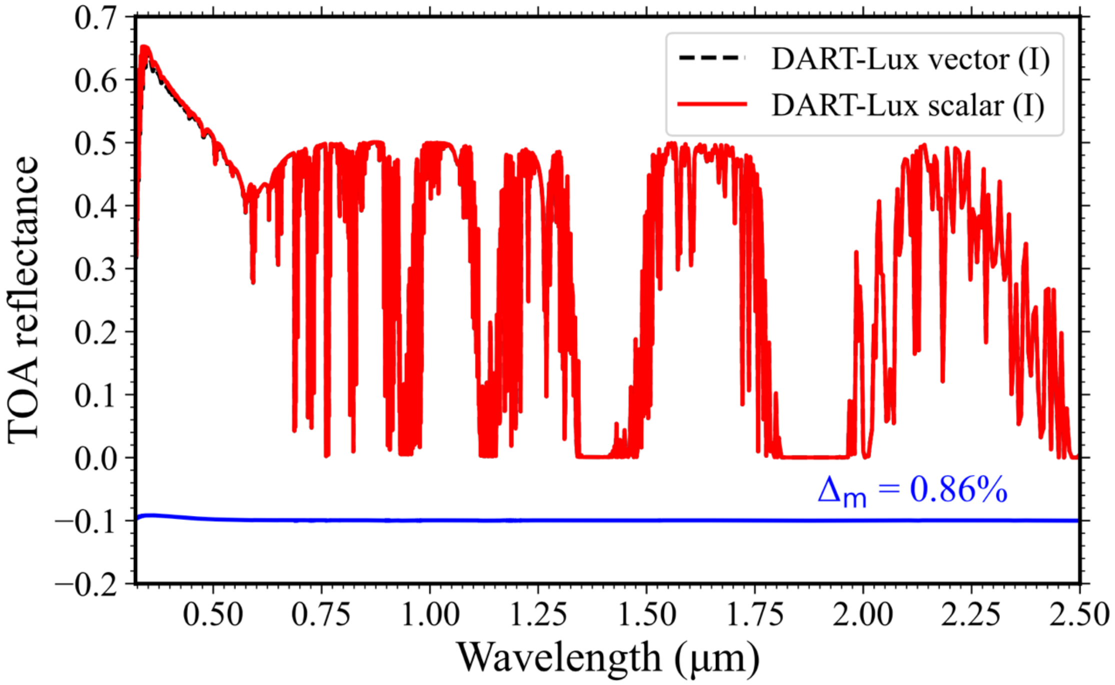

(c)

Figure 5.9. TOA scalar (red solid line) and vector (black dashed line) DART Lux reflectance from 0.32 $\mu$m to 2.5 $\mu$m with 10 cm$^{-1}$ spectral interval for viewing zenith angle at nadir (a), 30° (b) and 60° (c). Solar zenith $\theta_s$=60°. USSTD76 atmosphere. Ground albedo is 0.5 at all wavelengths. The residual “scalar DART-Lux - vector DART-Lux” is plotted (blue solid line) with the relative root mean square difference is indicated.

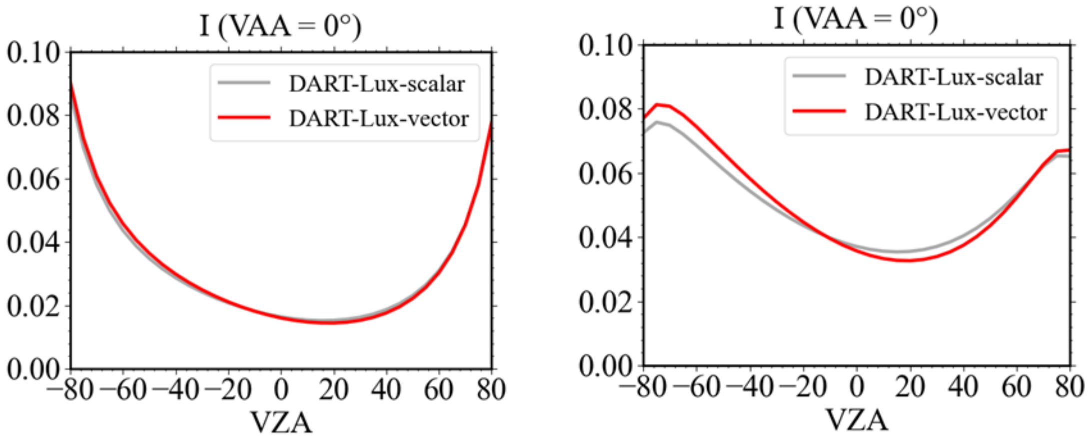

Case B1

Case B2

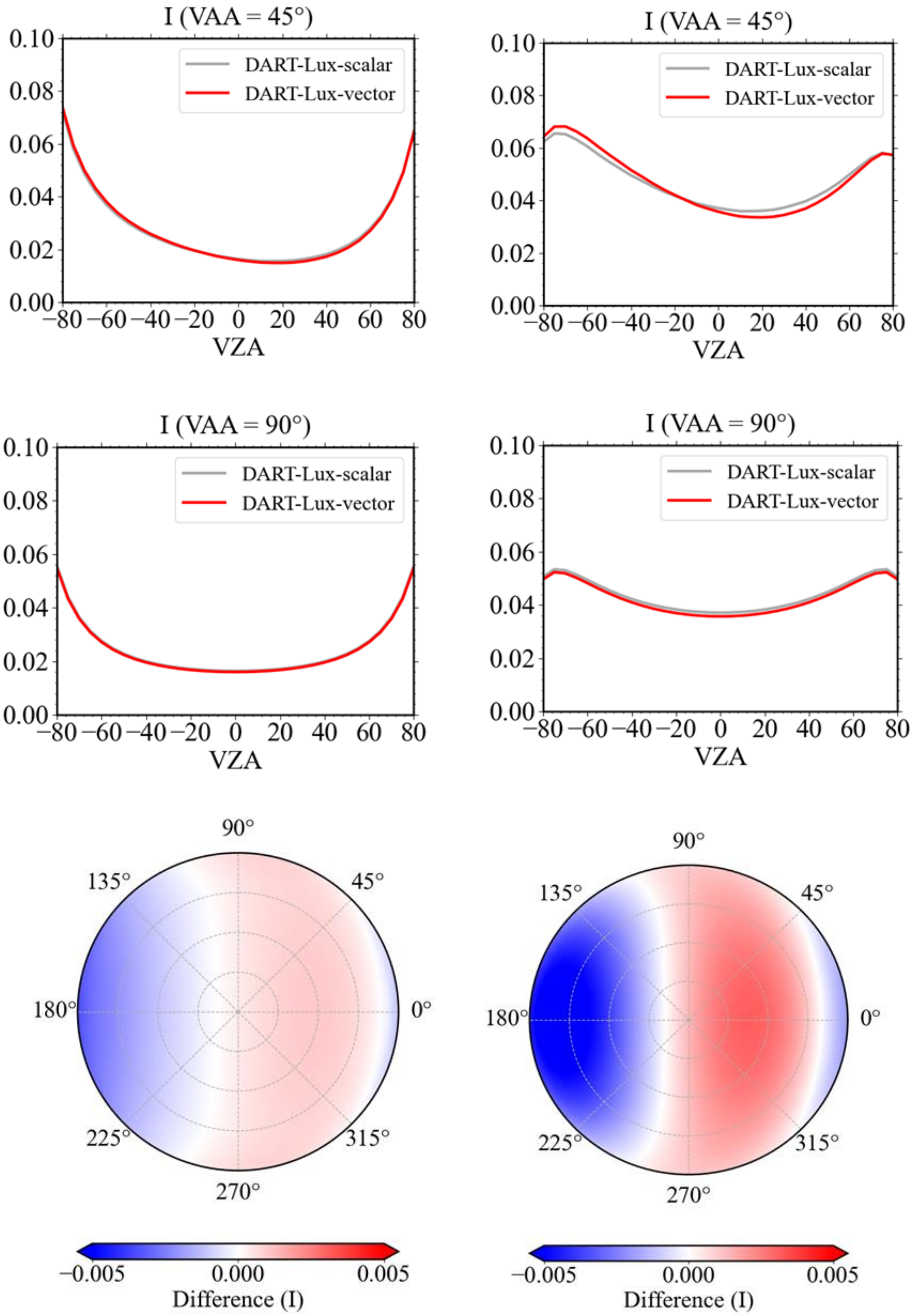

Figure 5.10. Component $I$ of vector DART-Lux and scalar DART-Lux for three viewing azimuth angles $VAA$=0°, 45° and 90° and for the whole upper hemisphere.

Table 5.2. Relative root mean square difference $\Delta_m$ of component $I$ between vector and scalar DART-lux for Cases B1 and B2 of the phase A of the IPRT project. Differences are for the whole viewing hemisphere and for three view azimuth angles.

| **Region** | **Case B1** | **Case B2** |
|---|---|---|
| Hemisphere | 2.72% | 4.11% |
| VAA = 0° | 3.54% | 5.38% |
| VAA = 45° | 2.83% | 4.19% |
| VAA = 90° | 1.89% | 2.98% |

## 5.5 Conclusions

Polarization is a major radiation characteristic. In addition to scalar intensity, information on linear and circular polarization improves the physical understanding of remote sensing observations, including their relationship with land surface parameters. This chapter adapted the theory and algorithm of atmosphere and land surface polarized radiative transfer modelling to DART-Lux. The DART-Lux atmosphere polarized radiative transfer modelling has been validated with six benchmark vector atmospheric radiative transfer models of the IPRT intercomparison project. The average vector DART-Lux relative difference is less than 0.2% with most IPRT benchmark results with few exceptions reaching 0.6%. The results of polarized radiative transfer modelling in land surfaces are under the preparation.

The error of scalar approximation was evaluated by comparing simulations of vector DART-Lux and scalar DART-Lux. The scalar approximation tends to underestimate backscattering and to overestimate forward scattering. This error is wavelength dependent. It generally decreases with the increase of wavelength since the scattering that gives rise to polarization decreases with the wavelength. For USSTD76 atmosphere, with oblique illumination at 60 °sun zenith angle and 30 °view zenith angle, the relative error of TOA reflectance spectra is ≈4.6% at ≈0.32 $\mu$m; it decreased down to 0.1% at 0.70 $\mu$m.

In short, the new vector radiative transfer modelling is more accurate than the scalar modelling. It improves DART capacity for better interpretation of remote sensing signals and preparation of polarimetric satellites.

## 5.Appendix A IPRT case B1: Rayleigh scattering

The case B1 of the phase A of IPRT considers a standard atmosphere with only Rayleigh scattering, *i.e.*, no absorption extinction. The depolarization factor (Eq. (5.11)) is set to 0.03. The atmosphere is modelled with 30 layers, each with 1 km thickness. Typical scattering optical depth at wavelength 0.450 $\mu$m is given for each layer. Ground albedo is zero to emphasize the atmosphere signal. The solar zenith and azimuth angles are $\theta_s$=60° and $\varphi_s$=0°, respectively. The viewing direction is set over the whole upper hemisphere at TOA level with zenith ($\theta_v \in [0°, 80°]$) and azimuth ($\varphi_v \in [0°, 360°]$) 5° steps.

The atmosphere vertical profiles and benchmark results of the six participant models (3DMCPOL, IPOL, MYSTIC, PSTAR, SHDOM and TROPOS) are publicly available at: https://www.meteo.physik.uni-muenchen.de/~iprt/doku.php?id=intercomparisons:b1_rayleigh. Below, we display the results for these models (Figure 5.A.1) and their difference with the recommended benchmark model MYSTIC (Figure 5.A.2).

3DMCPOL

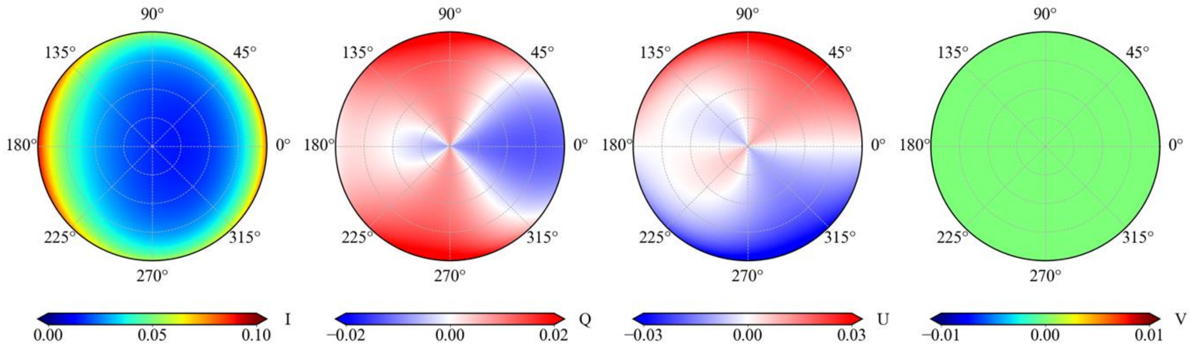

IPOL

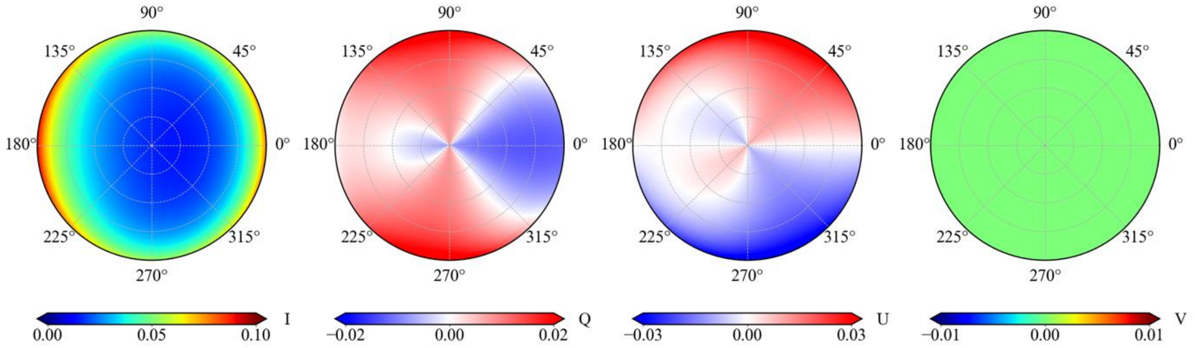

MYSTIC

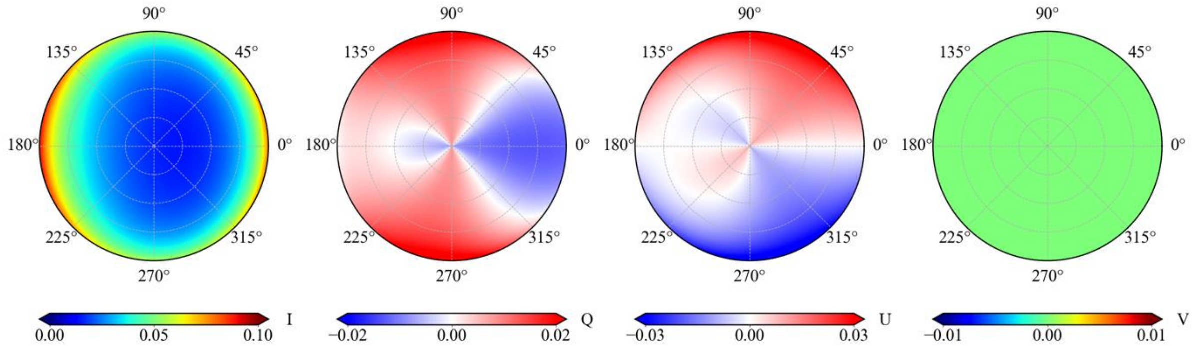

PSTAR

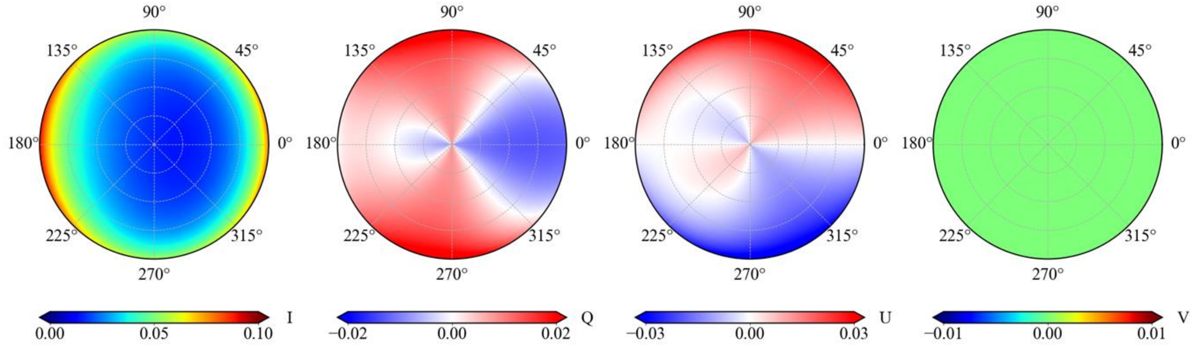

SHDOM

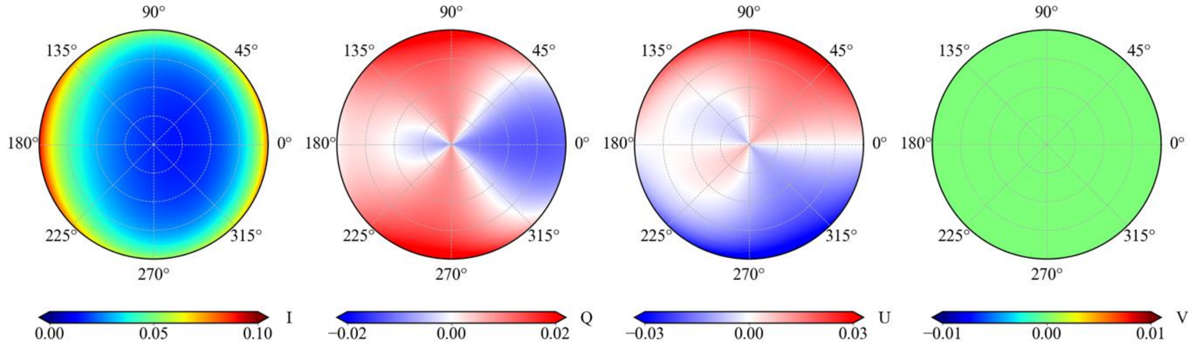

TROPOS

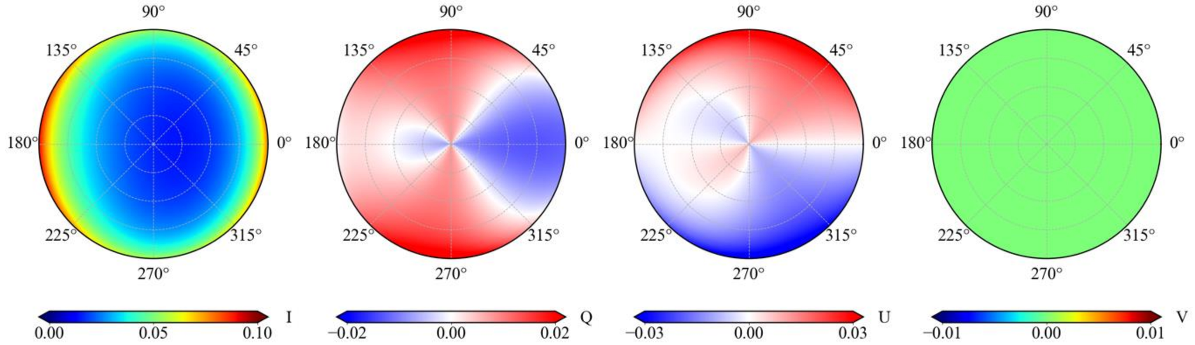

Figure 5.A.1. Polarized results (case B1) of six participants in the IPRT project. Stokes components $I$, $Q$, $U$, $V$ are marked.

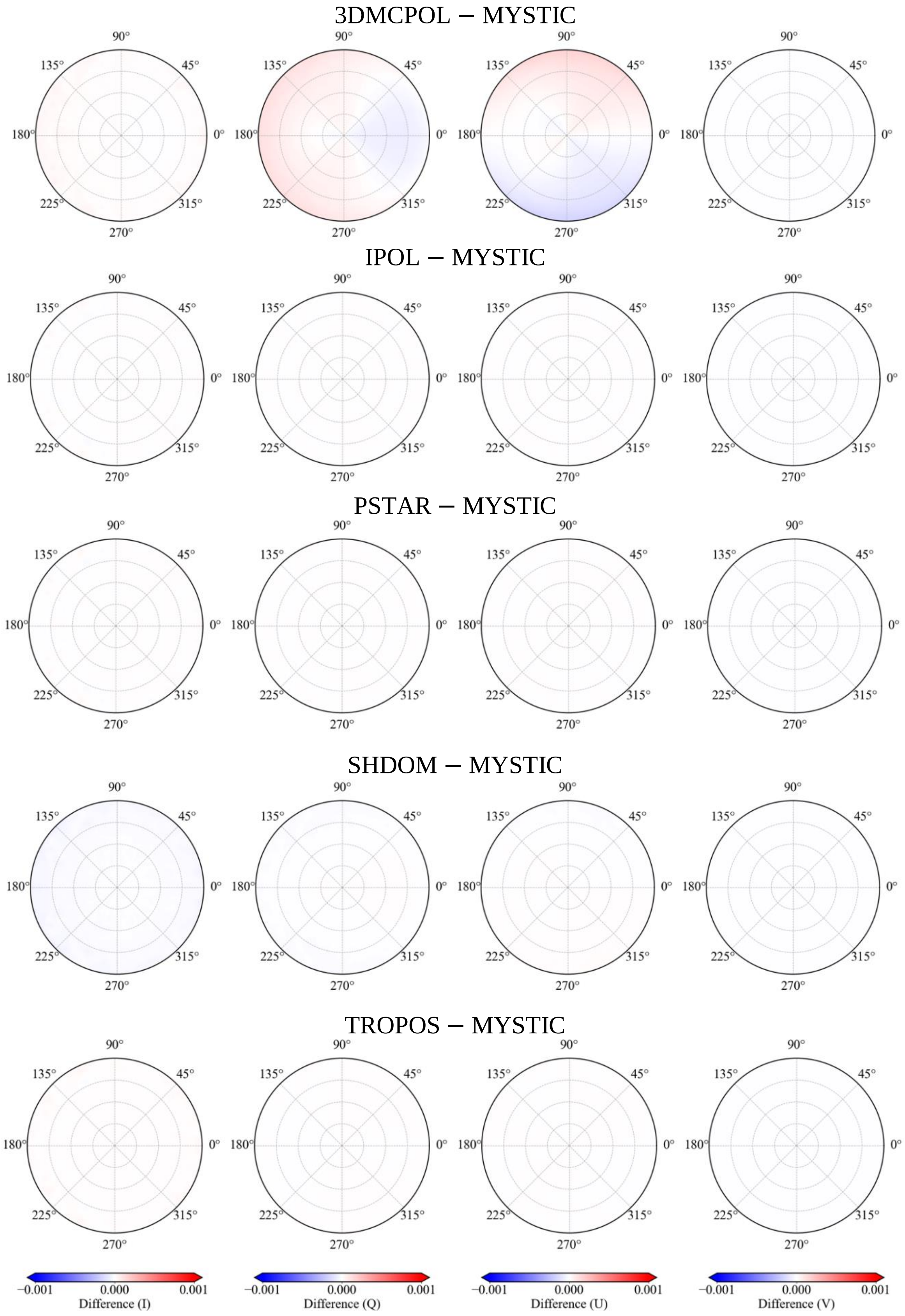

Figure 5.A.2. Difference between participant models (Figure 5.A.1) and the recommended benchmark model MYSTIC. Stokes components $I$, $Q$, $U$, $V$ are marked.

# 5.Appendix B IPRT case B2: Rayleigh scattering and molecular absorption

The case B2 of the phase A of IPRT considers a standard atmosphere with Rayleigh scattering and molecular absorption. The depolarization factor (Eq. (5.11)) is set to 0.03. The atmosphere is modelled with 30 layers, each with 1 km thickness. Typical scattering optical depth at wavelength 0.325 $\mu$m is given for each layer. Ground albedo is zero to emphasize the atmosphere signal. Solar zenith and azimuth angles are $\theta_s$=60° and $\varphi_s$=0°, respectively. Viewing directions are over the whole upper hemisphere at TOA level with zenith ($\theta_v \in [0°, 80°]$) and azimuth ($\varphi_v \in [0°, 360°]$) 5° steps.

The vertical profiles of the atmosphere and the benchmark results of the six participant models are publicly available through the link: https://www.meteo.physik.uni-muenchen.de/~iprt/doku.php?id=intercomparisons:b2_absorption. Below, we display the results for the six atmospheric radiative transfer models (Figure 5.B.1), namely 3DMCPOL, IPOL, MYSTIC, PSTAR, SHDOM and TROPOS and their difference with the recommended benchmark model MYSTIC (Figure 5.B.2).

3DMCPOL

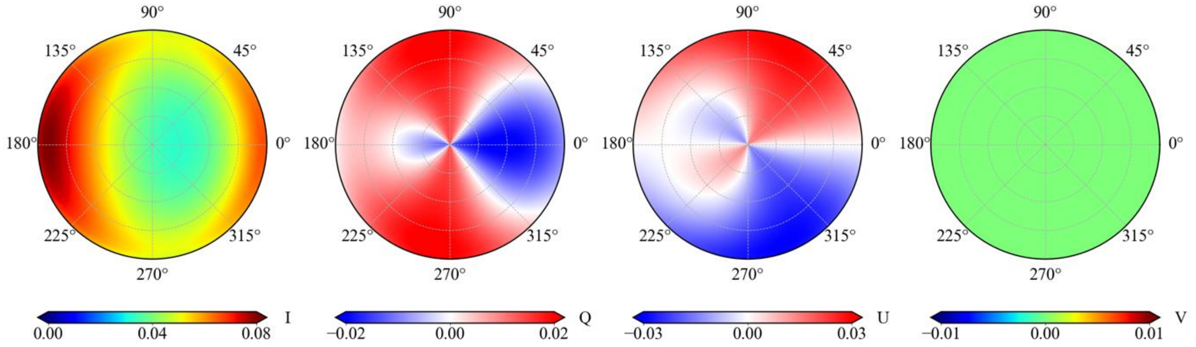

IPOL

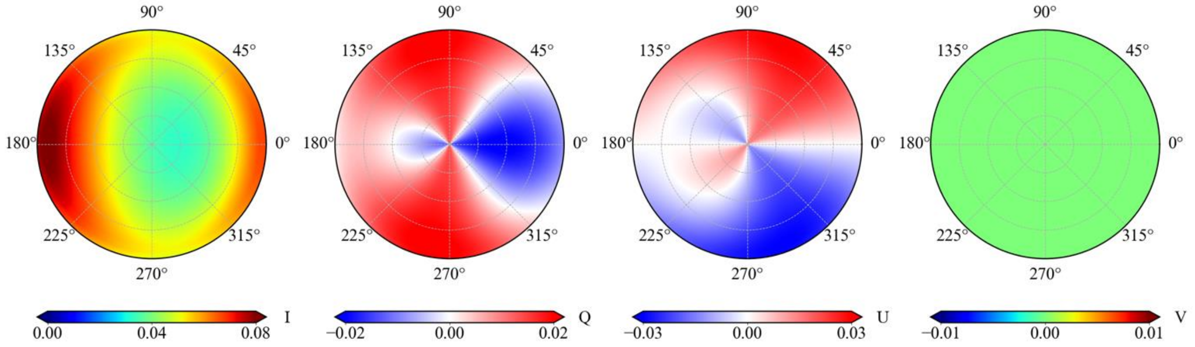

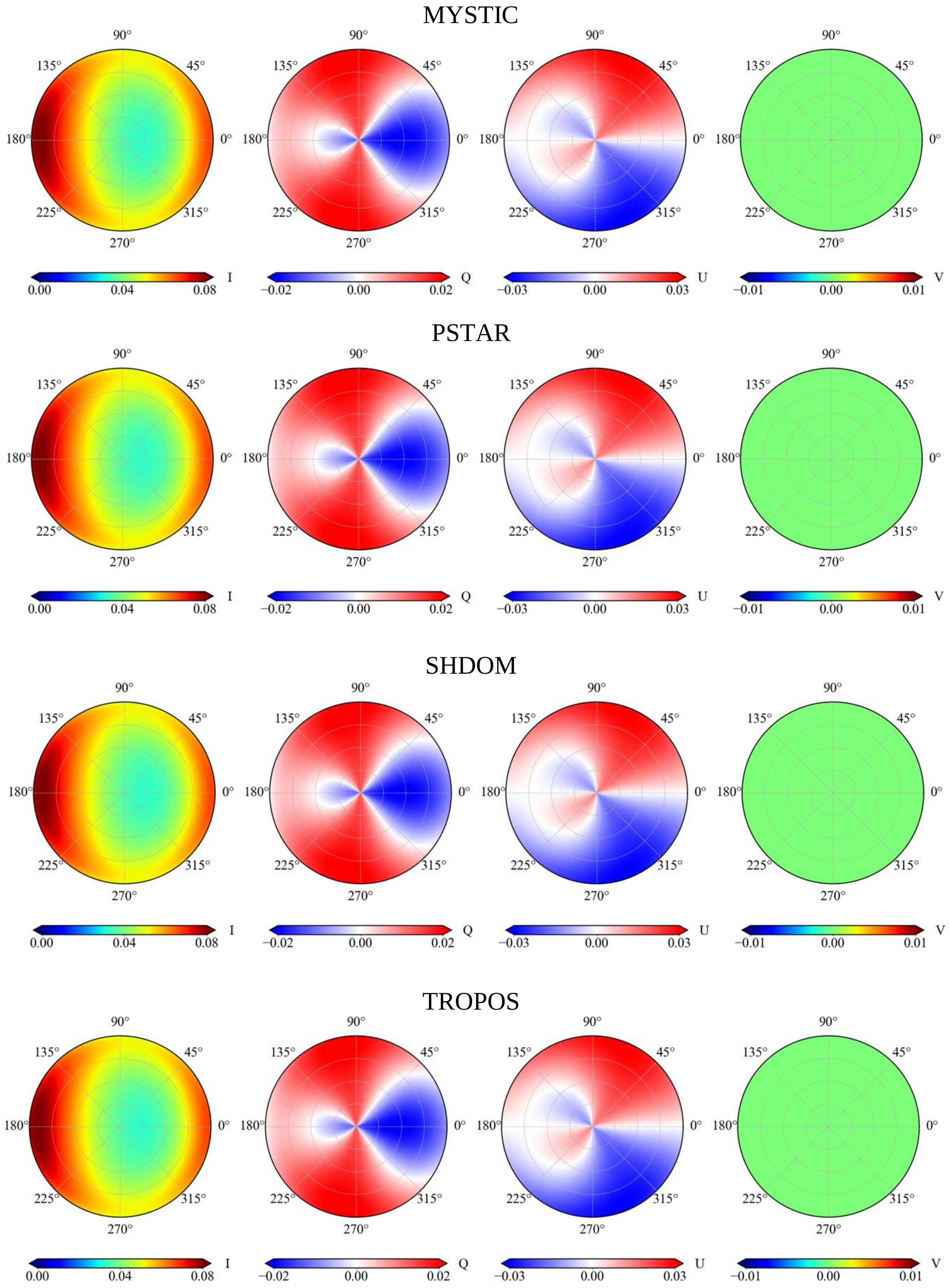

Figure 5.B.1. Polarized results (case B2) of six participant models in the IPRT project. Stokes components $I$, $Q$, $U$, $V$ are marked.

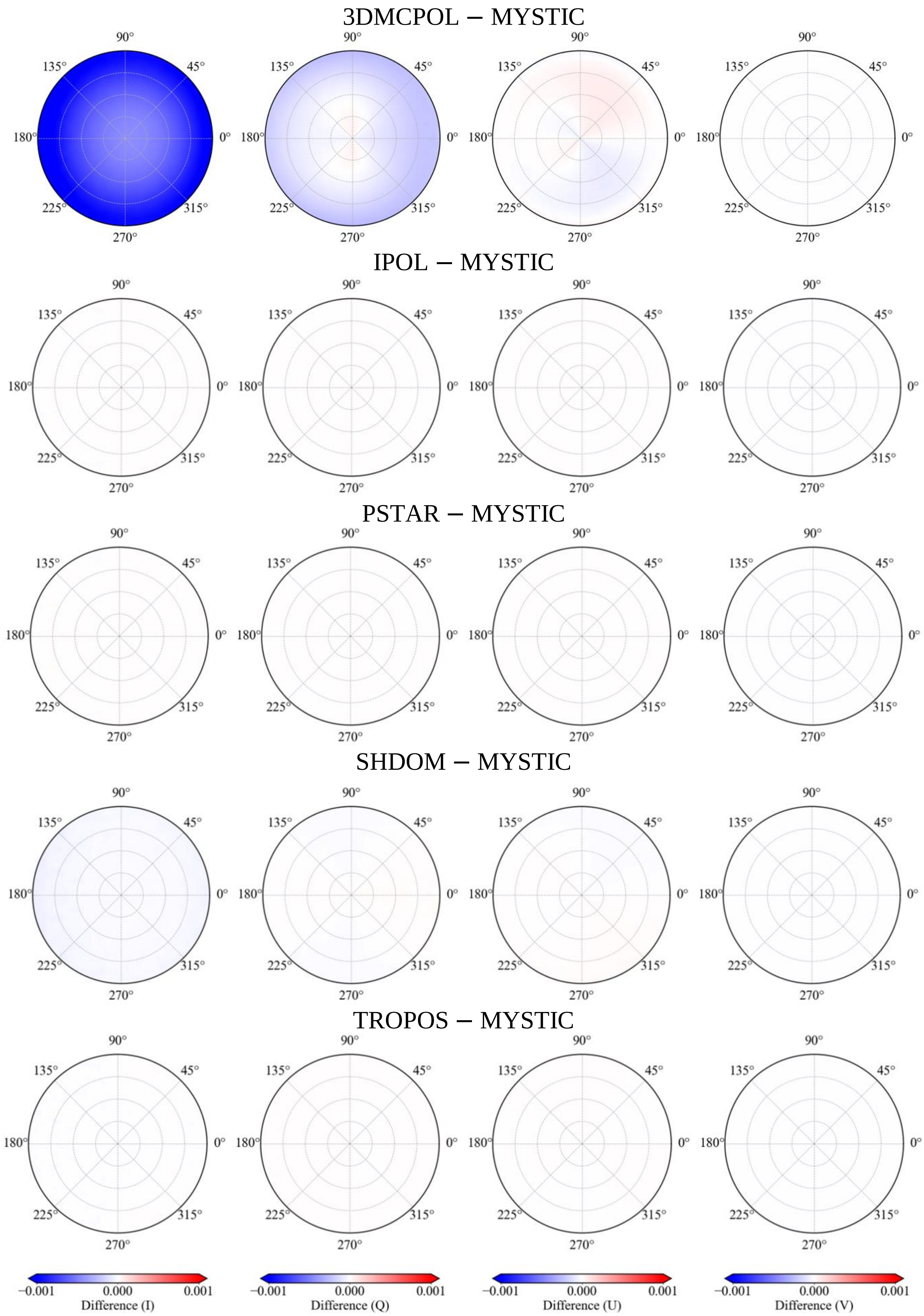

3DMCPOL − MYSTIC

IPOL − MYSTIC

PSTAR − MYSTIC

SHDOM − MYSTIC

TROPOS − MYSTIC

Figure 5.B.2. Difference between participant models (Figure 5.B.1) and the recommended benchmark model MYSTIC. Stokes components $I$, $Q$, $U$, $V$ are marked.

# Conclusions and perspectives

This dissertation is motivated by the need to better understand the functioning of land surfaces at different spatial and temporal scales. This knowledge is crucial in many fields, such as agriculture, urban and ecosystem dynamics, water, carbon and energy cycles, global change, *etc*. Land surface functioning is typically represented by a number of parameters (*e.g.*, temperature, biomass, photosynthesis efficiency, *etc*.) and some of them can be derived from remote sensing observations through some inversion techniques or based on the application of RTMs that simulate remote sensing observations and/or the radiative budget of the observed surfaces (*i.e.*, natural and urban landscapes). These RTMs also improve the understanding of some land surface processes. The increasing need of accurate information about land surfaces at different spatial and temporal scales combined with the continuous advances of remote sensing instruments boost the improvement of accuracy in the simulation of remote sensing observations. So far, two types of improvements are particularly needed: (1) more accurate radiative transfer modelling with better computer efficiency (*i.e.*, computer time and memory) in particular for large-scale studies (*i.e.*, large-scale landscapes); (2) more realistic 3D representation of land surfaces, accounting for their 3D complexity and the different spatial scales.

The design (*i.e.*, the discrete ordinates method) of the initial version of DART (*i.e.*, DART-FT) is not able to adapt the required improvements. On the other hand, in the last decades, scientists have greatly accelerated the radiation transfer modelling in complex 3D environment, with consideration of complex radiation mechanisms such as anisotropic scattering. The improvements in the display of the realistic artificial world in video games illustrates this progress. Considering this progress, in collaboration with DART team, I have developed in DART a new vector Monte Carlo radiative transfer mode, called DART-Lux, which has adapted the latest advances in computer graphics. The adapted approach transforms the radiative transfer problem as a multi-dimensional path integral problem and solves it based on the bidirectional path tracing algorithm. To estimate this integral, it generates a group of stochastic paths that connect the light sources and the sensor and combines them with the multiple importance sampling. The originality is that each path is generated by connecting two sub-paths, one starting from the light sources and another one starting from the sensor. Each path of length $n$ (*i.e.*, path with $n$ edges) can be generated in at most $n + 2$ ways, with each way having specific advantages and disadvantages depending on the experimental and instrumental configurations. A robust and efficient 3D radiative transfer modelling for a wide variety of scenarios is then realized by weighting and summing the contribution of all possible paths that are generated in different ways.

In addition to describing the theoretical formalism, this manuscript also details the implementation of a variety of useful light sources (*e.g.*, sun, sky), sensors (*e.g.*, perspective camera, orthographic camera, BRF camera) and BSDF models (*e.g.*, Lambertian, RPV, specular, mix). It presents how to sample the path vertices and to generate stochastic path samples based on the importance sampling principles. Furthermore, it demonstrates how to evaluate the final measurements incrementally without any redundant computations.

The preliminary implementation of DART-Lux was evaluated through the cross comparison with DART-FT. Three land surfaces were considered, the schematic scene was created by DART itself, the actual urban scene was provided by the Toulouse townhall, and the actual forest scene was derived from RAMI. DART-Lux and DART-FT have very good agreements for the three land surfaces with reflectance difference less than 1% in relative. The great interest of DART-Lux is that it is in general at least hundredfold times faster and much less costly in memory allocation. Indeed, DART-Lux only tracks the light paths that contribute to observations whereas DART-FT tracks all possible paths starting from the light sources until they are absorbed or exit the scene. In addition, DART-Lux uses a cloning method that largely reduces the memory allocation if the scene contains a lot of elements (*e.g.*, tree) that are similar by shifting and/or rotation. In this case, only one 3D element per “type” of tree is stored in memory. In contrast, DART-FT straightforwardly loads all elements of the scene into memory. Because of its Monte Carlo algorithm, DART-Lux converges with the increase of number of samples. A sensitivity study showed that image mean values converge much faster than pixel values, and that the convergence is all the faster if the scene elements have low reflectance values.

In a next step, the path integral problem for both surfaces and volumes are unified. It shows the probability to generalize the theory and algorithm of DART-Lux for land surfaces with atmosphere or any other media (*e.g.*, turbid vegetation, fluids). Then, I designed a quasi-finite Earth-Atmosphere system (default dimension: X × Y × Z = 500 × 500 × 50 km) with the target scene in its bottom centre. It allows one to model the adjacency effect due to the neighbouring surface of the studied scene, homogeneous or not, and the atmosphere. Then, I described how to compute the continuous atmospheric profiles and the atmospheric optical properties, how to characterize the scattering distribution of atmospheric constituents, how to sample a free path and a scattering direction in presence of medium as well as how to generate stochastic paths and to evaluate their contribution efficiently. The accuracy of the atmospheric radiative transfer modelling was evaluated by the reference model MODTRAN. For the standard USSTD76 atmosphere, the difference of TOA directional reflectance spectra from 0.32 to 2.5 $\mu$m between DART-Lux and MODTRAN is less than 1% in relative. Based on this new modelling, I studied the impact of the adjacency effect on observations at four Sentinel-2A bands, which is of relevance to the calibration of remote sensing images. Results show that we can quantify how the adjacency perturbation increases with the increase of (1) the albedo of the surrounding surface, (2) the atmosphere scattering for example the more or less large optical depth of gases and aerosols and (3) the sensor altitude. The impact of the 3D structure of the surrounding landscape and the atmospheric absorption is less important but is still not negligible.

The Monte Carlo radiative transfer modelling in the plane parallel atmosphere is very accurate since nearly no approximation is required, but it is usually long compared to the discrete ordinates radiative transfer mode. In configurations where the adjacency effect is not so important or the studied landscape is spatially homogeneous, I designed a hybrid method that efficiently couples the atmospheric radiative transfer of DART-FT (*i.e.*, discrete ordinates in the atmosphere) and the Monte Carlo radiative transfer in the land surface. This method is very fast for simulating satellite and airborne observations. It simulates satellite images very close to these simulated by DART-FT with difference below 1% in relative. Its accuracy in the thermal infrared region was assessed by MODTRAN using realistic atmospheric profiles provided by the European Centre for Medium-Range Weather Forecasts (ECMWF). The average difference between the hybrid method and MODTRAN is less than 1 K in the region from 3.5 to 20 $\mu$m, with differences usually less than 0.2 K for major thermal bands in satellite missions such as Landsat 8, Sentinel-3, and TRISHNA.

Finally, I introduced the modelling of polarization in the atmosphere based on the characterization of the polarized light by Stokes vector and the adaptation of the bidirectional path tracing formalism. The surface and volume scattering are characterized by the scattering matrix that are derived from Maxwell's equations. This new modelling was assessed by the benchmark results in the frame of IPRT intercomparison initiative. For standard USSTD76 atmosphere, DART-Lux simulates accurate TOA directional Stokes vector components with difference commonly below 0.2% in relative compared to benchmark results, with only a few exceptional differences up to 0.6%. I also investigated the impact of polarization on the radiance intensity. Results show that the scalar approximation tends to underestimate the backscattering and overestimate the forward scattering. Also, this error is wavelength dependent. It generally decreases with the increase of wavelength since the scattering that gives rise to polarization decreases with the wavelength.

DART-Lux greatly enhances the DART capability for studying the land surface functioning and for preparing Earth observation satellite missions. It can accurately simulate polarimetric remote sensing observations of kilometre-scale complex land surfaces coupled with plane-parallel atmosphere. Also, it well simulates the anisotropic scattering (*e.g.*, specular reflection, aerosol peak forward scattering) and the thermal emission (*e.g.*, atmospheric heterogeneous emission, thermal infrared hot-spot). DART-Lux has already been successfully used in scientific studies about vegetation functioning (*e.g.*, forest and crop photosynthesis and SIF emission), urban studies (*e.g.*, inversion of satellite images), the cross comparison and benchmark of RTMs (*e.g.*, RAMI-V[2]), and the preparation of satellite missions (*e.g.*, CNES and ISRO TRISHNA satellite mission, ESA next generation Sentinel-2 and LSTM satellite missions, NASA CHANGE mission).

---

[2] I managed the participation of CESBIO (France), NASA GSFC (USA) and CAS (China) in RAMI-V. The proposed measurements of abstract and actual canopies were all simulated. This work is not presented in this manuscript.

Despite its versatility, DART-Lux should be further improved in several directions:

- Jacobian matrices. These matrices store the derivative of the observed radiation with respect to scene parameters (*e.g.*, reflectance, transmittance, temperature, illumination direction). They are very useful for sensitivity studies, and for retrieving land surface parameters from space. The differentiable radiative transfer modelling can compute them relying on the formalism presented in Chapter 3. Indeed, instead of estimating the path integral, DART-Lux estimates the derivative of the path integral with respect to scene parameters while using the same path samples and probability densities.

- Integrating the measured and modelled directional distribution of reflectance factor: current directional scattering distributions of surface and volume implemented in DART-Lux are mostly derived from geometric optics, electromagnetic theory, and empirical analysis. Sometimes, they cannot reproduce the scattering patterns of certain media or surfaces. Besides, there are available scalar and polarimetric measurements of directional distributions from laboratory or field experiments. Several microscale RTMs, such as those that model the leaf optical properties as a function of its cellular structure, are also able to simulate particle and surface scattering distribution function and even the scattering matrix.

- Extending vector radiative transfer modelling at land surfaces: the specular surfaces, such as the water, architecture windows, leaf surface waxes, *etc*., can produce strong polarization signature, either from scattering or from emission. Knowing that the consideration of polarization in the interaction mechanisms alters the radiation intensity and brings more information about the target. It is thus important to extend current vector radiative transfer modelling to land surfaces.

- Optimizing the radiative budget modelling: the DART-Lux modelling is very optimal to simulate remote sensing observations. However, it is less efficient to simulate the radiative budget, because the adapted approach relies only on the bidirectional path tracing. It treats all surface elements for which the radiative budget needs to be computed as a sensor and this computation is even more intensive than DART-FT. It is thus necessary to design a new modelling that avoids generating redundant light paths. It will allow one to couple DART radiative budget with models that simulate land surface energy and gas fluxes, such as the DART-EB model (Belot, 2007) that is presently being redesigned in CESBIO (Nguyen, 2022[3]), the global land surface model ORCHIDEE (https://orchidee.ipsl.fr) and the urban surface model SOLENE (https://aau.archi.fr/crenau/solene).

---

[3] Nguyen Thang, 2022, Development of a 3D energy budget model inspired by SCOPE model. CESBIO. Internal report is in preparation.

# Conclusions et perspectives

Cette thèse est motivée par la nécessité de mieux comprendre le fonctionnement des surfaces terrestres à différentes échelles spatiales et temporelles. Ces connaissances sont cruciales dans de nombreux domaines, comme l’agriculture, la dynamique urbaine et des écosystèmes, les cycles de l’eau, du carbone et de l’énergie, le changement global, *etc*. Le fonctionnement des surfaces terrestres est en général représenté par des paramètres de surface (*e.g.*, température, biomasse, efficacité de la photosynthèse) dont certains peuvent être dérivés de mesures de télédétection via des techniques d'inversion ou d'assimilation basées sur l'emploi de MTRs qui simulent les mesures de télédétection et/ou le bilan radiatif des surfaces observées (*i.e.*, paysages naturels et urbains). De plus, ces MTRs permettent d'améliorer la compréhension physique de certains processus des surfaces terrestres. Le besoin urgent de paramètres de surface de plus en plus précis à différentes échelles spatiales et temporelles, combiné au progrès continu des instruments de télédétection, nécessite d'améliorer la précision des simulations des mesures de télédétection. A ce jour, deux types d’améliorations sont en particulier nécessaires : (1) modélisation plus précise des MTRs, avec une meilleure efficacité informatique (*i.e.*, temps de calcul et volume mémoire) en particulier pour les études à grande échelle (*i.e.*, grands paysages); (2) représentation plus réaliste des surfaces terrestres avec prise en compte de leur complexité 3D, avec une adaptation aux différentes échelles spatiales d'analyse.

Le concept de base (*i.e.*, méthode des ordonnées discrètes), de la version initiale de DART (*i.e.*, DART-FT) ne permet pas d'apporter les améliorations requises. Par contre, durant ces dernières décennies, les scientifiques ont beaucoup accéléré la modélisation du transfert radiatif dans les environnements 3D complexe, avec prise en compte de mécanismes radiatifs complexes comme la diffusion anisotrope. L'amélioration des jeux vidéos illustre les progrès réalisés. Compte tenu de ces progrès, en collaboration avec l'équipe DART, j'ai donc développé dans DART un nouveau mode Monte Carlo de transfert radiatif vectoriel, appelé DART-Lux. L’approche adoptée transforme le problème du transfert radiatif en un problème d’intégrale multidimensionnelle et le résout avec une approche basée sur l'algorithme de tracé de rayons bidirectionnel. Pour estimer cette intégrale, DART-Lux génère un groupe de trajets de rayon stochastiques entre les sources de lumière et le capteur et les combine avec l'échantillonnage préférentiel multiple. Une originalité est que chaque trajet de rayon est généré en reliant deux sous-trajets, l'un partant de la source ou des sources de lumière et l'autre partant du capteur. Tout trajet de longueur $n$ (*i.e.*, chemin avec $n$ arêtes) peut être généré d'au plus $n + 2$ façons, chacune ayant des avantages et inconvénients spécifiques selon les configurations expérimentales et instrumentales d'observation. Une modélisation du transfert radiatif 3D à la fois robuste et efficace pour une grande variété de scénarios est obtenue en pondérant et additionnant la contribution de tous les trajets possibles générés de manières différentes.

En plus de décrire le formalisme théorique de DART-Lux, ce manuscrit détaille sa mise en œuvre avec différentes configurations de sources lumière (*e.g.*, soleil, ciel), de capteurs (*e.g.*, caméra perspective, caméra orthographique, caméra BRF) et de modèles BSDF (*e.g.*, Lambertian, RPV, spéculaire, mixte). Il présente aussi la manière d'échantillonner les sommets de trajet et de générer des échantillons de trajet stochastiques basés sur les principes d'échantillonnage préférentiel. De plus, l'approche adoptée pour évaluer les mesures finales de manière incrémentielle sans aucun calcul redondant est aussi présentée.

La mise en œuvre préliminaire de DART-Lux a été évaluée par comparaison avec DART-FT. Trois types de surfaces terrestres ont été considérés : scène schématique créée par DART, scène urbaine réelle fournie par la mairie de Toulouse et scène forestière issue de RAMI. Les simulations DART-Lux et DART-FT des trois surfaces concordent très bien avec une différence relative de réflectance inférieure à 1 %. Le grand intérêt de DART-Lux est qu'il est en général au moins cent fois plus rapide et beaucoup moins coûteux en allocation mémoire. En effet, il ne suit que les trajets de rayon qui contribuent aux observations alors que DART-FT suit tous les trajets de rayon possibles à partir des sources de lumière jusqu'à ce qu'elles soient absorbées ou sortent de la scène étudiée. De plus, DART-Lux utilise une méthode de clonage qui réduit énormément le volume mémoire requis si le paysage simulé comprend beaucoup d'éléments (*e.g.*, arbre) similaires à une homothétie et/ou rotation xyz près. Dans ce cas, un seul élément 3D par "type" d'arbre est stocké en mémoire. Par contre, DART-FT charge tous les éléments de la scène en mémoire. En raison de son algorithme Monte Carlo, DART-

Lux converge avec l'augmentation du nombre d'échantillons. Une étude de sensibilité a montré que les valeurs moyennes des images convergent beaucoup plus vite que les valeurs des pixels, et que la convergence est d'autant plus rapide que les réflectances des éléments de la scène sont faibles.

Dans une étape suivante, la gestion du problème de l'intégrale pour les surfaces et les volumes a été unifiée. Cela montre la possibilité de généraliser la théorie et l'algorithme de DART-Lux aux surfaces terrestres avec atmosphère et tout autre milieu (*e.g.*, végétation turbide, fluide). J'ai ensuite créé un système Terre-Atmosphère quasi-infini (dimension par défaut : X × Y × Z = 500 × 500 × 50 km) où le paysage terrestre étudié se trouve au bas au centre. Il permet de modéliser l'effet d'adjacence dû au voisinage du paysage étudié, spatialement homogène ou non, en présence d'atmosphère. J'ai décrit comment calculer les profils atmosphériques continus et les propriétés optiques atmosphériques, comment caractériser la distribution de diffusion des constituants atmosphériques, comment échantillonner un parcours libre et une direction de diffusion en présence de milieu et aussi comment générer des trajets stochastiques et évaluer efficacement leur contribution. La précision de la modélisation du transfert radiatif atmosphérique a été évaluée avec le modèle de référence MODTRAN. Pour un modèle standard de l'atmosphère USSTD76, la différence relative des spectres de réflectance directionnelle TOA de 0.32 à 2.5 $\mu$m entre DART-Lux et MODTRAN est inférieure à 1%. Cette nouvelle modélisation m'a permis d'étudier l'impact de l'effet d'adjacence sur les observations de quatre bandes du satellite Sentinel-2A, ce qui est utile pour l'étalonnage des images de télédétection. Les résultats montrent que nous pouvons quantifier comment l'effet d'adjacence augmente avec l'augmentation de (1) l'albédo de la surface autour de la surface étudiée, (2) la diffusion de l'atmosphère par exemple du fait de la plus ou moins grande épaisseur optique des gaz et aérosols, et (3) l'altitude du capteur. L'impact de la structure 3D du paysage étudié et l'absorption atmosphérique est moindre, mais peut jouer un rôle non négligeable.

La modélisation Monte Carlo du transfert radiatif dans l'atmosphère plane parallèle est très précise, car elle ne requiert quasiment pas d'approximation. Par contre, elle requiert de plus grands, voire beaucoup plus grands, temps de calcul que la méthode des ordonnées discrètes. Dans des configurations où l'effet d'adjacence n'est pas trop important ou que le paysage étudié est spatialement homogène, j'ai conçu une méthode hybride qui couple efficacement le transfert radiatif atmosphérique de DART-FT (*i.e.*, ordonnées discrètes dans l'atmosphère) et le transfert radiatif Monte Carlo dans les surfaces terrestres. Cette méthode est très rapide pour simuler des observations satellitaires et aéroportées. Elle donne des images satellites très proches de celles simulées avec DART-FT avec une différence relative inférieure à 1%. Sa précision dans la région de l'infrarouge thermique a été évaluée avec MODTRAN et des profils atmosphériques fournis par le Centre Météorologique Européen ECMWF. La différence moyenne entre la méthode hybride et MODTRAN est inférieure à 1 K dans la région de 3.5 à 20 $\mu$m, avec des différences généralement inférieures à 0.2 K pour les bandes thermiques des missions satellitaires telles que Landsat 8, Sentinel-3 et TRISHNA.

J'ai introduit de la modélisation de la polarisation dans l'atmosphère à partir de la représentation du rayonnement polarisé par le vecteur de Stokes et en l'adaptant au formalisme du suivi de rayon bidirectionnel. Les surfaces et l'atmosphère sont caractérisées par une matrice de diffusion dérivée des équations de Maxwell. Cette modélisation a été évaluée à partir de simulations de modèles de référence réalisées dans le cadre de l'initiative d'intercomparaison IPRT. Avec le modèle standard d'atmosphère USSTD76, DART-Lux simule avec précision les composantes vectorielles Stokes directionnelles TOA : différence relative en général inférieure à 0.2 % par rapport aux simulations de référence, avec de manière exceptionnelle quelques différences jusqu'à 0.6 %. J'ai également étudié l'impact de la polarisation sur l'intensité de rayonnement. Les résultats montrent que l'approximation scalaire a tendance à sous-estimer la diffusion vers l'arrière et à surestimer la diffusion vers l'avant. De plus, cette erreur dépend de la longueur d'onde. Elle diminue généralement avec l'augmentation de la longueur d'onde, car la diffusion qui donne lieu à la polarisation diminue avec la longueur d'onde.

DART-Lux renforce considérablement la capacité du DART à étudier le fonctionnement des surfaces terrestres et à préparer des missions satellites d'observation de la Terre. Il permet de simuler avec précision des observations de télédétection polarimétrique de surfaces terrestres complexes à l'échelle kilométrique couplées à une atmosphère plane parallèle. En outre, il simule bien la diffusion anisotrope (*e.g.*, réflexion spéculaire et diffusion vers l'avant des aérosols) et l'émission thermique (*e.g.*, émission hétérogène atmosphérique et hot spot infrarouge thermique). DART-Lux a déjà été utilisé avec succès dans des études scientifiques sur le fonctionnement de la végétation (*e.g.*, photosynthèse et émission SIF des forêts et cultures), les études urbaines (*e.g.*, inversion d'images satellites), la comparaison croisée et le benchmark des MTRs (*e.g.*, RAMI-V[4]), et la préparation de missions satellitaires (*e.g.*, mission TRISHNA de CNES et ISRO, LSTM et nouvelle génération des satellites Sentinel-2 de l'ESA, et mission CHANGE de la NASA).

Malgré sa polyvalence, DART-Lux doit encore être amélioré dans plusieurs directions :

- Matrices Jacobiennes. Ces matrices stockent la dérivée des luminances des couverts par rapport aux paramètres de la scène (*e.g.*, réflectance, transmittance, température et direction solaire). Elles seront très utiles pour les études de sensibilité et pour récupérer des paramètres des surfaces terrestres depuis l'espace. La modélisation différentiable du transfert radiatif doit permettre de les calculer à partir du formalisme présenté au chapitre 3. Ainsi, en plus d'estimer une intégrale, DART-Lux pourrait estimer la dérivée de l'intégrale par rapport aux paramètres de la scène en utilisant les mêmes échantillons de trajet et densités de probabilité.

- Intégration de distribution directionnelle de facteurs de réflectance mesurés ou issus de modèles : les distributions directionnelles de surfaces et volumes (e.g., modèles lambertiens, RPV, Hapke, etc.) actuelles de DART-Lux sont surtout dérivées de l'optique géométrique, de la théorie électromagnétique et de l'analyse empirique. Cependant, elles ne peuvent pas reproduire les motifs de diffusion de certains milieux ou surfaces. En outre, il existe des mesures scalaires et polarimétriques directionnelles de terrain ou en laboratoire. De plus, les MTRs à micro-échelle qui modélisent les propriétés optiques foliaires en fonction de leur structure cellulaire simulent la fonction de distribution de diffusion des particules et de la surface et même la matrice de diffusion.

- Extension de la modélisation du transfert radiatif vectoriel aux surfaces terrestres : les surfaces spéculaires, telles que l'eau, les fenêtres d'architecture, les cires de surface des feuilles, *etc.*, peuvent produire un fort signal de polarisation par diffusion ou par émission. Vu que la prise en compte de la polarisation dans les mécanismes d'interaction modifie

---

[4] J'ai géré la participation de CESBIO (France), NASA GSFC (USA) et CAS (Chine) à RAMI-V. Les mesures proposées des canopée abstraits et réels ont toutes été simulées. Ce travail n'est pas présenté dans ce manuscrit.

l’intensité du rayonnement et apporte donc des informations sur la cible, il est important d’étendre la modélisation actuelle du transfert radiatifs vectoriel aux surfaces terrestres.

- Optimisation de la modélisation du bilan radiatif : DART-Lux est très efficace pour simuler les observations de télédétection. Cependant, il est beaucoup moins efficace pour simuler le bilan radiatif, car l'approche adoptée ne peut s'appuyer sur le suivi de rayons bidirectionnel. Elle traite tout élément de surface dont l'on veut calculer le bilan radiatif comme un capteur, avec des temps de calcul supérieurs à ceux de DART-FT. Il est prévu de concevoir une nouvelle modélisation qui évite de dupliquer les calculs de trajets de rayons. Elle permettra de coupler DART-Lux avec des modèles de simulation des flux d’énergie et de gaz des surfaces terrestres, comme le modèle DART-EB (Belot, 2007) en cours de développement au CESBIO (Nguyen, 2022[5]), le modèle de surface urbaine SOLENE (https://aau.archi.fr/crenau/solene) et le modèle global de surface terrestre ORCHIDEE (https://orchidee.ipsl.fr).

---

[5] Nguyen Thang, 2022, Développement d'un modèle de bilan d'énergie 3D inspiré du modèle SCOPE. CESBIO. Rapport interne en préparation.

# Bibliography

Abdelmoula, H., Kallel, A., Roujean, J.-L., Gastellu-Etchegorry, J.-P., 2021. Dynamic retrieval of olive tree properties using Bayesian model and Sentinel-2 images. IEEE J. Sel. Top. Appl. Earth Obs. Remote Sens. 14, 9267–9286.

Abramowitz, M., Stegun, I.A., 1948. Handbook of mathematical functions with formulas, graphs, and mathematical tables. US Government printing office.

Adams, C.N., Kattawar, G.W., 1993. Effect of volume-scattering function on the errors induced when polarization is neglected in radiance calculations in an atmosphere–ocean system. Appl. Opt. 32, 4610–4617.

Amanatides, J., Woo, A., 1987. A fast voxel traversal algorithm for ray tracing., in: Eurographics. pp. 3–10.

Anderson, G.P., Clough, S.A., Kneizys, F.X., Chetwynd, J.H., Shettle, E.P., 1986. AFGL atmospheric constituent profiles (0.120 km). AIR FORCE GEOPHYSICS LAB HANSCOM AFB MA.

Bablet, A., Vu, P.V.H., Jacquemoud, S., Viallefont-Robinet, F., Fabre, S., Briottet, X., Sadeghi, M., Whiting, M.L., Baret, F., Tian, J., 2018. MARMIT: A multilayer radiative transfer model of soil reflectance to estimate surface soil moisture content in the solar domain (400–2500 nm). Remote Sens. Environ. 217, 1–17.

Bates, D.R., 1984. Rayleigh scattering by air. Planet. Space Sci. 32, 785–790.

Beckmann, P., Spizzichino, A., 1987. The scattering of electromagnetic waves from rough surfaces. Norwood.

Belot, A., 2007. Simulation des échanges d’énergie et de masse d’un couvert végétal: Développement et validation d’un modèle quasi 3D, DART-EB.

Berk, A., Anderson, G.P., Acharya, P.K., Bernstein, L.S., Muratov, L., Lee, J., Fox, M., Adler-Golden, S.M., Chetwynd, J.H., Hoke, M.L., 2005. MODTRAN 5: a reformulated atmospheric band model with auxiliary species and practical multiple scattering options: update, in: Algorithms and Technologies for Multispectral, Hyperspectral, and

Ultraspectral Imagery XI. International Society for Optics and Photonics, pp. 662–667.

Berk, A., Anderson, G.P., Acharya, P.K., Shettle, E.P., 2008. MODTRAN5. 2.0. 0 user's manual. Spectr. Sci. Inc., Burlingt. MA, Air Force Res. Lab. Hanscom MA.

Berk, A., Bernstein, L.S., Robertson, D.C., 1987. MODTRAN: A moderate resolution model for LOWTRAN. SPECTRAL SCIENCES INC BURLINGTON MA.

Bodhaine, B.A., Wood, N.B., Dutton, E.G., Slusser, J.R., 1999. On Rayleigh optical depth calculations. J. Atmos. Ocean. Technol. 16, 1854–1861.

Borel, C.C., Gerstl, S.A.W., 1992. Adjacency-blurring effect of scenes modeled by the radiosity method, in: Atmospheric Propagation and Remote Sensing. International Society for Optics and Photonics, pp. 620–624.

Boucher, O., 1998. On aerosol direct shortwave forcing and the Henyey–Greenstein phase function. J. Atmos. Sci. 55, 128–134.

Brown, S.D., Schott, J.R., 2010. Verification and validation studies of the DIRSIG data simulation model. Rochester Inst. Technol. Rochester, NY, USA, Tech. Rep 1.

Bucholtz, A., 1995. Rayleigh-scattering calculations for the terrestrial atmosphere. Appl. Opt. 34, 2765–2773.

Bulgarelli, B., Zibordi, G., 2018. On the detectability of adjacency effects in ocean color remote sensing of mid-latitude coastal environments by SeaWiFS, MODIS-A, MERIS, OLCI, OLI and MSI. Remote Sens. Environ. 209, 423–438.

Chandrasekhar, S., 1960. Radiative Transfer. Courier Corporation.

Christensen, P.H., Salesin, D.H., DeRose, T.D., Aupperle, L., 1993. A continuous adjoint formulation for radiance transport, in: Proceedings of the Fourth Eurographics Workshop on Rendering. Citeseer, pp. 95–104.

Collett, E., 1992. Polarized light. Fundamentals and applications. Opt. Eng.

Collett, E., 1971. Mueller-Stokes matrix formulation of Fresnel's equations. Am. J. Phys. 39, 517–528.

Dave, J. V, 1980. Effect of atmospheric conditions on remote sensing of a surface nonhomogeneity. Photogramm. Eng. Remote Sensing 46, 1173–1180.

Diner, D.J., Boland, S.W., Brauer, M., Bruegge, C., Burke, K.A., Chipman, R., Di Girolamo, L., Garay, M.J., Hasheminassab, S., Hyer, E., 2018. Advances in multiangle satellite remote sensing of speciated airborne particulate matter and association with adverse health effects: from MISR to MAIA. J. Appl. Remote Sens. 12, 42603.

Disney, M.I., Lewis, P., North, P.R.J., 2000. Monte Carlo ray tracing in optical canopy reflectance modelling. Remote Sens. Rev. 18, 163–196.

Dupiau, A., Jacquemoud, S., Briottet, X., Fabre, S., Viallefont-Robinet, F., Philpot, W., Di Biagio, C., Hébert, M., Formenti, P., 2022. MARMIT-2: An improved version of the MARMIT model to predict soil reflectance as a function of surface water content in the solar domain. Remote Sens. Environ. 272, 112951.

Emde, C., Barlakas, V., Cornet, C., Evans, F., Korkin, S., Ota, Y., Labonnote, L.C., Lyapustin, A., Macke, A., Mayer, B., 2015. IPRT polarized radiative transfer model intercomparison project–Phase A. J. Quant. Spectrosc. Radiat. Transf. 164, 8–36.

Farin, G., 2014. Curves and surfaces for computer-aided geometric design: a practical guide. Elsevier.

Feng, L., Hu, C., 2017. Land adjacency effects on MODIS Aqua top-of-atmosphere radiance in the shortwave infrared: Statistical assessment and correction. J. Geophys. Res. Ocean. 122, 4802–4818.

Féret, J.-B., Gitelson, A.A., Noble, S.D., Jacquemoud, S., 2017. PROSPECT-D: Towards modeling leaf optical properties through a complete lifecycle. Remote Sens. Environ. 193, 204–215.

Fougnie, B., Marbach, T., Lacan, A., Lang, R., Schlüssel, P., Poli, G., Munro, R., Couto, A.B., 2018. The multi-viewing multi-channel multi-polarisation imager–Overview of the 3MI polarimetric mission for aerosol and cloud characterization. J. Quant. Spectrosc. Radiat. Transf. 219, 23–32.

Frisvad, J.R., Christensen, N.J., Jensen, H.W., 2007. Computing the scattering properties of participating media using Lorenz-Mie theory, in: ACM SIGGRAPH 2007 Papers. pp. 60-es.

Gao, S., Huete, A., Kobayashi, H., Doody, T.M., Liu, W., Wang, Y., Zhang, Y., Lu, X., 2022. Simulation of solar-induced chlorophyll fluorescence in a heterogeneous forest using 3-D radiative transfer modelling and airborne LiDAR. ISPRS J. Photogramm. Remote Sens. 191, 1–17.

Gascon, F., Gastellu-Etchegorry, J.-P., Lefèvre, M.-J., 2001. Radiative transfer model for simulating high-resolution satellite images. IEEE Trans. Geosci. Remote Sens. 39, 1922–1926.

Gastellu-Etchegorry, J.-P., 2008. 3D modeling of satellite spectral images, radiation budget and energy budget of urban landscapes. Meteorol. Atmos. Phys. 102, 187.

Gastellu-Etchegorry, J.-P., Demarez, V., Pinel, V., Zagolski, F., 1996. Modeling radiative transfer in heterogeneous 3-D vegetation canopies. Remote Sens. Environ. 58, 131–156.

Gastellu-Etchegorry, J.-P., Lauret, N., Yin, T., Landier, L., Kallel, A., Malenovský, Z., Al Bitar, A., Aval, J., Benhmida, S., Qi, J., 2017. DART: recent advances in remote sensing data modeling with atmosphere, polarization, and chlorophyll fluorescence. IEEE J. Sel. Top. Appl. Earth Obs. Remote Sens. 10, 2640–2649.

Gastellu-Etchegorry, J.-P., Yin, T., Lauret, N., Cajgfinger, T., Gregoire, T., Grau, E., Feret, J.-B., Lopes, M., Guilleux, J., Dedieu, G., 2015. Discrete anisotropic radiative transfer (DART 5) for modeling airborne and satellite spectroradiometer and LIDAR acquisitions of natural and urban landscapes. Remote Sens. 7, 1667–1701.

Georgiev, I., Křivánek, J., Davidovic, T., Slusallek, P., 2012. Light transport simulation with vertex connection and merging. ACM Trans. Graph. 31, 191–192.

Goel, N.S., 1988. Models of vegetation canopy reflectance and their use in estimation of biophysical parameters from reflectance data. Remote Sens. Rev. 4, 1–212.

Goel, N.S., Rozehnal, I., Thompson, R.L., 1991. A computer graphics based model for scattering from objects of arbitrary shapes in the optical region. Remote Sens. Environ. 36, 73–104.

Goldstein, D.H., 2017. Polarized light. CRC press.

Goodenough, A.A., Brown, S.D., 2017. DIRSIG5: next-generation remote sensing data and image simulation framework. IEEE J. Sel. Top. Appl. Earth Obs. Remote Sens. 10, 4818–4833.

Govaerts, Y.M., 1996. A model of light scattering in three-dimensional plant canopies: a Monte Carlo ray tracing approach. Citeseer.

Govaerts, Y.M., Jacquemoud, S., Verstraete, M.M., Ustin, S.L., 1996. Three-dimensional radiation transfer modeling in a dicotyledon leaf. Appl. Opt. 35, 6585–6598.

Grau, E., Gastellu-Etchegorry, J.-P., 2013. Radiative transfer modeling in the Earth–Atmosphere system with DART model. Remote Sens. Environ. 139, 149–170.

Guillevic, P., Gastellu-Etchegorry, J.P., Demarty, J., Prévot, L., 2003. Thermal infrared radiative transfer within three-dimensional vegetation covers. J. Geophys. Res. Atmos. 108.

Hammersley, J., 2013. Monte carlo methods. Springer Science & Business Media.

Hapke, B., 1986. Bidirectional reflectance spectroscopy: 4. The extinction coefficient and the opposition effect. Icarus 67, 264–280.

Hapke, B., 1981. Bidirectional reflectance spectroscopy: 1. Theory. J. Geophys. Res. Solid Earth 86, 3039–3054.

Hecht, E., 1987. Optics 2nd edition. Opt. 2nd Ed. by Eugene Hecht Read.

Heitz, E., Bourlier, C., Pinel, N., 2013. Correlation effect between transmitter and receiver azimuthal directions on the illumination function from a random rough surface. Waves in Random and Complex Media 23, 318–335.

Hornero, A., North, P.R.J., Zarco-Tejada, P.J., Rascher, U., Martín, M.P., Migliavacca, M., Hernández-Clemente, R., 2021. Assessing the contribution of understory sun-induced chlorophyll fluorescence through 3-D radiative transfer modelling and field data. Remote Sens. Environ. 253, 112195.

Huang, H., 2018. Accelerated RAPID model using heterogeneous porous objects. Remote Sens. 10, 1264.

Huang, H., Qin, W., Liu, Q., 2013. RAPID: A Radiosity Applicable to Porous IndiviDual Objects for directional reflectance over complex vegetated scenes. Remote Sens. Environ. 132, 221–237.

Hulst, Hendrik Christoffel, van de Hulst, Hendrik C, 1981. Light scattering by small particles. Courier Corporation.

Imaoka, K., Kachi, M., Fujii, H., Murakami, H., Hori, M., Ono, A., Igarashi, T., Nakagawa, K., Oki, T., Honda, Y., 2010. Global Change Observation Mission (GCOM) for monitoring carbon, water cycles, and climate change. Proc. IEEE 98, 717–734.

Jacquemoud, S., Baret, F., 1990. PROSPECT: A model of leaf optical properties spectra. Remote Sens. Environ. 34, 75–91.

Janoutová, R., Homolová, L., Malenovský, Z., Hanuš, J., Lauret, N., Gastellu-Etchegorry, J.-P., 2019. Influence of 3D spruce tree representation on accuracy of airborne and satellite forest reflectance simulated in DART. Forests 10, 292.

Kajiya, J.T., 1986. The rendering equation, in: Proceedings of the 13th Annual Conference on Computer Graphics and Interactive Techniques. pp. 143–150.

Kallel, A., 2020. FluLCVRT: Reflectance and fluorescence of leaf and canopy modeling based on Monte Carlo vector radiative transfer simulation. J. Quant. Spectrosc. Radiat. Transf. 253, 107183.

Kallel, A., 2018. Leaf polarized BRDF simulation based on Monte Carlo 3-D vector RT modeling. J. Quant. Spectrosc. Radiat. Transf. 221, 202–224.

Kallel, A., Gastellu-Etchegorry, J.P., 2017. Canopy polarized BRDF simulation based on non-stationary Monte Carlo 3-D vector RT modeling. J. Quant. Spectrosc. Radiat. Transf. 189, 149–167.

Kalos, M.H., Whitlock, P.A., 2009. Monte carlo methods. John Wiley & Sons.

Kattawar, G.W., 1975. A three-parameter analytic phase function for multiple scattering calculations. J. Quant. Spectrosc. Radiat. Transf. 15, 839–849.

Kimes, D.S., Kirchner, J.A., 1982. Radiative transfer model for heterogeneous 3-D scenes. Appl. Opt. 21, 4119–4129.

Kneizys, F.X., Shettle, E.P., Gallery, W.O., Chetwynd Jr, J.H., Abreu, L.W., 1983. Atmospheric transmittance/radiance: computer code LOWTRAN 6. Supplement: Program listings. AIR FORCE GEOPHYSICS LAB HANSCOM AFB MA.

Kobayashi, H., Iwabuchi, H., 2008. A coupled 1-D atmosphere and 3-D canopy radiative transfer model for canopy reflectance, light environment, and photosynthesis simulation in a heterogeneous landscape. Remote Sens. Environ. 112, 173–185.

Kraska, T.A., 1996. DIRSIG: Digital Imaging and Remote Sensing Image Generation Model: Infrared Airborne Validation and Input Parameter Analysis. AIR FORCE INST OF TECH WRIGHT-PATTERSON AFB OH.

Lafortune, E.P., Willems, Y.D., 1996. Rendering participating media with bidirectional path tracing, in: Eurographics Workshop on Rendering Techniques. Springer, pp. 91–100.

Landier, L., Gastellu-Etchegorry, J.P., Al Bitar, A., Chavanon, E., Lauret, N., Feigenwinter, C., Mitraka, Z., Chrysoulakis, N., 2018. Calibration of urban canopies albedo and 3D shortwave radiative budget using remote-sensing data and the DART model. Eur. J. Remote Sens. 51, 739–753. https://doi.org/10.1080/22797254.2018.1462102

Lee, J.-S., Pottier, E., 2017. Polarimetric radar imaging: from basics to applications. CRC press.

Lewis, P., 1999. Three-dimensional plant modelling for remote sensing simulation studies using the Botanical Plant Modelling System. Agronomie 19, 185–210.

Li, Z., Hou, W., Hong, J., Zheng, F., Luo, D., Wang, J., Gu, X., Qiao, Y., 2018. Directional Polarimetric Camera (DPC): Monitoring aerosol spectral optical properties over land from satellite observation. J. Quant. Spectrosc. Radiat. Transf. 218, 21–37.

Liu, Q., Weng, F., 2006. Combined henyey-greenstein and rayleigh phase function. Appl. Opt.

45, 7475–7479.

Makhloufi, A., Kallel, A., Chaker, R., Gastellu-Etchegorry, J.-P., 2021. Retrieval of olive tree biophysical properties from Sentinel-2 time series based on physical modelling and machine learning technique. Int. J. Remote Sens. 42, 8542–8571.

Mekler, Y., Kaufman, Y.J., 1980. The effect of Earth's atmosphere on contrast reduction· for a nonuniform surface albedo and 'two-halves' field. J. Geophys. Res. Ocean. 85, 4067–4083.

Miraglio, T., 2021. Estimation de traits de végétation de canopées ouvertes méditerranéennes par télédétection hyperspectrale.

Mishchenko, M.I., 2002. Vector radiative transfer equation for arbitrarily shaped and arbitrarily oriented particles: a microphysical derivation from statistical electromagnetics. Appl. Opt. 41, 7114–7134.

Mishchenko, M.I., Hovenier, J.W., Travis, L.D., 1999. Light scattering by nonspherical particles: theory, measurements, and applications. Elsevier.

Mishchenko, M.I., Travis, L.D., Lacis, A.A., 2006. Multiple scattering of light by particles: radiative transfer and coherent backscattering. Cambridge University Press.

Mueller, H., 1948. The foundation of optics.

Myneni, R.B., Asrar, G., Gerstl, S.A.W., 1990. Radiative transfer in three dimensional leaf canopies. Transp. Theory Stat. Phys. 19, 205–250.

Myneni, R.B., Ross, J., Asrar, G., 1989. A review on the theory of photon transport in leaf canopies. Agric. For. Meteorol. 45, 1–153.

Nicodemus, F.E., 1978. Self-study manual on optical radiation measurements: Part I–Concepts, Chap. 4 and 5 p97. Nar. Bur. Stand (US). Tech. Note 910-2.

North, P.R.J., 1996. Three-dimensional forest light interaction model using a Monte Carlo method. IEEE Trans. Geosci. Remote Sens. 34, 946–956.

Pearce, W.A., 1977. A study of the effects of the atmosphere on Thematic Mapper observations.

Petty, G.W., 2006. A first course in atmospheric radiation. Sundog Pub.

Pharr, M., Jakob, W., Humphreys, G., 2016. Physically based rendering: From theory to implementation. Morgan Kaufmann.

Pinty, B., Gobron, N., Widlowski, J., Gerstl, S.A.W., Verstraete, M.M., Antunes, M., Bacour, C., Gascon, F., Gastellu, J., Goel, N., 2001. Radiation transfer model intercomparison (RAMI) exercise. J. Geophys. Res. Atmos. 106, 11937–11956.

Pinty, B., Widlowski, J., Taberner, M., Gobron, N., Verstraete, M.M., Disney, M., Gascon, F., Gastellu, J., Jiang, L., Kuusk, A., 2004. Radiation Transfer Model Intercomparison (RAMI) exercise: Results from the second phase. J. Geophys. Res. Atmos. 109.

Press, W.H., Teukolsky, S.A., Vetterling, W.T., Flannery, B.P., 2007. Numerical recipes 3rd edition: The art of scientific computing. Cambridge university press.

Qi, J., Xie, D., Yin, T., Yan, G., Gastellu-Etchegorry, J.-P., Li, L., Zhang, W., Mu, X., Norford, L.K., 2019a. LESS: LargE-Scale remote sensing data and image simulation framework over heterogeneous 3D scenes. Remote Sens. Environ. 221, 695–706.

Qi, J., Yin, T., Xie, D., Gastellu-Etchegorry, J.-P., 2019b. Hybrid Scene Structuring for Accelerating 3D Radiative Transfer Simulations. Remote Sens. 11, 2637.

Qin, W., Gerstl, S.A.W., 2000. 3-D scene modeling of semidesert vegetation cover and its radiation regime. Remote Sens. Environ. 74, 145–162.

Rahman, H., Pinty, B., Verstraete, M.M., 1993. Coupled surface-atmosphere reflectance (CSAR) model: 2. Semiempirical surface model usable with NOAA advanced very high resolution radiometer data. J. Geophys. Res. Atmos. 98, 20791–20801.

Reinersman, P.N., Carder, K.L., 1995. Monte Carlo simulation of the atmospheric point-spread function with an application to correction for the adjacency effect. Appl. Opt. 34, 4453–4471.

Richtsmeier, S.C., Berk, A., Bernstein, L.S., Adler-Golden, S.M., 2001. A 3-Dimensional radiative-transfer hyperspectral image simulator for algorithm validation, in: International Symposium on Spectral Sensing Research. p. 15.

Richtsmeier, S.C., Lynch, D.K., Dearborn, D.S.P., 2017. Antitwilight II: Monte Carlo simulations. Appl. Opt. 56, G169–G178.

Rubinstein, R.Y., Kroese, D.P., 2016. Simulation and the Monte Carlo method. John Wiley & Sons.

Schaepman-Strub, G., Schaepman, M.E., Painter, T.H., Dangel, S., Martonchik, J. V, 2006. Reflectance quantities in optical remote sensing—Definitions and case studies. Remote Sens. Environ. 103, 27–42.

Schlick, C., 1994. An inexpensive BRDF model for physically-based rendering, in: Computer Graphics Forum. Wiley Online Library, pp. 233–246.

Shettle, E.P., Fenn, R.W., 1979. Models for the aerosols of the lower atmosphere and the effects of humidity variations on their optical properties. Optical Physics Division, Air Force Geophysics Laboratory.

Smith, B., 1967. Geometrical shadowing of a random rough surface. IEEE Trans. Antennas Propag. 15, 668–671.

Sobrino, J.A., Del Frate, F., Drusch, M., Jiménez-Muñoz, J.C., Manunta, P., Regan, A., 2016. Review of thermal infrared applications and requirements for future high-resolution sensors. IEEE Trans. Geosci. Remote Sens. 54, 2963–2972.

Sobrino, J.A., Mattar, C., Gastellu-Etchegorry, J.-P., Jiménez-Muñoz, J.C., Grau, E., 2011. Evaluation of the DART 3D model in the thermal domain using satellite/airborne imagery and ground-based measurements. Int. J. Remote Sens. 32, 7453–7477.

Spada, F., Krol, M.C., Stammes, P., 2006. McSCIA: application of the Equivalence Theorem in a Monte Carlo radiative transfer model for spherical shell atmospheres. Atmos. Chem. Phys. 6, 4823–4842.

Stamnes, K., Tsay, S.-C., Wiscombe, W., Laszlo, I., 2000. DISORT, a general-purpose Fortran program for discrete-ordinate-method radiative transfer in scattering and emitting layered media: documentation of methodology.

Sterckx, S., Knaeps, S., Kratzer, S., Ruddick, K., 2015. SIMilarity Environment Correction (SIMEC) applied to MERIS data over inland and coastal waters. Remote Sens. Environ. 157, 96–110.

Sun, B., Kattawar, G.W., Yang, P., 2016. Radiance and polarization in the diffusion region with an arbitrary scattering phase matrix. J. Quant. Spectrosc. Radiat. Transf. 183, 154–161.

Tanre, D., Herman, M., Deschamps, P.Y., 1981. Influence of the background contribution upon space measurements of ground reflectance. Appl. Opt. 20, 3676–3684.

Tanré, D., Herman, M., Deschamps, P.Y., De Leffe, A., 1979. Atmospheric modeling for space measurements of ground reflectances, including bidirectional properties. Appl. Opt. 18, 3587–3594.

Thompson, R.L., Goel, N.S., 1998. Two models for rapidly calculating bidirectional reflectance of complex vegetation scenes: Photon spread (PS) model and statistical photon spread (SPS) model. Remote Sens. Rev. 16, 157–207.

Torrance, K.E., Sparrow, E.M., 1967. Theory for off-specular reflection from roughened surfaces. Josa 57, 1105–1114.

Tsang, L., Kong, J.A., Shin, R.T., 1985. Theory of microwave remote sensing.

Tynes, H.H., Kattawar, G.W., Zege, E.P., Katsev, I.L., Prikhach, A.S., Chaikovskaya, L.I., 2001. Monte Carlo and multicomponent approximation methods for vector radiative transfer by use of effective Mueller matrix calculations. Appl. Opt. 40, 400–412.

Veach, E., 1997. Robust Monte Carlo methods for light transport simulation. Stanford University PhD thesis.

Veach, E., Guibas, L., 1995a. Bidirectional estimators for light transport, in: Photorealistic Rendering Techniques. Springer, pp. 145–167.

Veach, E., Guibas, L.J., 1995b. Optimally combining sampling techniques for Monte Carlo rendering, in: Proceedings of the 22nd Annual Conference on Computer Graphics and Interactive Techniques. pp. 419–428.

Vermote, E.F., Tanré, D., Deuze, J.L., Herman, M., Morcette, J.-J., 1997. Second simulation of the satellite signal in the solar spectrum, 6S: An overview. IEEE Trans. Geosci. Remote Sens. 35, 675–686.

Vilfan, N., Van der Tol, C., Muller, O., Rascher, U., Verhoef, W., 2016. Fluspect-B: A model for leaf fluorescence, reflectance and transmittance spectra. Remote Sens. Environ. 186, 596–615.

Wald, I., Woop, S., Benthin, C., Johnson, G.S., Ernst, M., 2014. Embree: a kernel framework for efficient CPU ray tracing. ACM Trans. Graph. 33, 1–8.

Walter, B., Marschner, S.R., Li, H., Torrance, K.E., 2007. Microfacet Models for Refraction through Rough Surfaces. Render. Tech. 2007, 18th.

Wang, Y., Gastellu-Etchegorry, J.-P., 2021. Accurate and fast simulation of remote sensing images at top of atmosphere with DART-Lux. Remote Sens. Environ. 256. https://doi.org/10.1016/j.rse.2021.112311

Wang, Y., Kallel, A., Yang, X., Regaieg, O., Lauret, N., Guilleux, J., Chavanon, E., Gastellu-Etchegorry, J.-P., 2022. DART-Lux: An unbiased and rapid Monte Carlo radiative transfer method for simulating remote sensing images. Remote Sens. Environ. 274, 112973.

Wang, Y., Lauret, N., Gastellu-Etchegorry, J.-P., 2020. DART radiative transfer modelling for sloping landscapes. Remote Sens. Environ. https://doi.org/10.1016/j.rse.2020.111902

Widlowski, J.-L., Lavergne, T., Pinty, B., Verstraete, M., Gobron, N., 2006. Rayspread: A virtual laboratory for rapid BRF simulations over 3-D plant canopies, in: Computational Methods in Transport. Springer, pp. 211–231.

Widlowski, J.-L., Mio, C., Disney, M., Adams, J., Andredakis, I., Atzberger, C., Brennan, J., Busetto, L., Chelle, M., Ceccherini, G., 2015. The fourth phase of the radiative transfer model intercomparison (RAMI) exercise: Actual canopy scenarios and conformity testing.

Remote Sens. Environ. 169, 418–437.

Widlowski, J., Pinty, B., Lopatka, M., Atzberger, C., Buzica, D., Chelle, M., Disney, M., Gastellu-Etchegorry, J., Gerboles, M., Gobron, N., 2013. The fourth radiation transfer model intercomparison (RAMI-IV): Proficiency testing of canopy reflectance models with ISO-13528. J. Geophys. Res. Atmos. 118, 6869–6890.

Widlowski, J., Taberner, M., Pinty, B., Bruniquel-Pinel, V., Disney, M., Fernandes, R., Gastellu-Etchegorry, J., Gobron, N., Kuusk, A., Lavergne, T., 2007. Third Radiation Transfer Model Intercomparison (RAMI) exercise: Documenting progress in canopy reflectance models. J. Geophys. Res. Atmos. 112.

Woo, A., Pearce, A., Ouellette, M., 1996. It's really not a rendering bug, you see. IEEE Comput. Graph. Appl. 16, 21–25.

Woop, S., Benthin, C., Wald, I., 2013. Watertight ray/triangle intersection. J. Comput. Graph. Tech. 2, 65–82.

Yin, T., Gastellu-Etchegorry, J.-P., Lauret, N., Grau, E., Rubio, J., 2013. A new approach of direction discretization and oversampling for 3D anisotropic radiative transfer modeling. Remote Sens. Environ. 135, 213–223.

Yin, T., Lauret, N., Gastellu-Etchegorry, J.-P., 2016. Simulation of satellite, airborne and terrestrial LiDAR with DART (II): ALS and TLS multi-pulse acquisitions, photon counting, and solar noise. Remote Sens. Environ. 184, 454–468.

Young, A.T., 1980. Revised depolarization corrections for atmospheric extinction. Appl. Opt. 19, 3427–3428.

Zhao, F., Li, Y., Dai, X., Verhoef, W., Guo, Y., Shang, H., Gu, X., Huang, Y., Yu, T., Huang, J., 2015. Simulated impact of sensor field of view and distance on field measurements of bidirectional reflectance factors for row crops. Remote Sens. Environ. 156, 129–142.

Zhao, F., Li, Z., Verhoef, W., Fan, C., Luan, H., Yin, T., Zhang, J., Liu, Z., Tong, C., Bao, Y., 2022. Simulation of solar-induced chlorophyll fluorescence by modeling radiative coupling between vegetation and atmosphere with WPS. Remote Sens. Environ. 277, 113075.

# Annex A

# Fundamental definitions

## A.1 Radiative properties of molecules and particles

Any medium such as the atmosphere, made up of countable objects (*e.g.*, molecules, particles) can scatter, absorb and emit radiation. The proportion that accounts these processes depends on the nature of the objects (shape, size, density, *etc*.), the wavelength, and the incident direction. Quantities that describe the radiative properties of these objects are briefly described below.

**Size parameter $\boldsymbol{\chi}$.** It is a key criterion to characterize the scattering behaviour in media. It is the ratio of the object dimension to the radiation wavelength. Let $d$ be the diameter if the object is spherical, and the diameter of the sphere with the same volume or surface area as the object.

$$\chi = \frac{\pi d}{\lambda}$$

**Number density or Concentration $\boldsymbol{N_c}$ [1/m$^3$].** It is an intensive quantity used to describe the degree of concentration of countable objects (*e.g.*, particles, molecules, *etc*.) in the physical space. It is defined as the number of objects per unit volume.

**Extinction cross section $\boldsymbol{\sigma_e(\lambda,\Omega)}$ [m$^2$].** It is the area perpendicular to the direction $\Omega$ of the radiation that intersects it. It generally differs from the particle *geometrical cross section*. It depends on the radiation wavelength and the particle permittivity, shape, and size. It is called spherical if it does not depend on the incident direction $\Omega$. It is the sum of the absorption extinction cross section $\sigma_a(\lambda,\Omega)$ and the scattering extinction cross section $\sigma_s(\lambda,\Omega)$.

$$\sigma_e(\lambda,\Omega) = \sigma_a(\lambda,\Omega) + \sigma_s(\lambda,\Omega)$$

**Extinction coefficient $\boldsymbol{\alpha_e(\lambda,\Omega)}$ [1/m].** It defines the spectral attenuation of radiation by a medium in a direction $\Omega$. We have $\alpha_e(\lambda,\Omega) = \alpha_a(\lambda,\Omega) + \alpha_s(\lambda,\Omega)$ with $\alpha_a(\lambda,\Omega)$ the absorption coefficient and $\alpha_s(\lambda,\Omega)$ the scattering extinction coefficient.

$$\alpha_e(\lambda,\Omega) = \sigma_e(\lambda,\Omega)\cdot N_c, \quad \alpha_a(\lambda,\Omega) = \sigma_a(\lambda,\Omega)\cdot N_c, \alpha_s(\lambda,\Omega) = \sigma_s(\lambda,\Omega)\cdot N_c$$

The total extinction, absorption, and scattering coefficients of a multi component medium (*e.g.*, the atmosphere) are the sums of the corresponding coefficients per individual component *i*.

$$\alpha_e(\lambda,\Omega) = \sum_i \alpha_{e,i}(\lambda,\Omega) = \sum_i \sigma_{e,i}(\lambda,\Omega)\cdot N_{c,i}$$

$$\alpha_a(\lambda,\Omega) = \sum_i \alpha_{a,i}(\lambda,\Omega) = \sum_i \sigma_{a,i}(\lambda,\Omega)\cdot N_{c,i}$$

$$\alpha_s(\lambda,\Omega) = \sum_i \alpha_{s,i}(\lambda,\Omega) = \sum_i \sigma_{s,i}(\lambda,\Omega)\cdot N_{c,i}$$

**Single scattering albedo $\boldsymbol{\omega(\lambda,\Omega)}$.** It is the ratio of the scattering coefficient to the extinction coefficient in direction $\Omega$ for wavelength $\lambda$. It is said spherical if scattering is isotropic.

$$\omega(\lambda,\Omega) = \frac{\alpha_s(\lambda,\Omega)}{\alpha_e(\lambda,\Omega)} = \frac{\sigma_s(\lambda,\Omega)}{\sigma_e(\lambda,\Omega)}$$

Sometimes, the single scattering albedo is averaged over the $4\pi$ space to represent the fraction of the radiation lost due to scattering (Chandrasekhar, 1960), we have

$$\overline{\omega}(\lambda) = \frac{1}{4\pi}\int_{4\pi} \omega(\lambda,\Omega)d\Omega$$

**Optical depth $\boldsymbol{\tau(\lambda,\Omega)}$.** It is a measure of the distance the radiation will travel in a medium. It is the product of the extinction coefficient and distance along the line of sight in a medium.

$$\tau(\lambda,\Omega) = \int_{r_1}^{r_2} \alpha(\lambda,r,\Omega)dr$$

with $\alpha(\lambda,r,\Omega)$ the extinction coefficient at position $r$ along direction $\Omega$.

**Transmittance $\boldsymbol{\mathcal{T}(\lambda,\Omega)}$.** It is the ratio of the transmitted radiant flux to the incident radiant flux along the line of sight for a given wavelength in a medium. According to the *Beer's law*, the transmittance is the exponential of the minus optical depth along the line of sight.

$$\mathcal{T}(\lambda,\Omega) = e^{-\tau(\lambda,\Omega)}$$

## A.2 Radiative properties of surfaces

A radiation intercepted by a surface is reflected, transmitted, or absorbed. A surface also emits radiation as thermal emission over the spectrum and can emit fluorescence radiation in some spectral range. The proportion that accounts these processes depends on the surface nature and geometry, the wavelength, and the incident direction. Quantities that describe the radiative properties of surfaces are briefly described below.

**Reflectance $\boldsymbol{\mathcal{R}(\lambda)}$.** It is $\frac{\text{reflected radiant flux by a surface}}{\text{incident radiant flux onto the surface}}$. There exists several definitions.

Table A.1. Geometry of the incoming (dashed line) and reflected radiation (solid line) used to define the reflectance and reflectance factor, adapted from (Schaepman-Strub et al., 2006). A radiation can be along a unique direction, in a cone or in a hemisphere.

| **Incoming/Reflected** | Directional | Conical | Hemispherical |
|---|---|---|---|
| Directional | 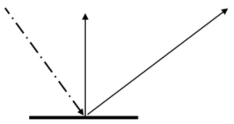 | 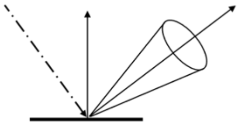 | 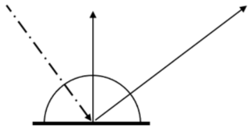 |
| Conical | 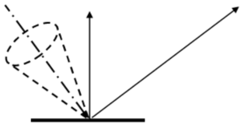 | 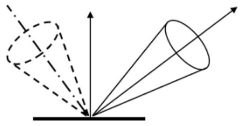 | 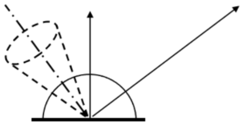 |
| Hemispherical | 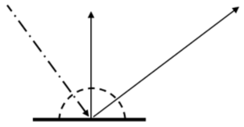 | 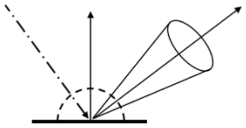 | 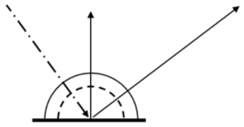 |

- **Reflectance factor $\boldsymbol{\rho(\lambda)}$**: ratio of the radiant flux reflected by a surface to that reflected into the same reflected-beam geometry by a white (lossless) and diffuse (Lambertian) standard surface, irradiated under the same conditions. It can be larger than 1, especially for strongly forward reflection such as specular surfaces. Different reflectance and reflectance factor terminologies (Table 1.B.1) are used depending on the measuring geometries (*i.e.*, along a unique direction, in a cone or in a hemisphere).

- **Bidirectional reflectance $\boldsymbol{\mathcal{R}_{\mathrm{DD}}(\lambda, \Omega' \rightarrow \Omega)}$**: ratio of the reflected radiant flux $d\Phi_r(\lambda, \Omega' \rightarrow \Omega)$ from a surface into a viewing direction $\Omega$ due to the direct incident radiant flux $d\Phi_i(\lambda, \Omega')$ in direction $\Omega'$ to the direct incident radiant flux (directional-directional case in Table 1.B.1).

$$\mathcal{R}_{\mathrm{DD}}(\lambda, \Omega' \rightarrow \Omega) = \frac{d\Phi_r(\lambda, \Omega' \rightarrow \Omega)}{d\Phi_i(\lambda, \Omega')} = \frac{dL_r(\lambda, \Omega' \rightarrow \Omega) \cdot \cos\theta \, d\Omega dA}{dL_i(\lambda, \Omega') \cdot \cos\theta' \, d\Omega' dA}$$

- **Bidirectional reflectance factor $\boldsymbol{\rho(\lambda, \Omega' \rightarrow \Omega)}$**: ratio of the reflected radiant flux $d\Phi_r(\lambda, \Omega' \rightarrow \Omega)$ from a surface into a direction $\Omega$ due to direct illumination from direction $\Omega'$ to the flux $d\Phi_r^{\mathrm{Lamb}}(\lambda, \Omega' \rightarrow \Omega)$ scattered by a white and Lambertian surface (directional-directional case in Table 1.B.1) under the same direct illumination from direction $\Omega'$.

$$\rho(\lambda, \Omega' \rightarrow \Omega) = \frac{d\Phi_r(\lambda, \Omega' \rightarrow \Omega)}{d\Phi_r^{\mathrm{Lamb}}(\lambda, \Omega' \rightarrow \Omega)} = \frac{dL_r(\lambda, \Omega' \rightarrow \Omega) \cdot \cos\theta \, d\Omega dA}{dL_r^{\mathrm{Lamb}}(\lambda, \Omega' \rightarrow \Omega) \cdot \cos\theta \, d\Omega dA}$$

- **Bidirectional reflectance distribution function (BRDF)**: ratio of the reflected radiance $dL_r(\lambda, \Omega' \rightarrow \Omega)$ by a surface into a direction $\Omega$ to the incident irradiance $dE_i(\lambda, \Omega')$ in direction $\Omega'$ that causes $dL_r(\lambda, \Omega' \rightarrow \Omega)$.

$$f_r(\lambda, \Omega' \rightarrow \Omega) = \frac{dL_r(\lambda, \Omega' \rightarrow \Omega)}{dE_i(\lambda, \Omega')} = \frac{dL_r(\lambda, \Omega' \rightarrow \Omega)}{L_i(\lambda, \Omega') \cdot \cos\theta' \, d\Omega'}$$

Because $dE_i(\lambda, \Omega') = \pi \cdot dL_r^{\mathrm{Lamb}}(\lambda, \Omega' \rightarrow \Omega)$ for a white and Lambertian surface, we have:

$$\rho(\lambda, \Omega' \rightarrow \Omega) = \pi \cdot f_r(\lambda, \Omega' \rightarrow \Omega)$$

- **Directional-hemispherical reflectance $\boldsymbol{\mathcal{R}_{\mathrm{DH}}(\lambda, \Omega)}$**: ratio of radiant flux $d\Phi_r(\lambda, \Omega \rightarrow 2\pi^+)$ reflected to the surface upper hemisphere $2\pi^+$ by a surface to the incident radiant flux $d\Phi_i(\lambda, \Omega)$ (directional-hemispherical case in Table 1.B.1) in direction $\Omega$ that causes $d\Phi_r(\lambda, \Omega \rightarrow 2\pi^+)$.

$$\mathcal{R}_{\mathrm{DH}}(\lambda,\Omega') = \frac{d\Phi_r(\lambda,\Omega' \to 2\pi^+)}{d\Phi_i(\lambda,\Omega')} = \frac{\int_{2\pi^+} dL_r(\lambda,\Omega' \to \Omega)\cdot\cos\theta\, d\Omega dA}{L_i(\lambda,\Omega')\cdot\cos\theta'\, d\Omega' dA}$$

Because $dL_r(\lambda,\Omega' \to \Omega)$=$L_i(\lambda,\Omega')$· $\cos\theta'$ ·$f_r(\lambda,\Omega' \to \Omega)d\Omega'$ is the radiance in direction Ω due to the direct incident radiant flux $d\Phi_i(\lambda,\Omega')$, we have

$$\mathcal{R}_{\mathrm{DH}}(\lambda,\Omega) = \int_{2\pi^+} f_r(\lambda,\Omega' \to \Omega)\cdot\cos\theta\, d\Omega$$

- **Albedo or bi-hemispherical reflectance $\mathcal{R}_{\mathrm{HH}}(\lambda)$**: ratio of the radiant flux $d\Phi_r(\lambda,2\pi^- \to 2\pi^+)$ reflected from a surface into the surface upper hemisphere to the incident radiant flux $d\Phi_i(\lambda,2\pi^-)$ from the surface lower hemisphere (hemispherical-hemispherical case in Table 1.B.1).

$$\mathcal{R}_{\mathrm{HH}}(\lambda) = \frac{d\Phi_r(\lambda,2\pi^- \to 2\pi^+)}{d\Phi_i(\lambda,2\pi^-)} = \frac{\int_{2\pi^+} L_r(\lambda,2\pi^- \to \Omega)\cdot\cos\theta\, d\Omega dA}{\int_{2\pi^-} L_i(\lambda,\Omega')\cdot\cos\theta'\, d\Omega' dA}$$

Because $\int_{2\pi^+} dL_r\big(\lambda,\Omega' \to \Omega\big)\cdot\cos\theta\, d\Omega = L_i(\lambda,\Omega')$·$\mathcal{R}_{\mathrm{DH}}(\lambda,\Omega')$· $\cos\theta'\, d\Omega'$, the directional-hemispherical reflectance is related to the bi-hemispherical reflectance by:

$$\mathcal{R}_{\mathrm{HH}}(\lambda) = \frac{\int_{2\pi^-} L_i(\lambda,\Omega')\cdot\mathcal{R}_{\mathrm{DH}}(\lambda,\Omega')\cdot\cos\theta'\, d\Omega'}{\int_{2\pi^-} L_i(\lambda,\Omega')\cdot\cos\theta'\, d\Omega'}$$

For isotropic illumination: $\mathcal{R}_{\mathrm{HH}}(\lambda) = \frac{1}{\pi}\int_{2\pi^-} \mathcal{R}_{\mathrm{DH}}(\lambda,\Omega')\cdot\cos\theta'\, d\Omega'$

**Transmittance $\mathcal{T}(\lambda)$.** It is the ratio of the transmitted radiant flux through a surface to the incident radiant flux. As for the reflectance terminology, it exists different definitions of transmittance depending on the geometry of the incident and the transmitted radiation.

- **Bidirectional transmittance $\mathcal{T}_{\mathrm{DD}}(\lambda,\Omega' \to \Omega)$**: ratio of the radiant flux $d\Phi_t(\lambda,\Omega' \to \Omega)$ transmitted through a surface in direction Ω to the incident radiant flux $d\Phi_i(\lambda,\Omega')$ in direction Ω' that causes $d\Phi_t(\lambda,\Omega' \to \Omega)$. The transmittance in a medium (*cf*. Annex A.1) is a special case of $\mathcal{T}_{\mathrm{DD}}$ with same incident and transmitted direction.

$$\mathcal{T}_{\mathrm{DD}}(\lambda,\Omega' \to \Omega) = \frac{d\Phi_t(\lambda,\Omega' 2\pi^- \to \Omega)}{d\Phi_i(\lambda,\Omega')} = \frac{dL_t(\lambda,\Omega' \to \Omega)\cdot\cos\theta\, d\Omega dA}{dL_i(\lambda,\Omega')\cdot\cos\theta'\, d\Omega' dA}$$

- **Bidirectional transmittance distribution function (BTDF)**: ratio of the transmitted radiance $dL_t(\lambda, \Omega' \to \Omega)$ through a surface in a direction $\Omega$ to the incident irradiance $dE_i(\lambda, \Omega')$ in direction $\Omega'$ that causes $dL_t(\lambda, \Omega' \to \Omega)$. If the wavelength changes after the transmission (e.g., refraction), the wavelength in vacuum $\lambda_0$ should be used instead of the wavelength in medium $\lambda$ that changes with the refractive index.

$$f_t(\lambda, \Omega' \to \Omega) = \frac{dL_t(\lambda, \Omega' \to \Omega)}{dE_i(\lambda, \Omega')} = \frac{dL_t(\lambda, \Omega' \to \Omega)}{L_i(\lambda, \Omega') \cdot \cos\theta' \, d\Omega'}$$

- **Directional-hemispherical transmittance $\boldsymbol{\mathcal{T}_{\mathrm{DH}}(\lambda, \Omega)}$**: ratio of the transmitted radiant flux $d\Phi_t(\lambda, \Omega \to 2\pi^-)$ through a surface into the surface lower hemisphere $2\pi^-$ due to the incident radiant flux $d\Phi_i(\lambda, \Omega')$ along direction $\Omega'$ to the incident radiant flux.

$$\mathcal{T}_{\mathrm{DH}}(\lambda, \Omega') = \frac{d\Phi_t(\lambda, \Omega \to 2\pi^-)}{d\Phi_i(\lambda, \Omega')} = \frac{\int_{2\pi^-} dL_t(\lambda, \Omega' \to \Omega) \cdot \cos\theta \, d\Omega dA}{L_i(\lambda, \Omega') \cdot \cos\theta' \, d\Omega' dA}$$

- **Bi-hemispherical transmittance $\boldsymbol{\mathcal{T}_{\mathrm{HH}}(\lambda)}$**: ratio of the transmitted radiant flux $d\Phi_t(\lambda, 2\pi^- \to 2\pi^-)$ through a surface into the surface lower hemisphere $2\pi^-$ to the incident radiant flux $\Phi_i(\lambda, 2\pi^-)$ from the surface lower hemisphere $2\pi^-$.

$$\mathcal{T}_{\mathrm{HH}}(\lambda) = \frac{d\Phi_t(\lambda, 2\pi^- \to 2\pi^-)}{d\Phi_i(\lambda, 2\pi^-)} = \frac{\int_{2\pi^-} L_t(\lambda, 2\pi^- \to \Omega) \cdot \cos\theta \, d\Omega dA}{\int_{2\pi^-} L_i(\lambda, \Omega') \cdot \cos\theta' \, d\Omega' dA}$$

**Absorptance $\boldsymbol{\mathcal{A}(\lambda)}$.** It is the ratio of the absorbed radiant flux by a surface to the incident radiant flux. Its definition depends on the geometry of incident radiation.

**Directional absorptance $\boldsymbol{\mathcal{A}_D(\lambda, \Omega)}$.** It is the ratio of the absorbed radiant flux $d\Phi_a(\lambda, \Omega)$ by a surface to the direct illumination radiant flux $d\Phi_i(\lambda, \Omega)$ from direction $\Omega$.

$$\mathcal{A}_D(\lambda, \Omega) = \frac{d\Phi_a(\lambda, \Omega)}{d\Phi_i(\lambda, \Omega)}$$

**Hemispherical absorptance $\boldsymbol{\mathcal{A}_{\mathrm{H}}(\lambda)}$.** It is the ratio of the absorbed radiant flux $\Phi_a(\lambda, 2\pi^-)$ by a surface to the incident hemispherical radiant flux $\Phi_i(\lambda, 2\pi^-)$.

$$\mathcal{A}_{\mathrm{H}}(\lambda) = \frac{\Phi_a(\lambda, 2\pi^-)}{\Phi_i(\lambda, 2\pi^-)}$$

Because the radiant energy conservation, the sum of reflectance, transmittance, and absorptance is equal to one. Therefore, we have:

$$\mathcal{A}_{\mathrm{D}}(\lambda,\Omega)=1-\mathcal{R}_{\mathrm{DH}}(\lambda,\Omega)-\mathcal{T}_{\mathrm{DH}}(\lambda,\Omega)\quad\text{and}\quad\mathcal{A}_{\mathrm{H}}(\lambda)=1-\mathcal{R}_{\mathrm{HH}}(\lambda)-\mathcal{T}_{\mathrm{HH}}(\lambda)$$

**Emissivity $\boldsymbol{\varepsilon(\lambda)}$.** The *emissivity* is the ratio of the emitted radiant flux by a surface to the emitted radiant flux emitted by the blackbody at the same temperature and wavelength. It characterizes the efficiency of the emission of a surface compared to the blackbody. The definition of the emissivity terminologies depends on the geometry of emitted radiation.

**Directional emissivity $\boldsymbol{\varepsilon_{\mathrm{D}}(\lambda,\Omega)}$.** The *directional emissivity* is the ratio of the emitted radiant flux $d\Phi_e(\lambda,\Omega)$ by a surface in a given direction $\Omega$ to the emitted radiant flux $d\Phi_{\mathrm{B}}(\lambda,\Omega)$ of the blackbody under the same condition.

$$\varepsilon_{\mathrm{D}}(\lambda,\Omega)=\frac{d\Phi_e(\lambda,\Omega)}{d\Phi_{\mathrm{B}}(\lambda,\Omega)}$$

**Hemispherical emissivity $\boldsymbol{\varepsilon_{\mathrm{H}}(\lambda)}$.** It is the ratio of the radiant flux $\Phi_e(\lambda,2\pi^+)$ emitted to the surface upper hemisphere $2\pi^+$ by a surface to the corresponding blackbody radiant flux $\Phi_{\mathrm{B}}(\lambda,2\pi^+)$.

$$\varepsilon_{\mathrm{H}}(\lambda)=\frac{\Phi_e(\lambda,2\pi^+)}{\Phi_{\mathrm{B}}(\lambda,2\pi^+)}$$

Under *thermodynamics equilibrium conditions*, according to the *Kirchhoff's law*, we have

$$\varepsilon_D(\lambda,\Omega)=\mathcal{A}_{\mathrm{D}}(\lambda,\Omega)\quad\text{and}\quad\varepsilon_{\mathrm{H}}(\lambda)=\mathcal{A}_{\mathrm{H}}(\lambda)$$

**Blackbody.** It is an idealized physical body that absorbs all incident radiation, regardless of its wavelength or incident angle. At thermal equilibrium (*i.e.*, constant temperature $T$), it emits an isotropic blackbody radiance $L_{\mathrm{B}}$ that follows the *Planck's law:*

$$L_{\mathrm{B}}(\lambda,T)=\frac{2hc^2}{\lambda^5}\cdot\frac{1}{\exp\left(\frac{hc}{\lambda k_{\mathrm{B}}T}\right)-1}$$

with $h=6.62607015\times10^{-34}$ J/Hz is the *Planck constant*, $k_{\mathrm{B}}=1.380649\times10^{-34}$ J/K is the *Boltzmann constant*, $c$ is the speed of light.

**Brightness temperature $\boldsymbol{T}_{\mathrm{B}}(\boldsymbol{\lambda}, \boldsymbol{\Omega})$ [K].** The *brightness temperature* is the equivalent blackbody temperature that emits the same monochromatic radiance at wavelength $\lambda$ along direction Ω in the thermodynamics equilibrium conditions as the measurement $L(\lambda, \Omega)$.

$$T_{\mathrm{B}}(\lambda, \Omega) = L_{\mathrm{B}}^{-1}\big(\lambda, L(\lambda, \Omega)\big)$$

## A.3 Sensor and measurement equation

A sensor is a device that outputs a signal due to the sensing of a physical phenomenon. Here, we focus on sensors that are sensitive to radiation energy. The quantities that characterize the sensor and the measurement are briefly described below.

**Field of view (FOV) [sr].** It is a solid angle through which a sensor captures the radiation.

**Sensor spectral response $\boldsymbol{S}(\boldsymbol{\lambda})$ [S/$\boldsymbol{\mu}$m].** It is the output signal per unit wavelength interval. The unit S suggested by (Nicodemus, 1978) can be volt, ampere, *etc*., depending on sensors.

**Flux responsivity $\boldsymbol{W}_{\boldsymbol{e}}^{(\boldsymbol{j})}(\boldsymbol{r}, \boldsymbol{\lambda}, \boldsymbol{\Omega})$ [/m²/sr].** It is the sensor response for pixel $j$, in terms of measured radiance, to the incident radiant flux at the entry of the sensor. It depends on the incident position $r$, the direction Ω and the wavelength $\lambda$ of the radiation.

$$W_e^{(j)}(r, \lambda, \Omega) = \frac{dL^{(j)}}{d\Phi(r, \lambda, \Omega)}$$

**Measurement equation.** It gives the measured radiance as a function of the incident radiant flux at the receiving aperture:

$$dL^{(j)}(\lambda, \Omega) = W_e^{(j)}(r, \lambda, \Omega) \cdot d\Phi(r, \lambda, \Omega) = W_e^{(j)}(r, \lambda, \Omega) \cdot L(r, \lambda, \Omega) \cdot \cos\theta d\Omega dA$$

for all incident direction in FOV and for the whole aperture surface that receives the radiation.

$$L^{(j)}(\lambda) = \int_A \int_\Omega W_e^{(j)}(r, \lambda, \Omega) \cdot L(r, \lambda, \Omega) \cdot \cos\theta d\Omega dA$$

The measured radiance $L^{(j)}$ for a spectral band $\Delta\lambda$ is the integral of $L^{(j)}(\lambda)$ over $\Delta\lambda$.

# Annex B

# The hybrid method

## B.1 Rapidly simulate TOA and sensor images

The Monte Carlo method presented in this chapter is relatively accurate in terms of the radiative transfer calculations since nearly no approximation is needed. However, it is usually long to converge. For example, the simulation of the 3D scenario in section 4.4 with atmosphere is 10 to 100 times longer to converge compared to the case without atmosphere. On the other hand, for the simple plane-parallel atmosphere, the discrete ordinates method is more efficient than the Monte Carlo method to compute the upwelling and downwelling radiation, but it is more approximate to compute the surface-atmosphere coupling. For the cases of relatively homogeneous the land surfaces (*e.g.*, dense forest, city), with small or no adjacency effects, we designed a hybrid method that couples the discrete ordinates radiative transfer in the atmosphere with the Monte Carlo radiative transfer at land surfaces (Wang and Gastellu-Etchegorry, 2021).

### B.1.1 Theory and algorithm

DART-FT simulates sequentially the atmospheric radiative transfer and land surface radiative transfer and couples them. Figure 2.3 illustrates the 5 major steps of its radiative transfer modelling in the coupled Earth-atmosphere system in order to simulate TOA and sensor images (Grau and Gastellu-Etchegorry, 2013; Wang et al., 2020):

(1) Sun illumination followed by atmosphere scattering and thermal emission.
(2) Land surface radiative transfer modelling.
(3) Surface-atmosphere radiative coupling.
(4) Land surface radiative transfer of atmosphere backscattered radiation.
(5) Transfer of upward radiation from BOA to sensor and TOA.

In this hybrid method, the DART-FT atmospheric radiative transfer modelling realizes the steps 1, 3 and 5 of the five major radiative steps (Figure 2.3), while DART-Lux land surface radiative transfer modelling realizes the steps 2 and 4, plus an additional step 6. Steps 1 to 5 give spatially averaged radiance values conversely to step 6 that gives images. These steps are detailed below.

1) DART-FT atmospheric radiative transfer modelling. TOA direct irradiance $E_{\text{TOA}}^{\text{dir}}$ gives diffuse radiance $L_{\text{TOA}}^{\text{diff}}(\Omega_n^{\uparrow})$ per discrete upward direction $\Omega_n^{\uparrow}$, BOA direct irradiance $E_{\text{BOA}}^{\text{dir}}$, BOA diffuse irradiance $E_{\text{BOA}}^{\text{diff}}$ and BOA diffuse radiance $L_{\text{BOA}}^{\text{diff}}(\Omega_n^{\downarrow})$ per discrete downward direction $\Omega_n^{\downarrow}$.

2) DART-Lux land surface radiative transfer modelling. It uses two light sources: sunlight with direct irradiance $E_{\text{BOA}}^{\text{dir}}$ and anisotropic light from the sky with BOA diffuse radiance $L_{\text{BOA}}^{\text{diff}}(\Omega_n^{\downarrow})$ (*cf.* direct sun light and the anisotropic light from the sky in section 3.3.1). The surface average radiance $L_{\text{BOA}}^{\text{scene}}(\Omega_n^{\uparrow})$ per discrete upward direction $\Omega_n^{\uparrow}$ is computed based on the radiance map (Figure B.1) generated by the BRF camera (*cf.* section 3.3.2). Pixel $(i,j)$ gives the radiance $L(\Omega_{i,j})$ for direction $\Omega_{i,j}$ on the hemisphere (Figure 3.9.b), which allows one to compute the upward radiance $L_{\text{BOA}}^{\text{scene}}(\Omega_n^{\uparrow})$ along any discrete direction $\Omega_n$:

$$L_{\text{BOA}}^{\text{scene}}(\Omega_n^{\uparrow})=\frac{\int_{\Delta\Omega_n} L(\Omega)\cdot\cos\theta\cdot\sin\theta\, d\theta d\varphi}{\int_{\Delta\Omega_n}\cos\theta\cdot\sin\theta\, d\theta d\varphi}=\frac{\sum_{i=i_0}^{i_1}\sum_{j=j_0}^{j_1} L(\Omega_{i,j})\cdot\sin(2\theta_i)\cdot\sin\Delta\theta\cdot\Delta\varphi}{\cos\theta_n^c\cdot\Delta\Omega_n} \quad \text{(B.1)}$$

where solid angle $\Delta\Omega_n$ covers pixel region from line $i_0$ to $i_1$ and from column $j_0$ to $j_1$. The effective zenith angle $\theta_n^c$ of direction $\Omega_n$ verifies: $\cos\theta_n^c\cdot\Delta\Omega_n=\int_{\Delta\Omega_n}\cos\theta\cdot\sin\theta\, d\theta d\varphi$.

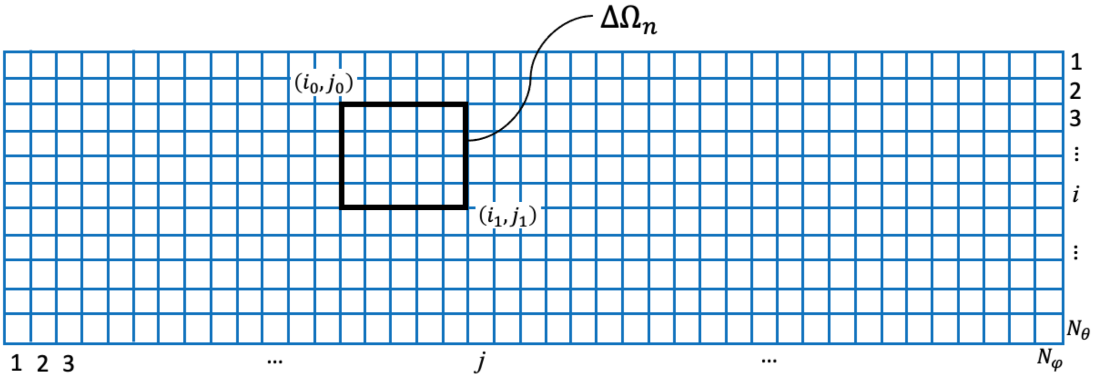

Figure B.1. Radiance map simulated by the BRF camera. It has $N_\theta$ lines and $N_\varphi$ columns. The value of pixel $(i,j)$ is the scene radiance along direction $\Omega_{i,j}$. The black rectangle outlines the region of a solid angle $\Delta\Omega_n$ of discrete direction $\Omega_n$. $\theta_i$ and $\varphi_j$ represent the zenith and azimuth angle at centre of pixel $(i,j)$ respectively.

3) DART-FT atmospheric radiative transfer modelling. It computes transfer functions: $\mathrm{TF}_{\text{BA-BA}}$ (*i.e.*, BOA downward radiance $L_{\mathrm{BOA}}^{\mathrm{coupl}}(\Omega_n^{\downarrow})$ caused by BOA upward radiance $L_{\mathrm{BOA}}^{\mathrm{scene}}(\omega_n^{\uparrow})$) and $\mathrm{TF}_{\text{BA-TOA}}$ (*i.e.*, TOA radiance $L_{\mathrm{TOA}}^{\mathrm{coupl}}(\Omega_n^{\uparrow})$ caused by BOA upward radiance $L_{\mathrm{BOA}}^{\mathrm{scene}}(\Omega_n^{\uparrow})$). Then, $L_{\mathrm{BOA}}^{\mathrm{coupl}}(\Omega_n^{\downarrow})$ is extrapolated to infinite coupling order radiance $L_{\mathrm{BOA}}^{\mathrm{coupl}(\infty)}(\Omega_n^{\downarrow})$ using the Earth scene albedo $\mathcal{R}_{\mathrm{HH}}$ and atmosphere backscattering albedo $\mathcal{R}'_{\mathrm{HH}}$.

$$L_{\mathrm{BOA}}^{\mathrm{coupl}(\infty)}(\Omega_n^{\downarrow}) = \frac{1}{1-\mathcal{R}_{\mathrm{HH}}\cdot\mathcal{R}'_{\mathrm{HH}}}\cdot L_{\mathrm{BOA}}^{\mathrm{coupl}}(\Omega_n^{\downarrow})$$

$$\text{with } \mathcal{R}_{\mathrm{HH}} = \frac{\sum_{\Omega_n^{\uparrow}} L_{\mathrm{BOA}}^{\mathrm{scene}}(\Omega_n^{\uparrow})\cdot\cos\theta_n^c\cdot\Delta\Omega_n}{E_{\mathrm{BOA}}^{\mathrm{dir}}+E_{\mathrm{BOA}}^{\mathrm{diff}}} \quad \text{and} \quad \mathcal{R}'_{\mathrm{HH}} = \frac{\sum_{\Omega_n^{\downarrow}} L_{\mathrm{BOA}}^{\mathrm{coupl}}(\Omega_n^{\downarrow})\cdot\cos\theta_n^c\cdot\Delta\Omega_n}{\sum_{\Omega_n^{\uparrow}} L_{\mathrm{BOA}}^{\mathrm{scene}}(\Omega_n^{\uparrow})\cdot\cos\theta_n^c\cdot\Delta\Omega_n}$$

The backscattered irradiance $E_{\mathrm{BOA}}^{\mathrm{coupl}(\infty)}$ is computed accordingly using $L_{\mathrm{BOA}}^{\mathrm{coupl}(\infty)}(\Omega_n^{\downarrow})$:

$$E_{\mathrm{BOA}}^{\mathrm{coupl}(\infty)} = \sum_{\Omega_n^{\downarrow}} L_{\mathrm{BOA}}^{\mathrm{coupl}(\infty)}(\Omega_n^{\downarrow})\cdot\cos\theta_n^c\cdot\Delta\Omega_n$$

4) DART-Lux Land surface radiative transfer modelling. It uses a single light source: the extrapolated anisotropic light from the sky with radiance $L_{\mathrm{BOA}}^{\mathrm{coupl}(\infty)}(\Omega_n^{\downarrow})$. It computes the scene radiance per upward direction $\Omega_n^{\uparrow}$ using Eq. (B.1), which is added to $L_{\mathrm{BOA}}^{\mathrm{scene}}(\Omega_n^{\uparrow})$ giving $L_{\mathrm{BOA}}^{\mathrm{scene,coupl}}(\Omega_n^{\uparrow})$.

5) $\mathrm{TF}_{\mathrm{BA-TOA}}$ is applied to compute direct transmitted radiance $L_{\mathrm{TOA}}^{\mathrm{dir}}(\Omega_n^{\uparrow})$ and scattered radiance $L_{\mathrm{TOA}}^{\mathrm{coupl}}(\Omega_n^{\uparrow})$ per upward direction using $L_{\mathrm{BOA}}^{\mathrm{scene,coupl}}(\Omega_n^{\uparrow})$.

6) DART-Lux Land surface radiative transfer modelling. It uses two light sources: sunlight with irradiance $E_{\mathrm{BOA}}^{\mathrm{dir}}$ and anisotropic light from the sky with BOA diffuse radiance $L_{\mathrm{BOA}}^{\mathrm{diff}}(\Omega_n^{\downarrow}) + L_{\mathrm{BOA}}^{\mathrm{coupl}(\infty)}(\Omega_n^{\downarrow})$. It gives BOA upward radiance images $L_{\mathrm{BOA}}(i,j,\Omega_n^{\uparrow})$. It gives:

- TOA radiance images: $L_{\mathrm{TOA}}(i,j,\Omega_n^{\uparrow}) = L_{\mathrm{BOA}}(i,j,\Omega_n^{\uparrow})\cdot\frac{L_{\mathrm{TOA}}^{\mathrm{dir}}(\Omega_n^{\uparrow})}{L_{\mathrm{BOA}}^{\mathrm{scene,coupl}}(\Omega_n^{\uparrow})} + L_{\mathrm{TOA}}^{\mathrm{diff}}(\Omega_n^{\uparrow}) + L_{\mathrm{TOA}}^{\mathrm{coupl}}(\Omega_n^{\uparrow})$

- TOA reflectance images: $\mathcal{R}_{\mathrm{BOA}}(i,j,\Omega_n^{\uparrow}) = \frac{L_{\mathrm{BOA}}(i,j,\Omega_n^{\uparrow})}{E_{\mathrm{BOA}}^{\mathrm{dir}}+E_{\mathrm{BOA}}^{\mathrm{diff}}+E_{\mathrm{BOA}}^{\mathrm{coupl}(\infty)}}$

$$\mathcal{R}_{\mathrm{TOA}}(i,j,\Omega_n^{\uparrow}) = \frac{L_{\mathrm{TOA}}(i,j,\Omega_n^{\uparrow})}{E_{\mathrm{TOA}}^{\mathrm{dir}}}$$

The simulation of the sensor plane image is exactly the same, one only needs to replace the quantities and equations at TOA level by those at the SENSOR level.

### B.1.2 Consistency test with DART-FT

The accuracy and efficiency of the hybrid method are assessed by comparing it with DART-FT for a 30 m × 30 m plot of Järvselja Birch forest (summer) from RAMI experiment (https://rami-benchmark.jrc.ec.europa.eu; (Widlowski et al., 2015)) (Figure B.2). This plot contains 91 trees: 50 birch trees, 18 linden trees, 15 aspen trees, 5 spruce trees, and 3 ash and maple trees (Figure E.2). We did not consider the full 100 m × 100 m birch forest with its 550 million of facets because it would have required too much computer memory and time for DART-FT.

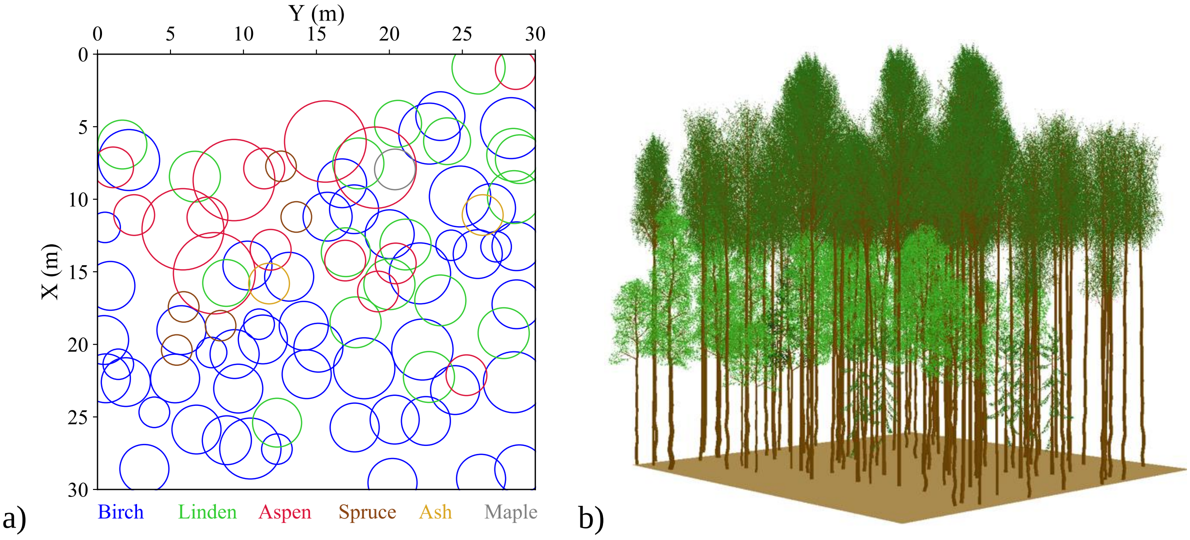

Figure B.2. The 30 m × 30 m plot of Järvselja birch forest. a) Spatial distribution of tree species. b) DART 3D mock-up.

DART-FT and DART-Lux simulations are conducted with direct sun illumination ($\theta_{\text{sun}} = 36.6°, \varphi_{\text{sun}} = 270.69°$), THKUR TOA irradiance spectra (Berk et al., 2008), a 0.125 m spatial resolution and 4 spectral bands (blue: 0.44 $\mu$m, green: 0.55 $\mu$m, red: 0.66 $\mu$m, NIR: 0.87 $\mu$m), with 6 scattering orders at most. The atmosphere model is mid-latitude summer (Anderson et al., 1986) and the aerosol model is rural (Shettle and Fenn, 1979). Specific optical properties were assigned per tree species. Here, DART-Lux is run with 800 samples per pixel and DART-FT is run with 62500 illumination rays per pixel, and 1000 discrete directions. DART-FT and DART-Lux BOA colour composite images are shown in Figure B.3.a, d. The associated scatter plot of BOA pixel reflectance (Figure B.4.a) gives {R-squared > 0.92 and bias ≈ 0.01}.

Densities of scatter points are shown by colours in order to stress that most points are on the diagonal. TOA colour composite images are shown in Figure E.3.b, e. The associated scatter plot of TOA pixel reflectance (Figure B.4.b) gives {R-squared ≈ 0.92 and bias ≈ 0.01}. Scatter points outside the diagonal are mainly due to DART-Lux Monte Carlo noises and to DART-FT discretization. By averaging the image resolution from 0.125 m to 1.0 m, which more or less mitigates these effects, scatter plots become more linear, with {R-square > 0.998 and bias ≈ 0.0002} (Figure B.4.c). We also assessed the BRF accuracy in the solar plane by computing the average absolute relative "DART-Lux - DART-FT" BRF difference

$$\bar{\varepsilon}=\frac{1}{N_{\theta_v}}\cdot\sum\nolimits_{\theta_v}\frac{|\rho_{\mathrm{DART-Lux}}(\theta_v)-\rho_{\mathrm{DART-FT}}(\theta_v)|}{\rho_{\mathrm{DART-FT}}(\theta_v)}\cdot 100\%$$

with $N_{\theta_v}$ viewing directions in the solar plane with zenith angle step $\Delta\theta_v = 2°$. Here, $\bar{\varepsilon}$ is 1.0% at BOA level and 0.8% at TOA level.

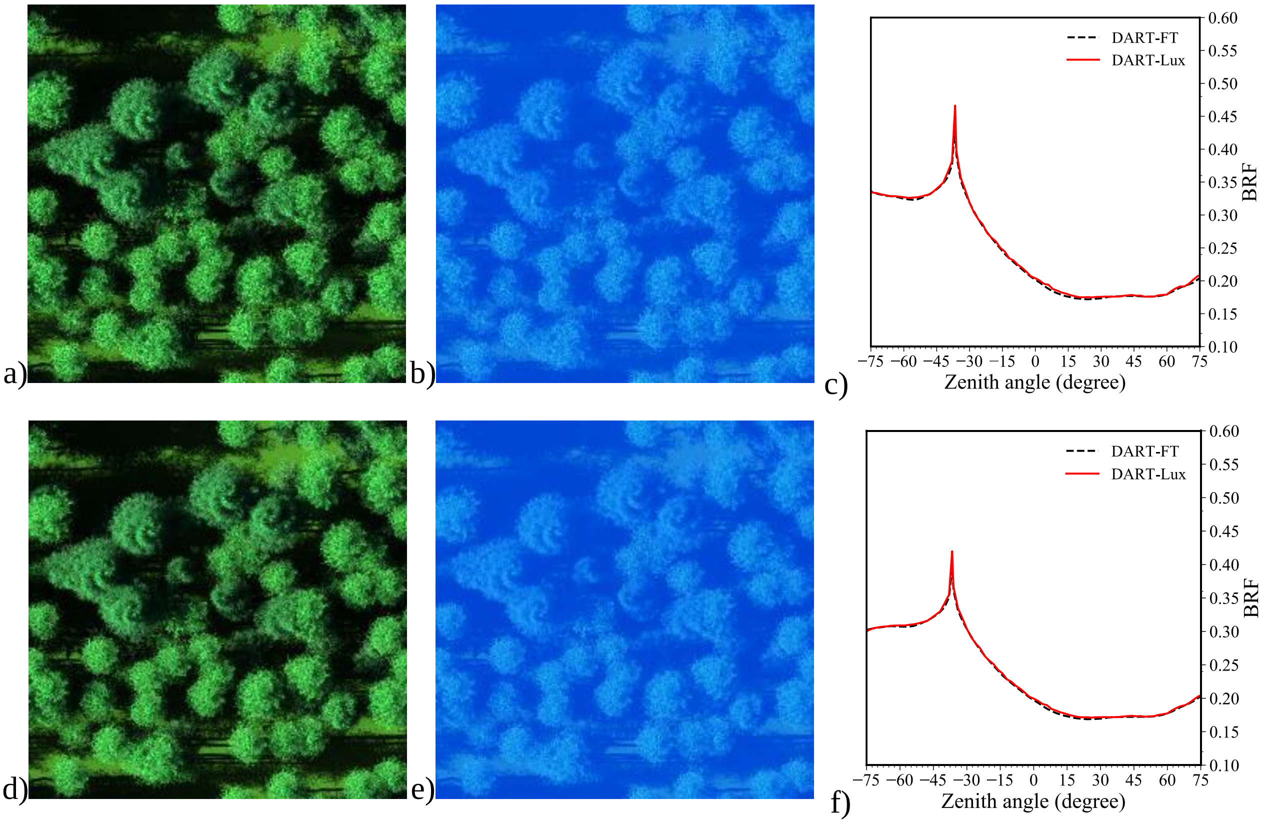

Figure B.3. Nadir colour composite images of the forest plot shown in Figure D.2. DART-FT BOA (a) and TOA (b) images. DART-Lux BOA (d) and TOA (e) images. DART-FT and DART-Lux BOA (c) and TOA (f) BRFs at NIR band in the solar plane, with 2° zenith angle step.

The results show that the hybrid method and DART-FT are consistent. In terms of efficiency, the hybrid method has two major advantages: much smaller computer time and RAM. In this simulation, DART-FT takes 86.35 hours and 305.5 Gb RAM on a server (Intel Xeon E5-2687W @ 3.1 GHz, 40 cores) for steps 2 and 4 in Figure 2.3 whereas the hybrid method takes only 2.3 minutes and 1.2 Gb RAM to simulate the spectral nadir image or the spectral radiance map (*i.e.*, steps 2, 4 and 6 take a total of 6.9 minutes). Compared to DART-FT, the hybrid method reduces the computer time by a factor of 750 and reduces the required RAM by a factor of 255. Since the atmospheric radiative transfer modelling for stratified 1D atmosphere in steps 1, 3 and 5 takes much less time than the Earth surface radiative transfer modelling in steps 2 and 4, the hybrid method greatly accelerates the simulation with homogeneous atmospheric effect.

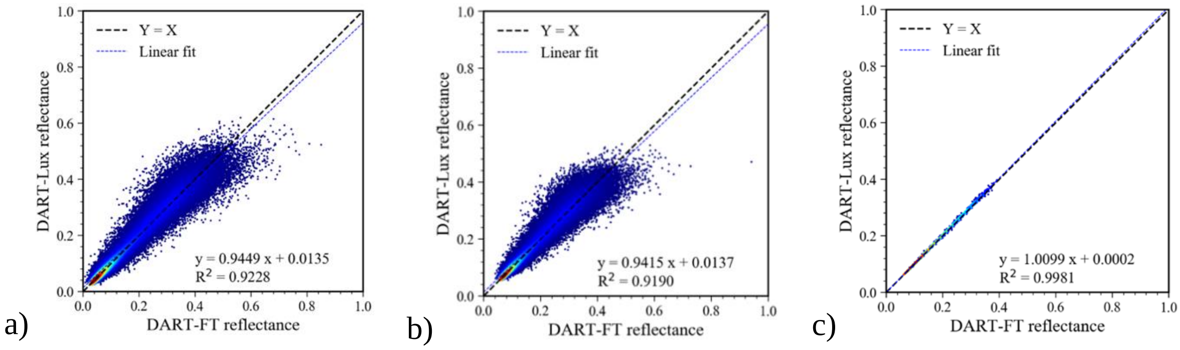

Figure B.4. Pixelwise comparison of DART-FT and DART-Lux nadir images at NIR band. a) BOA. 0.125 m resolution. b) TOA. 0.125 m resolution. c) TOA. 1.0 m resolution.

## B.2 Validation by intercomparison with MODTRAN

In the frame of the preparation of CNES and ISRO TRISHNA satellite mission, the accuracy and performance in the thermal infrared region is particularly important. In this context, we conducted an intercomparison with MODTRAN (brightness temperature accuracy 1 K) in [3.5 $\mu$m, 20 $\mu$m] region with realistic atmosphere profiles from ECMWF (European Centre for Medium-range Weather Forecasts) reanalysis dataset: ERA-Interim (https://apps.ecmwf.int/datasets/). These profiles include the pressure, temperature, specific humidity (mass of water vapour per kilogram of moist air, nearly equal to mass mixing ratio within a few percent) and $O_3$ mass mixing ratio (mass of ozone per kilogram of dry air) at 60 ECMWF model levels (https://www.ecmwf.int/en/forecasts/documentation-and-support/60-

model-levels) as well as the surface albedo, skin temperature over France (49°N, -1°W, 44°S, 7°E) and the Mediterranean Sea (37°N,12°W, 34°S, 26°E) from 01/06/2018 to 31/08/2018. These data were averaged over time and space and the vertical profiles were interpolated into 37 altitude levels (1 km interval from 0 to 25 km, and 5 km interval from 30 to 80 km) that are configured in both DART and MODTRAN. The number density profile $N_{m_i}(z)$ of other gases ($N_2$, $CO_2$, CO, $CH_4$, $N_2O$, $O_2$, $NH_3$, NO, $NO_2$, $SO_2$, $HNO_3$, $CFC_{12}$, $CFC_{13}$, $CFC_{14}$, $CFC_{22}$, $CFC_{113}$, $CFC_{114}$, $CFC_{115}$, $CLONO_2$, $HNO_4$, $CHCL_2F$, $CCL_4$, $N_2O_5$) and the relative density profile $\rho_m^s(z)$ of scattering gases are adjusted by MODTRAN based on the MIDLATSUM atmosphere and the actual pressure and temperature profile from ERA-Interim dataset.

Figure B.5.a shows the pressure, temperature, $H_2O$, $O_3$ and $CO_2$ number density profiles for three summer atmospheres in the mid-latitude region: France, Mediterranean Sea, and the standard MIDLATSUM atmosphere. Figure B.5.b shows the corresponding maximum difference values of profiles per altitude level. Temperature varies up to 10 K at around 11 km, water vapour mass varies up to 38% at the Earth surface and $O_3$ mass varies up to 40% at around 16 km. The averaged continental surface albedo and skin temperature of France are 0.132 and 292 K, respectively. For the Mediterranean Sea, they are 0.07 and 296 K, respectively.

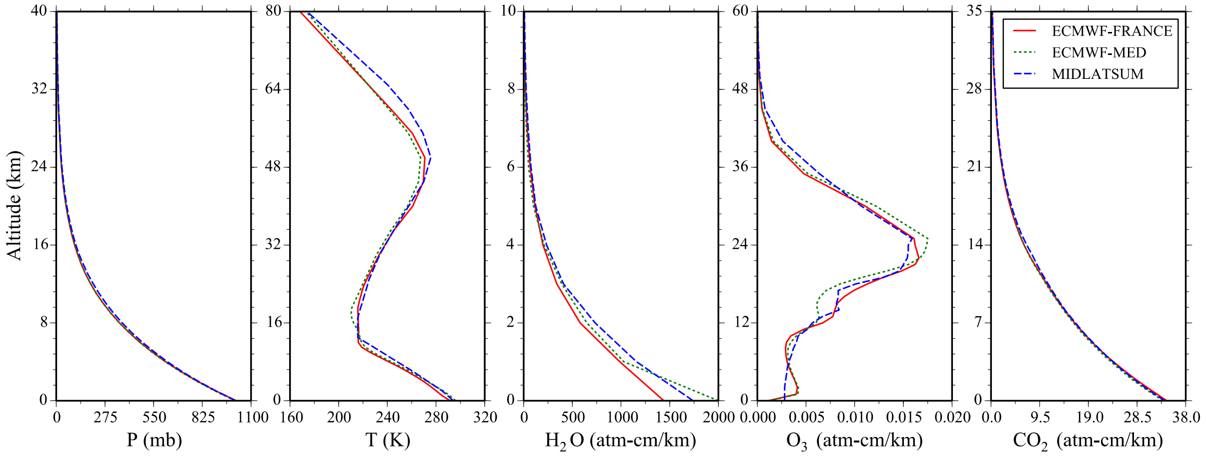

a)

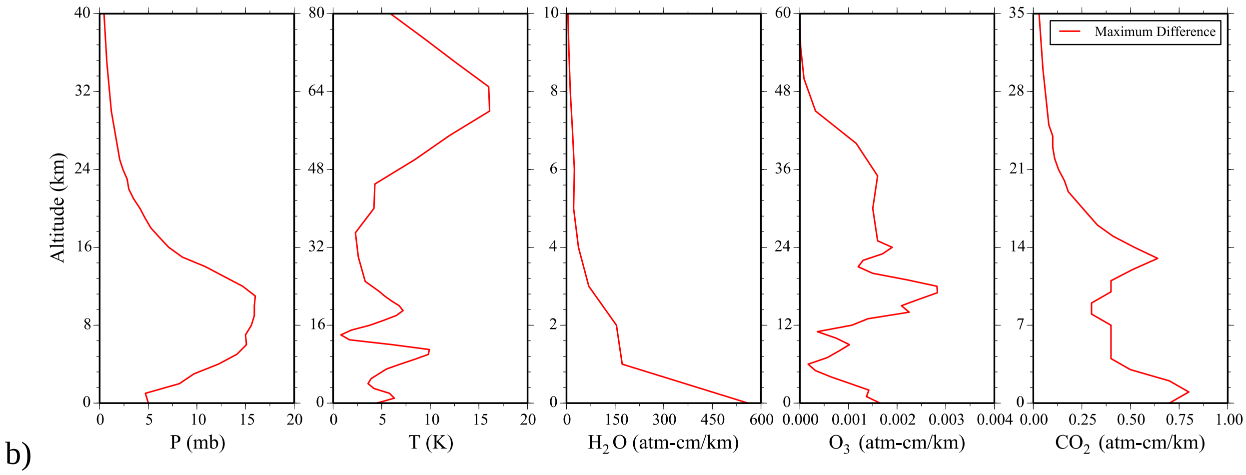

Figure B.5. a) Vertical profiles of pressure (mb), temperature (K), and $H_2O$, $O_3$ and $CO_2$ number densities (atm-cm/km) for three summer atmospheres: France, Mediterranean Sea and MIDLATSUM atmosphere. b) Maximum difference of vertical profiles.

DART and MODTRAN were run in full radiance mode (simulation with solar radiation and thermal emission), with the same sun viewing angle ($\theta_{\mathrm{sun}} = 30°$, $\varphi_{\mathrm{sun}} = 225°$), surface parameters, discrete altitude levels, pressure, temperature profiles and gas number density profiles. Eq. (E.2) indicates how the gas optical depth was adjusted in DART using the user-defined density profiles $N_{m_i}(z)$ and $\rho^s_m(z)$.

$$\tau^a_{m_i}(\lambda) = \begin{cases} -\ln\left(t^a_{m_i,DB}(\lambda)\right)\cdot\dfrac{\int_0^\infty \sigma^a_{m_i,DB}(\lambda,z)\cdot N_{m_i}(z)dz}{\int_0^\infty \sigma^a_{m_i,DB}(\lambda,z)\cdot N_{m_i,DB}(z)dz}, m_i = \mathrm{H_2O, CO_2, O_3, CH_4, N_2O} \\ -\ln\left(t^a_{m_i,DB}(\lambda)\right)\cdot\dfrac{\int_0^\infty \sigma^a_{m_i}(\lambda)\cdot N_{m_i}(z)dz}{\int_0^\infty \sigma^a_{m_i}(\lambda)\cdot N_{m_i,DB}(z)dz}, \qquad m_i \neq \mathrm{H_2O, CO_2, O_3, CH_4, N_2O} \end{cases} \qquad (B.2)$$

$$\tau^s(\lambda) = -\ln\left(t^s_{m,DB}(\lambda)\right)\cdot\frac{\int_0^\infty \rho^s_m(z)dz}{\int_0^\infty \rho^s_{m,DB}(z)dz}$$

Note that $m_i$ represents 13 gases ($H_2O$, $O_3$, $N_2$, $CO_2$, CO, $CH_4$, $N_2O$, $O_2$, $NH_3$, NO, $NO_2$, $SO_2$, $HNO_3$) and the sum of other minor gases ($CFC_{12}$, $CFC_{13}$, $CFC_{14}$, $CFC_{22}$, $CFC_{113}$, $CFC_{114}$, $CFC_{115}$, $CLONO_2$, $HNO_4$, $CHCL_2F$, $CCL_4$, $N_2O_5$).

Figure B.6 shows the MODTRAN and DART TOA nadir radiance spectra over France and Mediterranean Sea and the corresponding residuals. The mean absolute difference (MAE) of brightness temperature is 1.0 K for both cases. Table B.1 shows the differences between DART and MODTRAN for the thermal infrared bands of three Earth observation satellites for TOA thermal spectra over France, all of them are $\leq 0.2$ K. We can also note that the residuals between DART and MODTRAN over [3.5 $\mu$m, 5.0 $\mu$m] region where solar radiation contributes most to TOA radiance is relatively small (< 0.1 W/m$^2$/sr/$\mu$m for both cases). Also, the corresponding MAE of brightness temperature in this spectral region is less than 1.0 K.

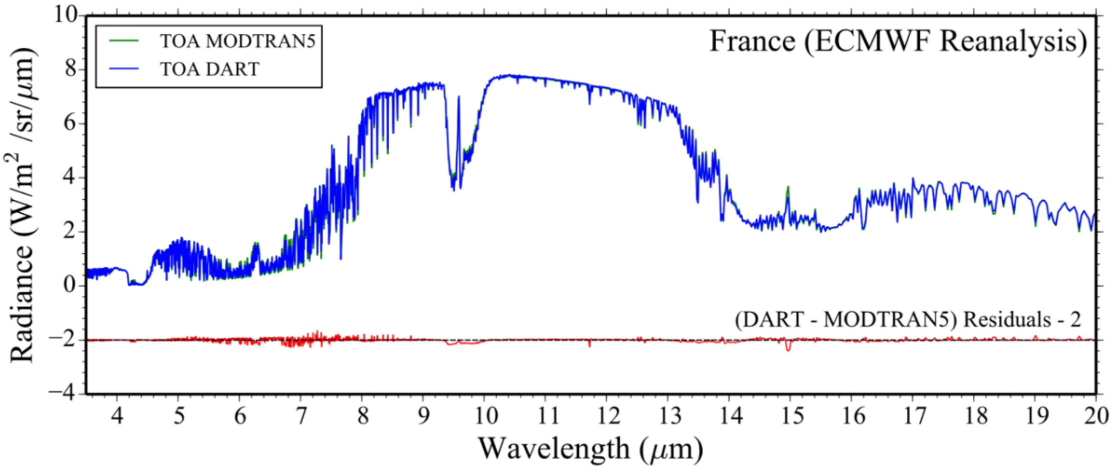

a)

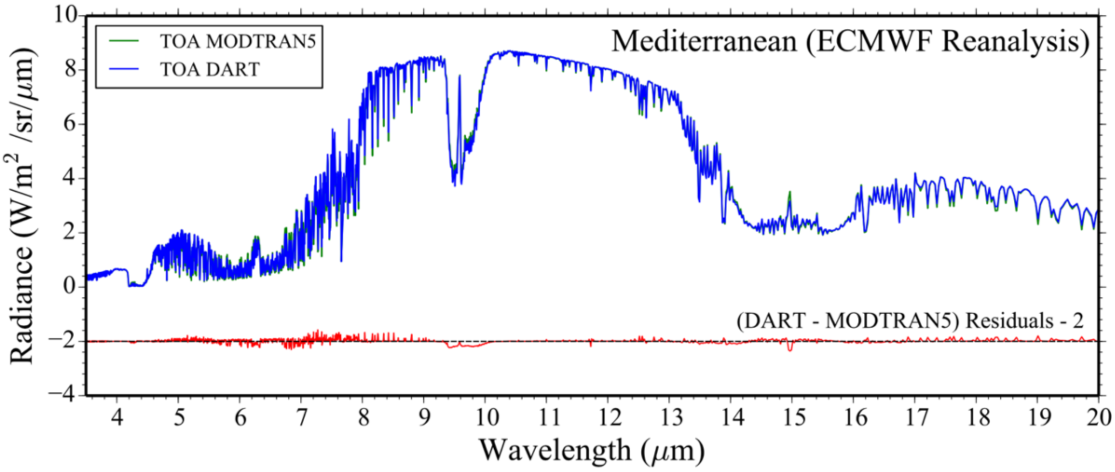

b)

Figure B.6. TOA spectral radiance of DART compared to MODTRAN with ECMWF reanalysis profile and surface parameter. a) France. b) Mediterranean Sea.

Table B.1. TOA brightness temperature difference (DIFF) between DART and MODTRAN in the TIR bands of three Earth observation satellite missions for realistic atmospheric profiles over France (Figure E.6.a).

| Satellite | Launch date | Organization | Central wavelength | Bandwidth | Sensitivity (NeDT) | DIFF |
|---|---|---|---|---|---|---|
| Trishna | Foreseen 2024-2025 | CNES+ISRO | 8.6 $\mu$m | 0.35 $\mu$m | 0.3 K@300 K | 0.13 K |
| | | | 9.1 $\mu$m | 0.35 $\mu$m | 0.3 K@300 K | 0.11 K |
| | | | 10.3 $\mu$m | 1.0 $\mu$m | 0.3 K@300 K | 0.04 K |
| | | | 11.5 $\mu$m | 1.0 $\mu$m | 0.3 K@300 K | 0.19 K |
| Landsat 8 | 2013 | NASA | 10.9 $\mu$m | 0.6 $\mu$m | 0.4 K@300 K | 0.20 K |
| | | | 12.0 $\mu$m | 1.0 $\mu$m | 0.4 K@300 K | 0.17 K |
| Sentinel-3 | 2016 | ESA | 3.74 $\mu$m | 0.38 $\mu$m | 0.08 K@270 K | 0.15 K |
| | | | 10.95 $\mu$m | 0.9 $\mu$m | 0.05 K@270 K | 0.18 K |
| | | | 12.0 $\mu$m | 1.0 $\mu$m | 0.05 K@270 K | 0.15 K |

# Annex C

# Monte Carlo integration

Many of the integrals arise in the radiative transfer modelling are difficult or impossible to evaluate directly. For example, to compute the exit radiance from a surface according to Eq. (1.21), we must integrate the product of the incident radiance and the BRDF over the upper hemisphere. This is almost impossible because the incident radiance distribution is never available in close form due to the complex direct and indirect illumination in realistic environment. Monte Carlo integration methods provide effective solution to this kind of problem. They use randomness to evaluate integrals with a convergence rate that is independent of the dimensionality of the integrand. It is robust and flexible to deal with smooth or discontinuous, low- or high-dimensional integrand. This chapter first reviews the basic concepts of probability theory. Then, we introduce the Monte Carlo integration and the variance reduction methods that have proven useful in radiative transfer modelling.

Good references about the probability theory and the Monte Carlo methods are (Hammersley, 2013), (Rubinstein and Kroese, 2016) and (Kalos and Whitlock, 2009). (Veach, 1997) and (Pharr et al., 2016) are good sources of Monte Carlo methods and techniques that are used in the radiative transfer modelling.

## C.1 A review of probability theory

### C.1.1 Random variables

A *random event* is an event with a countable set of random outcomes. *Probability* is a numerical measure of the chance of happening of the event, it is a number lying between 0 and 1, both inclusive. The notation for probability of event $E_A$ is $\mathbb{P}(E_A)$. Also, the notation for the probability of event $E_A$ on condition that event $E_B$ happens is $\mathbb{P}(E_A|E_B)$, it is also called the *conditional probability* of $E_A$ given $E_B$.

In many cases, the outcome of a random event can be mapped into a numerical value, such value is called *random variable*. We will generally use capital letter to denote random numbers, with exceptions made for a few Greek symbols that represent special random variables. The random variable $X$ can be discrete (*e.g.*, $X \in \{1, 2, 3, 4, 5, 6\}$ in dice roll game) or continuous (*e.g.*, $X \in [0, 360]$ when one chooses a random horizonal direction]. Applying one-to-one mapping function $f$ to a random variable $X$ results another random variable $Y$:

$$Y = f(X)$$

In the radiative transfer modelling, continuous variables are common, such as the directional radiance, the BRDF, the scattering phase function. However, there are still moments we need to deal with discrete variables. For example, we might need to select a random light source from a group of light sources according to their emission power. We might need to select a random pixel among all pixels on the image plane. In these cases, we map the $n$ discrete variables $X_i$ ($i \in \{1, 2, 3, \cdots, n\}$) that represent the discrete random events to a continuous, uniformly distributed random variable $\xi \in [0, 1]$, *i.e.*, $\xi = f(X_i)$ (Pharr et al., 2016), choosing $X_i$ if

$$\sum_{j=1}^{i-1} \mathbb{P}(X_j) \leq \xi < \sum_{j=1}^{i} \mathbb{P}(X_j)$$

Since the discrete random variables in the radiative transfer modelling can be always converted to the continuous random variables, below, all random variables are supposed to be continuous.

### C.1.2 Probability distributions

The random variable $X$ is associated with the *cumulative distribution function* (CDF) $P_X(x)$ that is the probability that a value from the variable's distribution is less than or equal to some value $x$.

$$P_X(x) = \mathbb{P}(X \leq x)$$

The derivate of the cumulative distribution function is the *probability density function* (PDF) $p(x)$ that describes the relative likelihood of the random variable to have some value $x$.

$$p(x) = \frac{dP_X(x)}{dx}$$

The probability density function, the cumulative distribution function and the probability are related by

$$\mathbb{P}(a \leq X \leq b) = \int_a^b p(x)dx = P_X(b) - P_X(a)$$

For a list of random variables $X_1, \cdots, X_n$, we can accumulate them into a *random vector* $\hat{X} = (X_1, \cdots, X_n)$. The corresponding notations for random vector are the *joint cumulative distribution function*

$$P_X(\hat{x}) = P_X(x_1, \cdots, x_n) = \mathbb{P}(X_i \leq x_i, \forall\, i = 1, \cdots, n)$$

and the *joint probability density function*

$$p(\hat{x}) = p(x_1, \cdots, x_n) = \frac{\partial^n P_X(x_1, \cdots, x_n)}{\partial x_1 \cdots \partial x_n}$$

So, for any Lebesgue measurable subset $\mathcal{D}_n \in \mathbb{R}^n$ ($\mathbb{R}$ is the set of all real numbers), we have the relationship:

$$\mathbb{P}(\hat{x} \in \mathcal{D}_n) = \int_{\mathcal{D}_n} p(x_1, \cdots, x_n)\, dx_1 \cdots dx_n$$

Suppose we have another $n$-dimensional random vector $\hat{Y} = f(\hat{X})$ that is the one-to-one mapping of $\hat{X}$ by the bijection $f$ ($Y_i = f_i(\hat{X}), \forall\, i = 1, \cdots, n$). The corresponding joint probability density function is $p(\hat{y})$. The two probability densities are then related by

$$p(\hat{y}) = p\big(f(\hat{x})\big) = \frac{p(\hat{x})}{\left|\mathcal{J}_f(\hat{x})\right|}$$

where $\left|\mathcal{J}_f(\hat{x})\right|$ is the absolute value of the Jacobian determinant of bijection $f$:

$$\mathcal{J}_f(\hat{x}) = \frac{\partial(f_1, \cdots, f_n)}{\partial(x_1, \cdots, x_n)} = \begin{bmatrix} \frac{\partial f_1}{\partial x_1} & \cdots & \frac{\partial f_1}{\partial x_n} \\ \vdots & \ddots & \vdots \\ \frac{\partial f_n}{\partial x_1} & \cdots & \frac{\partial f_n}{\partial x_n} \end{bmatrix}$$

### C.1.3 Marginal and conditional distributions

For a list of random variables $X_1, \cdots, X_n$, if it so happens that the joint probability density function is the product of the probability density function of each variable

$$p(x_1, \cdots, x_n) = \prod_{i=1}^{n} p(x_i)$$

these random variables are so called *independent*. Otherwise, some random variables can be dependent, in this case, it is necessary to introduce the *marginal probability density function* and the *conditional probability density function*.

Let $X, Y$ be a pair of random variables, the corresponding joint probability density function is $p(x, y)$. The marginal probability density function of variable $X$ is defined as the integral of $p(x, y)$ over all values of variable $Y$

$$p(x) = \int_y p(x, y) dy$$

while the conditional probability density function of variable $Y$ given $X$ is related by

$$p(y|x) = \frac{p(x, y)}{p(x)}$$

The corresponding *marginal cumulative distribution function* and the *conditional cumulative distribution function* are represented by $P_X(x) = \mathbb{P}(X \leq x)$ and $P_{Y|X}(y|x) = \mathbb{P}(Y \leq y|X = x)$, respectively.

The marginal probability density function of variable $Y$ and the conditional probability density function $p(x|y)$ can be derived in the similar way. We can write another useful identity:

$$p(x, y) = p(x) \cdot p(y|x) = p(y) \cdot p(x|y)$$

### C.1.4 Expected value and variance

The *expected value* or the *expectation* of a random variable $X$ is defined as the weighted average of all possible values:

$$\mathbb{E}(X) = \int_x x \cdot p(x) dx$$

Also, the expected value of a random variable $Y = f(X)$ mapping from $X$ is defined as

$$\mathbb{E}(Y) = \mathbb{E}\big(f(X)\big) = \int_x f(x) \cdot p(x) dx$$

The expected value scales linearly with a multiplicative constant

$$\mathbb{E}\big(a \cdot f(X)\big) = a \cdot \int_x f(x) \cdot p(x) dx = a \cdot \mathbb{E}\big(f(X)\big)$$

For a list of random variables $\hat{Y} = f\big(\hat{X}\big), \hat{X} = (X_1, \cdots, X_n)$, the expected value of the sum of random variables $\mathbb{E}(\sum_{i=1}^{n} f(X_i))$ is equal to the sum of the expected value of individual random variable $\sum_{i=1}^{n} \mathbb{E}\big(f(X_i)\big)$ (Eq. (C.1)).

$$\begin{aligned}
\mathbb{E}\left(\sum_{i=1}^{n} f(X_i)\right) &= \int_{x_1} \dots \int_{x_n} \left(\sum_{i=1}^{n} f(x_i)\right) \cdot p(x_1, \dots, x_n) dx_1 \dots dx_n \\
&= \sum_{i=1}^{n} \int_{x_1} \dots \int_{x_n} f(x_i) \cdot p(x_1, \dots, x_n) dx_1 \dots dx_n \\
&= \sum_{i=1}^{n} \int_{x_i} f(x_i) \cdot p(x_i) dx_i \\
&= \sum_{i=1}^{n} \mathbb{E}\big(f(X_i)\big)
\end{aligned} \tag{C.1}$$

where $p(x_i)$ is the marginal probability density function of $x_i$. If variables $X_1, \cdots, X_n$ are independent, we have expected value of the product of random variables $\mathbb{E}(\prod_{i=1}^{n} f(X_i))$ is equal to the product of the expected value of individual random variable $\prod_{i=1}^{n}\mathbb{E}\big(f(X_i)\big)$ (Eq. (C.2)).

$$\begin{aligned}\mathbb{E}\left(\prod_{i=1}^{n} f(X_i)\right) &= \int_{x_1} \dots \int_{x_n} \left(\prod_{i=1}^{n} f(x_i)\right) \cdot p(x_1, \dots, x_n) dx_1 \dots dx_n \\ &= \int_{x_1} \dots \int_{x_n} \left(\prod_{i=1}^{n} f(x_i) \cdot p(x_i)\right) dx_1 \dots dx_n \\ &= \prod_{i=1}^{n} \int_{x_i} f(x_i) \cdot p(x_i) dx_i \\ &= \prod_{i=1}^{n} \mathbb{E}\big(f(X_i)\big)\end{aligned} \tag{C.2}$$

The *variance* is a measure of dispersion of a random variable. Let a random variable $Y = f(X)$ mapping from $X$, its variance is defined as:

$$\begin{aligned}\mathbb{V}(Y) &= \mathbb{E}\left(\big(Y - \mathbb{E}(Y)\big)^2\right) \\ &= \int_{x} \left[f(x) - \mathbb{E}\big(f(X)\big)\right]^2 \cdot p(x) dx \\ &= \int_{x} \left[f(x)^2 - 2 \cdot f(x) \cdot \mathbb{E}\big(f(X)\big) + \mathbb{E}\big(f(X)\big)^2\right] \cdot p(x) dx \\ &= \int_{x} f(x)^2 \cdot p(x) dx - 2 \cdot \mathbb{E}\big(f(X)\big) \cdot \int_{x} f(x) \cdot p(x) dx + \mathbb{E}\big(f(X)\big)^2 \\ &= \mathbb{E}(Y^2) - \mathbb{E}(Y)^2\end{aligned} \tag{C.3}$$

According to its definition, the variance is scaled by the square of a constant if all variables are scaled by this constant

$$\mathbb{V}(a \cdot Y) = \mathbb{E}\left(\big(a \cdot Y - \mathbb{E}(a \cdot Y)\big)^2\right) = a^2 \cdot \mathbb{V}(Y)$$

For a list of independent random variables $\hat{Y} = f\big(\hat{X}\big)$, $\hat{X} = (X_1, \cdots, X_n)$, the variance of the sum of random variables $\mathbb{V}(\sum_{i=1}^{n} f(X_i))$ is equal to the sum of the variance of individual random variable $\sum_{i=1}^{n} \mathbb{V}\big(f(X_i)\big)$ (Eq. (C.4)).

$$\begin{aligned}\mathbb{V}\left(\sum_{i=1}^{n} f(X_i)\right) &= \int_{x_1} \dots \int_{x_n} \left(\sum_{i=1}^{n}\left[f(x_i) - \mathbb{E}\big(f(X_i)\big)\right]\right)^2 \cdot p(x_1, \dots, x_n) dx_1 \dots dx_n \\ &= \sum_{i=1}^{n}\sum_{i'=1}^{n} \int_{x_1} \dots \int_{x_n} \left[f(x_i) - \mathbb{E}\big(f(X_i)\big)\right]\left[f(x_{i'}) - \mathbb{E}\big(f(X_{i'})\big)\right] \\ &\qquad \cdot p(x_1, \dots, x_n) dx_1 \dots dx_n \\ &= \sum_{i}^{n} \int_{x_i} \left[f(x_i) - \mathbb{E}\big(f(X_i)\big)\right]^2 \cdot p(x_i) dx_i \\ &= \sum_{i=1}^{n} \mathbb{V}\big(f(X_i)\big)\end{aligned} \tag{C.4}$$

For a pair of random variables $X, Y$, their correlation (joint variability) is measured by the *covariance* $Cov(X, Y)$.

$$\begin{aligned}Cov(X, Y) &= \mathbb{E}([X - \mathbb{E}(X)] \cdot [Y - \mathbb{E}(Y)]) \\ &= \mathbb{E}\big(XY - X\mathbb{E}(Y) - Y\mathbb{E}(X) + \mathbb{E}(X)\mathbb{E}(Y)\big) \\ &= \mathbb{E}(XY) - \mathbb{E}(X)\mathbb{E}(Y)\end{aligned}$$

The covariance is zero if $X$ and $Y$ is independent. The variance is a special case of the covariance in which the two variables are identical, that is

$$Cov(X, X) = \mathbb{V}(X)$$

The upper boundary of the covariance is described by the famous *Cauchy-Schwarz inequality*

$$Cov(\mathrm{X}, \mathrm{Y}) \leq \sqrt{\mathbb{V}(\mathrm{X}) \cdot \mathbb{V}(\mathrm{Y})}$$

For a list of random variables $\hat{X} = (X_1, \cdots, X_n)$, the variance of the sum of random variables $\mathbb{V}(\sum_{i=1}^{n} X_i)$ can be alternatively represented by

$$\mathbb{V}\left(\sum_{i=1}^{n} X_i\right) = \sum_{i=1}^{n}\sum_{i'=1}^{n} Cov(X_i, X_{i'}) = \sum_{i=1}^{n} \mathbb{V}(X_i) + \sum_{i=1}^{n}\sum_{i'=1, i' \neq i}^{n} Cov(X_i, X_{i'}) \tag{C.5}$$

If variables $X_1, \cdots, X_n$ are independent, $\sum_{i=1}^{n}\sum_{i'=1,i'\neq i}^{n} Cov(X_i, X_{i'}) = 0$, Eq. (C.5) can lead to the same conclusion as Eq. (C.5).

# C.2 Monte Carlo integration

## C.2.1 The basic Monte Carlo estimator

The idea of the Monte Carlo estimator is to evaluate an integral

$$\int_x f(x)dx$$

by independently drawing $N$ random samples $X_1, \cdots, X_N$ according to some probability density function $p(x)$ and then computing the estimate of the integral by:

$$F_N = \frac{1}{N}\sum_{i=1}^{N}\frac{f(X_i)}{p(X_i)} \tag{C.6}$$

The *estimate* $F_N$ of the Monte Carlo estimator is a random variable whose properties depend on the number of samples. $p(x)$ must be positive when ever $f(x)$ is non-zero. In average, $F_N$ gives the correct estimate of the integral, we have

$$\begin{aligned}
\mathbb{E}(F_N) &= \mathbb{E}\left(\frac{1}{N}\sum_{i=1}^{N}\frac{f(X_i)}{p(X_i)}\right) \\
&= \frac{1}{N}\sum_{i=1}^{N}\mathbb{E}\left(\frac{f(X_i)}{p(X_i)}\right) \\
&= \frac{1}{N}\sum_{i=1}^{N}\int_x \frac{f(x)}{p(x)}\cdot p(x)dx \\
&= \int_x f(x)dx
\end{aligned}$$

Eq. (C.6) can be extended for $n$-dimensional integral

$$\int_{\mathcal{D}_n} f(x_1, \cdots, x_n)\, dx_1 \cdots dx_n$$

by independently drawing $N$ vector random samples $\hat{X}_1, \cdots, \hat{X}_N$ according to the joint probability density function $p(x_1, \cdots, x_n)$. The corresponding Monte Carlo estimator is

$$F_N = \frac{1}{N}\sum_{i=1}^{N}\frac{f(\hat{X}_i)}{p(\hat{X}_i)} = \frac{1}{N}\sum_{i=1}^{N}\frac{f\left(X_1^{(i)}, \cdots, X_n^{(i)}\right)}{p\left(X_1^{(i)}, \cdots, X_n^{(i)}\right)}$$

### C.2.2 Sampling random variables

To compute the estimate $F_N$ of a Monte Carlo estimator (Eq. (C.6)), it is necessary to draw random samples from the predefined probability distribution. The most common approach is called the *inversion method.* Let $P_X(x)$ the cumulative distribution function of a distribution $p(x)$. A random sample $X$ can be computed through the inverse cumulative distribution function using a uniformly distributed variable $\xi$ in $[0,1)$ (probability density function $p(u_\xi) = 1$).

$$X = P_X^{-1}(\xi)$$

It is easy to verify that the random sample $X$ has the required probability density function $p(x)$.

$$p(x) = p(u_\xi)\left|\frac{du_\xi}{dx}\right| = \frac{dP_X(x)}{dx}$$

This method can also be extended to draw random vector samples $\hat{X} = (X_1, \cdots, X_n)$, by computing the conditional and marginal distributions and inverting each random sample $X_i$ separately. It can be generally represented by:

$$\hat{X} = P_X^{-1}(\hat{\xi}) \tag{C.7}$$

We give an example of a two-dimensional random sample $X, Y$, the corresponding marginal cumulative distribution function and conditional cumulative distribution function are $P_X(x)$ and $P_{Y|X}(y|x)$, respectively. The samples are derived using two uniformly distribution variables $\xi_x, \xi_y$ in $[0,1)^2$.

$$\begin{aligned} X &= P_X^{-1}(\xi_x) \\ Y &= P_{Y|X}^{-1}(\xi_y|X) \end{aligned} \tag{C.8}$$

Sometimes, there is no analytical expression of the probability density function, or its analytical integration is impossible. We can construct a piecewise-constant function that has a constant value in each small region piece in the distribution space and draw continuous random samples with the inversion method. Considering a case of a two-dimensional function $f^{(i,j)}(x,y)$ defined over $[0,1]^2$ by an array of $n_x \times n_y$ values. $c_{i,j}$ ($i = 0, \cdots, n_x - 1$ and $j = 0, \cdots, n_y - 1$) denotes the value of $f^{(i,j)}(x,y)$ over the region $x \times y = [\,i/n_x, (i+1)/n_x) \times [j/n_y, (j+1)/n_y)$. We have:

$$
\begin{aligned}
p^{(i,j)}(x,y) &= \frac{f^{(i,j)}(x,y)}{\int_0^1\int_0^1 f^{(i,j)}(x,y)dxdy} = \frac{c_{i,j}}{\frac{1}{n_x \cdot n_y}\sum_{i=1}^{n_x}\sum_{j=1}^{n_y} c_{i,j}} \\
p^{(i)}(x) &= \int_0^1 p^{(i,j)}(x,y)dy = \frac{n_x\sum_{j=1}^{n_y} c_{i,j}}{\sum_{i=1}^{n_x}\sum_{j=1}^{n_y} c_{i,j}} \\
p^{(j)}(y|x) &= \frac{p^{(i,j)}(x,y)}{p^{(i)}(x)}
\end{aligned}
\tag{C.9}
$$

Both marginal and conditional distributions are piecewise-constant, the integrated cumulative distribution function are thus piecewise and continuous, with constant slope in each region.

$$
\begin{aligned}
P_X(x) &= \int_0^x p^{(i)}(x)dx \\
P_{Y|X}(y|x) &= \int_0^y p^{(j)}(y|x)dy
\end{aligned}
$$

Then, a pair of continuous random samples $X, Y$ are drawn by Eq. (C.10) using two uniformly distribution variables $\xi_x, \xi_y$ in $[0,1)^2$.

$$
\begin{aligned}
X &= P_X^{-1}(\xi_x) = \frac{i}{n_x} + \frac{\xi_x - P_X\left(\frac{i}{n_x}\right)}{p^{(i)}(x)}, \forall\ \frac{i}{n_x} \le X \le \frac{i+1}{n_x} \\
Y &= P_{Y|X}^{-1}\left(\xi_y|X\right) = \frac{j}{n_y} + \frac{\xi_y - P_{Y|X}\left(\frac{j}{n_y}|X\right)}{p^{(j)}(y|x)}, \forall\ \frac{i}{n_x} \le X \le \frac{i+1}{n_x}, \frac{j}{n_y} \le Y \le \frac{j+1}{n_y}
\end{aligned}
\tag{C.10}
$$

In case that the cumulative distribution function is not invertible whereas it can be represented by the weighted sum of invertible element cumulative distribution functions $F_i(x)$ (Eq. (C.11)), a typical example is the double Henyey-Greenstein phase function (Eq. (1.13)). The random sample can be draw with the *composition method* (Rubinstein and Kroese, 2016).

$$
P_X(x) = \sum_{i=1}^{n} w_i \cdot F_i(x) \tag{C.11}
$$

where the weight satisfies

$$
w_i > 0\ \forall\ i, \qquad \sum_{i=1}^{n} w_i = 1
$$

Let $F_i(x)$ be the cumulative distribution function of variable $X_i$, and let $Y$ be a discrete random variable with $\mathbb{P}(Y = i) = w_i$, independent of $X_i$, for $1 \le i \le n$. In order to generate $X$ from

$P_X(x)$, we first generate $Y$ with the inversion method or the *alias method* (Rubinstein and Kroese, 2016) and then, given $Y = i$, generate $X_i$ from $F_i(x)$ with the inversion method (Eq. (C.12)).

$$X = \sum_{i=1}^{n} F_i^{-1}(\xi_i) \cdot I_{\{Y=i\}} \tag{C.12}$$

where $I_{\{Y=i\}}$ is an indicator function, it returns 1 if $Y = i$ and returns 0 otherwise. $\xi_i$ is a random variable uniformly distributed in $[0, 1)$. Similarly for multi-dimensional case $P_X(\hat{x}) = \sum_{i=1}^{n} w_i \cdot F_i(\hat{x})$, $\hat{X}$ is sampled by $\hat{X} = \sum_{i=1}^{n} F_i^{-1}(\hat{\xi}_i) \cdot I_{\{Y=i\}}$.

Another basic approach to generate random samples are the *acceptance-rejection method* proposed by Stan Ulam and John von Neumann, it is adapted for sampling any distributions without the explicitly knowledge of the probability density function or the cumulative distribution function. A disadvantage is that this method may be less efficient, that is, many trials are rejected before one sample is accepted. Let a variable $X$ with an arbitrary probability density $p(x)$. We can always bound it with a proposed probability density $p^*(x)$ using a constant $C$, that is

$$p(x) \leq Cp^*(x), \forall\, x$$

Then, a pair of random variables $X, \xi$ are repeatedly sampled according to $p(x)$ and the uniform distribution on $[0, 1)$, respectively. $X$ is accepted until the point $\left(X, Y = \xi Cp^*(X)\right)$ lies under $p(X)$. It is easy to verify that the sampled $X$ has distribution identical to $p(x)$ since the probability that the sampled points $(X, Y)$ are enclosed by the region $y = 0$, $y = p(x)$, $x = a$, $x = b$ is equal to the enclosed area $\int_a^b p(x)dx$. Also, the closer $Cp^*(x)$ to $p(x)$, the more efficient the acceptance-rejection method, since the sample $X$ is less likely to be rejected. This method can also be extended to multi-dimensional sampling.

## C.2.3 Performance of estimators

Eq. (C.6) are standard ways to estimate the value of an integral with random numbers, namely the basic Monte Carlo estimator. However, there are a variety of Monte Carlo estimators with different mathematical forms and different sample generating methods. They can be generally represented by:

$$F_N = F_N(X_1, \cdots, X_N)$$

where the $X_i$ are random variables, they are not necessarily independent and can have different distributions, $N$ is the sample size. It is necessary to design or to choose the desirable estimator $F_N$ according to the application context. Thus, knowledge of their performance is very useful. Here we review some important properties of Monte Carlo estimators.

**Bias.** The objective of a Monte Carlo estimator is to evaluate the *estimand* $F$(a quantity of interest). And a particular value of variable $F_N$ is called an *estimate*. The difference between $F_N$ and $F$ is called *error* and the bias is defined as the expected value of the error.

$$\beta(F_N) = \mathbb{E}(F_N - F) = \mathbb{E}(F_N) - F \tag{C.13}$$

An estimator is called *unbiased* if $\beta(F_N) = 0, \forall\, N \geq 1$. Otherwise, it is called *biased.*

**Consistency.** An estimator is called *consistent* if the estimate $F_N$ converges to $F$ as $N$ approaches infinity, that is:

$$\mathbb{P}\left(\lim_{n\to\infty}(F_N - F)\right) = 1$$

For an estimator to be consistent, it is sufficient to have its expected value and variance go to zero when the sample size increases, that is

$$\lim_{n\to\infty}\mathbb{E}(F_N) = \lim_{n\to\infty}\mathbb{V}(F_N) = 0$$

**Convergence rate.** Usually, a desirable estimator should not be introduced with an expense of a large variance, the *convergence rate* describes how fast the *standard error* $\sigma$ of estimates decreases (Hammersley, 2013). For a basic Monte Carlo estimator with independent samples $X_i$, we have:

$$\mathbb{V}(F_N) = \mathbb{V}\left(\frac{1}{N}\sum_{i=1}^{N}\frac{f(X_i)}{p(X_i)}\right) = \frac{1}{N^2}\mathbb{V}\left(\sum_{i=1}^{N}\frac{f(X_i)}{p(X_i)}\right) = \frac{1}{N}\mathbb{V}\left(\frac{f(X_i)}{p(X_i)}\right) = \frac{1}{N}\sigma^2\left(\frac{f(X)}{p(X)}\right)$$

Then, the convergence rate for a basic Monte Carlo estimator is $O\left(1/\sqrt{N}\right)$ since:

$$\sigma(F_N) = \frac{1}{\sqrt{N}}\sigma\left(\frac{f(X)}{p(X)}\right)$$

**Efficiency.** It is always possible to reduce the standard error of a Monte Carlo estimator by increasing the number of samples. However, to decrease the standard error of an estimator with convergence rate $O\left(1/\sqrt{N}\right)$ by a factor of $k$, the sample size needs to be increased $k^2$-fold, that is, the computer time is increased $k^2$-fold. An efficient Monte Carlo estimator optimizes both the convergence rate and the sample size. Following (Hammersley, 2013; Veach, 1997), the *efficiency* is defined as inversely proportional to the product of the variance and the time.

$$\epsilon(F_N) = \frac{1}{\mathbb{V}(F_N) \cdot \mathbb{T}(F_N)} \tag{C.14}$$

# C.3 Variance reduction method

The design of efficient estimators is a fundamental research of Monte Carlo integration. A variety of methods have been developed to improve the efficiency of estimators which are commonly called *variance-reduction method* (*cf.* (Hammersley, 2013; Kalos and Whitlock, 2009; Rubinstein and Kroese, 2016; Veach, 1997)), such as the stratified sampling, importance sampling, adaptive sampling, antithetic variates, *etc*. This section presents some most important unbiased variance reduction methods in Monte Carlo radiative transfer modelling.

## C.3.1 Importance sampling

The *importance sampling* refers to the sampling of a random variable according to the importance of the distribution of the integrand $f(x)$, that is, the probability density function $p(x)$ is similar to $f(x)$. Ideally:

$$p(x) = \frac{f(x)}{\int_x f(x)dx}$$

It leads to an estimator with zero variance since:

$$F_N = \frac{1}{N}\sum_{i=1}^{N}\frac{f(X_i)}{p(X_i)} = \int_x f(x)dx$$

is equal to the desired integral for any sample points $X_i$ and for any sample size.

Unfortunately, it is not practical because we must evaluate the desired integral in advance in order to derive the probability density whereas the integral evaluation is the objective of the estimator. Nevertheless, it proves that the variance can be reduced if $p(\hat{x})$ is close to $f(\hat{x})$ for one- and multi-dimensional estimators. There are several strategies to reproduce a probability that is close to $f(x)$. For low-dimensional integration, we can construct a discrete approximation of $f(\hat{x})$, such as a piecewise-constant function, then the probability densities of each variable can be derived similarly as in Eq. (C.9). Another commonly used strategy is to discard or to approximate some parameters in the integrand. For example, we can discard the incident radiance in the integration Eq. (1.21). We can approximate the product of microfacet distribution function and the masking-shadowing function by the *Schlick approximation* (Schlick, 1994).

Since the most distributions or functions in the radiative transfer modelling are not uniform or isotropic, the importance sampling is widely used. It is particularly useful for some distribution where the probability density is large in a small region. A typical case is the estimate of exit radiance from a specular surface.

## C.3.2 Multiple importance sampling

The *multiple importance sampling* was introduced by (Veach, 1997) to increase the reliability and efficiency of Monte Carlo integration, especially for high-dimensional integral problem such as the radiative transfer modelling. The idea is to combine more than one importance sampling estimator to evaluate the same integral. It is very useful when the distributions of the values of parameters in the integrand are not known at the time the estimator is designed. In this case, it is difficult to predict a probability density that is similar to the integrand. For example, we can construct two importance sampling estimators to estimate the integral of Eq. (1.21), the first one is constructed by discarding the incident radiance and the second one is constructed by discarding the BRDF. An estimate of the first estimator is like:

$$L_r(\Omega) = \frac{L(\Omega') \cdot f_r(\Omega' \to \Omega) \cdot \cos\theta'}{p(\Omega')}, \text{with } p(\Omega') = \frac{L(\Omega') \cdot \cos\theta'}{\int_{2\pi^+} L(\Omega') \cdot \cos\theta' \, d\Omega'}$$

and an estimate of the second is like:

$$L_r(\Omega) = \frac{L(\Omega') \cdot f_r(\Omega' \to \Omega) \cdot \cos\theta'}{p(\Omega')}, \text{with } p(\Omega') = \frac{f_r(\Omega' \to \Omega) \cdot \cos\theta'}{\int_{2\pi^+} f_r(\Omega' \to \Omega) \cdot \cos\theta' \, d\Omega'}$$

It happens that the first estimator is far more efficient if the light source is small and the BRDF is diffuse, and the second estimator is far better when the light source is large and the BRDF is specular. In this case, we can combine the two estimators by some weights that are proportional to the efficiency of the estimators.

The general form of multiple importance estimator is a weighted sum of $n$ importance estimators $f\left(X_{i,j}\right)/p_i\left(X_{i,j}\right)$, each with a sampling method using the probability density function $p_i(x)$ and is weighted by a *weighting function* $w_i(x)$.

$$F_N = \frac{1}{N}\sum_{i=1}^{n}\frac{1}{n_i}\sum_{j=1}^{n_i} w_i\left(X_{i,j}\right)\cdot\frac{f\left(X_{i,j}\right)}{p_i\left(X_{i,j}\right)} \tag{C.15}$$

with $N{=}\sum_{i=1}^{n} n_i$ the total number of samples and $n_i{\ge}1$ the number of samples for estimator $f\left(X_{i,j}\right)/p_i\left(X_{i,j}\right)$. For this estimate to be unbiased, the weighting functions must verify two conditions: (1) $\sum_{i=1}^{n} w_i(x) = 1$ whenever $f(x) > 0$; (2) $w_i(x){=}0$ whenever $p_i(x){=}0$ so that:

$$\mathbb{E}(F_N) = \mathbb{E}\left(\frac{1}{N}\sum_{i=1}^{n}\frac{1}{n_i}\sum_{j=1}^{n_i} w_i\left(X_{i,j}\right)\cdot\frac{f\left(X_{i,j}\right)}{p_i\left(X_{i,j}\right)}\right) = \frac{1}{N}\sum_{i=1}^{n}\frac{1}{n_i}\sum_{j=1}^{n_i}\mathbb{E}\left(w_i\left(X_{i,j}\right)\cdot\frac{f\left(X_{i,j}\right)}{p_i\left(X_{i,j}\right)}\right)$$

$$= \sum_{j=1}^{n_i}\int_x w_i(x)\cdot\frac{f(x)}{p_i(x)}\cdot p_i(x)dx = = \int_x \left(\sum_{j=1}^{n_i} w_i(x)\right)\cdot f(x)dx = \int_x f(x)dx$$

The appropriate weighting functions are crucial to the performance of the multiple importance estimator. (Veach, 1997) proves that the *power heuristic* weighting function works well to estimate the exit radiance (Eq. (1.21)) from a surface with a wide range of roughness, $k{=}2$ is a reasonable value.

$$w_i(x) = \frac{\left(n_i\cdot p_i(x)\right)^k}{\left(\sum_{i'=1}^{n_i} n_{i'}\cdot p_{i'}(x)\right)^k}$$

### C.3.3 Russian roulette

The *Russian roulette* is a useful method to decrease the sample density where the integrand is small. It increases the efficiency of an estimator by increasing the likelihood that each sample will have relatively large contribution to the final estimate. Its general form is

$$F_i^{RR} = \begin{cases}\frac{1}{q}\cdot F_i, & \xi \le q\\ 0, & \xi > q\end{cases}$$

with $F_i$ an estimate of the original estimator $F_N = \sum_{i=1}^{N} F_i$ and $F_i^{RR}$ an estimate of the estimator $F_N^{RR}$ using Russian roulette. $0 < q \leq 1$ is the surviving probability defined so that the sample is rejected if its contribution is small. $\xi$ is a random variable uniformly distributed on $[0, 1)$.

It is obvious that the Russian roulette estimator is unbiased whenever $F_N$ is, since:

$$\mathbb{E}(F_N^{RR}) = \sum_{i=1}^{N} \mathbb{E}(F_i^{RR}) = \sum_{i=1}^{N} \left[ q \cdot \mathbb{E}\left(\frac{1}{q} \cdot F_i\right) + (1-q) \cdot 0 \right] = \sum_{i=1}^{N} \mathbb{E}(F_i) = \mathbb{E}(F_N)$$

whereas it increases the variance:

$$\begin{aligned}
\mathbb{V}(F_N^{RR}) &= \frac{1}{N^2} \mathbb{V}\left(\sum_{i=1}^{N} F_i^{RR}\right) = \frac{1}{N^2} \sum_{i=1}^{N} \sum_{i'=1}^{N} Cov\left(F_i^{RR}, F_{i'}^{RR}\right) \\
&= \frac{1}{N^2} \sum_{i=1}^{N} \sum_{i'=1}^{N} \left[\mathbb{E}\left(F_i^{RR} \cdot F_{i'}^{RR}\right) - \mathbb{E}(F_i^{RR}) \cdot \mathbb{E}\left(F_{i'}^{RR}\right)\right] \\
&= \frac{1}{N^2} \sum_{i=1}^{N} \sum_{i'=1, i' \neq i}^{N} \left[\mathbb{E}\left(F_i^{RR} \cdot F_{i'}^{RR}\right) - \mathbb{E}(F_i^{RR}) \cdot \mathbb{E}\left(F_{i'}^{RR}\right)\right] + \frac{1}{N^2} \sum_{i=1}^{N} \mathbb{E}(F_i^{RR} \cdot F_i^{RR}) \\
&= \frac{1}{N^2} \sum_{i=1}^{N} \sum_{i'=1, i' \neq i}^{N} \left[\mathbb{E}(F_i \cdot F_{i'}) - \mathbb{E}(F_i) \cdot \mathbb{E}(F_{i'})\right] + \frac{1}{N^2} \sum_{i=1}^{N} \frac{\mathbb{E}(F_i^2)}{q} \\
&= \frac{1}{N^2} \sum_{i=1}^{N} \sum_{i'=1}^{N} \left[\mathbb{E}(F_i \cdot F_{i'}) - \mathbb{E}(F_i) \cdot \mathbb{E}(F_{i'})\right] + \frac{1-q}{q \cdot N^2} \cdot \sum_{i=1}^{N} \mathbb{E}(F_i^2) \\
&= \mathbb{V}(F_N) + \frac{1-q}{q \cdot N^2} \cdot \sum_{i=1}^{N} \mathbb{E}(F_i^2) > \mathbb{V}(F_N)
\end{aligned}$$

Nevertheless, the Russian roulette method reduces the computer time by a factor $1 - q$ since only around $q \cdot N$ estimates are really computed. According to Eq. (C.14), if the increase of variance due to the Russian roulette is less than a factor of $1/q$, the overall efficiency is increased. It is particularly useful to optimize the efficiency of the stochastic process in radiative transfer modelling. Indeed, the energy of the radiation decreases almost exponentially through its interactions (absorption, scattering) in the environment, we are facing the problem that the $k$-th interaction takes the same time as the first interaction while its contribution to the final measurement is much smaller. After certain interactions, the radiation trajectory can be cut off by the Russian roulette since the increase of variance is less than the decrease of computer time.

# Annex D

# First and second author publications

## D.1 Article 1

Remote Sensing of Environment 247 (2020) 111902

Contents lists available at ScienceDirect

Remote Sensing of Environment

journal homepage: www.elsevier.com/locate/rse

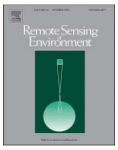

### DART radiative transfer modelling for sloping landscapes

Yingjie Wang*, Nicolas Lauret, Jean-Philippe Gastellu-Etchegorry

*CESBIO, CNES-CNRS-IRD-UPS, University of Toulouse, 31401 Toulouse CEDEX 09, France*

ARTICLE INFO

*Keywords:*
Topography
DART
Infinite slope
Radiative transfer
Environmental effects

ABSTRACT

Topography is one of the key factors that impact remotely sensed data and their interpretation. Indeed, combined with the viewing geometry and neighbour effects, it strongly affects the direct, diffuse and multi-scattered scene irradiance, which in turn impacts the radiative budget and remote sensing signals of the landscapes. The increased availability of digital elevation models (DEM) and the advancement of 3D radiative transfer (RT) models allow us to better address these topographic effects. DART (Discrete Anisotropic Radiative Transfer) is one of the most accurate and comprehensive 3D RT models that simulate remote sensing observations of natural and urban landscapes with topography and atmosphere. It simulates environmental effects (i.e., impact of adjacent landscape on the observed landscape) using a so-called infinite slope mode that infinitely duplicates the observed landscape while ensuring the continuity of slope and altitude at the DEM edges. Up to DART version 5.7.4, this mode was slightly inaccurate and computer intensive, depending on the topography. This paper presents an innovative modelling strategy that greatly improves it in terms of accuracy, image quality and computer efficiency. For that, a fictive auxiliary oblique plane, adapted to the landscape topography, is introduced for managing the scene illumination, the Earth-Atmosphere coupling and the storage of the radiation that exits the scene before being projected onto the sensor plane. Improvements and validations are illustrated both visually and quantitatively by DART images, radiometric products and radiative budget. For example, the observed reflectance of a Lambertian slope is equal to the expected analytical value. In addition, the solar plane reflectance of a forest on a mountain slope (experimental scene) has an average error of about 0.01% relative to the reflectance of the same forest stand in the reference scene (i.e., nine duplications of the experimental scene). This new modelling is already integrated in the official DART version (https://dart.omp.eu).

#### 1. Introduction

Mountain regions cover around a quarter of the Earth's land surface (Liang, 2005) and are home to around one-tenth of the world's population (Denniston, 1996). They also provide vital economic and ecological resources to the world's population, thanks to their rich biodiversity, water-storing capacity, mineral reserve, *etc* (Price, 1998). Therefore, mountain areas are more and more surveyed with remote sensing (RS) data (Boori et al., 2015; Barrachina et al., 2015; Reinhold and Schläpfer, 2011; Santini and Palombo, 2019), notably through the development of numeric models (Table 1).

Empirical models (e.g., Cosine Correction, C correction, SCS) are the simplest and most practical for topographic correction, but the lack of generality and physical considerations limits their accuracy. Geometric optical models (e.g., GOMST, GOST) use a geometric approach to quantify how canopy directional reflectance depends on slopes, solar direct irradiance and 3D tree crowns. However, they usually neglect sky diffuse illumination and multiple scattering in landscapes. Also, the solo

# D.2 Article 2

Remote Sensing of Environment 251 (2020) 112082

Contents lists available at ScienceDirect

Remote Sensing of Environment

journal homepage: www.elsevier.com/locate/rse

## DART: Improvement of thermal infrared radiative transfer modelling for simulating top of atmosphere radiance

Yingjie Wang*, Jean-Philippe Gastellu-Etchegorry

*CESBIO, CNES-CNRS-IRD-UPS, University of Toulouse, 31401, Toulouse, CEDEX 09, France*

A R T I C L E  I N F O

*Keywords:*
DART
Radiative transfer
Atmosphere
Thermal infrared
Absorption cross-section
MODTRAN

A B S T R A C T

Land surface temperature (LST) is increasingly needed for studying the functioning of the Earth's surface at local to global scale. Radiative transfer (RT) models that simulate top of atmosphere (TOA) radiance are essential tools to derive accurate LST from thermal infrared (TIR) signals of Earth observation (EO) satellites. DART (Discrete Anisotropic Radiative Transfer) is one of the most accurate and comprehensive three-dimensional models that simulate RT in the Earth-atmosphere system. Up to version 5.7.3, the mean absolute error (MAE) of DART atmospheric TIR radiance of six standard atmospheres (USSTD76, TROPICAL, MIDDLATSUM, MIDDLATWIN, SUBARCSUM, SUBARCWIN) over 3.5 μm - 20 μm was 3.1 K compared to the reference atmospheric RT model MODTRAN, which is much larger than the 1 K accuracy needed by most LST applications. Also, the radiance error reached 2.6 K for some TIR bands whereas the noise equivalent differential temperature (NeDT) of satellite TIR sensor is usually less than 0.4 K. Recently, the DART atmospheric RT modelling was greatly improved by (1) introducing the equivalent absorption cross-section of five most absorbing gases ($H_2O$, $CO_2$, $O_3$, $CH_4$, $N_2O$), and (2) implementing a double-layer thermal emission method. The MAE of DART atmospheric TIR radiance of six standard atmospheres and actual atmospheres over France and the Mediterranean Sea is now better than 1.0 K. The band radiance error is less than 0.2 K in the EO satellite TIR bands. DART is still accurate if the temperature profiles of standard atmospheres are offset by less than 6 K and if the viewing zenith angle is less than 50°. In short, the improved DART meets the requirements of both LST applications, and present and future TIR EO satellite missions. It is already available to scientists (https://dart.omp.eu).

### 1. Introduction

Land surface temperature (LST) has a wide range of applications in different fields: evapotranspiration, soil moisture, precision agriculture, urban climate, river environments, oceanography, etc. (Dugdale, 2016; Khanal et al., 2017; Kilpatrick et al., 2015; Voogt and Oke, 2003; Wang et al., 2006; Wang and Qu, 2009). Due to its high temporal resolution, broad coverage and low cost, thermal infrared (TIR) remote sensing is an ideal tool to measure LST (Li et al., 2013). Therefore, an increasing number of space missions embark sensors with TIR bands. For example, the Trishna mission of French Space Agency (CNES) and Indian Space Research Organization (ISRO), to be launched in 2024–2025, will embark a sensor that has four TIR bands with noise equivalent differential temperature (NeDT) of 0.3 K at 300 K (Lagouarde et al., 2018). The sea and land surface temperature radiometer on board the European Space Agency (ESA) Sentinel 3 satellite has three TIR bands with NeDT of 0.05 K at 270 K (Donlon et al., 2012). The National Aeronautics and Space Administration (NASA) Landsat 8 satellite has a TIR sensor with NeDT of 0.4 K at 300 K (Irons et al., 2012). Landsat 9 satellite, due to be launched on 2021, should embark a TIR sensor similar to the Landsat 8 TIR sensor (McCorkel et al., 2018).

Most LST applications require accuracy less than 1 K (Sobrino et al., 2016). Although the sensibility (NeDT) of most satellite TIR sensors is less than 0.4 K, the LST derived from remotely sensed data is usually less accurate, mainly due to atmospheric conditions, topography, land surface heterogeneity, and directional effects (Bento et al., 2017; Bonafoni, 2016; Ermida et al., 2018; He et al., 2019; Price, 1983; Vermote et al., 2002). Therefore, there is a need to better link LST and observations from satellite TIR sensors. Physical models that accurately simulate TIR radiative transfer (RT) in the Earth-atmosphere system are essential tools. However, most RT models are either for the atmosphere (e.g., 4A/OP, MODTRAN, LBLRTM, RFM, ARTS) or for the Earth surfaces (e.g., Rayspread, RAPID3, FLiES, SAIL) (Berk et al., 2015; Buehler et al., 2018; Clough et al., 2005; Huang, 2018; Kobayashi and Iwabuchi, 2008; Scott, 1974; Verhoef, 1984; Vincent and Dudhia, 2017; Widlowski et al., 2006). DART (Discrete Anisotropic Radiative

---

* Corresponding author.
*E-mail address:* yingjiewang1102@gmail.com (Y. Wang).

https://doi.org/10.1016/j.rse.2020.112082
Received 11 July 2019; Received in revised form 26 August 2020; Accepted 6 September 2020

## D.3 Article 3

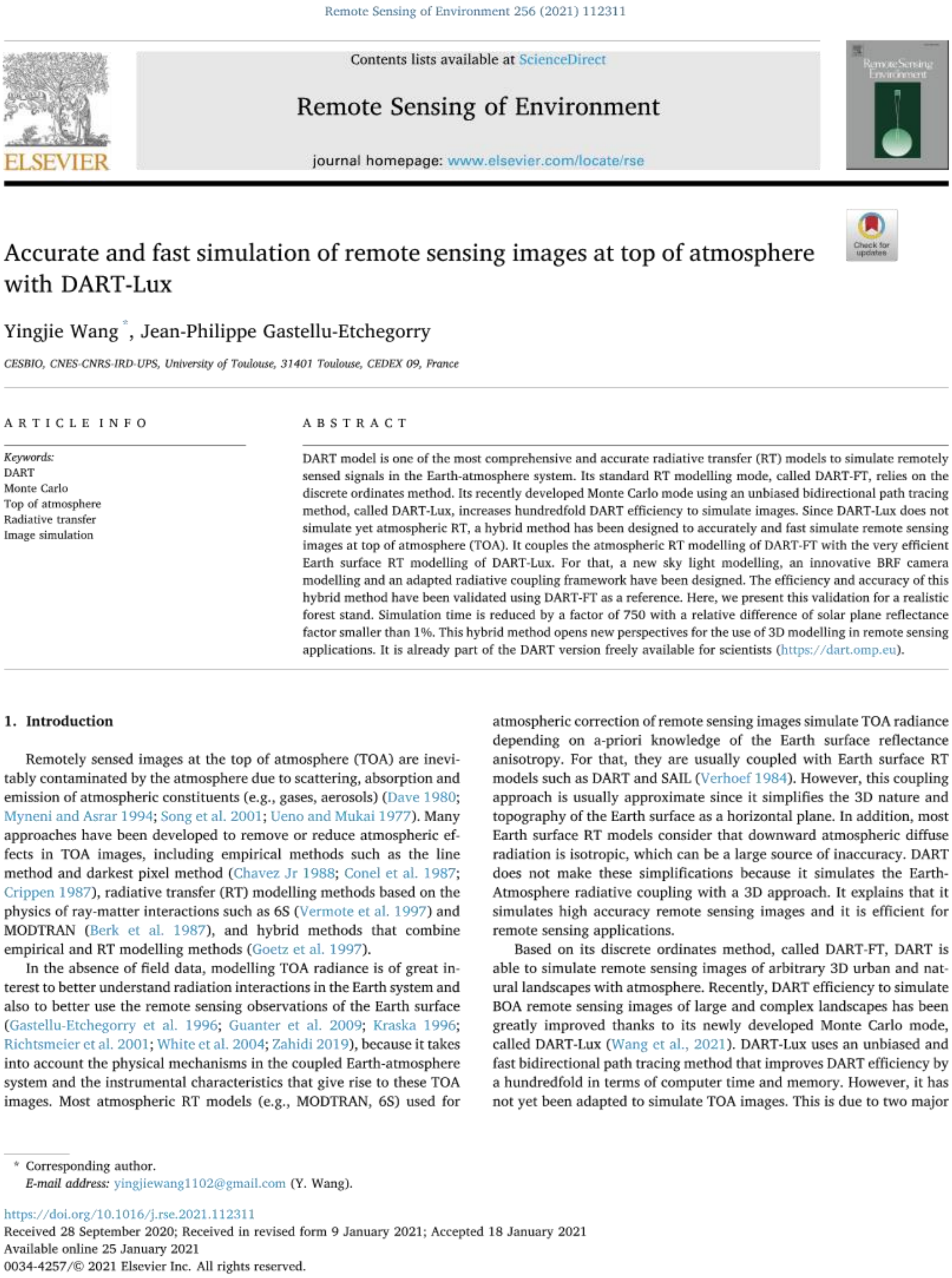

Remote Sensing of Environment 256 (2021) 112311

Contents lists available at ScienceDirect

Remote Sensing of Environment

journal homepage: www.elsevier.com/locate/rse

# Accurate and fast simulation of remote sensing images at top of atmosphere with DART-Lux

Yingjie Wang *, Jean-Philippe Gastellu-Etchegorry

*CESBIO, CNES-CNRS-IRD-UPS, University of Toulouse, 31401 Toulouse, CEDEX 09, France*

ARTICLE INFO

*Keywords:*
DART
Monte Carlo
Top of atmosphere
Radiative transfer
Image simulation

ABSTRACT

DART model is one of the most comprehensive and accurate radiative transfer (RT) models to simulate remotely sensed signals in the Earth-atmosphere system. Its standard RT modelling mode, called DART-FT, relies on the discrete ordinates method. Its recently developed Monte Carlo mode using an unbiased bidirectional path tracing method, called DART-Lux, increases hundredfold DART efficiency to simulate images. Since DART-Lux does not simulate yet atmospheric RT, a hybrid method has been designed to accurately and fast simulate remote sensing images at top of atmosphere (TOA). It couples the atmospheric RT modelling of DART-FT with the very efficient Earth surface RT modelling of DART-Lux. For that, a new sky light modelling, an innovative BRF camera modelling and an adapted radiative coupling framework have been designed. The efficiency and accuracy of this hybrid method have been validated using DART-FT as a reference. Here, we present this validation for a realistic forest stand. Simulation time is reduced by a factor of 750 with a relative difference of solar plane reflectance factor smaller than 1%. This hybrid method opens new perspectives for the use of 3D modelling in remote sensing applications. It is already part of the DART version freely available for scientists (https://dart.omp.eu).

### 1. Introduction

Remotely sensed images at the top of atmosphere (TOA) are inevitably contaminated by the atmosphere due to scattering, absorption and emission of atmospheric constituents (e.g., gases, aerosols) (Dave 1980; Myneni and Asrar 1994; Song et al. 2001; Ueno and Mukai 1977). Many approaches have been developed to remove or reduce atmospheric effects in TOA images, including empirical methods such as the line method and darkest pixel method (Chavez Jr 1988; Conel et al. 1987; Crippen 1987), radiative transfer (RT) modelling methods based on the physics of ray-matter interactions such as 6S (Vermote et al. 1997) and MODTRAN (Berk et al. 1987), and hybrid methods that combine empirical and RT modelling methods (Goetz et al. 1997).

In the absence of field data, modelling TOA radiance is of great interest to better understand radiation interactions in the Earth system and also to better use the remote sensing observations of the Earth surface (Gastellu-Etchegorry et al. 1996; Guanter et al. 2009; Kraska 1996; Richtsmeier et al. 2001; White et al. 2004; Zahidi 2019), because it takes into account the physical mechanisms in the coupled Earth-atmosphere system and the instrumental characteristics that give rise to these TOA images. Most atmospheric RT models (e.g., MODTRAN, 6S) used for atmospheric correction of remote sensing images simulate TOA radiance depending on a-priori knowledge of the Earth surface reflectance anisotropy. For that, they are usually coupled with Earth surface RT models such as DART and SAIL (Verhoef 1984). However, this coupling approach is usually approximate since it simplifies the 3D nature and topography of the Earth surface as a horizontal plane. In addition, most Earth surface RT models consider that downward atmospheric diffuse radiation is isotropic, which can be a large source of inaccuracy. DART does not make these simplifications because it simulates the Earth-Atmosphere radiative coupling with a 3D approach. It explains that it simulates high accuracy remote sensing images and it is efficient for remote sensing applications.

Based on its discrete ordinates method, called DART-FT, DART is able to simulate remote sensing images of arbitrary 3D urban and natural landscapes with atmosphere. Recently, DART efficiency to simulate BOA remote sensing images of large and complex landscapes has been greatly improved thanks to its newly developed Monte Carlo mode, called DART-Lux (Wang et al., 2021). DART-Lux uses an unbiased and fast bidirectional path tracing method that improves DART efficiency by a hundredfold in terms of computer time and memory. However, it has not yet been adapted to simulate TOA images. This is due to two major

---

* Corresponding author.
*E-mail address:* yingjiewang1102@gmail.com (Y. Wang).

https://doi.org/10.1016/j.rse.2021.112311
Received 28 September 2020; Received in revised form 9 January 2021; Accepted 18 January 2021

## D.4 Article 4

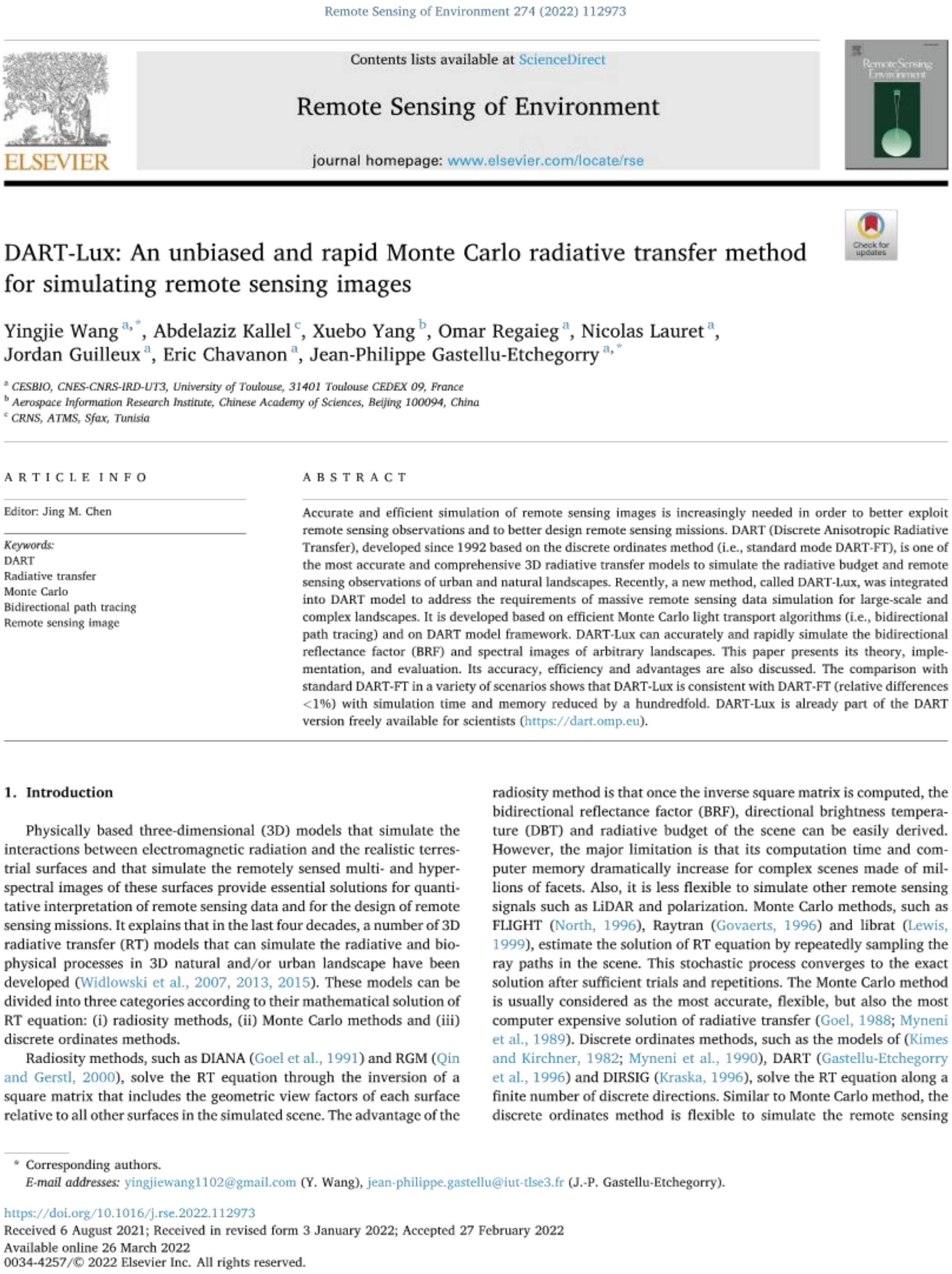

Remote Sensing of Environment 274 (2022) 112973

Contents lists available at ScienceDirect

Remote Sensing of Environment

journal homepage: www.elsevier.com/locate/rse

# DART-Lux: An unbiased and rapid Monte Carlo radiative transfer method for simulating remote sensing images

Yingjie Wang [a,*], Abdelaziz Kallel [c], Xuebo Yang [b], Omar Regaieg [a], Nicolas Lauret [a], Jordan Guilleux [a], Eric Chavanon [a], Jean-Philippe Gastellu-Etchegorry [a,*]

[a] *CESBIO, CNES-CNRS-IRD-UT3, University of Toulouse, 31401 Toulouse CEDEX 09, France*
[b] *Aerospace Information Research Institute, Chinese Academy of Sciences, Beijing 100094, China*
[c] *CRNS, ATMS, Sfax, Tunisia*

ARTICLE INFO

Editor: Jing M. Chen

*Keywords:*
DART
Radiative transfer
Monte Carlo
Bidirectional path tracing
Remote sensing image

ABSTRACT

Accurate and efficient simulation of remote sensing images is increasingly needed in order to better exploit remote sensing observations and to better design remote sensing missions. DART (Discrete Anisotropic Radiative Transfer), developed since 1992 based on the discrete ordinates method (i.e., standard mode DART-FT), is one of the most accurate and comprehensive 3D radiative transfer models to simulate the radiative budget and remote sensing observations of urban and natural landscapes. Recently, a new method, called DART-Lux, was integrated into DART model to address the requirements of massive remote sensing data simulation for large-scale and complex landscapes. It is developed based on efficient Monte Carlo light transport algorithms (i.e., bidirectional path tracing) and on DART model framework. DART-Lux can accurately and rapidly simulate the bidirectional reflectance factor (BRF) and spectral images of arbitrary landscapes. This paper presents its theory, implementation, and evaluation. Its accuracy, efficiency and advantages are also discussed. The comparison with standard DART-FT in a variety of scenarios shows that DART-Lux is consistent with DART-FT (relative differences <1%) with simulation time and memory reduced by a hundredfold. DART-Lux is already part of the DART version freely available for scientists (https://dart.omp.eu).

## 1. Introduction

Physically based three-dimensional (3D) models that simulate the interactions between electromagnetic radiation and the realistic terrestrial surfaces and that simulate the remotely sensed multi- and hyperspectral images of these surfaces provide essential solutions for quantitative interpretation of remote sensing data and for the design of remote sensing missions. It explains that in the last four decades, a number of 3D radiative transfer (RT) models that can simulate the radiative and biophysical processes in 3D natural and/or urban landscape have been developed (Widlowski et al., 2007, 2013, 2015). These models can be divided into three categories according to their mathematical solution of RT equation: (i) radiosity methods, (ii) Monte Carlo methods and (iii) discrete ordinates methods.

Radiosity methods, such as DIANA (Goel et al., 1991) and RGM (Qin and Gerstl, 2000), solve the RT equation through the inversion of a square matrix that includes the geometric view factors of each surface relative to all other surfaces in the simulated scene. The advantage of the radiosity method is that once the inverse square matrix is computed, the bidirectional reflectance factor (BRF), directional brightness temperature (DBT) and radiative budget of the scene can be easily derived. However, the major limitation is that its computation time and computer memory dramatically increase for complex scenes made of millions of facets. Also, it is less flexible to simulate other remote sensing signals such as LiDAR and polarization. Monte Carlo methods, such as FLIGHT (North, 1996), Raytran (Govaerts, 1996) and librat (Lewis, 1999), estimate the solution of RT equation by repeatedly sampling the ray paths in the scene. This stochastic process converges to the exact solution after sufficient trials and repetitions. The Monte Carlo method is usually considered as the most accurate, flexible, but also the most computer expensive solution of radiative transfer (Goel, 1988; Myneni et al., 1989). Discrete ordinates methods, such as the models of (Kimes and Kirchner, 1982; Myneni et al., 1990), DART (Gastellu-Etchegorry et al., 1996) and DIRSIG (Kraska, 1996), solve the RT equation along a finite number of discrete directions. Similar to Monte Carlo method, the discrete ordinates method is flexible to simulate the remote sensing

---

[*] Corresponding authors.
*E-mail addresses:* yingjiewang1102@gmail.com (Y. Wang), jean-philippe.gastellu@iut-tlse3.fr (J.-P. Gastellu-Etchegorry).

https://doi.org/10.1016/j.rse.2022.112973
Received 6 August 2021; Received in revised form 3 January 2022; Accepted 27 February 2022

## D.5 Article 5

Remote Sensing of Environment 272 (2022) 112952

Contents lists available at ScienceDirect

Remote Sensing of Environment

journal homepage: www.elsevier.com/locate/rse

# Comprehensive LiDAR simulation with efficient physically-based DART-Lux model (I): Theory, novelty, and consistency validation

Xuebo Yang [a,b,c,*], Yingjie Wang [c], Tiangang Yin [d], Cheng Wang [a], Nicolas Lauret [c], Omar Regaieg [c], Xiaohuan Xi [a], Jean Philippe Gastellu-Etchegorry [c,**]

[a] *Aerospace Information Research Institute, Chinese Academy of Sciences, Beijing 100094, China*
[b] *China National Laser Products Quality Supervising Test Center, Beijing 100094, China*
[c] *Centre d'Etudes Spatiales de la BIOsphère (CESBIO) – Université de Toulouse, UT3, CNES, CNRS, IRD, 31401 Toulouse Cedex 9, France*
[d] *Earth System Science Interdisciplinary Center, University of Maryland, College Park, MD 20740-3823, USA*

ARTICLE INFO

Editor: Jing M. Chen

*Keywords:*
LiDAR
Radiative transfer model
DART
Bidirectional path tracing
Monte Carlo

ABSTRACT

Light Detection And Ranging (LiDAR) remote sensing is increasingly needed to assess the 3D architecture of Earth's surface. Physically-based LiDAR radiative transfer (RT) models are essential tools for interpreting LiDAR signals, designing LiDAR systems, and validating information retrieval methods. Discrete Anisotropic Radiative Transfer (DART) is one of the most accurate and comprehensive 3D RT models that simulate LiDAR signals of urban and natural landscapes. Its physical modeling relies on a forward Monte Carlo mode optimized by a ray-tracing technique, also called DART-RC (Ray Carlo) mode. However, DART-RC is not adapted to simulate massive LiDAR signals of large landscapes due to its constraints of high memory demand and long computational time. Therefore, we developed a novel computationally efficient LiDAR modeling method based on a new DART modeling mode called DART-Lux. It simulates LiDAR signal by adapting the bidirectional path tracing algorithm of DART-Lux to the time and power measurements and by implementing the LiDAR instrument and multiple product outputs in DART-Lux. We verified the accuracy of DART-Lux for LiDAR modeling using DART-RC as a reference for several case studies with different LiDAR configurations (*i.e.*, single-pulse waveform, multi-pulse point cloud, multi-pulse photon counting, with and without solar signal) on realistic scenes from the RAMI experiment. Results stress that i) DART-Lux is consistent with DART-RC, for example, $R^2 = 1$ and rRMSE = 0.21% for the waveform of a forest simulated with a huge number of rays; ii) DART-Lux converges faster than DART-RC: its processing time is usually about half that of DART-RC, and over ten times smaller if the solar signal is simulated; iii) DART-Lux memory usage can be a hundred times less than DART-RC. Also, several sensitivity studies with various sensor configurations and solar directions illustrate the usefulness of DART-Lux for impact studies. This new DART-Lux LiDAR model opens promising perspectives for large-scale LiDAR applications with 3D modeling. It is already part of the official DART version freely available to scientists (https://dart.omp.eu).

### 1. Introduction

Light Detection And Ranging (LiDAR) is a well-developed active remote sensing (RS) technology that maps three-dimensional (3D) structures of Earth's landscapes by measuring time of flight of laser pulses (Wulder et al., 2012). With its advantage of 3D spatial measurement, LiDAR is widely used in many domains: topography surveying (Jaboyedoff et al., 2012), virtual smart city (Dwivedi et al., 2014), atmosphere constituent (Weitkamp, 2006), forest biomass monitoring (Zhao et al., 2018), *etc.* Driven by various application requirements and increasingly advanced devices, LiDAR system is developing towards more sophisticated instruments with higher pulse repetition frequency (PRF), higher ranging accuracy, longer battery life, *etc.* For instance, multiple spaceborne LiDAR missions were successively launched in the past twenty years, including ICESat (Ice, Cloud, and land Elevation Satellite) (Zwally et al., 2002), ICESat-2 (Markus et al., 2017), and GEDI (Global Ecosystem Dynamics Investigation) (Dubayah et al., 2020). The PRF of these LiDAR missions increases from 40 Hz for ICESat up to 242

---

* Corresponding author at: Aerospace Information Research Institute, Chinese Academy of Sciences, Beijing 100094, China.
** Corresponding author.
*E-mail addresses:* yangxb@aircas.ac.cn (X. Yang), jean-philippe.gastellu@cesbio.cnes.fr (J.P. Gastellu-Etchegorry).

https://doi.org/10.1016/j.rse.2022.112952
Received 14 September 2021; Received in revised form 13 January 2022; Accepted 5 February 2022

# Annex E

# My contributions to DART-Lux

DART-Lux development is a collaborative work constantly contributed by physicists (Gastellu-Etchegorry Jean-Philippe, Kallel Abdelaziz, Paugam Ronan, Reigaieg Omar, Yang Xuebo, Yin Tiangang), remote sensing researchers (Benromdhane Najmeddine, Boitard Paul, Malenovsky Zbynek, Zhen Zhijun, …), and computer scientists (Chavanon Eric, Guilleux Jordan, Lauret Nicolas). The following table details my contributions to DART-Lux since the first idea in 2018.

Table E.1. Indication of the works I have done (red colour) and where my contribution has been important (blue colour).

| Date | Contribution(s) |
|---|---|
| 2019-04 | - Theory and algorithm (Georgiev et al., 2012; Pharr et al., 2016; Veach, 1997)<br>- Parallel sun light<br>- Preliminary validation tests |
| 2019-12 | - Isotropic/anisotropic sky light modelling |
| 2020-04 | - LiDAR laser and receiver modelling<br>- LiDAR waveform modelling<br>- SIF emission |
| 2020-08 | - BRF camera modelling<br>- Hybrid atmospheric RT method to simulate satellite and airborne images |
| 2020-12 | - Monte Carlo atmospheric radiative transfer modelling |
| 2021-04 | - LiDAR modelling with atmosphere |
| 2021-08 | - RPV model |
| 2021-12 | - Atmospheric thermal emission |
| 2022-04 | - Specular surface BSDF<br>- Microfacets rough surface BSDF<br>- Atmospheric polarized radiative transfer |
| 2022-08 | - Land surface polarized radiative transfer |

# Annex F

## Functionalities of 3D RTMs

Since the emergence of pioneering 3D RTMs designed to simulate the radiative transfer in land surfaces in the 1980s, their functionalities are continuously improved and completed with respect to the increasing requirements of scientific and societal applications. At the same time, many new 3D RTMs are developed. Table F.1 lists major characteristics of some of the best 3D RTMs as provided by their authors.

Table F.1 Functionalities of 3D RTMs (Green: YES; Orange: POSSIBLY; Red: NO), with corresponding references.

| **Model name** | **Radiative transfer method(s)** | **References** |
|---|---|---|
| DART | MC/DOM | (Gastellu-Etchegorry et al., 1996)<br>(Wang et al., 2022) |
| DIRSIG | MC | (Kraska, 1996)<br>(Goodenough and Brown, 2017) |
| Eradiate | MC | (https://www.eradiate.eu/site/) |
| FLiES | MC | (Kobayashi and Iwabuchi, 2008)<br>(Gao et al., 2022) |
| FLIGHT | MC | (North, 1996)<br>(Hornero et al., 2021) |
| LCVRT | MC | (Kallel and Gastellu-Etchegorry, 2017)<br>(Kallel, 2020) |
| LESS | MC | (Qi et al., 2019a) |
| Librat | MC | (Lewis, 1999) |
| MCScene | MC | (Richtsmeier et al., 2001)<br>(Richtsmeier et al., 2017) |
| RAPID | Radiosity | (Huang et al., 2013)<br>(Huang, 2018) |
| Raytran | MC | (Govaerts et al., 1996)<br>(Widlowski et al., 2006) |
| WPS | MC | (Zhao et al., 2015)<br>(Zhao et al., 2022) |

# *ANNEX F: FUNCTIONALITIES OF 3D RTMS*

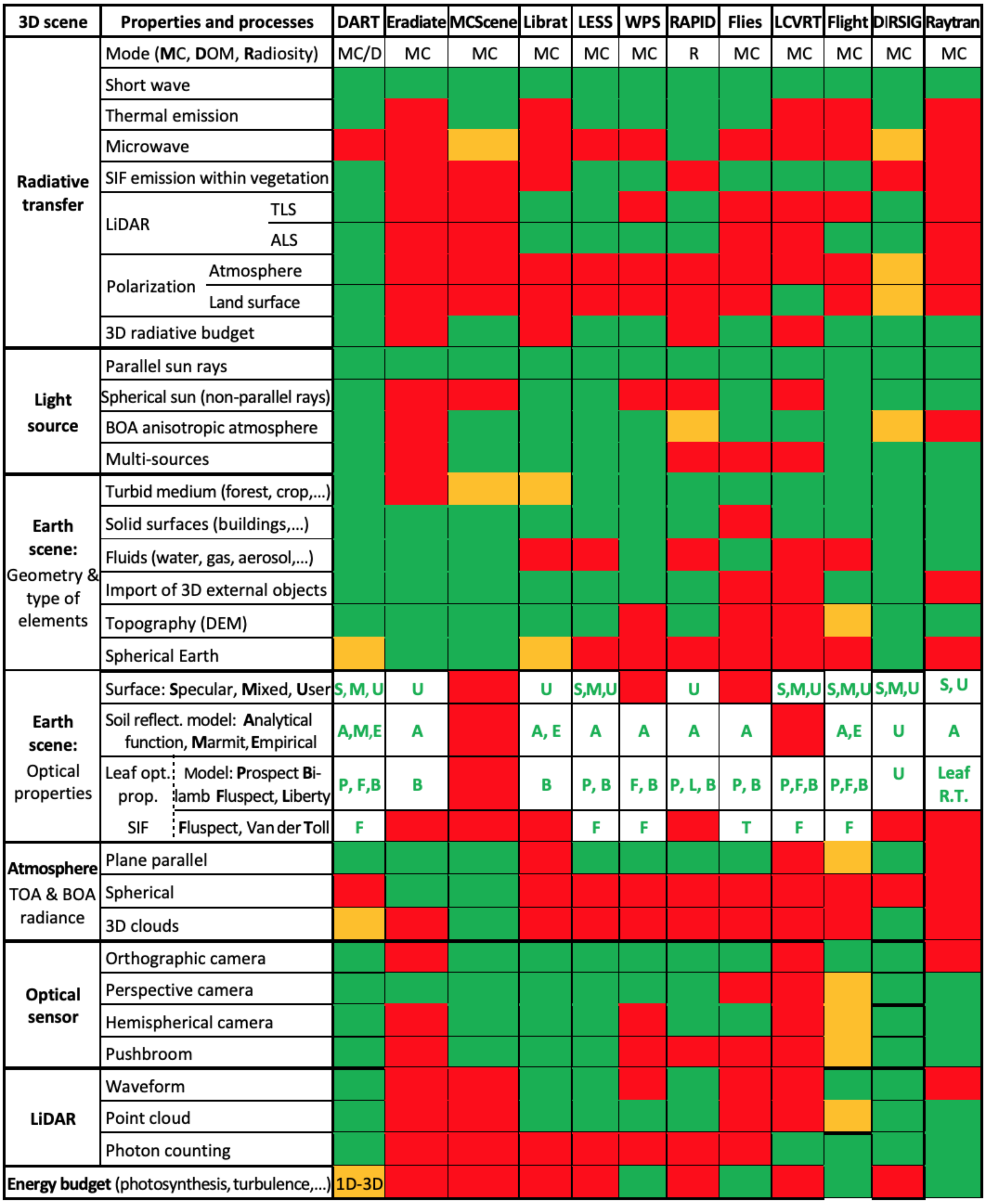

| 3D scene | Properties and processes | | DART | Eradiate | MCScene | Librat | LESS | WPS | RAPID | Flies | LCVRT | Flight | DIRSIG | Raytran |
|---|---|---|---|---|---|---|---|---|---|---|---|---|---|---|
| **Radiative transfer** | Mode (**M**C, **D**OM, **R**adiosity) | | MC/D | MC | MC | MC | MC | MC | R | MC | MC | MC | MC | MC |
| | Short wave | | 🟩 | 🟩 | 🟩 | 🟩 | 🟩 | 🟩 | 🟩 | 🟩 | 🟩 | 🟩 | 🟩 | 🟩 |
| | Thermal emission | | 🟩 | 🟥 | 🟩 | 🟥 | 🟩 | 🟩 | 🟩 | 🟩 | 🟥 | 🟥 | 🟩 | 🟥 |
| | Microwave | | 🟥 | 🟥 | 🟨 | 🟥 | 🟥 | 🟥 | 🟩 | 🟥 | 🟥 | 🟥 | 🟨 | 🟥 |
| | SIF emission within vegetation | | 🟩 | 🟥 | 🟥 | 🟥 | 🟩 | 🟩 | 🟥 | 🟩 | 🟩 | 🟩 | 🟥 | 🟥 |
| | LiDAR | TLS | 🟩 | 🟥 | 🟥 | 🟩 | 🟩 | 🟥 | 🟩 | 🟥 | 🟥 | 🟥 | 🟩 | 🟥 |
| | | ALS | 🟩 | 🟥 | 🟥 | 🟩 | 🟩 | 🟩 | 🟩 | 🟥 | 🟥 | 🟩 | 🟩 | 🟥 |
| | Polarization | Atmosphere | 🟩 | 🟥 | 🟥 | 🟥 | 🟥 | 🟥 | 🟥 | 🟥 | 🟥 | 🟥 | 🟨 | 🟥 |
| | | Land surface | 🟩 | 🟥 | 🟥 | 🟥 | 🟥 | 🟥 | 🟥 | 🟥 | 🟩 | 🟥 | 🟨 | 🟥 |
| | 3D radiative budget | | 🟩 | 🟥 | 🟩 | 🟥 | 🟩 | 🟩 | 🟥 | 🟩 | 🟥 | 🟩 | 🟩 | 🟩 |
| **Light source** | Parallel sun rays | | 🟩 | 🟩 | 🟩 | 🟩 | 🟩 | 🟩 | 🟩 | 🟩 | 🟩 | 🟩 | 🟩 | 🟩 |
| | Spherical sun (non-parallel rays) | | 🟩 | 🟥 | 🟥 | 🟩 | 🟩 | 🟥 | 🟥 | 🟩 | 🟥 | 🟩 | 🟩 | 🟩 |
| | BOA anisotropic atmosphere | | 🟩 | 🟥 | 🟩 | 🟩 | 🟩 | 🟩 | 🟨 | 🟩 | 🟩 | 🟩 | 🟨 | 🟥 |
| | Multi-sources | | 🟩 | 🟥 | 🟩 | 🟩 | 🟩 | 🟩 | 🟥 | 🟥 | 🟥 | 🟩 | 🟩 | 🟩 |
| **Earth scene:** Geometry & type of elements | Turbid medium (forest, crop,…) | | 🟩 | 🟥 | 🟨 | 🟨 | 🟩 | 🟩 | 🟩 | 🟩 | 🟩 | 🟩 | 🟩 | 🟩 |
| | Solid surfaces (buildings,…) | | 🟩 | 🟩 | 🟩 | 🟩 | 🟩 | 🟩 | 🟩 | 🟥 | 🟩 | 🟩 | 🟩 | 🟩 |
| | Fluids (water, gas, aerosol,…) | | 🟩 | 🟩 | 🟩 | 🟥 | 🟥 | 🟩 | 🟥 | 🟩 | 🟥 | 🟥 | 🟩 | 🟩 |
| | Import of 3D external objects | | 🟩 | 🟩 | 🟩 | 🟩 | 🟩 | 🟩 | 🟩 | 🟥 | 🟥 | 🟩 | 🟩 | 🟥 |
| | Topography (DEM) | | 🟩 | 🟩 | 🟩 | 🟩 | 🟩 | 🟥 | 🟩 | 🟥 | 🟥 | 🟨 | 🟩 | 🟩 |
| | Spherical Earth | | 🟨 | 🟩 | 🟩 | 🟨 | 🟥 | 🟥 | 🟥 | 🟥 | 🟥 | 🟥 | 🟩 | 🟥 |
| **Earth scene:** Optical properties | Surface: **S**pecular, **M**ixed, **U**ser | | S, M, U | U | 🟥 | U | S,M,U | 🟥 | U | 🟥 | S,M,U | S,M,U | S,M,U | S, U |
| | Soil reflect. model: **A**nalytical function, **M**armit, **E**mpirical | | A,M,E | A | 🟥 | A, E | A | A | A | A | 🟥 | A,E | U | A |
| | Leaf opt. prop. | Model: **P**rospect **B**i-lamb **F**luspect, **L**iberty | P, F,B | B | 🟥 | B | P, B | F, B | P, L, B | P, B | P,F,B | P,F,B | U | Leaf R.T. |
| | SIF | **F**luspect, Van der **T**oll | F | 🟥 | 🟥 | 🟥 | F | F | 🟥 | T | F | F | 🟥 | 🟥 |
| **Atmosphere** TOA & BOA radiance | Plane parallel | | 🟩 | 🟩 | 🟩 | 🟥 | 🟩 | 🟩 | 🟩 | 🟩 | 🟥 | 🟨 | 🟩 | 🟥 |
| | Spherical | | 🟥 | 🟩 | 🟩 | 🟥 | 🟥 | 🟥 | 🟥 | 🟥 | 🟥 | 🟥 | 🟥 | 🟥 |
| | 3D clouds | | 🟨 | 🟥 | 🟩 | 🟥 | 🟥 | 🟥 | 🟥 | 🟥 | 🟥 | 🟥 | 🟩 | 🟥 |
| **Optical sensor** | Orthographic camera | | 🟩 | 🟥 | 🟩 | 🟩 | 🟩 | 🟩 | 🟩 | 🟩 | 🟥 | 🟩 | 🟩 | 🟥 |
| | Perspective camera | | 🟩 | 🟩 | 🟩 | 🟩 | 🟩 | 🟩 | 🟩 | 🟥 | 🟥 | 🟨 | 🟩 | 🟩 |
| | Hemispherical camera | | 🟩 | 🟥 | 🟩 | 🟩 | 🟩 | 🟥 | 🟩 | 🟩 | 🟥 | 🟨 | 🟩 | 🟩 |
| | Pushbroom | | 🟩 | 🟥 | 🟩 | 🟩 | 🟩 | 🟥 | 🟥 | 🟥 | 🟥 | 🟨 | 🟩 | 🟩 |
| **LiDAR** | Waveform | | 🟩 | 🟥 | 🟥 | 🟩 | 🟩 | 🟥 | 🟩 | 🟥 | 🟥 | 🟩 | 🟩 | 🟥 |
| | Point cloud | | 🟩 | 🟥 | 🟥 | 🟩 | 🟩 | 🟩 | 🟩 | 🟥 | 🟥 | 🟨 | 🟩 | 🟩 |
| | Photon counting | | 🟩 | 🟥 | 🟥 | 🟥 | 🟥 | 🟥 | 🟥 | 🟥 | 🟩 | 🟩 | 🟩 | 🟩 |
| **Energy budget** (photosynthesis, turbulence,…) | | | 1D-3D | 🟥 | 🟥 | 🟥 | 🟥 | 🟩 | 🟥 | 🟩 | 🟥 | 🟩 | 🟥 | 🟩 |

# Annex G

# Nomenclature

The following tables provide a list of the acronyms and variables utilized in this thesis. The acronyms are listed alphabetically. The variables are arranged alphabetically starting with English letters, followed by Greek letters.

| **Acronym** | **Description** |
|---|---|
| BDPT | Bi-directional path tracing |
| BRF | Bidirectional reflectance factor |
| BRDF | Bidirectional reflectance distribution function |
| BSDF | Bidirectional scattering distribution function |
| BTDF | Bidirectional transmittance distribution function |
| BOA | Bottom of atmosphere |
| CDF | Cumulative distribution function |
| DART | Discrete anisotropic radiative transfer |
| DART-FT | Classic discrete ordinates radiative transfer mode of DART model |
| DART-Lux | New Monte Carlo radiative transfer mode of DART model |
| DBT | Directional brightness temperature |
| DEM | Digital elevation model |
| ECMWF | European centre for medium-range weather forecasts |
| FOV | Field of view |
| IPRT | International polarized radiative transfer |
| LiDAR | Light detection and ranging |
| MIS | Multiple importance sampling |
| PDF | Probability distribution function |

| | |
|---|---|
| PSF | Point spread function |
| RAMI | Radiation transfer model intercomparison |
| RMSE | Root mean square error |
| RPV | Rahman-Pinty-Verstraete reflectance model |
| RTM | Radiative transfer model |
| SIF | Solar induced fluorescence |
| TOA | Top of atmosphere |

| Symbol | Description |
|---|---|
| $\mathcal{A}(\lambda)$ | Absorptance |
| $\mathcal{A}_D(\lambda,\Omega)$ | Directional absorptance |
| $\mathcal{A}_{\mathrm{H}}(\lambda)$ | Hemispherical absorptance |
| $A$ | All surfaces of the scene |
| $A_{\mathrm{img}}^{(j)}$ | Area of pixel *j* |
| $c$ | Speed of light |
| $c_0$ | Speed of light in vacuum |
| $C_{\mathcal{D}_n}$ | Contribution to radiance measurement of the $(n-1)$-th scattering order |
| $Cov(X,Y)$ | Covariance of variable $X$ and $Y$ |
| $\mathcal{D}$ | Set of all light paths |
| $D_{\mathrm{m}}(\Omega_{\mathrm{f}})$ | Microfacet distribution function |
| $\mathcal{D}_n$ | Set of paths of length *n* |
| $E(\lambda)$ | Irradiance |
| $E_{\mathrm{BOA}}$ | Irradiance at bottom of atmosphere |
| $E_{\mathrm{BOA}}^{\mathrm{dir}}$ | Direct irradiance at bottom of atmosphere |
| $E_{\mathrm{BOA}}^{\mathrm{diff}}$ | Diffuse irradiance at bottom of atmosphere |
| $E_{\mathrm{TOA}}^{\mathrm{dir}}$ | Direct irradiance at top of atmosphere |
| $\mathbb{E}(X)$ | Expected value of variable *X* |
| $F_{\mathrm{IS}}^{(j)}$ | Estimate of the importance sampling |
| $F_{\mathrm{MIS}}^{(j)}$ | Estimate of the multiple importance sampling |
| $f_r(\lambda,\Omega'\to\Omega)$ | Bidirectional reflectance distribution function |
| $f_t(\lambda,\Omega'\to\Omega)$ | Bidirectional transmittance distribution function |
| $f_s(\lambda,\Omega'\to\Omega)$ | Bidirectional scattering distribution function |
| $f_s^*(\lambda,\Omega'\to\Omega)$ | Adjoint bidirectional scattering distribution function |
| $\boldsymbol{f_s}(\lambda,\Omega'\to\Omega)$ | Bidirectional scattering matrix |
| $\boldsymbol{f_s}^*(\lambda,\Omega'\to\Omega)$ | Adjoint bidirectional scattering matrix |
| $\tilde{f}_s(\lambda,\Omega'\to\Omega)$ | Generalized scattering distribution function |
| $\tilde{f}_s^*(\lambda,\Omega'\to\Omega)$ | Generalized adjoint scattering distribution function |
| $\tilde{\boldsymbol{f}}_{\boldsymbol{s}}(\lambda,\Omega'\to\Omega)$ | Generalized scattering matrix |
| $\tilde{\boldsymbol{f}}_{\boldsymbol{s}}^*(\lambda,\Omega'\to\Omega)$ | Generalized adjoint scattering matrix |
| $f^{(j)}(\bar{r})$ | Measurement contribution function of path $\bar{r}$ at pixel *j* |

| | |
|---|---|
| $\boldsymbol{f}^{(j)}(\bar{r})$ | Vector measurement contribution function of path $\bar{r}$ at pixel $j$ |
| g | Asymmetry parameter of scattering phase function |
| $G(r' \leftrightarrow r'')$ | Geometric term |
| $\tilde{G}(r' \leftrightarrow r'')$ | Generalized geometric term |
| $G_{\mathrm{m}}(\Omega, \Omega_{\mathrm{f}})$ | Masking-shadowing function |
| $I(\lambda)$ | Radiant intensity |
| $\mathcal{J}_T$ | Jacobian determinant |
| $\mathbf{K}_e(\lambda, \Omega)$ | Extinction matrix |
| $L(\lambda, \Omega)$ | Radiance |
| $\tilde{L}(\lambda, \Omega)$ | Generalized effective radiance |
| $\tilde{\boldsymbol{L}}(\lambda, \Omega)$ | Generalized effective radiance vector averaged over particle state |
| $L_i(\lambda, \Omega)$ | Incident radiance |
| $L_r(\lambda, \Omega)$ | Reflected radiance |
| $L_t(\lambda, \Omega)$ | Transmitted radiance |
| $L_o(\lambda, \Omega)$ | Exit radiance |
| $L_e(\lambda, \Omega)$ | Scalar thermal emitted radiance |
| $L_{\mathrm{adj}}$ | Adjacency radiance |
| $\bar{L}_{\mathrm{adj}}$ | Average adjacency radiance of the study area |
| $L_{\mathrm{B}}(\lambda, T)$ | Blackbody emission |
| $\mathcal{M}$ | All surfaces or volumes of the scene, depending on the vertex location |
| $M(\lambda)$ | Exitance |
| $\mathbf{M}(\lambda, \Omega' \rightarrow \Omega)$ | Scattering matrix |
| $\mathbf{M_r}(\lambda, \Omega' \rightarrow \Omega)$ | Reduced Rayleigh scattering matrix |
| $n(\lambda)$ | Refractive index |
| $P(\lambda, \Omega' \rightarrow \Omega)$ | Scattering phase function |
| $\mathbf{P}(\lambda, \Omega' \rightarrow \Omega)$ | Phase matrix |
| $\mathbb{P}(E_A)$ | Probability of event $E_A$ |
| $P_X(x)$ | Cumulative distribution function of variable $X$ |
| $P_{Y\|X}(y\|x)$ | Conditional cumulative distribution function of variable $Y$ given $X$ |
| $p(x)$ | Probability density function of variable $X$ |
| $p(y\|x)$ | Conditional probability density function of variable $Y$ given $X$ |
| $\bar{p}_{N_v}$ | Light sub-path with $N_v$ vertices |

| | |
|---|---|
| $Q(\lambda)$ | Perpendicular/parallel polarization |
| $\bar{q}_{N_v}$ | Sensor sub-path with $N_v$ vertices |
| $\mathcal{R}(\lambda)$ | Reflectance |
| $\mathcal{R}_{\mathrm{DD}}(\lambda, \Omega' \rightarrow \Omega)$ | Bidirectional reflectance |
| $\mathcal{R}_{\mathrm{DH}}(\lambda, \Omega)$ | Directional-hemispherical reflectance |
| $\mathcal{R}_{\mathrm{HH}}(\lambda)$ | Albedo |
| $\mathbf{R}(\eta)$ | Rotation matrix, $\eta > 0$ indicates anticlockwise rotation |
| $\bar{r}$ | Light path connecting the light source and the sensor |
| $\bar{r}_{s,t}$ | Light rath generated by connecting a light sub-path with $s$ vertices and a sensor sub-path with $t$ vertices. |
| $S(\lambda)$ | Sensor response |
| $\boldsymbol{S}(\lambda)$ | Stokes vector |
| $T$ | Temperature |
| $\mathcal{T}(\lambda)$ | Transmittance |
| $\mathcal{T}_{\mathrm{DD}}(\lambda, \Omega' \rightarrow \Omega)$ | Bidirectional transmittance |
| $\mathcal{T}_{\mathrm{DH}}(\lambda, \Omega)$ | Directional-hemispherical transmittance |
| $\mathcal{T}_{\mathrm{HH}}(\lambda)$ | Bi-hemispherical transmittance |
| $T_{\mathrm{B}}(\lambda, \Omega)$ | Brightness temperature |
| $T(\bar{p}_s)$ | Throughput of sub-path $\bar{p}_s$ |
| $\boldsymbol{T}(\bar{p}_s)$ | Throughput vector of sub-path $\bar{p}_s$ |
| $T(\bar{q}_t)$ | Throughput of sub-path $\bar{q}_t$ |
| $\boldsymbol{T}(\bar{q}_t)$ | Throughput matrix of sub-path $\bar{q}_t$ |
| $U(\lambda)$ | Diagonal polarization |
| $V(\lambda)$ | Circular polarization |
| $V(r' \leftrightarrow r'')$ | Visibility function between vertices $r'$ and $r''$ |
| $V$ | All volumes of the scene |
| $\mathbb{V}(X)$ | Variance of variable $X$ |
| $W_e(r_0, \Omega_0)$ | Importance function |
| $W_e{}^{(j)}(r_0, \Omega_0)$ | Importance function in the support of pixel *j* |
| $\boldsymbol{W_e}(r_0, \Omega_0)$ | Importance matrix |
| $\boldsymbol{W_e}{}^{(j)}(r_0, \Omega_0)$ | Importance matrix in the support of pixel *j* |
| $w_{s,t}(\bar{r}_{s,t})$ | MIS weight of path sample $\bar{r}_{s,t}$ |
| $\alpha_e(\lambda, \Omega)$ | Extinction coefficient |

| | |
|---|---|
| $\alpha_a(\lambda,\Omega)$ | Absorption extinction coefficient |
| $\alpha_s(\lambda,\Omega)$ | Scattering extinction coefficient |
| $\delta(x)$ | Dirac function |
| $\Delta_m$ | Relative root mean square difference |
| $\varepsilon(\lambda)$ | Emissivity |
| $\varepsilon_{\mathrm{D}}(\lambda,\Omega)$ | Directional Emissivity |
| $\varepsilon_{\mathrm{H}}(\lambda)$ | Hemispherical Emissivity |
| $\epsilon$ | Efficiency of a Monte Carlo method |
| $\zeta_{\mathrm{adj}}$ | Adjacency perturbation |
| $\theta$ | Zenith angle |
| $\lambda$ | Wavelength of radiation |
| $\Delta\lambda$ | Spectral region or bandwidth |
| $\lambda_0$ | Wavelength of radiation in vacuum |
| $\mu(\bar{r})$ | Area-product measure of path $\bar{r}$ |
| $\nu$ | Frequency of radiation |
| $\xi$ | Random variable between 0 and 1 |
| $2\pi^+$ | Surface upper hemisphere that contains the incident radiation |
| $2\pi^-$ | Surface lower hemisphere that contains the transmitted radiation |
| $\rho(\lambda)$ | Reflectance factor |
| $\rho(\lambda,\Omega' \rightarrow \Omega)$ | Bidirectional reflectance factor |
| $\sigma_e(\lambda,\Omega)$ | Extinction cross section |
| $\sigma_a(\lambda,\Omega)$ | Absorption extinction cross section |
| $\sigma_s(\lambda,\Omega)$ | Scattering extinction cross section |
| $\tau(\lambda,\Omega)$ | Optical depth |
| $\varphi$ | Azimuth angle |
| $\Phi(\lambda)$ | Radiant flux |
| $\chi$ | Size parameter |
| $\omega(\lambda,\Omega)$ | Single scattering albedo |
| $\Omega$ | Direction vector |